Stimuli-Responsive Liquid Crystal Elastomer Microparticles

James Taylor

Submitted for the degree of Doctor of Philosophy

Lancaster University

Department of Chemistry

2019

Abstract

This thesis centres on the creation of nematic and chiral nematic polymer and elastomer microparticles, with defined confinement textures due to surface anchoring from the host solvent, using a series of novel nematic and chiral nematic monomers. Droplets were produced using a homemade microfluidic technique and photo-polymerised into particles, followed by an analysis of the responsive properties. The synthesis of nematic and chiral nematic monomers, polymers and elastomers, as well as the characterisation of their thermal and optical properties is presented. Chiral nematic mixtures were polymerised into thin-films capable of visible selective reflection and which experience a pitch contraction upon removal of a chiral dopant. The design and development of a microfluidic chip to create monodisperse droplets is discussed. The droplets were photo-polymerised by two methods into elastomer particles and the reversible shape change responses to temperature were analysed. Monodisperse chiral nematic droplets and particles were made, using the monomer mixtures established together with the microfluidic technique developed, and concluded with an investigation of the responsiveness of the particles to external stimuli.

Table of Contents

Table of Figures

Table of Schemes

Table of Tables

List of Abbreviations

AR	Aspect ratio
$A_{\parallel}$	Absorbed light parallel to the director
$A_{\perp}$	Absorbed light perpendicular to the director
Bn	Benzyl group
Bp	Boiling point
br, m	Broad multiplet
br, s	Broad singlet
C*a*	Capillary number
CB15	(*S*)-4'-(2-Methylbutyl)-4-cyanobiphenyl
$CDCl_3$	Deuterated chloroform
$CHCl_3$	Chloroform
CL	Crosslinker
Cr	Crystalline
CV	Coefficient of variation
d	Doublet
D	Initial isotropic droplet diameter
D_{LC}	Final liquid crystal droplet diameter
DCM	Dichloromethane
dd	Doublet of doublets
DIAD	Diisopropyl azodicarboxylate
DMAP	4-Dimethylaminopyridine
DMF	Dimethylformamide
DP	Degree of polymerisation
DR	Dichroic ratio
DSC	Differential scanning calorimetry
EA	Elemental analysis
EDAC	1-Ethyl-3-(3-dimethylaminopropyl)carbodiimide
ESI	Electrospray ionisation
EtOAc	Ethyl acetate
EtOH	Ethanol
FT-IR	Fourier transform infra-red
F_v	Contribution to Frank free energy from distortion
g	Grams

g mol^{-1}	Grams per mole
GPC	Gel permeation chromatography
H_2O_2	Hydrogen peroxide
hrs	Hours
HTP	Helical twisting power
Iso	Isotropic phase
IR	Infrared
K_{11}	Splay elastic constant
K_{22}	Twist elastic constant
K_{33}	Bend elastic constant
$KHCO_3$	Potassium hydrogen carbonate
L	Linear dimension of fluid flow
$l_{nematic}$	Particle length in the nematic phase
l_{iso}	Particles length in the isotropic phase
LC	Liquid crystal
LCE	Liquid crystal elastomer
LCP	Liquid crystal polymer
m	Multiplet
MCLCP	Main chain liquid crystal polymer
mg	Milligrams
$MgSO_4$	Magnesium sulphate
mm	Millimetre
M_n	Number average molecular weight
mmol	Millimoles
mol	Moles
mol%	Percentage by moles
Mp	Melting point
HRMS	High resolution mass spectrometry
M_w	Weight average molecular weight
m/z	Mass to charge ratio
N	Nematic phase
N*	Chiral nematic phase
$\bar{n}$	Average refractive index
n_e	Extraordinary refractive index
NIR	Near infrared
nm	Nanometre

NMR	Nuclear Magnetic Resonance
n_o	Ordinary refractive index
o/w	Oil in water emulsion
p	Pitch
Pd/C	Palladium on carbon
PDI	Polydispersity index
POM	Polarised optical microscopy
PEG200	Polyethylene glycol (M_w: 200 g mol^{-1})
PVA	Poly(vinyl alcohol)
ppm	Parts per million
q	Quartet
Q	Velocity of the outer fluid flow
$R_{\parallel}$	Polymerisation rate parallel to the director
$R_{\perp}$	Polymerisation rate perpendicular to the director
R*e*	Reynolds number
S	Order parameter
s	Singlet
SANS	Small angle neutron scattering
SCLCP	Side chain liquid crystal polymer
SEM	Scanning electron microscopy
SmA	Smectic A phase
SmC	Smectic C phase
T	Temperature
t	Triplet
T_g	Glass transition temperature
THF	Tetrahydrofuran
TLC	Thin layer chromatography
T_{NI}	Nematic to isotropic transition temperature
TPP	Triphenylphosphine
u	Velocity of a fluid
UV	Ultraviolet
Vis	Visible
w/o	Water in oil emulsion
wt%	Percentage by weight
w/v	Weight by volume
w/w	Weight by weight

5CB	4’-Pentyl-4-cyanobiphenyl
Δn	Birefringence
ΔP	Interfacial Laplace pressure
γ	Interfacial tension
η	Viscosity of the outer fluid
λ	Wavelength
σ	Standard deviation/interfacial tension
θ	Angle
μ	Mean
μL	Microliter
μm	Micrometre
ν	Kinematic viscosity of a fluid
χ	Volume ratio of liquid crystal to chloroform

List of Accompanying Material

Accompanying this thesis is a CD-ROM which can be found in an envelope on the inside back cover and contains videos referred to in Chapter 4.

Acknowledgements

Firstly, I would like to thank my supervisor Verena Görtz for allowing me the opportunity to work on such a great project. You put a lot of trust in me, supported me when things got tough and showed huge amounts of patience. Without you this would not have been possible.

I'd like to thank the inhabitants of Faraday Building C Floor, in particular Charlie, Patch, David and Tom for their friendship, laughter and the many nights out in Lancaster. Thanks to Alex for always checking up on me and to Elizabeth and the Thornton Gals for ensuring I've been well looked after this past year.

Finally, to Mum and Dad, for supporting me through this whole journey.

Author’s Declaration

I declare that this thesis is my own work and has not been submitted for the award of a higher degree elsewhere.

Word Count: 56,210

Chapter 1:

Introduction

1 Introduction

1.1 Thesis Overview

Liquid crystals have long been studied in planar topologies. However, confined to droplets, they present unique optical textures and properties. Transformation of droplets into harder particles by polymerisation allows for more robust applications, and responsive elastomers that exhibit useful shape changing potential can be created through the addition of a crosslinker. The focus of this thesis centres on the creation of nematic and chiral nematic polymer and elastomer microparticles, using a series of novel nematic and chiral nematic monomers, with defined confinement textures. Droplets were produced using a homemade microfluidic technique and photo-polymerised into particles, followed by an analysis of the responsive properties.

The fundamental background to discuss the nematic and chiral nematic liquid crystals within this thesis is presented in Chapter 1. It introduces the field of liquid crystal polymers and elastomers as well as covering the confinement of nematic and chiral nematic liquid crystals to spherical geometries and the unique phenomenon of selective reflection. The synthesis of the nematic and chiral nematic monomers, polymers and elastomers, as well as the characterisation of their thermal and optical properties is discussed in Chapter 2. Leading on from this, Chapter 3 describes the fabrication of chiral nematic thin-films capable of visible selective reflection and which experience a pitch contraction upon removal of a chiral dopant. Chapter 4 introduces the area of microfluidics and chronicles the development and design of a microfluidic chip to create monodisperse droplets. The droplets were photo-polymerised by two methods and the resulting polymer and elastomer particles' reversible shape change responses to temperature were analysed. Chapter 5 ties a number of strands together by discussing the creation of monodisperse chiral nematic droplets and particles, using the mixtures established in Chapter 3 and the microfluidic technique developed in Chapter 4, and the investigation of the particles' responsiveness to temperature and pressure. Finally, the conclusions of the project are summarised in Chapter 6 and the synthetic experimental procedures and results detailed in Chapter 7.

1.2 Liquid Crystals - Fundamentals

The development of liquid-crystalline materials over the past 50 years has arguably been one of the principal contributors to the rapid technological development of our society. Their now ubiquitous use in display technology has allowed the development of applications that would have been hard to imagine at the time of their initial discovery in 1888 by Friedrich Reinitzer when studying derivatives of cholesterol.[1]

Liquid crystals are a fourth state of matter, being the intermediate state between the solid crystalline state and the liquid state.[2] They possess properties of both, such as long-range order and fluidity, from which new and useful properties arise. The ordering, or self-organisation, of the liquid crystal state is a consequence of the shape of the molecules (referred to as mesogens) and the intermolecular forces between them. A thermotropic liquid crystal phase arises when mesogens possess an anisometric shape, of which there are two extremes: calamitic (rod-like) and discotic (disk-like). A calamitic liquid crystal has the dimensions $l >> w$ (where l is the length and w is the width), whilst a discotic liquid crystal has $w >> l$, as shown in Figure 1.1.

On heating a thermotropic liquid-crystalline material from the solid state, a phase transition to the liquid crystal phase occurs. Phase transitions that occur on heating and cooling are known as enantiotropic phase transitions, while ones that only occur on cooling are known as monotropic phase transitions. The temperature at which a phase transition into the isotropic liquid phase occurs is known as the clearing point. There are many different liquid-crystalline phases now known, the most common being the smectic A (SmA), smectic C (SmC), and nematic phases (N) as shown in Figure 1.2. The nematic phase is the most disordered of the liquid crystal phases and so typically appears at higher temperatures than any smectic phases for a particular compound. The mesogens possess

Figure 1.1 Cartoon representation of calamitic (left) and discotic (right) liquid crystal molecules illustrating the different aspect ratios.

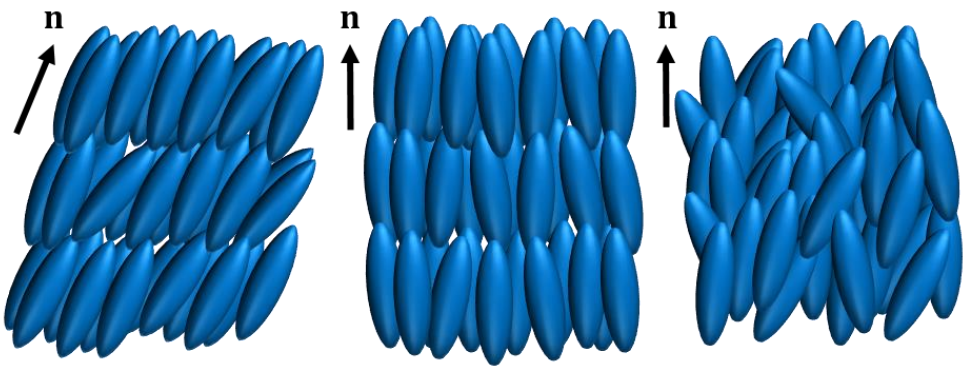

Figure 1.2. The orientation of molecules within the common calamitic liquid crystal phases: smectic C (SmC), smectic A (SmA) and nematic (N). The director of each phase is indicated by an arrow.

no positional order but do have long-range orientational order. The smectic phases have both positional order (possessing a layered periodicity) and orientational order (all pointing in a similar direction). In the smectic A phase, the mesogens have a periodic layered ordering, with the long axis of the molecule perpendicular to the layer normal. The smectic C phase is similar to the smectic A phase, however the molecules are tilted with respect to the layers. The focus of this thesis will be on thermotropic materials that display a nematic phase, and its chiral counterpart, the chiral nematic phase.

1.3 The Nematic Phase

1.3.1 Structure of Mesogens

The chemical structure of a material has profound effects on its liquid-crystalline behaviour. The general structure of a rod-like nematic liquid crystal is illustrated in Figure 1.3. Often, the core of the molecule (A and B) is composed of rigid benzene ring moieties to maintain the overall rod-like shape and increase the nematic phase stability, with linking groups (X) to extend the molecular length. Flexible alkyl chains (R and R') can be attached to the periphery, also contributing to the overall length of the molecule and therefore aiding the intermolecular ordering. The length of these peripheral chains can be important in influencing the phase stability (T_{MI}) of the liquid crystal phases - longer chain lengths generally depress the clearing point. Further modification *via* lateral substitution (Y and Z in Figure 1.3) can also have important consequences to the material's properties, such as birefringence, by altering the dielectric anisotropy.

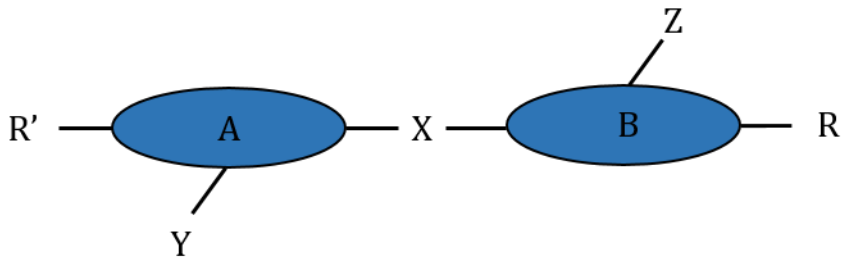

Figure 1.3. The general structure of a rod-like nematogen.

1.3.2 Order Parameter

As previously mentioned, the mesogens in the nematic phase possess long-range orientational order. Locally they behave as a disordered fluid, but their molecular axes are statistically averaged to point in one direction called the director, **n** (Figure 1.2). The nematic phase typically has a low viscosity, due to the low degree of order, which allows it to be easily influenced by external fields - something that is exploited in their use in electronic displays.

The degree of order in a nematic phase can be expressed as an order parameter, S (Equation 1.1). It can be calculated by averaging the angle, θ, between the director and the molecular axis of the mesogen, over a time period. Thus, for an isotropic liquid $S = 0$, whilst for a perfect crystal $S = 1$. Nematic liquid crystals typically have order parameters in the range 0.3-0.8.[2] The order parameter is temperature dependent, gradually decreasing with increasing temperature, before abruptly becoming equal to zero at the phase transition.

$$S = \left\langle \frac{3\cos^2\theta - 1}{2} \right\rangle \qquad \text{Equation 1.1}$$

1.3.3 Birefringence

For an optically isotropic material the refractive index is the same in all directions. However, for a uniaxial anisotropic material, such as a nematic liquid crystal, there are two refractive indices in orthogonal directions. Light that is polarised parallel to the director is termed the extraordinary ray and has an index of refraction n_e, whilst the ordinary ray polarised perpendicular to the director has a refractive index n_o. The difference between the two is the birefringence (Equation 1.2) and can be positive or negative.

$$\Delta n = n_e - n_o \qquad \text{Equation 1.2}$$

This has important consequences when viewing a liquid crystal between two polarisers crossed at 90° to each other. Light that has passed through the first polariser will have a certain linear polarisation. As the light propagates through the liquid crystal, the ordinary and extraordinary rays travel at different speeds and so when they emerge they do so out of phase, by an amount called optical retardation. A portion of this light is therefore able to pass through the second polariser to the observer. Since optical retardation not only depends on the thickness of the sample but also is dependent on the wavelength, some wavelengths pass through with more intensity than others, resulting in a coloured image. A maximum brightness can be obtained by rotating the director to 45° relative to the polarisers. However, if the director of the sample is parallel with either polariser, or the sample is viewed down the optic axis of the molecule, light only experiences a single refractive index. This results in the polarisation state remaining unchanged; therefore, light is extinguished by the second polariser and a dark region is observed.[2]

1.3.4 Elasticity

The director of a liquid crystal phase is not fixed and can be distorted by external influences or surfaces - it possesses elasticity. A uniform director would be the lowest energy state and so the liquid crystal seeks to minimise any elastic distortion. The splay (K_{11}), twist (K_{22}) and bend (K_{33}) elastic constants govern the energetics of each distortion and are unique to each material. As it may be expected, they are positively dependent on the order parameter of the phase but typically are about 10^{-11} N.[2] The free energy per unit volume of a nematic liquid crystal is given in Equation 1.3, where F_v is the contribution to the free energy, K_{11}, K_{22} and K_{33} are the elastic constants, and n is the director.

$$F_V = \frac{1}{2}\mathrm{K}_{11}[\nabla \cdot \mathrm{n}]^2 + \frac{1}{2}\mathrm{K}_{22}[\mathrm{n} \cdot (\nabla \times \mathrm{n})]^2 + \frac{1}{2}\mathrm{K}_{33}[\mathrm{n} \times (\nabla \times \mathrm{n})]^2 \qquad \text{Equation 1.3}$$

The most energetically favourable elastic deformation will be the most likely to be observed. The splay deformation causes the director to ‘fan out’ from a point, the twist deformation results in the director rotating around a perpendicular axis and the bend deformation causes the director to turn in the same plane (Figure 1.4).

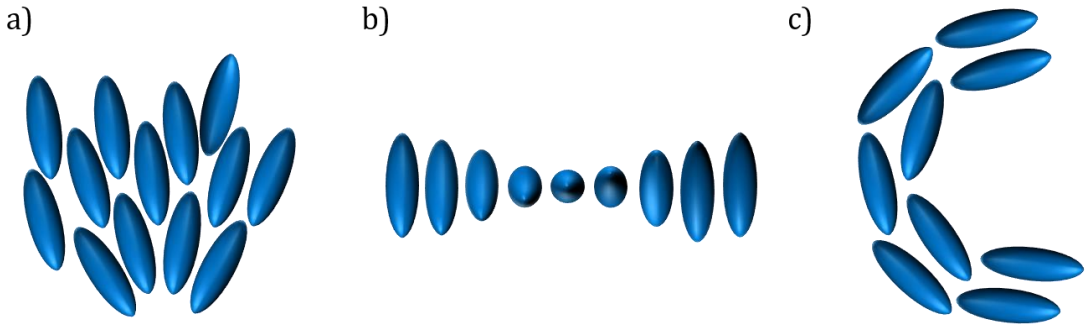

Figure 1.4. The elastic deformations of a nematic liquid crystal: a) Splay (K_{11}) b) Twist (K_{22}) c) Bend (K_{33}).

1.3.5 Defects and Textures

Despite the lowest energy director state being uniform, in the absence of any external influences, there can be instances where the director is undefined. This leads to the formation of a defect, however, as mentioned above, the liquid crystal seeks to minimise the energetic cost. When viewed through crossed polarisers, defects appear as either two or four-brushes, due to extinction, depending on how the mesogens are aligned around the defect, as illustrated in Figure 1.5.

The characteristic optical textures that result from the birefringence, described in 1.3.3, and the observed defects allow for the identification of liquid crystal phases through polarised optical microscopy (POM). For example, a typical texture for the nematic phase is the *schlieren* texture, as shown in Figure 1.6.

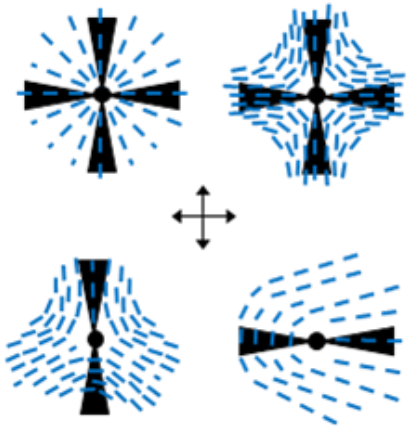

Figure 1.5. Cartoon illustrating some possible orientations of nematic liquid crystal mesogens resulting in defects and the corresponding brushes observed through crossed polarisers. Adapted from reference [2].

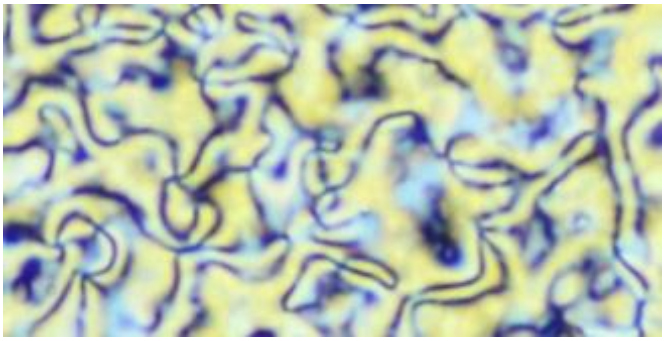

Figure 1.6. Polarised photomicrograph of the *schlieren* texture of the nematic phase of **M1** (refer to page 18/Figure 1.17 for structure) on cooling from the isotropic phase. Due to the lack of a surface alignment layer, resulting in a polydomain alignment of the mesogens, many defects connected by *schlieren* brushes are observed.

For many applications, it is critical to create a defect-free sample and therefore it is necessary to align the orientation of the mesogens throughout. This can be achieved through the application of external electric or magnetic fields, or through a surface treatment. A common approach is to sandwich the liquid crystal between two glass surfaces treated with a rubbed polymer such as polyimide or an amphiphile such as Lecithin; chosen to encourage the mesogens to orient parallel (homogeneous) or perpendicular (homeotropic) to the surface respectively, as illustrated in Figure 1.7. The chain orientation of the polymer can be distorted by rubbing with a cloth fibre and it is from this that orientation is transferred to the liquid crystal.[3] However, the penetration depth of this aligning effect is only a few μm so alignment cells are limited in thickness. The confinement of a liquid crystal to a spherical geometry leads to the generation of point defects either on the surface or in the centre of the droplet but this will be discussed later.

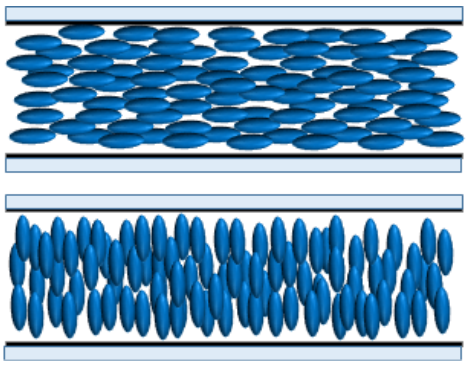

Figure 1.7. Cartoon demonstrating the orientation of nematic liquid crystal molecules in a cell with an alignment layer promoting homogeneous alignment (top) and homeotropic alignment (bottom).

1.4 The Chiral Nematic Phase

1.4.1 Formation

A molecule that has an absence of symmetry, and therefore a non-superimposable mirror image, is known as a chiral molecule. Commonly, this is created through the inclusion of a chiral centre, where an sp^3 carbon atom is bound to four distinct chemical components, and leads to (*R*) and (*S*) enantiomers that are mirror images (Figure 1.8). The interaction with plane polarised light, where one enantiomer rotates it in one direction, and the other enantiomer in the opposite direction, is termed its optical activity.

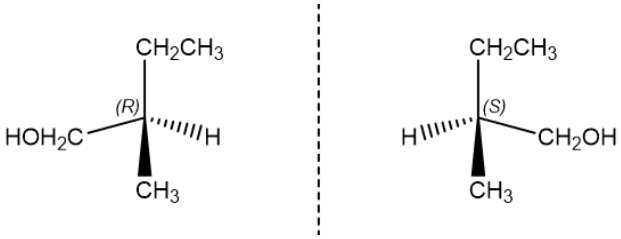

Figure 1.8. The (*R*) and (*S*) enantiomers of 2-methylbutan-1-ol.

If some, or all, of the molecules of a liquid crystal mixture are chiral, the molecular chirality typically alters the supramolecular arrangement such that macroscopic chiral phase properties are observed. Within the chiral nematic phase (N*) the mesogens behave locally as a nematic, however over a longer range a helical superstructure manifests itself perpendicular to the director, with a handedness that relates to the enantiomer. The director rotates 360° over a distance referred to as the pitch, *p*, as shown in Figure 1.9.

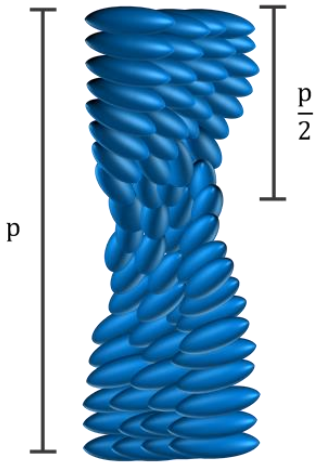

Figure 1.9. The supramolecular helix of the chiral nematic phase. The director repeats every $p/2$.

However, because the director is defined as **n** = **-n** the pitch actually repeats itself twice for every full 360° rotation.[4] The phase stability of a chiral nematic material is typically reduced compared to its achiral analogue as the asymmetry leads to a perturbation of the packing and therefore a reduction in the stabilisation energy. This can present challenges depending on the intended application and so requires careful molecular design. The N* phase can also be induced by mixing a small amount of an enantiopure chiral dopant such as CB15 (Figure 1.10) with an achiral nematic host material. The dopant should preferably have a similar structure to encourage mixing and prevent phase separation.

$$HTP = \frac{1}{p \cdot c} \qquad \text{Equation 1.3}$$

The helical twisting power (HTP), expressed in μm^{-1}, is a measure of how the dopant influences the twisting of the helix (Equation 1.3) and by varying the concentration of the dopant, *c*, the pitch can be proportionally increased or decreased.[5] However, a dopant generally acts as a contaminant that supresses the clearing point, therefore using a dopant with a large HTP is desirable as this minimises the amount required for a given pitch and the disruption to the phase stability.

In addition to varying the concentration of a chiral dopant, the pitch length of a chiral nematic has a temperature dependence. In the majority of chiral nematic materials, a decrease in pitch with increasing temperature is observed. It has been proposed that thermal expansion can cause an increase in the pitch but a competing mechanism of increasing thermal motion of the mesogens leads to an increased angle of rotation of the director and therefore a decrease in the pitch.[5] Likewise, at lower temperatures the pitch increases as the molecular motion is reduced and the twisting angle decreases.

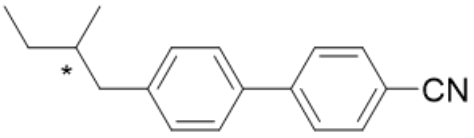

Figure 1.10. The chiral dopant 4'-(2-methylbutyl)-4-cyanobiphenyl (CB15).

1.4.2 Alignment and Textures

Like the nematic phase, the chiral nematic phase can be identified from characteristic textures using polarised optical microscopy of a sample. The alignment of the helix relative to the substrate determines which texture is observed; homeotropic alignment

leads to the *fingerprint* texture, the *Grandjean* texture is characteristic of homogeneous alignment and a multi-domain alignment leads to a *focal conic* texture.[6] Homeotropic alignment of a chiral nematic with a long pitch (in the μm range) leads to the observation of repeating dark bands, from which the pitch can be calculated (Figure 1.11, a), whilst with a short pitch the texture can appear uniform and exhibit optical extinction on rotation, like a nematic or smectic A phase. The *Grandjean* texture is identified by 'oily streaks' (Figure 1.11, b) - defect lines between well-orientated domains, although with time these can disappear to leave a uniform colour that does not vary with rotation. The pitch length can be calculated from the reflection or transmission spectrum and the observed λ_{max}, as discussed below. The *focal conic* texture arises from a more random alignment of the helical axis and is highly light scattering (Figure 1.11, c).

Figure 1.11. Polarised photomicrographs of the chiral nematic phase taken from reference [6]: a) the *fingerprint* texture due to homeotropic alignment, b) the *Grandjean* texture arising from homogeneous alignment, c) the *focal conic* texture of a short pitch chiral nematic.

1.4.3 Selective Reflection

When both the N* helix is aligned in a *Grandjean* alignment and the wavelength of incident light approximately equals the pitch, an optical phenomenon known as selective reflection can occur. This is a Bragg-like reflection where the wavelength reflected has an angular dependence described using Equation 1.4, where *n* is the average refractive index, *p* is the helical pitch length and θ is the angle of incidence from the normal.

$$\lambda = npcos\theta \qquad \text{Equation 1.4}$$

Linearly polarised incident light can be thought of as having a left and right circular polarisation that interacts with the chiral helix. Wavelengths of light, centred on $\lambda_{max,}$ matching the pitch and handedness of the N* helix are forbidden from propagating through the sample and are reflected, whilst the opposite handedness is transmitted

(Figure 1.12). The bandwidth of this reflected light is related to the birefringence (Equation 1.5) and so for a narrow-band reflection a small birefringence is required, while conversely a large birefringence leads to wide-band reflection.[5]

$$\Delta\lambda = \Delta np \qquad \text{Equation 1.5}$$

If these wavelengths reside in the visible region, the sample appears coloured to the naked eye and is the reason chiral nematic materials have found widespread use as temperature sensors. Due to the temperature dependence of the pitch, a blue-shift on heating and a red-shift on cooling is common, correlating with a shortening and lengthening of the pitch respectively.

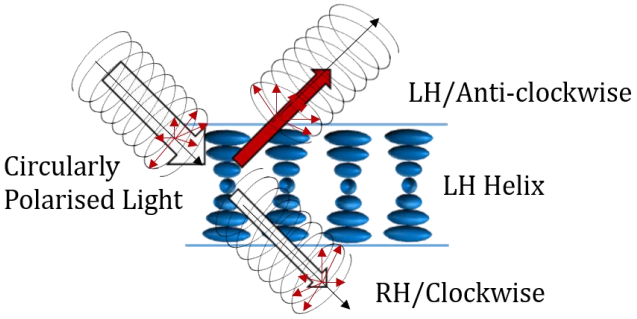

Figure 1.12. Cartoon illustrating how a chiral nematic with homogeneous alignment can selectively reflect 50% of the incident light of a particular wavelength that has a circular polarisation matching the handedness of the helix, while the remaining 50% is transmitted.

1.5 Liquid Crystal Polymers & Elastomers

1.5.1 Nematic Polymers

Liquid crystal polymers (LCPs) are a class of hybrid material broadly combining the characteristics of polymeric and liquid-crystalline materials.[5,7] Polymers are large macromolecules built from smaller units termed monomers. If the monomer has a shape that is conducive to the formation of a liquid crystal phase this can be transferred to the polymer material. As such, LCPs can also develop liquid crystal phases similar to those of low-molar mass liquid crystals, although those exhibited are usually higher order phases than the monomer, due to the backbone providing inherent ordering.[8]

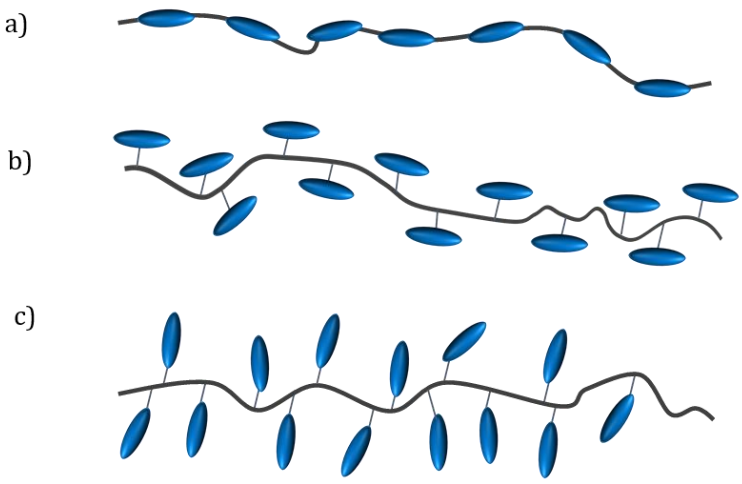

Figure 1.13. a) Main chain b) side-on and c) end-on liquid crystal polymers.

There are two types of LCP - main chain (MCLCP) and side chain (SCLCP). Main chain LCPs incorporate the mesogens directly into the polymer backbone (Figure 1.13, a), whilst in side chain LCPs the mesogens are attached to the backbone *via* a flexible spacing unit. Side chain LCPs can be further split into two classes, depending on how the mesogen is attached – side-on (Figure 1.13, b) or end-on (Figure 1.13, c). Polymerisation of the monomer units into the larger polymer macromolecule can, for example, be achieved by the free-radical polymerisation of a mixture of a vinyl monomer and a radical initiator, and can be triggered by thermal or photochemical means. Thermal initiation, using an initiator such as azobisisobutyronitrile (AIBN), can be used for the formation of polymers, however this is potentially limiting for liquid crystal polymers, as the thermal decomposition temperature needs to be within the nematic phase of the monomer to maintain the alignment. Photo-initiation is more convenient, as the decomposition is largely temperature independent, and the absorption maximum of the initiators closely matches the output of common UV sources. Polymerisation can also occur in the presence of a metal catalyst, as is typically done with polysiloxanes. Analysis of the degree of polymerisation (DP) and polydispersity index (PDI) gives an indication of the length of the polymer chains and the variation in chain lengths respectively; to avoid influence on the liquid crystal phase properties the molecular weight should be above 10,000 g mol^{-1}.[9]

As well as by the mesogen structure, the thermal and mechanical properties of the polymer are heavily influenced by its backbone composition. The more flexible the backbone, the lower the glass transition temperature (T_g); which in the case of a nematic polymer often leads to a wider nematic range.[10] Below T_g the polymer is in a glassy state

and the orientational order is 'frozen' in. Of the examples in Figure 1.14, polysiloxanes are the most flexible, followed by polyacrylates, then polymethacrylates. The acrylate group will be used in this thesis due to its good compatibility with radical polymerisation and its low glass transition temperature.

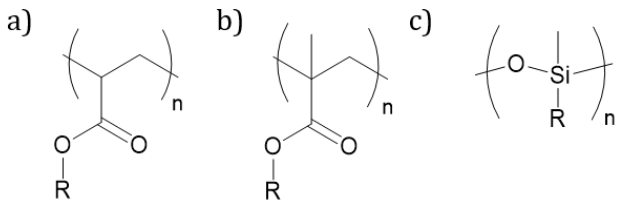

Figure 1.14. The backbone of: a) polyacrylate b) polymethacrylate and c) polysiloxane polymers.

Due to the chemically-bound nature of an LCP, the nematic order parameter and the polymer chain are coupled.[8] In an isotropic environment, the polymer chains adopt an entropy-driven random coil conformation with an isotropic radius of gyration.[11] However in an anisotropic environment, e.g. one arising due to the presence of a nematic phase, the chains adopt an anisotropic conformation - a prolate or oblate spheroid - and a corresponding anisotropic radius of gyration (Figure 1.15). This coupling can be controlled through variation of the length of the spacer - a main chain LCP or a side chain LCP with a short spacer has a strong coupling between the mesogenic units and the backbone, whilst a long spacer is more flexible and so results in a weaker coupling and therefore weaker response. The prolate or oblate orientation is dependent on the side-on or end-on orientation of the mesogen in respect to the backbone as well as the length of the spacer – in end-on LCPs, even carbon numbers align with the backbone, whilst odd

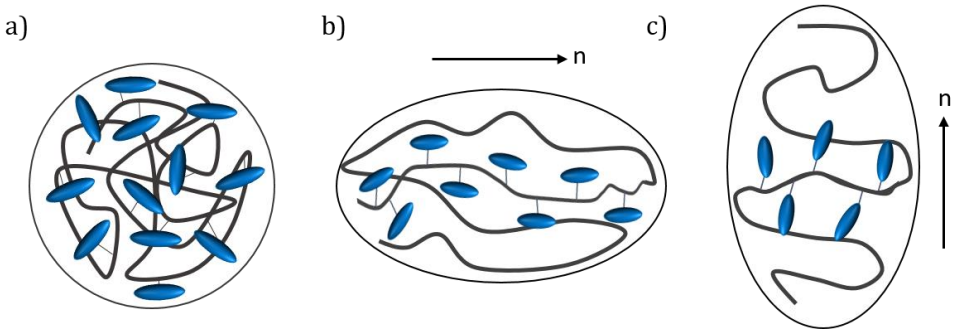

Figure 1.15. a) The isotropic random coil conformation of a polymer, b) The side-on attached mesogens of a SCLCP align the polymer backbone parallel to the director typically resulting in a prolate orientation, c) whilst end-on attached mesogens align the polymer backbone typically perpendicular to the director into an oblate orientation.

numbers align perpendicular to it.[12] By polymerising in the nematic phase, the orientational order at that moment in time is retained. However, when the isotropic phase is induced the memory of the captured orientation is lost when cooled back into the nematic phase, unless there are strong aligning forces present or there is a high degree of crosslinking of the polymer network.

1.5.2 Nematic Elastomers

Elastomers, better known as rubbers, are a type of soft matter possessing a low shear modulus and capable of withstanding very large deformations due to stress, deforming at near constant volume.[8] With a low percentage of crosslinking binding the polymer chains together, elastomers are able to resist viscoelastic deformation.

Liquid crystal elastomers (LCEs) combine the self-organisational properties of liquid crystals and the elastic properties of elastomers to form materials capable of a reversible change in shape, or actuation, when subjected to an external stimulus such as temperature or light.[13–17] This reversible contraction and expansion is similar to the action of an actuating muscle and was foreseen by de Gennes.[18] The mesogens' attachment in a side-chain or main-chain manner is the same as in an LCP.[19] Strong coupling of the mesogens with the polymer backbone causes the backbone to adopt a strongly anisotropic shape that follows the alignment of the mesogen in the liquid crystal phase.[8,16] Crosslinking allows the restoration of the original mesogen orientation, and therefore shape, upon re-entering the nematic phase after isotropisation, unlike an LCP. The degree of crosslinking affects the elastic properties of the elastomer; an increase causes the elastomer to behave more as a rigid thermoset polymer (and vice-versa) and so the extent of the actuation can be tuned.[20] Typically only a small percentage of crosslinker is required to produce an elastomer.[21]

Like an LCP, at the transition to the isotropic phase the nematic order parameter is approximately zero and so, without any further constraints, the elastomer assumes a random coil conformation. However, if the director profile is uniform, a prolate orientation results in a contraction of the elastomer in the direction parallel to the director and an expansion perpendicular, as volume is conserved, which is observed macroscopically (Figure 1.16). The extent of this response is dependent on the prolate or

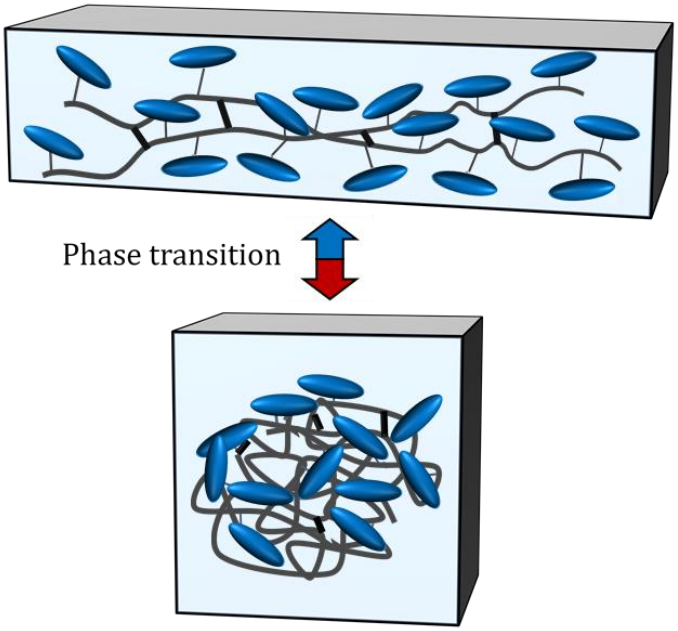

Figure 1.16. An aligned LCE (top) loses the orientational order imposed by the mesogens and adopts a random coil conformation upon isotropisation (bottom). For an LCE with a prolate radius of gyration, this results in a macroscopic contraction parallel, and expansion perpendicular, to the director. This change is reversible in an elastomer.

oblate orientation, as the director is oriented differently in respect to the polymer backbone; a prolate orientation leads to a greater chain anisotropy and therefore stronger response. As such, in a side-chain LCE a side-on attached mesogen is preferable over an end-on attached mesogen to elicit the strongest shape change response. Any areas without anisotropic alignment of the polymer backbone, arising from defects, will average out in all directions, leading to a reduction in the magnitude of the overall shape change; therefore to maximise the response it is important to create a monodomain sample.[22]

One of the main challenges in creating actuating nematic elastomers is ensuring this monodomain alignment. This is further complicated by the fact that the growing polymer chains provide points where defects can be generated. To aid and maintain the alignment, the use of alignment layers, as described in Section 1.3.5, can be applied to thin films of LCEs[23], although the thickness of the sample is limited. This is due to the fact that the alignment stems from the mesogen interaction at the interface of the polyimide layer and the penetration depth is only a few μm. Removal of the elastomer film from the alignment cell can also be challenging if the elastomer becomes bonded to the glass. High strength magnetic fields have been successfully employed to reorient the mesogens prior to polymerisation and this has allowed the creation of freestanding elastomer films, using a

sacrificial water-soluble layer between the elastomer and glass substrate.[24] Magnetic fields have also been used to create a radial alignment in a torus-shaped film, leading to the creation of an LCE aperture that can variably open and close on heating.[25]

Alternatively, the two-step process originally developed by Finkelmann *et al* involves mechanically stretching a partially crosslinked polysiloxane, followed by fully crosslinking it.[22] This mechanical stretching orientates the polymer backbone and mesogens into a monodomain, which is then locked in *via* polymerisation. However, crosslinking under load requires being able to physically grasp the material to stretch it, which limits the practicality of this method. A recently developed type of LCE, that does not involve the use of external fields to align, has been termed xLCEs – LCEs with exchangeable links. While it does require that the sample have a uniaxial stress applied, it is quite versatile in its potential to mould the LCE to different shapes.[26] Furthermore, LCE microparticles have been incorporated into an isotropic elastomer matrix and aligned within a magnetic field. This meant that mechanical manipulation was not needed to create an aligned polymer-dispersed LCE of arbitrary shape and size that reversibly deformed, as the thermo-responsiveness of the microparticles was transferred to the bulk elastomer.[27]

Main chain elastomers are predicted to be capable of the largest expansions and contractions due to the extremely strong prolate coupling of the mesogen and backbone, up to 300-400%.[28,29] However, the synthetic methods to produce main chain LCEs have traditionally employed platinum-catalysed siloxane reactions, which are not so straightforwardly adapted to use in droplet systems, compared to the acrylate-based side chain LCEs, although progress has been made in the use of thiol-ene, thiol-yne and thiol-acrylate Michael additions to create combined side chain/main chain macromolecules.[30–32]

The nematic elastomer system derived from the acrylate monomer shown in Figure 1.17, where the mesogen is attached side-on to a polymerisable acrylate unit, has been studied extensively.[21,23,33–37] The rigid aromatic cores and ester linking groups lead to a mesogen with a high phase stability, while the short spacer leads to a strong coupling of the mesogenic unit and polymer backbone. Thomsen *et al* demonstrated that LCE films made from this monomer with 10 mol% 1,6-hexanediol diacrylate as a crosslinker were capable of reversible shape changes of ~40%.[23] The thermal properties of T_g = 40 °C and T_{NI} = 120

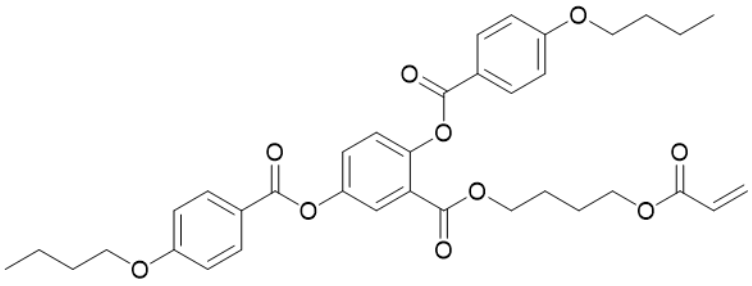

Figure 1.17. The structure of the laterally attached side-chain nematic monomer 4'-acroyloxybutyl-2,5-di((4-butyloxy)benzoyloxy)benzoate, **M1**.

°C result in a wide nematic range, which is favourable for responsive applications. In previous work in the group, Davey investigated this monomer system, varying both the peripheral side chain length and spacer length and studying the effects on the phase stability and glass transition temperature.[38] It was found that longer chains decreased the phase stability, and an odd-even effect was observed. Based on this work, the same structural motif will be utilised in this thesis.

1.5.2.1 Applications

As well as from a thermal transition, the loss of orientational order in a liquid crystal phase can be induced by photochemical processes.[39] Composites or hybrid materials containing LCEs have been developed. Azobenzene undergoes a *trans-cis* isomerisation with exposure to UV light and a *cis-trans* isomerisation on exposure to blue light or by thermal relaxation. Incorporation of the azobenzene moiety into a mesogen results in a rod-like unit in the *trans* state but a bent shape in the *cis* state. Triggering the isomerisation from *trans-cis* disrupts the nematic packing, causing the transition to the isotropic phase. This effect has been successfully utilised to control the actuation through UV irradiation *via* the incorporation of an azo-containing co-monomer into the LCE.[34] A light-driven motor has been developed that converts photons into kinetic energy through the use of a film of LCE that is exposed to UV and visible light on different sides of the device.[40] The incorporation of nanoparticles into the elastomer matrix allows the phase transition to be controlled by magnetic field-induced heating[41] and a conjugated polymer/LCE hybrid was able to convert IR photons into heat to trigger the phase transition.[42] Alternatively, a dye can be swollen into the elastomer matrix, as demonstrated by Camacho-Lopez *et al* to produce 'swimming' LCEs that move away from a light source.[43]

Arrays of micro-pillars of LCEs from this monomer have been created using a soft moulding technique.[21,33,36,37] The monomer was aligned in a magnetic field and polymerised. The LCE micro-pillars can actuate ~35% and could be used in devices that change their surface 'wettability' or in tactile-responsive devices.[44,45] A wide variety of other applications using LCEs have been developed, such as a controllable microfluidic valve[46], a micro-gripper[47], biocompatible scaffolds[48], hinges for foldable 3D-printed objects[49], anisotropic thermal insulators[50], a 'crawling' LCE[51], a chemical sensor[52] and micro-objects with variable photoluminescent properties.[37]

1.5.3 Chiral Nematic Polymers and Elastomers

Introducing chirality into a liquid crystal polymer or elastomer , either in the mesogenic unit, the crosslinking unit[53,54] or the polymer backbone[55], can produce chiral LCPs and chiral LCEs. Many chiral side chain liquid crystal polymers that incorporate a peripheral side chain with a chiral centre derived from natural products such as menthyl[56–58], cholesteryl[59,60], 2-octanol[61,62] or 2-methylbutan-1-ol[10,63–68] have been investigated. Like a low-molar mass chiral nematic liquid crystal, chiral LCPs and LCEs can selectively reflect visible light if the pitch length is appropriate, as discussed in Section 1.4.3.

As in nematic LCPs, the side-on or end-on method of attachment also greatly influences the chiral liquid crystal phases observed; a number of end-on attached LCPs have been studied and largely found to possess chiral smectic phases as well as chiral nematic phases.[56,59,61,63] The length of the spacer also influences the phase behaviour, with a shorter 4 carbon spacer found to favour the N* phase, whilst a longer 11 carbon spacer favours the SmC* phase.[69,70] Lewthwaite *et al* has shown the incorporation of a pendent chain derived from (*S*)-2-methylbutan-1-ol into a SCLCP of similar structure to **M1** leads to a chiral nematic phase with a suspected tight pitch, although the exact length was not reported.[10,68] Polysiloxanes, also bearing a (*S*)-2-methylbutyloxy chain, were synthesised by Hu *et al*[71], yet these possessed multiple smectic phases at elevated temperatures due to the end-on attachment of the mesogens. In the case of an end-on attached cholesteryl polymer, a longer spacer was found to allow visible selective reflection.[72]

The pitch length, and therefore selective reflection colour, can also be modified using azo-containing mesogens. The degree to which a photosensitive chiral dopant can alter its HTP by varying the time exposed to UV light was demonstrated.[73–75] Alternatively, the electrophoretic deposition of an ionic chiral dopant was employed to create bistable

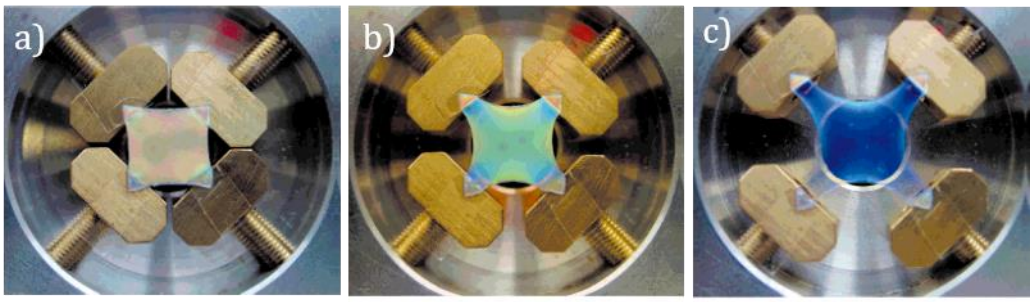

Figure 1.18. A chiral nematic LCE prepared by Finkelmann *et al,* taken from reference [83], changes colour as the elastomer is stretched; a blue-shift occurs as the helix is compressed.

reflection colours when a voltage was applied to the polymer.[76] By heating into the N* phase and rapidly quenching below T_g, the helix can be frozen in the glass, leading to thermally recordable films.[57,77] One of the limitations of the chiral nematic phase is the 50% limit on reflectance due to the handedness of the helix and its interaction with circularly polarised light. However, by employing a 'wash out/wash in' process, where the polymer network is imprinted with a chiral nematic of one handedness, washed out and then refilled with a chiral nematic of the opposite handedness, leading to the simultaneous reflection of both left and right circularly polarised light, films reaching close to 100% reflectance have been created.[78,79] Films capable of anisotropically reflecting different wavelengths have also been made.[80,81]

The elastic properties of monodomain chiral LCEs permit reversible selective reflection of light of different wavelengths with mechanical deformation, promising applications such as tuneable lasers and sensors.[82] Finkelmann *et al* demonstrated that when doped with an appropriate dye, films of N*LCEs were capable of lasing at different wavelengths depending on the extent of stretching.[83,84] Biaxial stretching in the planes perpendicular to the chiral nematic helix causes the thickness of the sample to decrease to preserve the internal volume.[85] This deformation leads to a compression of the helix, causing a blue-shift of the selective reflection wavelength (Figure 1.18, a-c). Urayama *et* al prepared chiral nematic elastomer gels, with an end-on side chain chiral nematic monomer and swollen with 5CB.[86] On the application of an electric field the gels were capable of changing shape >30%, due to the monodomain alignment, and as the film thickness changed, the wavelength of the selective reflection also changed. Wood *et al* were also able to create stretchable chiral nematic gels capable of laser emission.[87] As well as bulk aligned samples, the use of microparticles can also impart colour changing functionality; an elastomer film of microparticles arranged into a photonic crystal could reversibly change colour with strain.[88]

1.6 Nematic Liquid Crystals in Non-Planar Confinement

So far, we have only discussed the confinement of a nematic liquid crystal as a thin film between two planar alignment surfaces. However, nematic materials can also be confined in different topologies, for example in cylindrical channels[89,90], spherical shells[91] or spherical droplets in an emulsion.[92]

1.6.1 Nematic Droplets

An emulsion of droplets is created simply through the mixing of two immiscible phases such as a liquid crystal and water. Alternatively, more sophisticated methods can be employed, such as microfluidics, to create droplets of controllable size.[93] The controlled formation of droplets occurs at the junction of a microchannel where two flowing immiscible liquids, commonly silicone oil, glycerol or a solution of PVA, and a monomer are introduced together. The flow rates of the two phases can be independently tuned to control the size of the droplets produced, ranging from 20 μm < d < 500 μm.[35,94] Another advantage of using microfluidics is the very low polydispersity that can be achieved,

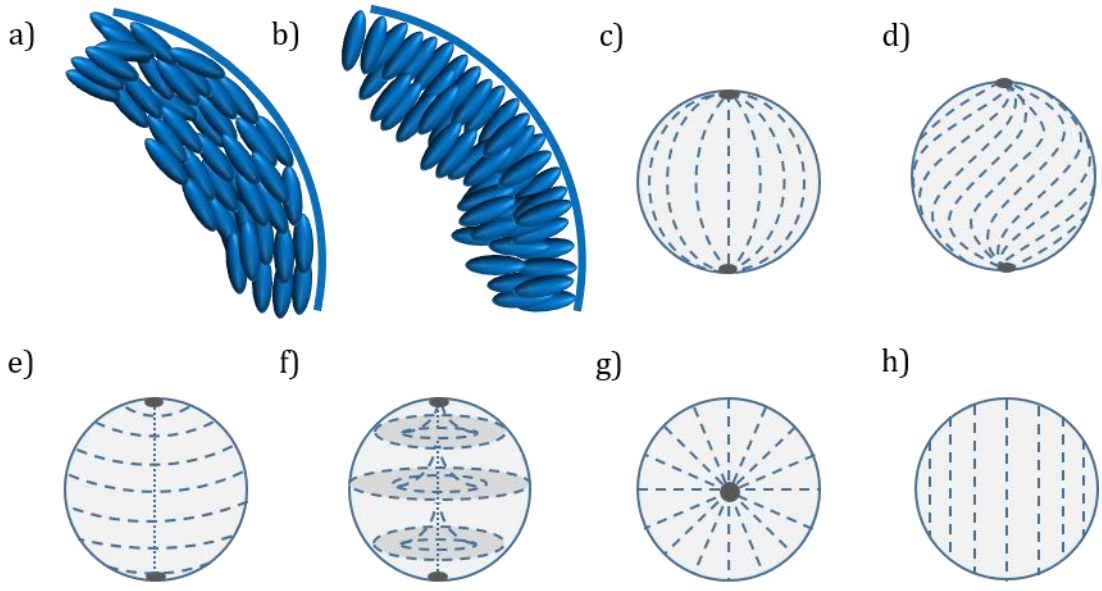

Figure 1.19. Cartoons of some of the possible alignment configurations of nematic liquid crystals confined to a droplet. Parallel anchoring (a) can result in bipolar alignment (c) with two point defects at the poles, twisted bipolar (d), concentric alignment with a defect line through the centre (e) or escaped concentric (f). Perpendicular anchoring (b) leads to a single hedgehog defect in the centre (g). A droplet with a monodomain alignment (h).

typically around 3%. This allows, for example, for the formation of monolayers of droplets which may be important for photonic applications.[95] Droplets of monomers can be polymerised continuously 'on-the-fly' or in a batch process, further broadening the scope of possibilities.[96]

To prevent coalescence of the droplets, an emulsifier, such as a water-soluble polymer such as polyvinyl alcohol (PVA) or a surfactant such as sodium dodecyl sulfate (SDS), can be added. The emulsifier can also influence the alignment within a droplet consisting of a liquid crystal material. A polymer such as PVA adopts a random coil conformation at the surface, acting as a stabiliser between the droplets, but does not directly influence the alignment. However, the use of PVA supports planar alignment (Figure 1.19, a) since this is the most favourable when in contact with water.[92]

The size of the droplet is an important variable in the observed nematic confinement texture. The bulk elastic energy of a nematic is proportional to the radius, *r*, while the surface energy is proportional to r^2.[97] Therefore small droplets are dominated to a larger degree by the bulk elasticity and larger droplets by the surface energy. With decreasing droplet size the curvature increases and therefore so too does the energy of the bend deformation. It was predicted that at some point the surface anchoring is ignored and the liquid crystal transitions to a uniform director configuration (Figure 1.19, h) for small droplets (<1 μm), although it is hard to observe droplets of this size and texture optically.[98] Larger droplets with strong planar alignment often adopt a lowest energy bipolar configuration with two point defects at the poles (Figure 1.19, c). Other possibilities are a concentric configuration with a defect line through the centre (Figure 1.19, e) or more likely an escaped concentric configuration (Figure 1.19, f).[99] The alignment is dependent on the ratios of the splay (K_{11}) and bend (K_{33}) elastic constants, where a high K_{33}/K_{11} favours a bipolar configuration, whilst a low value favours concentric.[100] A twisted bipolar configuration (Figure 1.19, d) is also possible if the twist (K_{22}) elastic constant is sufficiently small.[101] On the other hand, a surfactant imparts alignment through mixing of the long alkyl chains with the mesogens, which encourages perpendicular alignment (Figure 1.19, b) and a radial configuration (Figure 1.19, g). By gradually changing the concentration of surfactant, droplets can undergo transitions from bipolar to radial configurations.[102] This has been exploited to develop nematic droplets as biological sensors that transition from radial to bipolar in the presence of cancer cells and enzymes.[103,104]

Another method of surface alignment is *via* the flow of a viscous solvent around the droplet. Research into the director configurations of nematic droplets by Fernández-Nieves *et al* has shown that the director can be influenced by the shearing forces experienced by the droplet.[105] It was found that a bipolar droplet constrained in a microfluidic channel could transition into an escaped concentric configuration due to the flowing solvent but then, due to the constraints of a higher energy, highly bent intermediate configuration, could not return to the bipolar configuration.

As with thin-film preparations of nematic liquid crystals, a spherically confined, aligned nematic also displays characteristic textures when viewed through crossed polarisers. A well-aligned bipolar particle displays both the baseball and Maltese cross textures when rotated in respect to the polarisers, whilst radial particles only exhibit the Maltese cross texture, due their symmetric nature (Figure 1.20). Polymer dispersed liquid crystals (PDLCs) are dispersions of nematic droplets encased in a polymer and have long been used in applications such as privacy windows due to their electrically-switchable light scattering and non-scattering states.[106] Leading on from this, monodisperse emulsions of aligned nematic liquid crystal droplets encased in a polymer matrix have been used to create switchable diffraction gratings. Application of an electric field can reorient the mesogens within the droplets, modulating the transmission of light.[107]

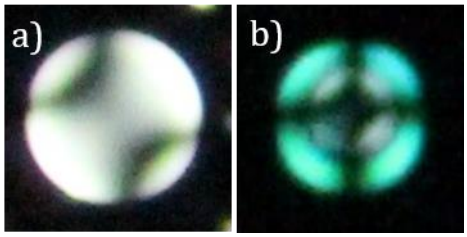

Figure 1.20. Polarised photomicrographs of a) baseball and b) Maltese cross textures of spherically confined nematic liquid crystal 5CB viewed between crossed polarisers.

1.6.2 Nematic Polymer and Elastomer Particles

Just like droplets, confinement of liquid crystal polymers and elastomers to particles has led to interesting and sometimes unexpected outcomes. The increased thermal stability and the retention of the optical properties allows for wide-ranging uses. Like an aligned LCE film, a particle with an anisotropic director configuration, would be expected to change shape reversibly. Polymer particles can be formed *via* a variety of heterogeneous polymerisation methods including emulsion, dispersion and suspension polymerisation.

This allows for a range of particle sizes to be accessed, from the nanometre scale up-to the millimetre scale.[108,109] The largest particles sizes (>10 μm) are most readily created using suspension polymerisation; where an emulsion of droplets is created by controlled shearing of a monomer in an immiscible host medium, followed by a bulk-like polymerisation. However, the drawback of this method is the large particle size polydispersity, which can only be partially improved with careful optimisation of experimental parameters or filtering.[110]

Hard, fully networked liquid crystal polymer particles are created, for example, by polymerising a bifunctional acrylate. Cairns *et al* prepared nematic polymer microspheres by first agitating a mixture of the biacrylate monomer RM257 (Figure 1.21) and a photoinitiator in glycerol to produce bipolar droplets (~10 μm); aligned due to the presence of the glycerol.[111] This was followed by exposure to UV light to capture the alignment within the nematic phase.[112] The microspheres were manipulated using electric fields due to the dielectric anisotropy of the aligned mesogens. Fernández-Nieves *et al* also created hard nematic polymer microspheres but used a modified microfluidic approach by using an organic solvent to dissolve the RMM14 reactive mesogen mixture. This removed the need to heat and maintain the temperature of the microfluidic chip system, which is one of the challenges when using liquid crystals that do not possess a room temperature nematic phase and also allowed for the fine tuning of the droplet size.[113] Davey developed polymeric and elastomeric microspheres (<5 μm) using an adapted dispersion polymerisation technique.[38] However, whilst these systems displayed defined confinement textures, crosslinking proved difficult and the particles did not show any actuation response on heating or swelling.

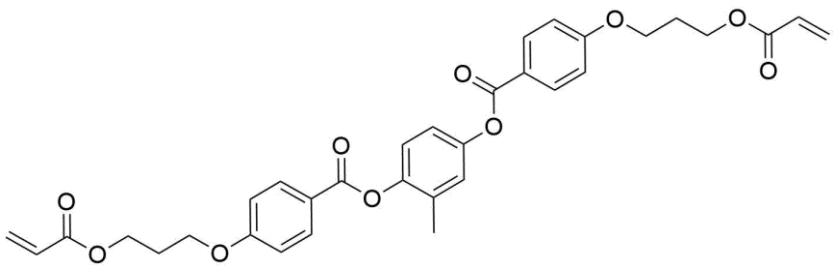

Figure 1.21. Structure of the reactive mesogen RM257. Cr 67 °C N 130 °C Iso.

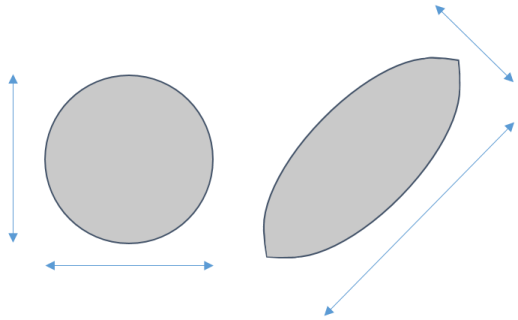

Figure 1.22. Cartoon of the relative dimensions of spherical and anisometric particles.

As well as spherical particles, there is a developing interest in shape-anisotropic, or anisometric, particles for uses such as micro-stirrers (Figure 1.22). Anisometric polymer microparticles have been fabricated by Abbott using a templating process.[114,115] Droplets of the reactive mesogen RM257 were swollen with the nematic liquid crystal 5CB to enhance the internal alignment and polymerised. The 5CB was subsequently removed and it was found that the network anisotropy leads to the de-swelling of the particles perpendicular to the director, leaving spindle-shaped particles.[116] There was no shape change observed on heating the particles, although that is perhaps to be expected, as they were not soft elastomeric networks but hard polymeric networks. However, the aspect ratio of the particles could be controlled by varying the concentration of RM257, and therefore the degree to which the network de-swells.

The development of microfluidics has led to the creation of different types of anisometric microactuators from LCEs[117], with the Zentel group in particular using microfluidics to create large LCE microparticles (>200 μm) that respond to heat and light.[118,119] They successfully created elastomer particles capable of shape changes up to ~65%[94,120,121] using the shearing effect of the viscous outer fluid to flow-align the mesogens within the droplet into a concentric configuration, before immediate polymerisation.[122] Large 'core shell' LCEs with a bipolar alignment have been fabricated and demonstrated as a micropump, with a length change of 1.5x on heating. The alignment is suggested to arise from the simultaneous shearing from the silicone outer phase and the inner glycerol phase within the shell.[123]

The flow alignment of the mesogens by stretching the droplets in a PVA matrix, followed by polymerisation, led to the creation of anisometric polymer particles[95], whilst elastomer particles were prepared by Marshall *et al* with a similar method and then released by

dissolving the matrix with water.[35] On heating and cooling, the elastomer particles were capable of a reversible shape change, from elongated to spherical, of ~30%.

To the best of my knowledge there are no examples in the literature of surface-aligned anisotropic LCE particles capable of actuation. Therefore, this will form some of the focus of this thesis.

1.6.3 Chiral Nematic Droplets and Polymer Particles

Like thin films, droplets of chiral nematic liquid crystal with planar alignment are also capable of selective reflection of light. A chiral nematic with a pitch in the μm range and confined to a droplet possesses a concentric shell appearance under crossed polarisers when the mesogens are aligned parallel to the droplet interface (Figure 1.23, a). The dark repeating bands are analogous to the *fingerprint* texture of a planar film and are due to the periodic variation of the refractive index, arising from a radial helical structure.[124] By decreasing the pitch and maintaining the parallel alignment, selective reflection in the visible region can be achieved (Figure 1.23, b). The selective reflection wavelength, λ_{max}, no longer has the viewing angle dependence that a flat film has. This is due to the radial alignment within the droplet (Figure 1.23, c), which leads to all incident light incoming at 0° to the helix axis. Therefore when a droplet is illuminated with white light, the light is reflected in all directions (omnidirectional) and it has been suggested that such droplets could be used in future optical communication devices[125] and omnidirectional lasing systems.[126–128]

Using microfluidics, Noh *et al* produced chiral nematic droplets capable of selective reflection in the visible range using a commercial nematic mixture and the chiral dopant

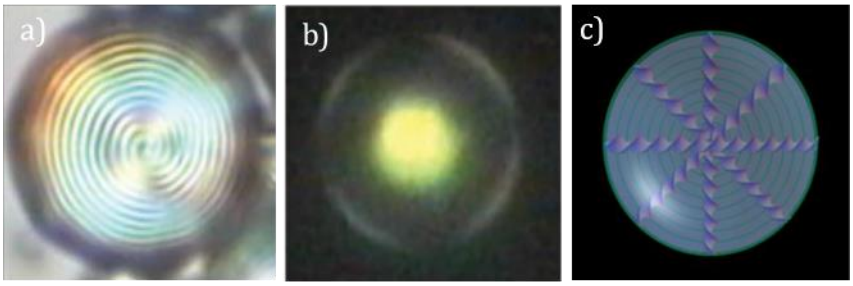

Figure 1.23. Hard chiral nematic polymer microspheres prepared by Cipparone *et al*: a) long pitch particle in transmission mode showing the radial alignment b) short pitch particle in reflection mode showing a green selective reflection c) the onion skin-like alignment within the droplet.[124]

CB15.[125] Due to the monodispersity of the sample, a monolayer of the droplets was formed and displayed 'photonic crosstalk' between neighbouring droplets, creating spots of different colours. They suggested that such patterns could be used in security and anti-counterfeiting applications due to the unique crosstalk patterns that are produced when droplets of N* with different pitch lengths are mixed together.

Chiral nematic droplets were also recently prepared by Fan *et al* using microfluidics and doping the commercial nematic mixture E7 with a photoswitchable chiral molecule.[129] The droplets formed were ~50 μm in diameter and exhibited selective reflection in the centre of the droplet, consistent with a radial alignment of the mesogens (Figure 1.24). The colour of the selective reflection could be tuned by varying the length of exposure to UV light. The HTP of the chiral photoswitch increased on irradiation, causing a blue-shift. By focusing the UV beam on individual droplets, different colours in the same sample could be produced. Wang *et al* went further with the idea of photoswitchable droplets and developed N* droplets that were capable of reversibly inverting the handedness of the helix on UV exposure by changing the dominance of the left or right handed twist.[130]

Another proposed use of N* droplets is as chemical or biological sensors. Like nematic droplets, the mesogen alignment is sensitive to the external conditions. Using surface functionalisation of N* droplets, Lee *et al* were able to change the alignment from planer

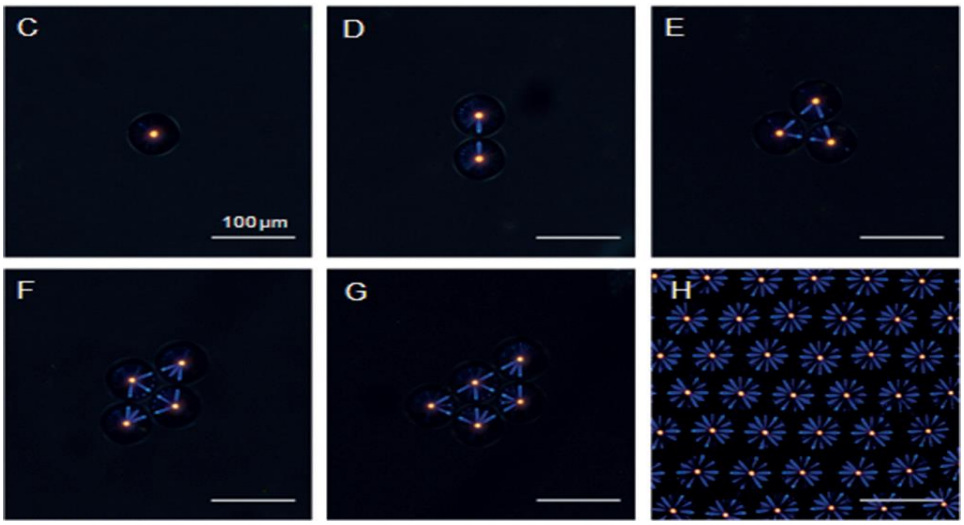

Figure 1.24. Photonic cross-talk observed in ordered arrays of chiral nematic droplets exhibiting a red selective reflection, prepared by Fan *et al*.[129]

to homeotropic on exposure to different biological compounds[131], while Jang *et al* were able to create pH-responsive droplets.[132]

The use of droplets in optical devices has some limitations. The lack of resistance to mechanical deformation and solvent swelling, plus their finite life before coalescence, even with a stabilising surfactant, means that their uses are restricted. Therefore, there is much effort in permanently creating hard and softer responsive particles to capture the optical properties. Lyotropic chiral nematic liquid crystal particles were prepared by Zentel using a cellulose derivative encased in a lightly crosslinked, swellable polymer matrix.[133] The particles were large (~300 μm) and displayed textures similar to those of thin films of the material, suggesting it was behaving more like a poorly-aligned bulk sample, than a confined well-aligned droplet. Polymerisation often leads to the creation of defects if the alignment is not strong and therefore a reduction in the optical quality is observed, as found by Aβhoff *et al*.[134] However, it was shown by Seo *et al* that extremely rapid curing can prevent phase separation and defect creation.[135] In constrast, Noh and Park limited the rate of defect creation by turning the UV source on/off quickly and were able to create responsive particles from bifunctional acrylate.[136] Maintaining the alignment throughout the droplet is a challenge for surface aligned droplets and so small droplet sizes are preferential to ensure good alignment and therefore reflection properties. Therefore, droplets of a few tens of micrometres should be investigated, as they are small enough for the alignment penetration depth to extend throughout the droplet but still have clearly visible textures using microscopy.

Identifying this problem, Geng *et al* demonstrated that shells of chiral nematic are also able to selectively reflect visible light.[137] Large shells (~250 μm) were produced using co-axial flow-focusing microfluidics by counter flowing a third phase, such as PVA or glycerol, that is immiscible with the liquid crystal mixture. At the junction of all three phases, a droplet of PVA within a droplet of liquid crystal is formed, creating a shell of liquid crystal. By varying the inner droplet size, the thickness of the shell can be tuned. The extra complexity required to produce shells using microfluidics makes this challenging to achieve but the thinner shell thickness (a few μm), compared to a droplet, leads to excellent planar alignment. This in turn makes it easier to retain the alignment during polymerisation of the shell. Making robust capsules of chiral nematic liquid crystal was also demonstrated as a viable solution to retaining the alignment by Lee *et al*.[138,139] An outer shell of PEGDA encapsulated a low-molecular weight chiral nematic whilst

simultaneously promoting parallel alignment. As the liquid crystal was not polymerised, no extra defects were generated.

Creating particles using alternative methods to microfluidics has also been explored. Hard chiral nematic polymer microspheres were made by Cipparone *et al* using a nematic monomer and chiral dopant that was shaken in distilled water and photo-polymerised.[124,140,141] This produced hard spheres in the range of 1-40 μm but the polydispersity is large due to the variable shearing forces when shaking. By varying the chiral dopant concentration, they were able to tune the selective reflection wavelength into the visible region and influence the director configuration with the use of surfactant to create solid omnidirectional lasers and particles that could be manipulated with optical tweezers.[142] Beltran-Gracia *et al* used suspension polymerisation and commercially available reactive mesogens to create hard Red/Green/Blue (RGB) particles, however the particle polydispersity was high and had to be improved using filtration.[143] The N* particles were embedded into a matrix to create films with no angle dependence, unlike a conventional chiral nematic film, and were also placed in a refractive index matched solvent to form coloured dispersions. Whilst this technique is scalable to industrial levels it lacks the fine control that microfluidics affords and that is likely to be required for high quality optical applications.

To the best of my knowledge, no examples exist in the literature of single component chiral nematic liquid crystal elastomer particles. At the beginning of the thesis, there were also no examples of doped chiral nematic RGB LCE particles. In 2017 Noh and Park published a study achieving this, however, by using a different commercial monomer, RMM727.[136]

1.7 Aims

The aims of this PhD centre on the creation of nematic and chiral nematic polymer and elastomer particles, the synthesis of the prerequisite monomers, and their characterisation. More specifically:

- To synthesise nematic and chiral nematic side-on side chain monomers and characterise them by NMR, MS, IR, POM and DSC.

- To characterise the liquid crystal phase properties, director configuration and molecular weight of the polymers/elastomers using NMR, GPC, POM and DSC.

- To investigate the effect on the optical and thermal properties of the achiral nematic monomers/polymers/elastomers through addition of a chiral dopant.

- To create monodisperse emulsions *via* microfluidics, followed by polymerisation to create nematic polymer and nematic elastomer particles with diameters >10 μm and investigate their properties such as size, size distribution and defined confinement configurations.

- To create chiral nematic polymer and elastomer particles, with diameters >10 μm and investigate their defined confinement configurations and their capability to selectively reflect light.

- To investigate the responsive properties of the materials, gained from confinement, to external stimuli such as temperature and pressure.

Chapter 2:

Synthesis & Characterisation

2 Synthesis & Characterisation

2.1 Introduction

This chapter describes the synthesis of the achiral and chiral monomers used to create polymer and elastomer microparticles within this thesis and details the method used to create polymer and elastomer thin-films. The characterisation of the monomers and the polymer films is described. The monomer structures were confirmed by nuclear magnetic resonance (NMR) and the thermal properties of the monomers and polymers were analysed by differential scanning calorimetry (DSC) and polarised optical microscopy (POM). The molecular weight distributions of the polymer films were analysed by gel permeation chromatography (GPC). The characterisation of chiral-doped elastomer films is discussed in Chapter 3.

2.1.1 Nomenclature

The monomers all share the general structure shown in Figure 2.1. For the monomers **M1**-**M4** the R_1 and R_2 groups are identical and achiral, whilst for the chiral monomers **CM1**-**CM9** one of them contains a chiral centre. The number of carbon atoms in the spacer component, and therefore its length, is also varied in both series. The polymers and elastomers follow the classification system based on the corresponding monomers: **P1**-**P4**, **CP1**-**9** and **E1**-**E4**.

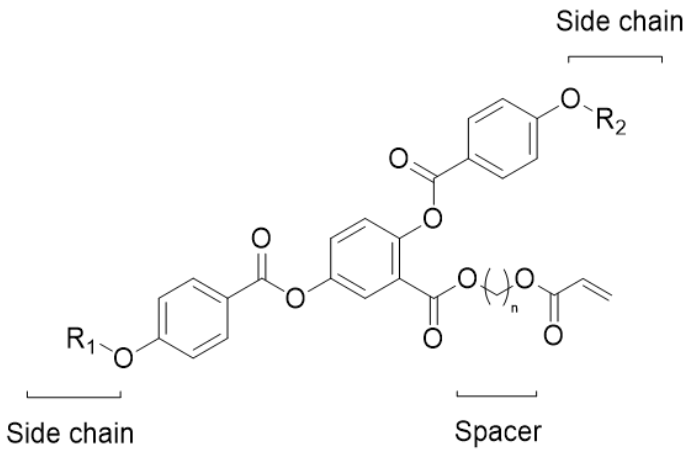

Figure 2.1. General structure of monomers.

2.2 Monomer Synthesis

A series of monomers (**M1**-**M4**, Scheme 2.1) were synthesised to investigate the effect of the monomer structure on the liquid crystal phase properties of the resulting polymers and elastomers. This would also allow a range of LCP and LCE microparticles with different thermal properties to be produced and compared. As discussed in the introduction, (4''-acryloyloxybutyl)-2,5-di(4-butyloxybenzyloxy)benzoate), **M1**, is a laterally-attached side chain liquid crystal monomer that has been extensively studied in the literature.[21,23,33–37] It possesses a wide range nematic phase in both polymers and elastomers (T_{NI}: ~120 °C) and has a low glass transition temperature (T_g: ~40 °C). In this research, the alkyl side chains were altered from butyl, in **M1** and **M3,** to heptyl, in **M2** and **M4**. Previous research in both the group and the literature has shown that an increase in the length of the side chain in this monomer system decreases both the phase stability and the glass transition temperature, further increasing the potential uses of the materials.[36,38]

Previous Small Angle Neutron Scattering (SANS) experiments performed on **M1** confirm that the short spacer imparts a highly anisotropic prolate polymer backbone, due to strong coupling between the mesogenic unit and the polymer, which is essential for good actuation characteristics in LCEs.[144] Two spacer lengths were used in our study - butyl (n = 4) in **M1** and **M2**, and undecyl (n = 11) in **M3** and **M4** - in order to influence the backbone; a longer spacer is known to reduce the anisotropy of the backbone conformation and therefore reduce the actuation properties of the microparticles.[144] Increasing the spacer length is also another strategy for reducing the phase stability and glass transition temperature.[21]

The monomers **M1**-**M4** were synthesised following a divergent synthetic route (Scheme 2.1).[23] Protection of the carboxylic acid of 2,5-dihydroxybenzoic acid was achieved using benzyl bromide and $NaHCO_3$ in DMF, to yield compound **1**. This was followed by a Steglich esterification using two equivalents of the appropriate alkoxybenzoic acid in dichloromethane (DCM), together with 1-ethyl-3-(3-dimethylaminopropyl)carbodiimide (EDAC) and 4-dimethylaminopyridine (DMAP) acting as coupling agents, leading to the isolation of compounds **2**-**3**. The benzyl group was removed *via* a palladium-catalysed hydrogenolysis in THF/ethanol to yield compounds **4**-**5** as white solids after column chromatography. A second Steglich esterification, using 4-hydroxybutyl acrylate or 11-acryloyloxyundecan-1-ol, attached the spacer component, to complete the monomers **M1**-**M4**. A more complete description of the experimental procedures can be found in Chapter 7 - Experimental.

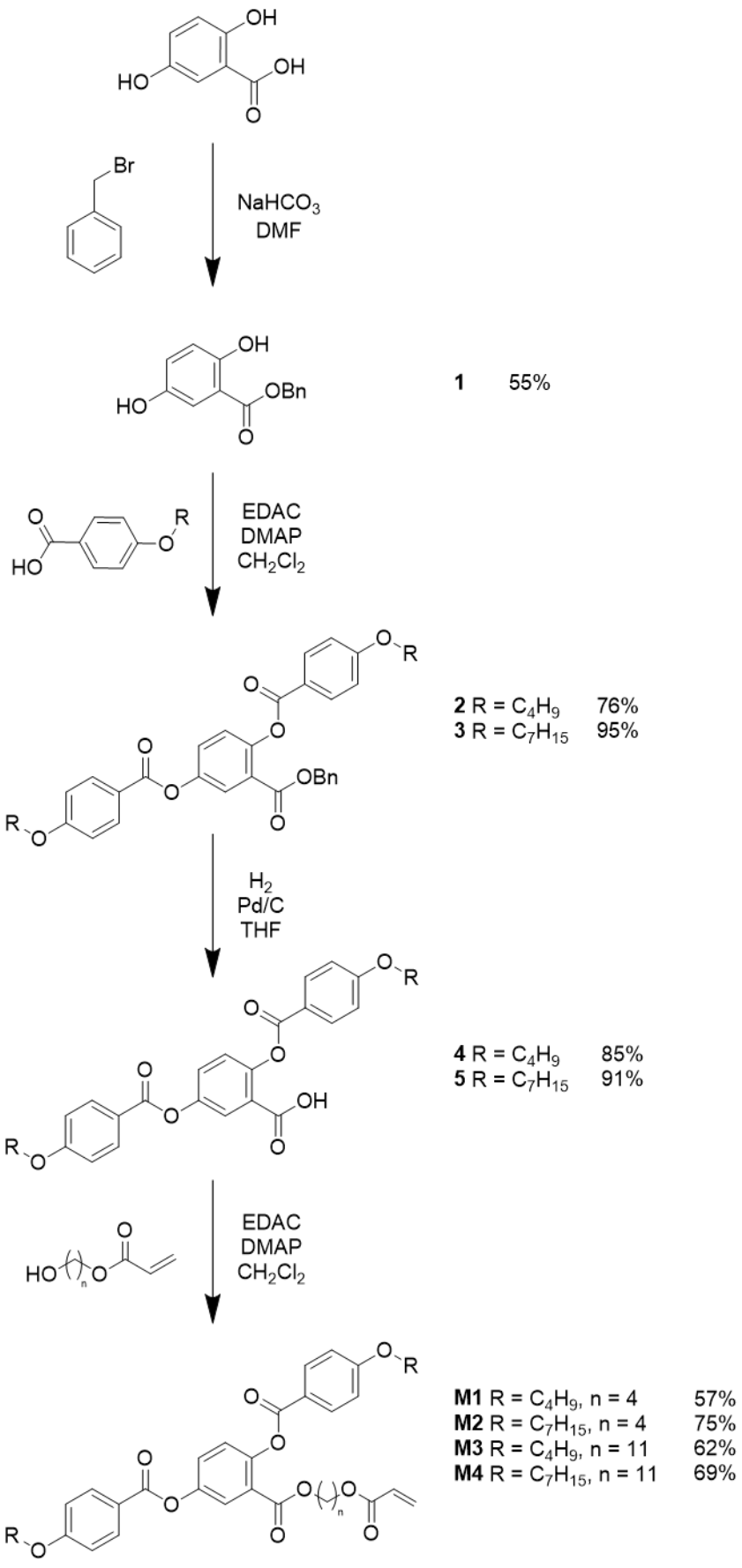

Scheme 2.1. Synthetic route to achiral monomers **M1**-**M4**.

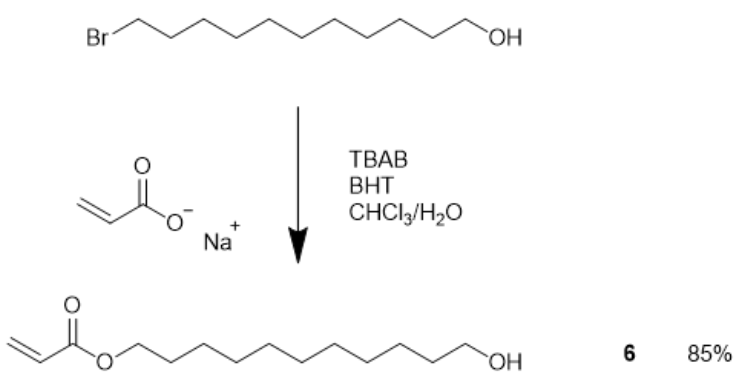

Scheme 2.2. Synthetic route to 11-acryloyloxyundecan-1-ol (**6**).

The spacer component 11-acryloyloxyundecan-1-ol (**6**) was synthesised according to Scheme 2.2, after adaptation of a literature procedure.[145] The 11-bromoundecan-1-ol and sodium acrylate were reacted, in the presence of tetrabutylammonium bromide in a mixture of chloroform and water, through a phase-transfer reaction. Premature polymerisation of the acrylate was inhibited through the addition of butylated hydroxytoluene acting as a radical scavenger.

2.3 Chiral Monomer Synthesis

Liquid crystal monomers with a chiral centre are likely to possess chiral phases such as a chiral nematic or chiral smectic phase. Lateral attachment of the mesogen to the polymer backbone is the preferential method to ensure only a chiral nematic phase is formed. Terminally-attached SCLCPs are capable of forming chiral nematic phases but, just as with achiral mesogens, smectic phases often dominate, likely due to the attachment of the mesogen to the backbone favouring a layered ordering. For example, various polysiloxanes containing a (*S*)-2-methylbutyloxy side chain have been synthesised yet these possess multiple smectic phases at elevated temperatures.[53,65,69]

The structure of the chiral monomers **CM1**-**9** is therefore based on that of **M1**; however, one of the peripheral alkoxybenzoates is replaced by an alkoxybenzoate with a chiral centre (Figure 2.2). The variation of the **M1** motif allows us to compare the resulting properties with the well-understood achiral analogue; along with its high phase stability, which should increase the likelihood of a chiral nematic phase with a useful temperature range. The low glass transition temperatures of polyacrylates are also advantageous for responsive devices at or near to room temperature.

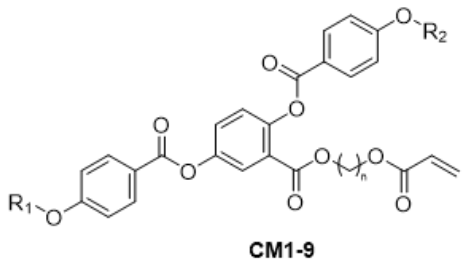

CM1 $R_1 = C_4H_9$, $R_2 = CH_2CH^*(CH_3)C_2H_5$, n = 4
CM2 $R_1 = CH_2CH^*(CH_3)C_2H_5$, $R_2 = C_4H_9$, n = 4
CM4 $R_1 = CH_2CH^*(CH_3)C_2H_5$, $R_2 = C_7H_{15}$, n = 4
CM5 $R_1 = C_4H_9$, $R_2 = CH_2CH^*(CH_3)C_2H_5$, n = 11
CM6 $R_1 = CH_2CH^*(CH_3)C_2H_5$, $R_2 = C_4H_9$, n = 11
CM7 $R_1 = C_7H_9$, $R_2 = CH_2CH^*(CH_3)C_2H_5$, n = 11
CM8 $R_1 = CH_2CH^*(CH_3)C_2H_5$, $R_2 = C_7H_{15}$, n = 11
CM9 $R_1 = C_7H_{15}$, $R_2 = CH^*(CH_3)C_6H_{13}$, n = 4

Figure 2.2. The structure of the chiral monomers **CM1-9**.

It is possible to design structural isomers of these monomers if the two peripheral alkoxy chains differ, for instance if only one alkoxy chain possesses the chiral centre. The chiral monomers, and structural isomers, **CM3** and **CM4** were first synthesised by a previous MChem student in the group, where it was noticed that there was an apparent difference in the phase stability and pitch of the chiral nematic phase of each isomer.[146] This was to be further investigated as part of this thesis, due to the divergent synthesis (Scheme 2.3) allowing for the relatively straightforward construction of a series of isomers.

To enable this investigation, it is necessary to selectively position the chiral moiety on the central core of the molecule. This is possible in benzyl 2,5-dihydroxybenzoate (**1**) due to the *ortho* phenol being sterically hindered, owing to its proximity to the bulky benzyl group, and contributing to an intramolecular hydrogen-bonded 6-membered ring, lowering its reactivity compared to the *meta* phenol.[10] By using only one equivalent of the intended alkoxybenzoic acid at a time (Step 2, Scheme 2.3) and switching the order of addition of the chiral and achiral alkoxybenzoic acids, it is possible to obtain both structural isomers.

When the spacer is laterally attached, the mesogenic core of the monomer is non-symmetric. For example, an asymmetrical naphthalene core was found to influence the ferroelectric or antiferroelectric ordering of a bent core material depending on the peripheral chain length, as the closed packing of the layers was affected.[147] Furthermore, it has been shown in both low and high molar mass systems that structural isomers can possess vastly different phase transition temperatures[148–151] or even lack mesomorphism entirely, likely due to increased steric anisotropy of one isomer.[62] Copolymerisation of constitutional isomers has also been shown to widen the phase stability and prevent side-chain crystallisation in polymers with long spacers.[152]

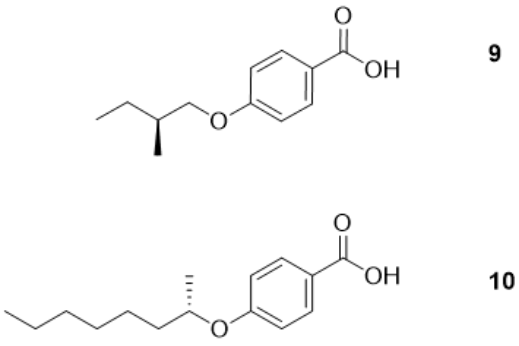

Figure 2.3. The chiral benzoic acids (*S*)-4-(2-methylbutyloxy)benzoic acid (**9**) and (*S*)-4-(1-methylheptyloxy)benzoic acid (**10**). The helical twisting power is influenced by the position of the chiral centre relative to the aromatic core of the molecule.

The position of the chiral centre on the alkyl chain can have an effect on the phase stability and the pitch.[153] As the chiral centre is moved closer to the mesogenic core, its rotational freedom is decreased, which leads to an amplification of its chiral properties to neighbouring molecules and therefore a reduction in the pitch. In a series of (*S*)-4-(alkyl-4'-cyanobiphenyls, moving the chiral centre away from the aromatic core by two carbon atoms increased the pitch by 2.6 times.[154] A mesogen with a large HTP and a tight helical pitch is desirable as the selective reflection wavelength will be small, however the phase stability will also be reduced and therefore a compromise is required. It has been shown that, by incorporating a chiral peripheral (*S*)-2-methylbutyloxy or (*S*)-1-methylheptyloxy chain (Figure 2.3) into a liquid crystal monomer, a chiral nematic phase with a tight pitch (0.23 μm) can be formed.[5,10,68] The closer proximity of the chiral centre to the mesogenic core in (*S*)-1-methylheptyloxy leads to a greater twist and therefore a tighter pitch, compared to (*S*)-2-methylbutyloxy; however, this also leads to a lower phase stability.[155–157] Molecules with more than one chiral centre possessing the same helical twist sense can display very high HTPs[158], however the structure of the mesogenic core needs to be designed to compensate for the increased phase disruption, for example with additional phenyl rings and ester linkages, otherwise it is possible that no liquid crystal phase occurs.[5] It is therefore conceivable that, due to steric effects, the position of the peripheral chiral group relative to the spacer also has an influence over the ordering of the mesophase and consequently over the phase stability and pitch.

2.3.1 Synthesis of (*S*)-4-(2-methylbutyloxy)benzoic acid and (*S*)-4-(1-methylheptyloxy)benzoic acid

The chiral benzoic acids (*S*)-4-(2-methylbutyloxy)benzoic acid (**9**) and (*S*)-4-(1-methylheptyloxy)benzoic acid (**10**) were synthesised according to the route shown in Scheme 2.3. The Mitsunobu reaction of a secondary alcohol leads to the inversion of stereochemistry at the chiral centre, whilst the stereochemistry of primary alcohols is unaffected.[159]

Firstly, the chiral alcohols (*S*)-(-)-2-methyl-1-butanol and (*R*)-2-octanol were reacted independently with benzyl-4-hydroxybenzoate, in THF in the presence of triphenylphosphine (TPP) and diisopropyl azodicarboxylate (DIAD), under an inert atmosphere, yielding compounds **7** and **8** as colourless oils. These were deprotected *via* palladium-catalysed hydrogenolysis in THF/ethanol to yield the chiral carboxylic acids **9** and **10** as white solids.

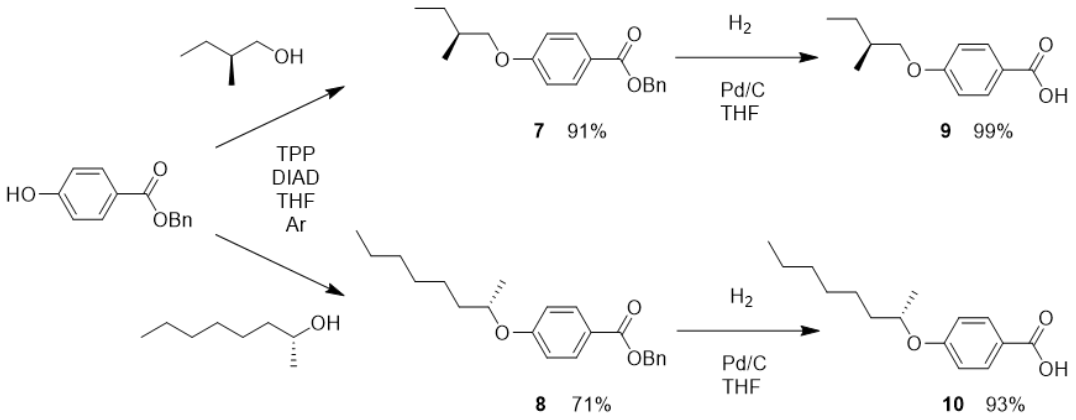

Scheme 2.3. Synthetic route to (*S*)-4-(2-methylbutyloxy)benzoic acid (**9**) and (*S*)-4-(1-methylheptyloxy)benzoic acid (**10**).

2.3.2 Synthesis of Laterally-Attached Chiral Acrylate Monomers CM1-2, CM4-9

The chiral monomers **CM1**-**2** and **CM4**-**9** were constructed in a divergent synthesis, adapted from the synthesis of **M1**-**M4** (Scheme 2.4). Compound **1** was reacted with one equivalent of the appropriate alkoxybenzoic acid (butyl, heptyl or (*S*)-(2-methylbutyl)) in DCM, together with EDAC and DMAP acting as coupling agents, leading to the isolation of compounds **14**-**16** respectively. A further Steglich esterification using one equivalent of a second alkoxybenzoic acid (butyl, heptyl, (*S*)-2-methylbutyl or (*S*)-1-methylheptyl) yielded compounds **17**-**21**. The benzyl group was removed *via* a palladium-catalysed hydrogenolysis in THF/ethanol to yield compounds **22**-**26** as white solids. The spacer component was attached in a final Steglich esterification, using 4-hydroxybutyl acrylate or 11-acryloyloxyundecan-1-ol, to obtain the chiral monomers **CM1**-**2** and **CM4**-**9**.

The chiral monomer **CM9** differs from **CM1**-**8** through the inclusion of a chiral (*S*)-1-methylheptyloxy alkyl chain instead of a (*S*)-2-methylbutyloxy chain. Compounds **8**, **10**, **21**, **26** and the chiral monomer **CM9** were synthesised by Adam Swarbrick within a BSc project conceived and supervised by me.

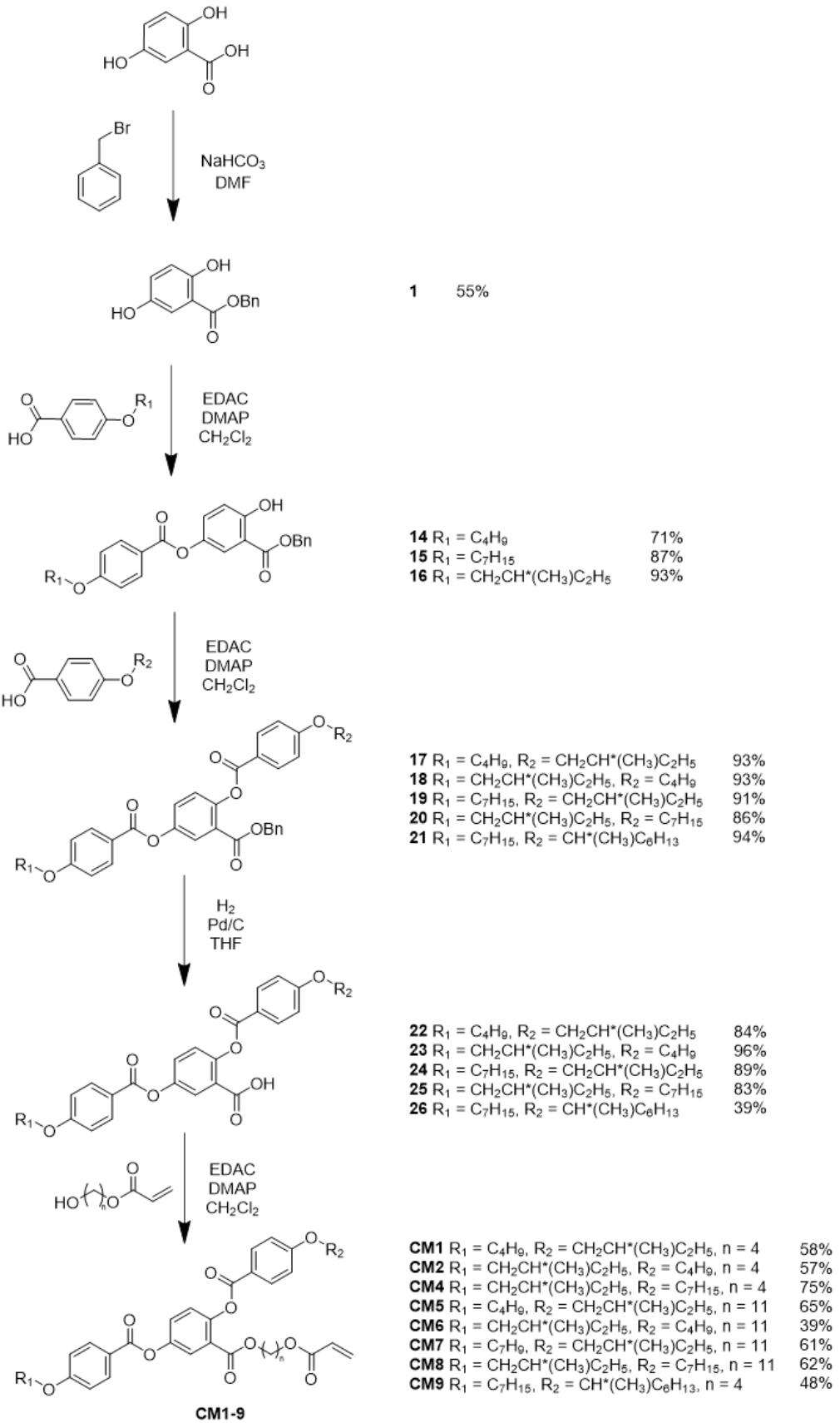

Scheme 2.4. Synthetic route to the chiral laterally-attached monomers **CM1**-**CM2** and **CM4**-**CM9**.

2.3.3 Synthesis of Laterally-Attached Chiral Acrylate Monomer CM3

An alternative synthetic route was used to prepare chiral monomer **CM3** (Scheme 2.5), adapting a convergent synthesis of monomer **M1** by Wei *et al* that requires fewer steps than the divergent synthesis used above. [21]

The monomer **CM3** was constructed in a convergent synthesis. The 2,5-dihydroxybenzoic acid was reacted with an excess of 1,4-dibromobutane, and potassium hydrogen carbonate in DMF, to afford compound **11**. This was further reacted with acrylic acid, again with potassium hydrogen carbonate in DMF, to complete the acrylate intermediate, compound **12**. The first alkoxybenzoic acid (heptyl) was coupled in a Steglich esterification reaction, using dicyclohexylcarbodiimide (DCC) and 4-pyrrolidinopyridine in DCM, to yield compound **13**. Finally, the chiral monomer **CM3** was completed by reacting compound **13** with one equivalent of (*S*)-4-(2-methylbutyloxy)benzoic acid (**8**) in a second Steglich esterification reaction, this time using EDAC/DMAP in DCM.

However, steps 1 and 3 (Scheme 2.5) were low yielding in comparison to the route used to synthesise the other monomers (Schemes 2.1 and 2.4). The difficulty in removing DMF in the work up of step 2 contributed to the low yield. The use of DCC instead of EDAC in the first Steglich esterification may also have been a factor, as the purification is simplified with the use of EDAC, due to the water soluble by-product. Therefore, only this monomer was created using this method.

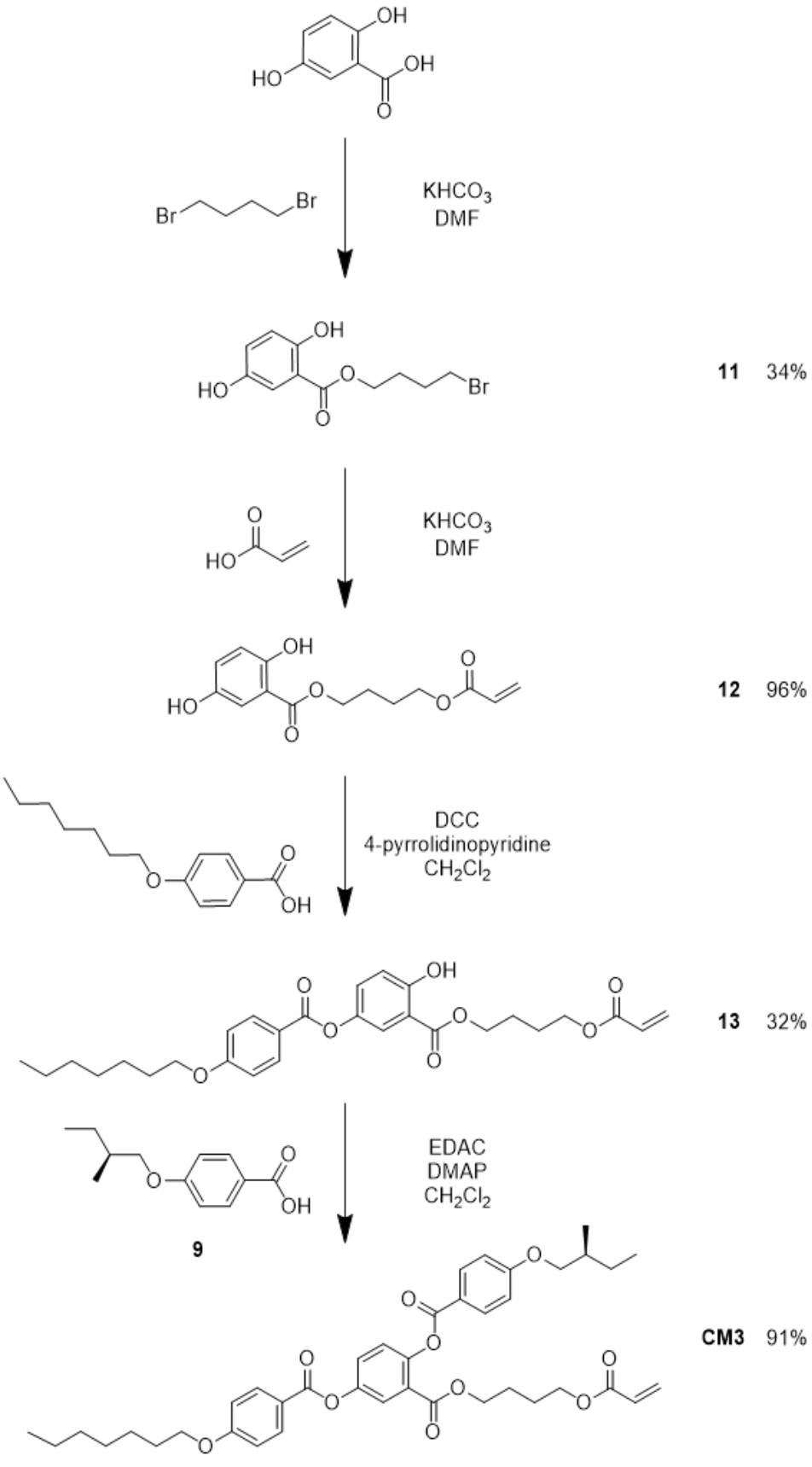

Scheme 2.5. Synthetic route to the chiral laterally-attached monomer **CM3**.

2.3.4 Structure Confirmation

The chiral monomers **CM1**-**CM9** were analysed by ^{1}H, ^{13}C, HSQC and HMBC NMR to confirm their structures. In particular, for the preparation of the structural isomers, it is necessary to confirm that singular attachment of the alkoxybenzoic acid has occurred in step two of Scheme 2.4 and step three of Scheme 2.5.

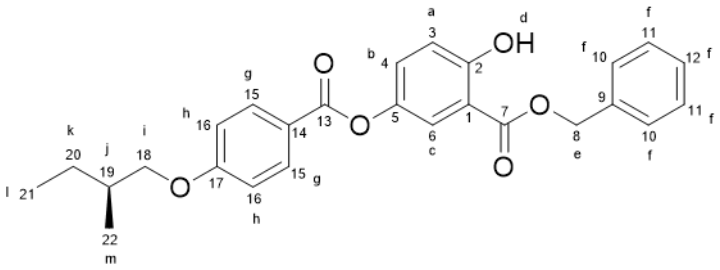

Figure 2.4. (*S*)-Benzyl-2-hydroxy-5-(4'-(2-methylbutyloxy)benzoyloxy)benzoate (**16**) with labelled protons and carbon atoms.

Using (*S*)-benzyl-2-hydroxy-5-(4'-(2-methylbutyloxy)benzoyloxy)benzoate (**16**) as an example, it is possible to elucidate by HSQC NMR (Figure 2.5) that the alkoxybenzoate moiety is attached to carbon "5" on the central benzene ring (Figure 2.4). This is based on the assignment of the protons (a-c), established through their splitting patterns and coupling constants using ^{1}H NMR, and then through their direct bonding with carbons "3", "4" and "6" respectively. Building on this, HMBC NMR (Figure 2.6) indicates a 'through-bond' interaction between the phenolic proton "d" and carbon "2". Therefore, due to the previously discussed difference in phenol reactivity, the single attachment of an alkoxybenzoic acid was completed to yield compounds **14**-**16**. This control enables the assembly of the structural isomers **CM1/2**, **CM3/4**, **CM5/6** and **CM7/8**.

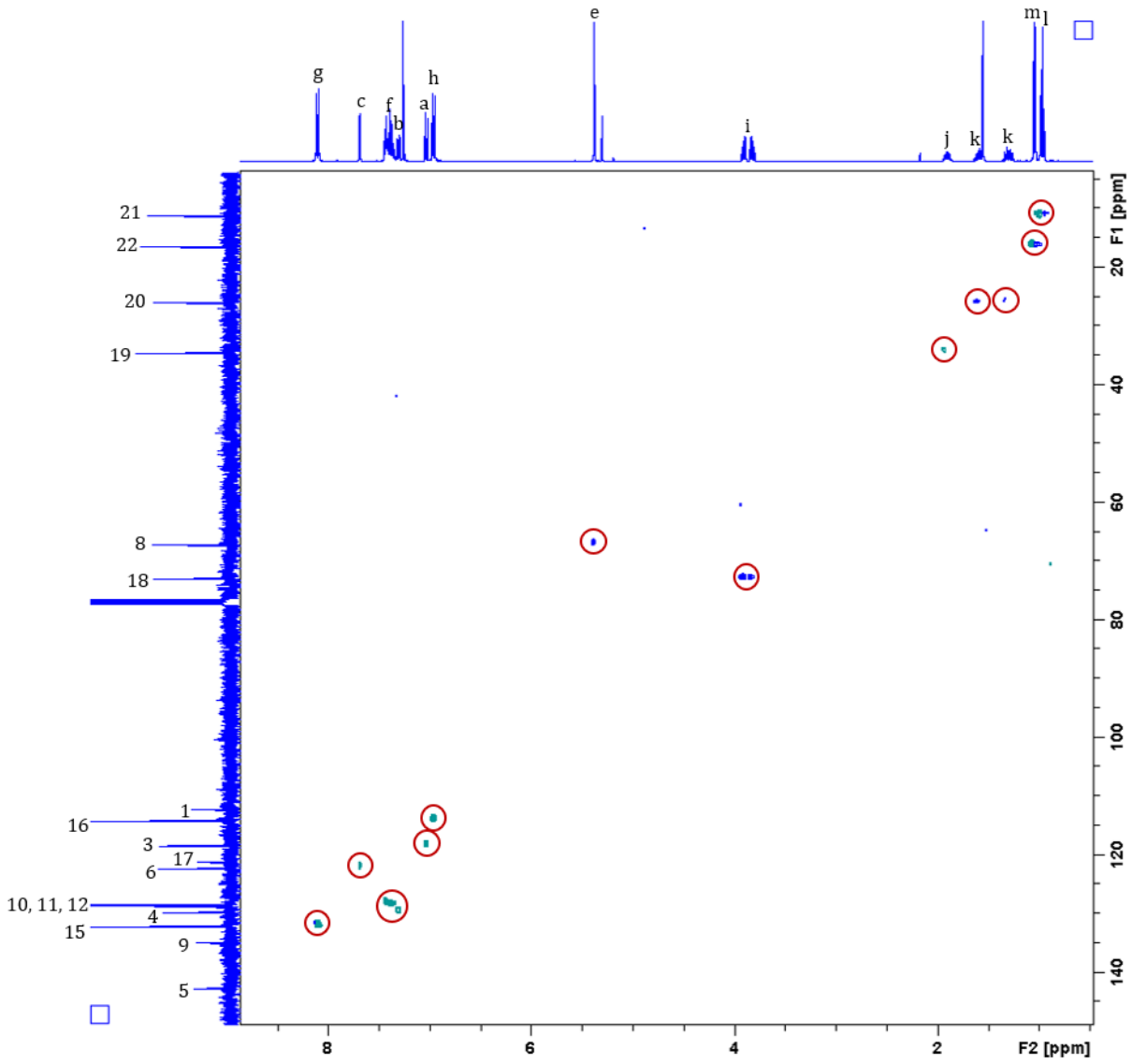

Figure 2.5. 2D HSQC NMR of (*S*)-benzyl-2-hydroxy-5-(4'-(2-methylbutyloxy)benzoyloxy)benzoate (**16**).

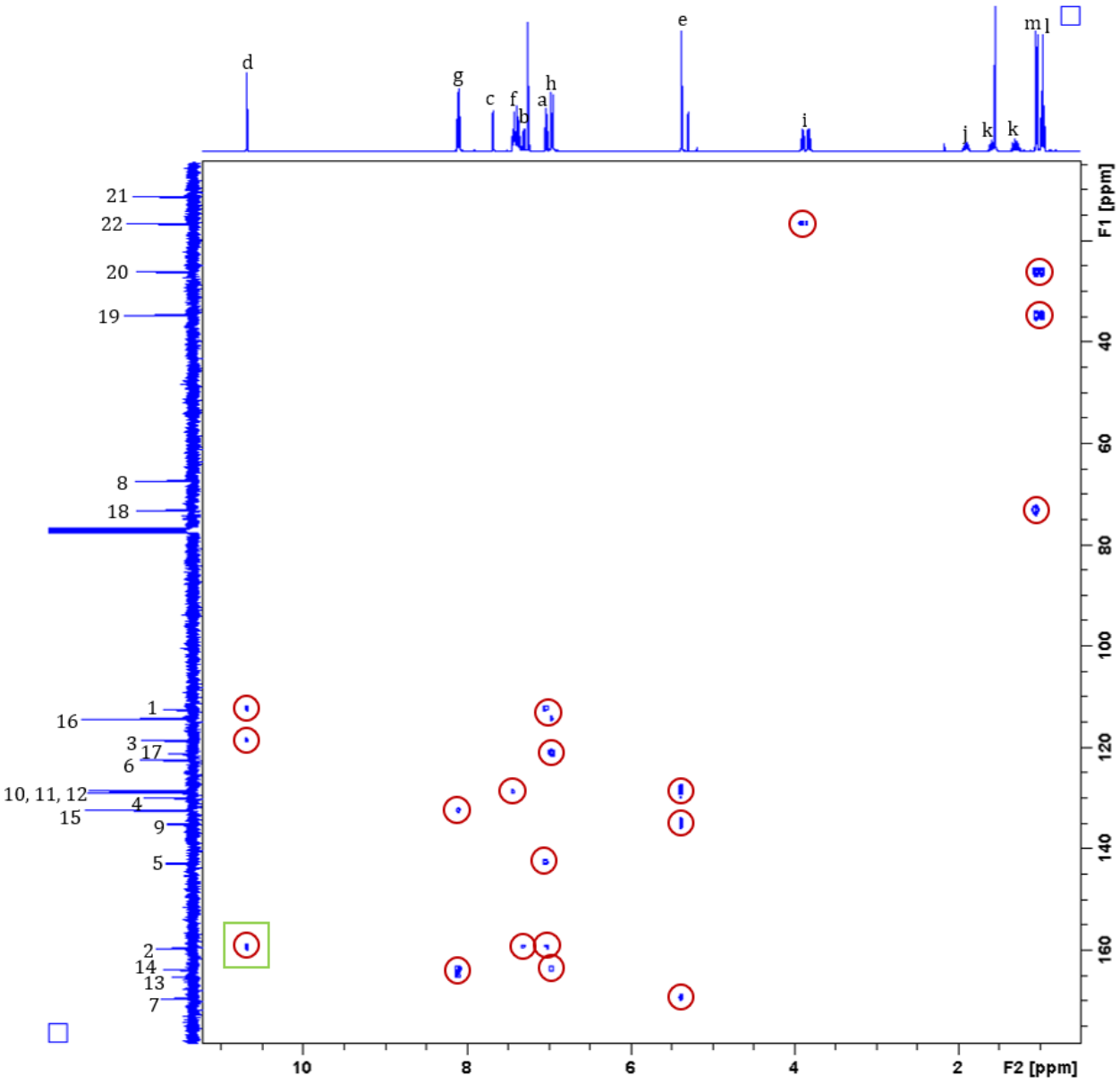

Figure 2.6. 2D HMBC NMR of (*S*)-benzyl-2-hydroxy-5-(4'-(2-methylbutyloxy)benzoyloxy)benzoate (**16**).

2.4 Synthesis of Thin Films

2.4.1 Choice of Radical Initiator

Just as with conventional polymers, the polymerisation of a liquid crystal monomer can proceed *via* a number of mechanisms. To create an aligned monodomain sample it is advantageous to use nematic acrylate monomers, polymerisable by a free radical mechanism directly in the aligned nematic phase (Figure 2.7). As discussed in the introduction, the use of a thermal initiator, such as azobisisobutyronitrile (AIBN), can sometimes be limited for liquid crystal polymers, as the thermal decomposition temperature needs to be within the nematic phase of the monomer to maintain the alignment. On the other hand, when using a photoinitiator the decomposition is largely temperature independent, and the absorption maximum of the initiators closely matches the output of common UV sources (Figure 2.8).[160]

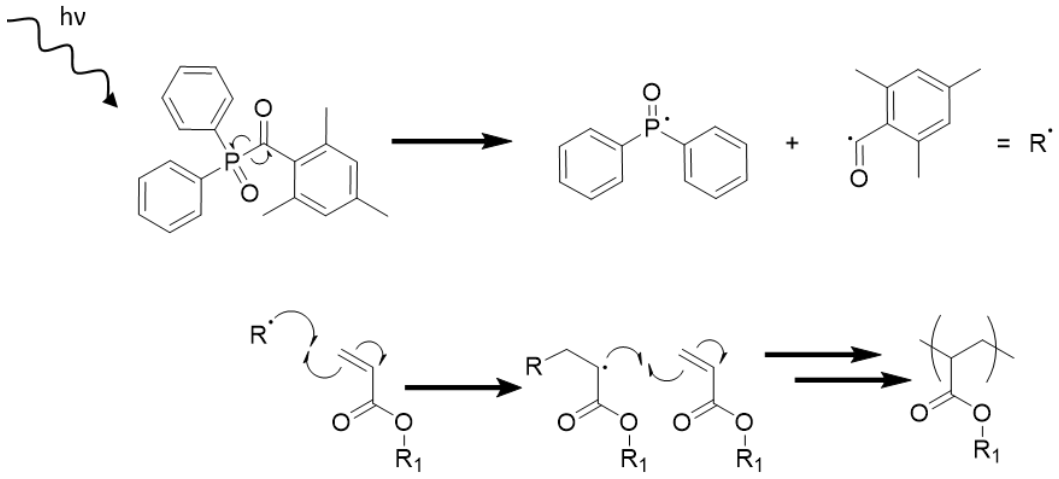

Figure 2.7. General mechanism of the photo-initiated radical polymerisation of an acrylate using 2,4,6-trimethylbenzoyldiphenylphosphine oxide.

The photoinitiator 2,4,6-trimethylbenzoyldiphenylphosphine oxide (Figure 2.7) is an acyl phosphine oxide that has been commonly used in the literature.[94,121–123,161] It has good miscibility with acrylates and a strong molar absorptivity at 365-385 nm (Figure 2.8), requiring only low loadings to generate free radicals, thereby ensuring the sample is cured throughout and not just at the interface, which would lead to poor mechanical properties.[162] The absorption of UV light cleaves the phosphorus-carbon bond and the rapid generation of radicals leads to fast curing times.

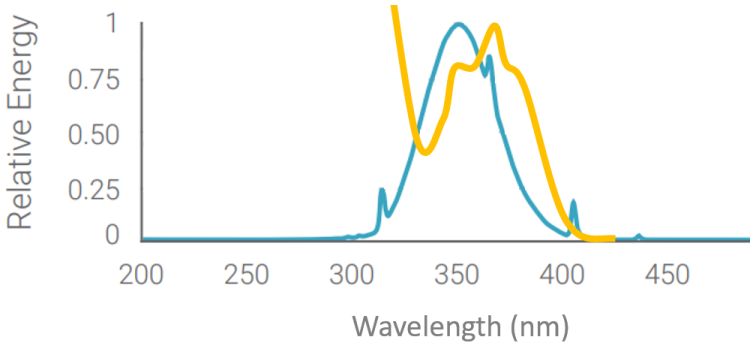

Figure 2.8. Overlay of the spectral output of a UV lamp peaking at 365 nm (blue) with the absorption profile of 2,4,6-trimethylbenzoyldiphenylphosphine oxide (yellow), adapted from references [160] and [162].

Two UV sources were used to initiate the homolysis of the photoinitiator used in this thesis: an RS Exposure Unit (LV202-E) with an output of 2.5 mW/cm^2 and an Omnicure LX500 with a peak output of 14000 mW/cm^2 at 10 mm distance.[163]

2.4.3 Polymer Films

Photo-polymerisable mixtures of monomer (**M1**-**M4** and **CM1**-**CM9**) and the photoinitiator 2,4,6-trimethylbenzoyldiphenylphosphine oxide (2 mol%) were created by dissolving the compounds in chloroform, in an amber glass vial, and evaporating the solvent at 100 °C. The mixtures were capillary-filled into 25-µm homogeneous-aligned glass cells in the isotropic phase on a temperature-controlled hot stage and then cooled into the (chiral) nematic phase and annealed. Due to the increased viscosity of the chiral nematic phase, the chiral nematic monomers required longer annealing times to eliminate defects compared to the nematic monomers. Annealing was followed by UV irradiation at 350 nm for 45 minutes using a RS Exposure Unit LV202-E to initiate the radical polymerisation of the acrylate, yielding the polymer films **P1**-**P4** and **CP1**-**CP9**. After analysis by POM, the glass cell was carefully opened with a scalpel, following immersion in liquid nitrogen, for further analysis by DSC.

2.4.4 Elastomer Films

Photo-polymerisable mixtures of monomer (**M1**-**M4**), the crosslinker 1,6-hexanediol diacrylate (10 mol%) and the photoinitiator 2,4,6-trimethylbenzoyldiphenylphosphine oxide (2 mol%) were created by dissolving in chloroform, in an amber glass vial, and

evaporating the solvent at 100 °C. The mixtures were capillary-filled into 10-µm homogeneous-aligned glass cells in the isotropic phase on a temperature-controlled hot stage, then cooled into the nematic phase and annealed for 10 minutes. Annealing was followed by UV irradiation at 365 nm using an Omnicure LX500, for 10 minutes, at 50% intensity and from a distance of 30 cm, to initiate the radical polymerisation of the acrylate, yielding the elastomer films **E1**-**E4**. After analysis by POM, the glass cell was carefully opened with a scalpel, following immersion in liquid nitrogen, for further analysis by DSC.

2.5 Characterisation

The optical and thermal phase properties of the monomers, **M1**-**M4** and **CM1**-**CM9**, the polymers, **P1**-**P4** and **CP1**-**CP9** and the elastomers **E1**-**E4** were investigated by polarised light optical microscopy (POM) and differential scanning calorimetry (DSC). The molecular weight distributions of the polymers were also analysed by gel permeation chromatography (GPC).

2.5.1 Nematic Monomers

The monomers **M1**-**M4** were analysed by POM and found to possess enantiotropic nematic phases as confirmed by the natural and aligned planar textures in Figure 2.9.

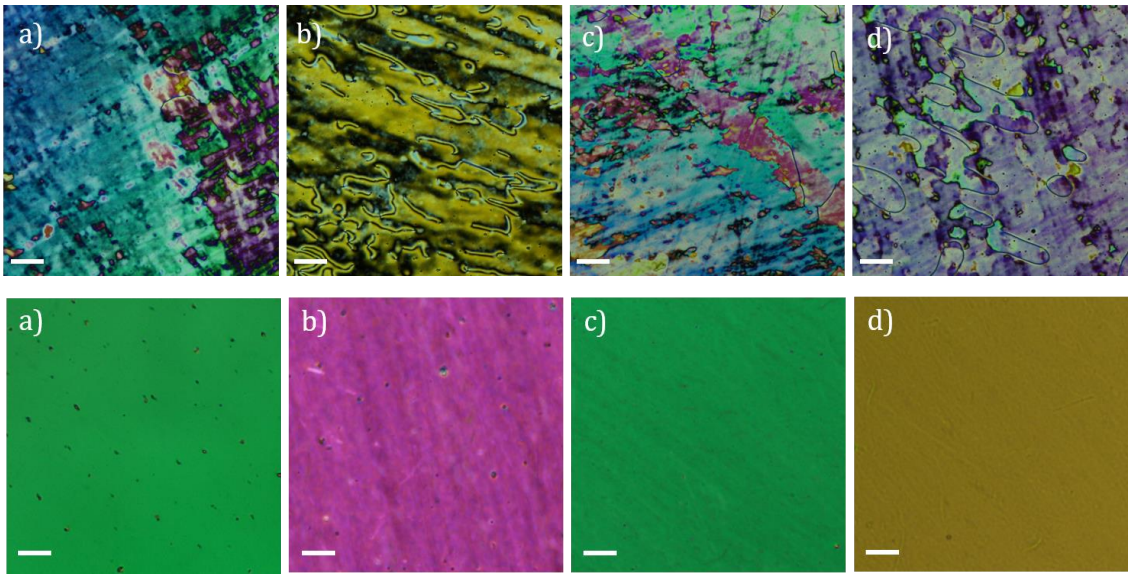

Figure 2.9. Polarised light photomicrographs of natural textures (top) and aligned textures (bottom) of nematic monomers on cooling at x100 magnification: a) **M1** at 55 °C, b) **M2** at 55 °C, c) **M3** at 45 °C and d) **M4** at 55 °C. Scale bar = 50 µm.

Table 2.1. Thermal properties of nematic monomers **M1-M4** obtained from DSC at a heating rate of 10 °C min^{-1} taken from the peak onset. Melting points taken from the first heat cycle.

Monomer	R	n	T_m /°C	T_{NI} /°C	ΔH_{NI} /J g^{-1}
M1	$-C_4H_9$	4	72.9	85.4	0.88
M2	$-C_7H_{15}$	4	54.6	70.8	1.50
M3	$-C_4H_9$	11	53.2	69.5	1.00
M4	$-C_7H_{15}$	11	41.7	62.9	0.91

The thermal analysis of the nematic monomers **M1**-**M4** was obtained from the first DSC heat cycle and the results summarised in Table 2.1. An example DSC curve of **M2** is shown in Figure 2.10.

The nematic to isotropic phase transition temperature of **M1** is in good agreement with the literature (T_{NI} = 87 °C).[21,23,38] By increasing the peripheral alkoxy chain in length, from butyl to heptyl, a decrease in the phase stability of **M2** of 14.6 °C is observed. Increasing the length of the spacer from butyl to undecyl in **M3** and **M4** also has a similar effect and consequently the phase stability is reduced by 15.9 °C and 22.5°C respectively.

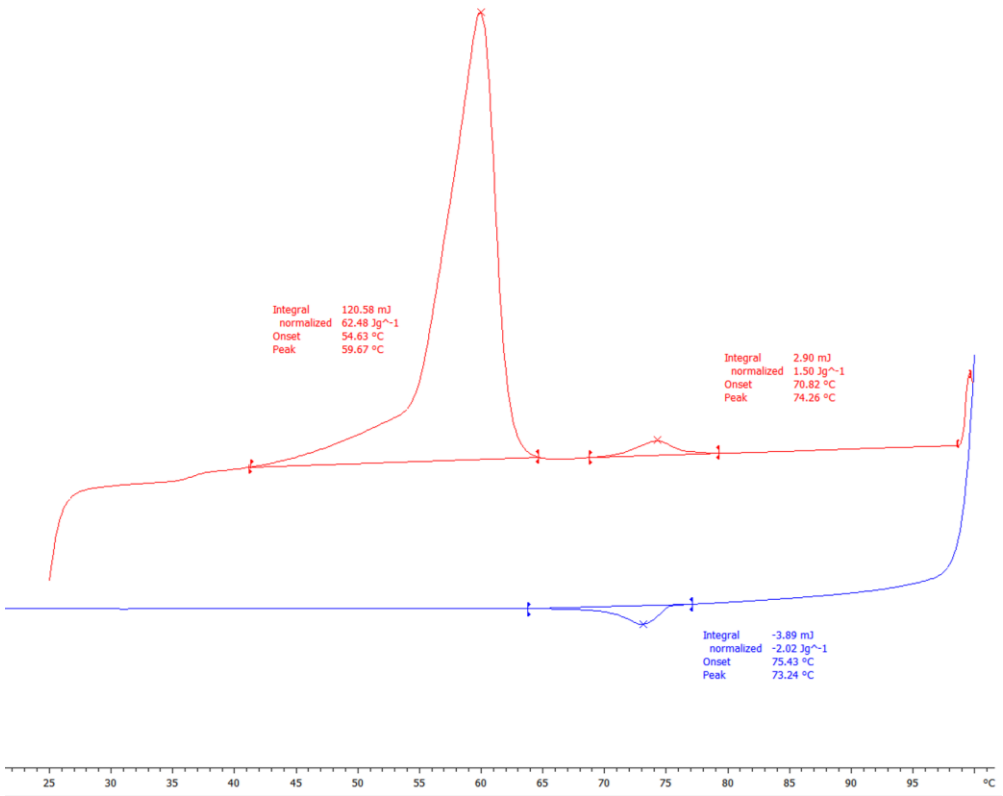

Figure 2.10. DSC curve of **M2** on first heat/cool cycle at 10 °C min^{-1}.

2.5.2 Chiral Nematic Monomers

The chiral monomers **CM1**-**CM9** were analysed by polarised optical microscopy and found to possess chiral nematic phases as confirmed by the *Grandjean* textures when sheared to induce homogenous alignment (Figure 2.11). It was found that the chiral monomers **CM1**-**8** had a long pitch and did not selectively reflect light in the visible region, although it was not possible to measure the exact location in the IR due to a lack of the necessary fibre optic probe for NIR spectroscopy. A contact preparation between **CM1** and the chiral dopant CB15 did however confirm a long pitch, as a visible selective reflection gradient was observed at the interface, due to the concentration gradient of CB15 in **CM1** decreasing the pitch (Figure 2.12). This is unexpected given the previous work by Lewthwaite *et al*, who reported that using (*S*)-2-methylbutan-1-ol with a structurally similar mesogen and the same lateral attachment of the spacer imparted a chiral nematic

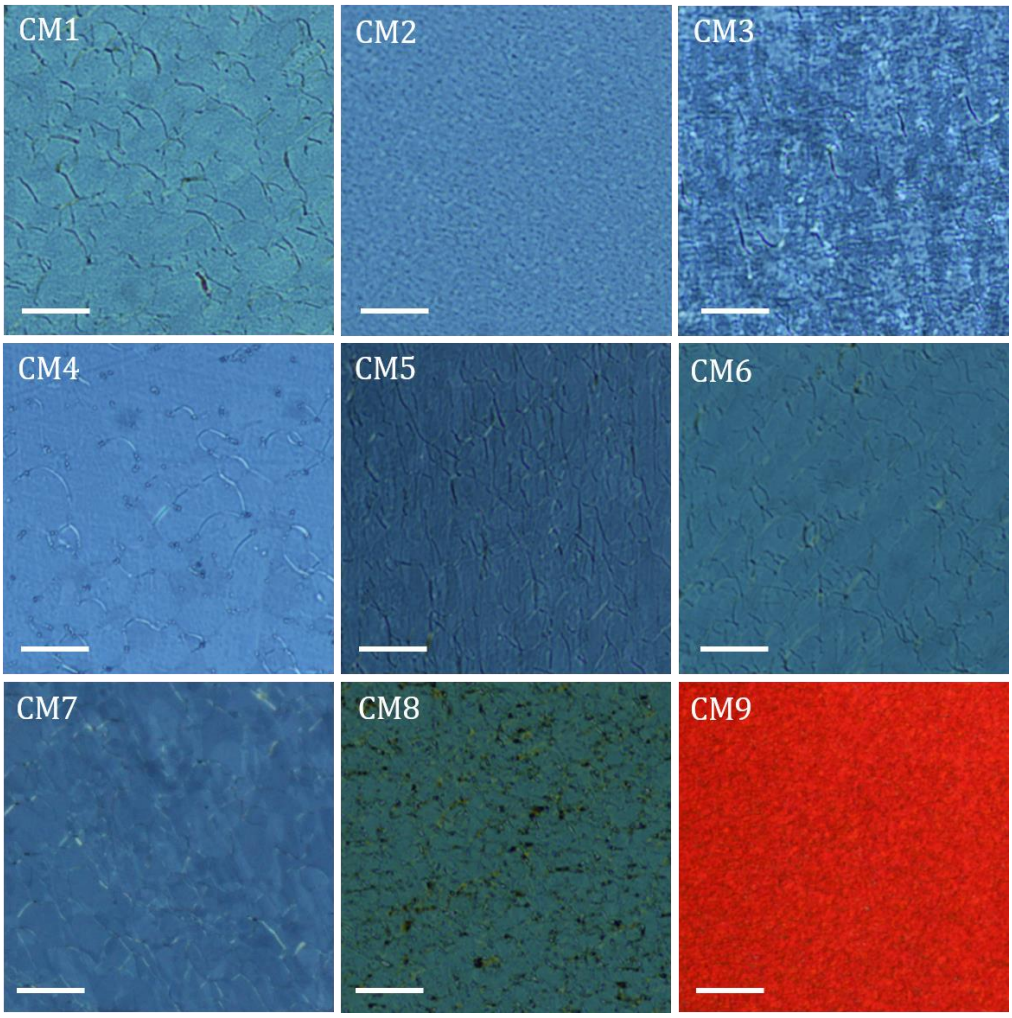

Figure 2.11. Polarised light photomicrographs of **CM1**-**8** in transmission mode at 30 °C and **CM9** in reflection mode at 10 °C, at x200 magnification. Scale bar = 25 μm.

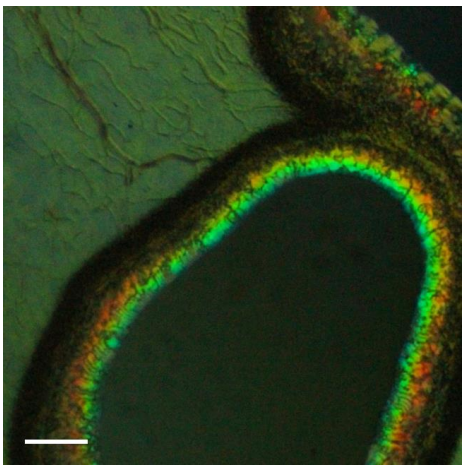

Figure 2.12. Polarised light photomicrograph of a contact preparation of **CM1** (top left of image) and CB15 (bottom right of image) in reflection mode at x100 magnification. Scale bar = 100 μm.

phase with a short pitch, although the exact pitch was not reported.[68] However, Tsukamoto *et al* compared a number of different chiral derivatives and reasoned that compared to 2-methylbutyl, the oxygen atom in 2-methylbutoxy reduces the twist angle due to the larger bond angle.[158] The chiral monomer **CM9,** however, contains the chiral terminal chain derived from (*R*)-2-octanol. The higher HTP of this moiety, caused by the chiral centre's closer proximity to the mesogenic core, induces a tighter pitch and consequently a red visible selective reflection was observed (Figure 2.11).

The chiral monomers **CM1**-**CM9** were analysed by DSC and their thermal properties were obtained from the first DSC heat cycle, summarised in Table 2.2. All of the chiral monomers are monotropic, except **CM7**, which was found to have an enantiotropic chiral nematic phase, and possess low temperature clearing points, which is useful for the intended polymerisations. The phase stabilities of the chiral monomers are much lower compared to the achiral **M1**-**M4**, as the chiral group destabilises the mesophase. The magnitude of the enthalpy values is consistent with a chiral nematic phase.[164]

In the chiral monomers with a short spacer (n = 4), by increasing the peripheral alkoxy chain in length, from butyl to heptyl, an increase in the phase stability of 7.7 °C (**CM1**/**3**) and 6.9 °C (**CM2**/**4**) is observed. This is in contrast to the decrease seen with the achiral monomers, **M1** and **M2**, and as would be expected when considering both an increase in the chain conformations and an odd-even effect – an even number of methylene units, as is the case with butyloxy, usually leads to a higher phase stability due to enhanced orientational anisotropy.[5] Of the chiral monomers with a long spacer (n = 11, **CM5**-**8**), the

Table 2.2. Thermal properties of chiral nematic monomers **CM1-CM9** obtained from DSC at a cooling rate of 10 °C min^{-1} taken from the peak onset. ( ) denotes a monotropic phase. Melting points taken from first heat cycle.

Monomer	R_1	R_2	n	T_m /°C	T_{N^*I} /°C	ΔH_{N^*I} /J g^{-1}
CM1	$-C_4H_9$	$-CH_2CH^*(CH_3)C_2H_5$	4	55.5	(44.2)	1.46
CM2	$-CH_2CH^*(CH_3)C_2H_5$	$-C_4H_9$	4	58.9	(43.6)	1.47
CM3	$-C_7H_{15}$	$-CH_2CH^*(CH_3)C_2H_5$	4	80.5	(51.9)	1.30
CM4	$-CH_2CH^*(CH_3)C_2H_5$	$-C_7H_{15}$	4	72.0	(50.5)	1.52
CM5	$-C_4H_9$	$-CH_2CH^*(CH_3)C_2H_5$	11	50.7	(40.8)	1.43
CM6	$-CH_2CH^*(CH_3)C_2H_5$	$-C_4H_9$	11	47.9	(43.9)	1.67
CM7	$-C_7H_{15}$	$-CH_2CH^*(CH_3)C_2H_5$	11	33.7	43.3	1.26
CM8	$-CH_2CH^*(CH_3)C_2H_5$	$-C_7H_{15}$	11	47.7	(41.9)	1.42
CM9	$-C_7H_{15}$	$-CH^*(CH_3)C_6H_{13}$	4	58.1	(19.5)	0.98

isomer pair **CM5/7** also follows this trend (increasing by 2.5 °C), however **CM6/8** does not (decreasing by 2.0 °C).

In addition to this, there is an indication that the position of the chiral group can affect the phase stability in the chiral monomers, when comparing isomeric pairs (**CM1/2** and **CM3/4**). If the chiral moiety is *meta (i.e. R_1)* to the spacer on the central benzene ring then, compared to when it is *ortho* (*i.e. R_2*), there is a decrease in the phase stability of 0.6 °C and 1.4 °C respectively. One of the longer chain pairs (*n* = 11, **CM7/8**) also displays this trend, where a decrease of 1.4 °C was found. However, **CM5/6** do not, as an increase of 3.1 °C was observed. Gomes *et al* found that the spatial position of the spacer in constitutional isomers played an important role in the phase properties of polymethyacrylates with long spacers (*n* = 11) and that this was likely due to an energy difference of the *trans* and *gauche* conformations.[151] Conformational modelling and synthesis of further isomeric pairs with different peripheral chain lengths could serve to gain a better understanding of this apparent trend.

Compared to the other chiral monomers, the phase stability of the chiral monomer **CM9** is far lower, to just below room temperature. The reduction in phase stability is due to the closer position of the chiral centre to the core of the mesogen, and the disruption to the mesophase that this causes.

2.5.3 Nematic Polymers and Elastomers

Following the UV-initiated free radical polymerisation, the thin films of polymers **P1**-**P4** were analysed by POM. Rotation of the films under crossed polarisers reveals that the overall alignment is retained although many defects that follow the rubbing direction are observed. (Figure 2.13).

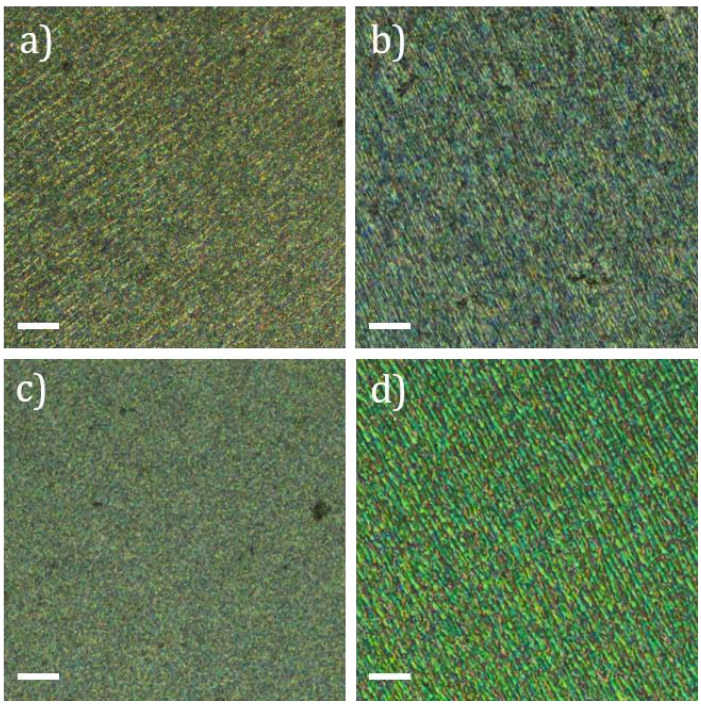

Figure 2.13. Polarised light photomicrographs of nematic polymers on cooling at x100 magnification: a) **P1** at 75 °C, b) **P2** at 65 °C, c) **P3** at 60 °C and d) **P4** at 60 °C. Scale bar = 50 μm.

The nematic polymers **P1**-**P4** were then analysed by DSC and the results are summarised in Table 2.3. The phase stability compared to the respective monomers is increased in all polymers, although the increase of T_{NI} in **P1** is larger than in **P2**-**P4**, and in all polymers **P1**-**P4** (and elastomers **E1**-**E4**) the phase stability is higher in polymers with short side chains (**P1**, **P3**, **E1**, **E3**) compared to longer side chains. Wei *et al* propose that this is due to an internal tension, where longer alkyl chains strengthen the correlation between the mesogen and backbone, leading to a larger chain anisotropy. This leads to greater distortion from the equilibrium conformation and so to maximise the entropy the phase stability is reduced.[21,36] Whilst the polymers **P1-P4** have been prepared previously in the group by Davey, the phase stability is considerably higher in all cases, indicating an improved level of purity and/or molecular weight.[38]

Table 2.3. Thermal properties of the nematic polymers **P1**-**P4** and nematic elastomers **E1**-**E4** obtained from DSC at heating/cooling rates of 10 °C min^{-1}. Phase transition temperatures obtained from the peak onset on heating, whilst glass transition temperatures were taken from the midpoint on cooling.

Polymer	R	n	T_g /°C	T_{NI} /°C	ΔH_{NI} /J g^{-1}
P1	$-C_4H_9$	4	41.3	117.1	2.93
P2	$-C_7H_{15}$	4	15.4	77.8	1.62
P3	$-C_4H_9$	11	13.4	89.8	1.31
P4	$-C_7H_{15}$	11	4.8	74.9	1.26
E1	$-C_4H_9$	4	42.8	116.1	1.48
E2	$-C_7H_{15}$	4	17.3	76.0	1.32
E3	$-C_4H_9$	11	15.6	86.3	1.28
E4	$-C_7H_{15}$	11	14.2	78.4	1.03

The glass transition temperatures of all the polymers are low, whilst **P2**-**P4** are below room temperature, which is useful for creating responsive microparticles, as the backbone is in the more flexible, rubbery state at temperatures that the particles would ideally be used. The T_g of the polymers decreases with increasing alkyl chain lengths of both the side chains and the spacer, as the greater chain mobility leads to an increase in the free volume. The temperature range (ΔT = T_{NI}-T_g) in which the particles are responsive is also maintained across the series.

The elastomers **E1**-**E4** also have increased phase stability relative to the monomers, albeit slightly reduced compared to the respective polymers, due to the presence of the crosslinker disrupting the nematic ordering. Compared to **E1**, the decreased phase stability of **E2**-**E4** is useful as any change in the microparticles' shape that may occur will be at lower temperatures. The phase transition temperature, glass transition temperature and enthalpy of elastomer **E1** agree well with the published literature values (T_g = 39.9 °C, T_{NI} = 119.3 °C, ΔH = 2.9 J g^{-1}).[23] A slight increase in the glass transition temperatures of the elastomers **E1**-**E4** compared to the polymers **P1**-**P4** was also observed, again due to the crosslinker restricting the polymer chain movement. However, this is only minor and the phase properties are favourable for creating responsive elastomer microparticles.

The molecular weight distributions and polydispersity of the polymers **P1**-**P4** were analysed by triple detection GPC in THF and the results are summarised in Table 2.4. All polymers show number average molecular masses >500,000 g mol^{-1}. Given the high molecular weights, the phase transition temperatures found by DSC can be considered independent of the exact molecular weight.[9]

Table 2.4. Molecular weights and polydispersity of nematic polymer films **P1**-**P4** obtained from GPC in THF, using polystyrene standards.

Polymer	M_n /g mol^{-1}	PDI
P1	1270000	1.8
P2	569100	1.9
P3	621200	2.3
P4	935800	2.0

2.5.4 Chiral Nematic Polymers

Following the UV-initiated free radical polymerisation, the thin films of polymers **CP1**-**CP9** were analysed by polarised light microscopy and found to retain the homogeneous alignment and *Grandjean* texture throughout the UV-initiated polymerisation, with only a small degradation of the texture (Figure 2.14). In reflection mode, **CP1**-**CP8** do not possess a visible selective reflection, indicating that the helical twisting power of this series of chiral polymers, bearing a 2-methylbutyloxy group, is low and therefore the selective reflection occurs in the IR. In transmission the mode, the observed grey/blue colour is instead mainly due to the wavelength dependence of the optical activity. The observed colours on the clockwise rotation of the analyser (blue to yellow to red) confirms a left handed helix.[165] The chiral polymer **CP9** has a shorter pitch, like the monomer **CM9**, and the selective reflection colour is red (Figure 2.14).

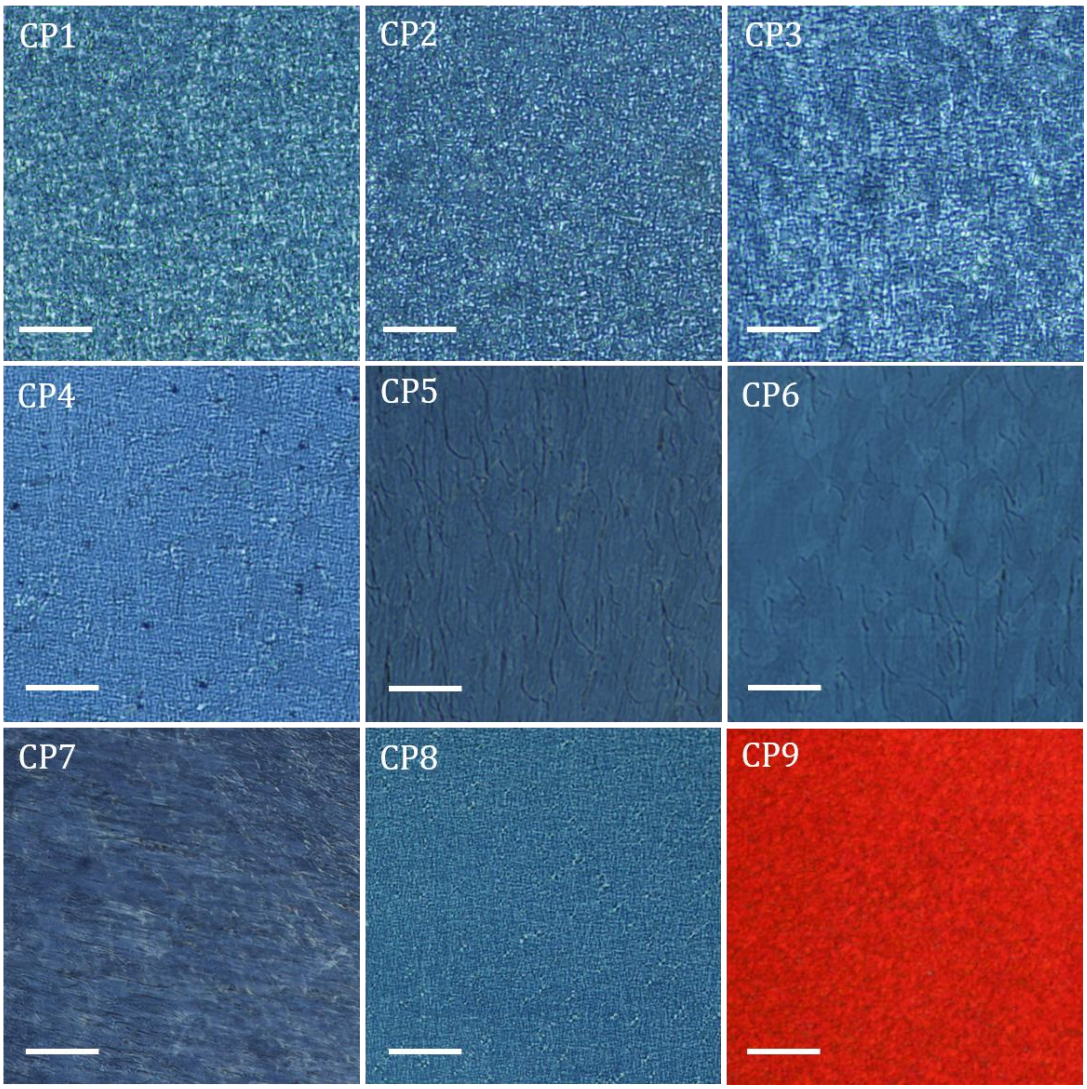

Figure 2.14. Polarised light photomicrographs of **CP1**-**8** in transmission mode and **CP9** in reflection mode at x200 magnification. Scale bar = 25 μm.

The thermal properties of the chiral polymers (**CP1**-**9**) were analysed by DSC and summarised in Table 2.5. Like the achiral polymers, the phase stability is increased relative to the monomers, although to varying amounts. All the polymers are enantiotropic, in contrast to the monomers, which has been observed to occur in side-chain LCPs.[166,167] The dependence of the phase stability on the polymer molecular weight leads to an increase of the clearing point to above that of the monomer melting point, above a certain number of polymeric units, as the ordered backbone leads to an increased ordering of the mesogens – dubbed 'the polymer effect'.[9,168] The chiral polymers with the undecyl spacer (*n* = 11, **CP5**-**8**) possess low glass transition temperatures, below room temperature, which is favourable as the chiral nematic phase range of the polymer is consequently increased compared to the polymers containing the shorter butyl spacer (*n*

= 4, **CP1**-**4**). The temperature range in which microparticles made from these materials would be stimuli-responsive is also widened and, importantly for device applications, includes room temperature. Like the achiral polymers, T_g of the chiral polymers decreases with increasing alkyl chain length of the side chains and the spacer as the greater chain mobility leads to an increase in the free volume.

Table 2.5. Thermal properties of the chiral nematic polymers **CP1**-**CP9** obtained from DSC at heating/cooling rates of 10 °C min^{-1}. Phase transition temperatures were obtained from the peak onset on heating, whilst glass transition temperatures were taken from the midpoint on cooling.

Polymer	R_1	R_2	n	T_g /°C	T_{N^*I} /°C	ΔH_{N^*I} /J g^{-1}
CP1	$-C_4H_9$	$-CH_2C^*H(CH_3)C_2H_5$	4	40.3	75.0	2.60
CP2	$-CH_2C^*H(CH_3)C_2H_5$	$-C_4H_9$	4	39.2	59.9	1.60
CP3	$-C_7H_{15}$	$-CH_2C^*H(CH_3)C_2H_5$	4	26.2	64.7	1.74
CP4	$-CH_2C^*H(CH_3)C_2H_5$	$-C_7H_{15}$	4	31.2	55.8	1.66
CP5	$-C_4H_9$	$-CH_2C^*H(CH_3)C_2H_5$	11	16.2	54.9	0.95
CP6	$-CH_2C^*H(CH_3)C_2H_5$	$-C_4H_9$	11	16.7	57.1	1.47
CP7	$-C_7H_{15}$	$-CH_2C^*H(CH_3)C_2H_5$	11	9.2	55.2	1.05
CP8	$-CH_2C^*H(CH_3)C_2H_5$	$-C_7H_{15}$	11	9.6	47.0	1.17
CP9	$-C_7H_{15}$	$-CH^*(CH_3)C_6H_{13}$	4	11.5	21.7	0.38

Similar to the monomers, comparing the thermal properties of the isomeric polymer pairs suggests a link between the position of the chiral group on the mesogen and the spacer/backbone with the phase stability. In all cases, except **CP5** and **CP6**, the polymer with the chiral group in the *ortho* position (R_2) has an increased phase stability compared to when the chiral group is in the *meta* position (R_1). Comparing **CP1**/**CP2**, the phase stability is increased by 15.6 °C; **CP3**/**CP4** is increased by 8.9 °C and **CP7**/**CP8** is increased by 8.2 °C. These much larger differences in the phase stability, compared to the monomers, could indicate that the conformation of the chiral mesogenic unit is influenced by the shape of the polymer backbone to a larger degree than when it is not present in the monomers.

In comparison to the other chiral polymers, the chiral polymer **CP9** has a much lower phase stability due to the 1-methylheptyloxy chain. Compared to **CP3**, which has the same

spacer length and achiral chain length, the phase stability is reduced by 43 °C to just above room temperature.

The molecular weight distributions and polydispersity of the chiral polymers **CP1**-**CP9** were analysed by triple detection GPC in THF and the results are summarised in Table 2.6. As with the nematic polymers, the high molecular weights, with the exception of **CP5**, mean that the phase transition temperatures found by DSC are molecular weight independent.

Table 2.6. Molecular weights and polydispersity of chiral nematic polymer films **CP1**-**CP9** obtained from GPC in THF, using polystyrene standards.

Polymer	M_n /g mol^{-1}	PDI
CP1	2456000	1.1
CP2	1319000	1.9
CP3	1670000	1.8
CP4	609700	2.5
CP5	36000	2.6
CP6	690000	1.5
CP7	2361000	1.7
CP8	2180000	1.6
CP9	302200	2.6

2.6 Conclusion

A series of laterally attached nematic acrylate monomers, **M1-M4**, were synthesised. All the monomers displayed enantiotropic nematic phases. The length of the peripheral alkyl side chains and the length of the spacer was varied. The effects of these structural changes on the nematic phase properties were studied by DSC and it was found that T_{NI} decreases with increasing chain length. Photo-polymerisation of the monomers allowed for the preparation of liquid crystal polymers and, with a crosslinking molecule, liquid crystal elastomers as thin films. The nematic phase stability increased on polymerisation, whilst a longer spacer decreased the glass transition temperature, widening the nematic phase

range. These achiral monomers are used in the following chapters to create nematic polymer and elastomer microparticles.

Also prepared were a series of laterally attached chiral nematic acrylate monomers, bearing a chiral pendent chain derived from (*S*)-2-methylbutan-1-ol and achiral alkoxy chains of different length, forming structural isomers (**CM1**-**8**). The monomers and polymers form chiral nematic phases with good phase stability and selective reflection outside the visible range, in the IR. A comparison of the chiral nematic-isotropic phase transition temperatures of the structural isomers suggested an influence related to the position of the chiral centre relative to the central core of the mesogen in the monomers and a larger influence in the polymers. It was found in three of the four isomer pairs studied that positioning the chiral moiety *ortho*, relative to the central core of the mesogen, and away from the spacer, increased T_{NI} compared to *meta* placement in the monomers and the polymers. There is relatively little literature on the effect of structural isomerism in chiral nematic polymer and elastomers, but these results suggest another method of modifying the phase stability of chiral nematic liquid crystals, although more isomer pairs should be studied to gain a better understanding of the apparent trends.

The synthesis and characterisation of a chiral monomer (**CM9**) and polymer (**CP9**) with a chiral group derived from (*R*)-2-octanol was also completed; with selective reflection in the visible range but with a low phase stability.

Chapter 3:
Imprinted Chiral Nematic Elastomer Films

3 Imprinted Chiral Nematic Elastomer Films

3.1 Introduction

This chapter describes the preparation of chiral nematic elastomers as thin-films. Mixtures were created using the nematic monomers synthesised in this thesis along with the commercial chiral dopant CB15 to induce the chiral nematic phase. The optical properties of the films were characterised by UV-vis spectroscopy. The stimuli-responsiveness of the elastomers was investigated using polarised optical microscopy (POM) and the thermal properties studied by differential scanning calorimetry (DSC).

Chiral nematic elastomers capable of selectively reflecting visible light of wavelength λ require a short pitch (p) helix as described by Equation 3.1, where $\bar{n}$ is the average refractive index.

$$\lambda = \bar{n} \cdot p \qquad \text{Equation 3.1}$$

It was established in the previous chapter that the pitch of the chiral nematic phase of the monomers **CM1**-**8** and polymers **CP1**-**8** was too long for selective reflection in the visible region to occur. The monomer **CM9** and polymer **CP9** showed a red selective reflection; however, the phase stability was low and initial experiments confirmed that the addition of a crosslinker needed to create liquid crystal elastomers further depresses the clearing point of the monomer below a useful range where polymerisation in the aligned state is very difficult to achieve and would require temperatures well below room temperature.

As discussed in the previous chapter, although the phase stability of the chiral monomers **CM1**-**9** is reasonable, initial experiments suggested that the addition of a chiral dopant in concentrations sufficient to shift the selective reflection to the visible caused the chiral nematic phase stability to drop below a useful range. On the other hand, the monomers **M1**-**4** possess much higher nematic phase stability and are therefore more suited to the creation of coloured chiral nematic LCE thin films and particles by doping with a chiral dopant.

3.2 Sample Preparation

3.2.1 Chiral Mixtures

Chiral nematic mixtures consisting of the laterally attached acrylate monomers **M1, M2, M3** or **M4**, the chiral dopant (*S*)-4'-(2-methylbutyl)-4-cyanobiphenyl (CB15), the crosslinker 1,6-hexanediol diacrylate (10 mol% relative to monomer) and the photoinitiator 2,4,6-trimethylbenzoyldiphenylphosphine oxide (2 mol% relative to monomer) were prepared. Variation of the monomer and concentration of the chiral dopant afforded the mixtures defined as **M1A-F**, **M2A-C**, **M3A** and **M4A-B**. The components were dissolved in chloroform to ensure good mixing, followed by evaporation of the solvent at 100 °C. Thin-films of the mixtures were drawn into 10-μm planar aligned glass cells by capillary action on a temperature-controlled hot stage, in the isotropic phase at 80 °C, in the dark, to reduce the chance of premature polymerisation; then cooled into the chiral nematic phase and annealed for 1 hour to improve the texture and minimise defects. The films were then analysed by polarised light microscopy to evaluate the optical properties.

3.2.2 Chiral Imprinted Elastomers

3.2.2.1 Polymerisation

The annealed pre-elastomer mixtures **M1A-F**, **M2A-C**, **M3A** and **M4A-B** were photo-polymerised for 10 minutes at 365 nm in the chiral nematic phase, using an Omnicure LX500 spot curing system at 50% intensity, at a distance of 30 cm from the LED, to produce chiral nematic elastomers **E1A-F** and **E2A-C**, **E3A** and **E4A-B**. The films were then analysed by polarised light microscopy and UV-vis spectroscopy.

3.2.2.2 Solvent Washing

The CB15 within the elastomer films was removed by washing with acetone to obtain washed elastomers **WE1A-F**, **WE2A-D**, **WE3A** and **WE4A-B**. Following polymerisation, the glass cells were submerged in liquid nitrogen and opened with a scalpel. Using a syringe, the films were doused with acetone onto tissue paper thereby washing the dopant out of the elastomer, and upon which the films went isotropic. Shortly after, once the acetone had evaporated at room temperature, the chiral nematic phase reappeared. This

washing step was repeated five times to ensure the dopant had been extracted. The films were then analysed by polarised light microscopy, DSC and UV-vis spectroscopy.

3.2.2.3 Stimuli Responsiveness

Small samples of the imprinted elastomers **WE1B**, **WE1D** and **WE2B** were carefully cut and removed from their glass cells using a scalpel and immersed in PEG200. The films were heated to above the glass transition temperature of the elastomers to ensure good chain mobility and, therefore, responsiveness to external stimuli. The elastomers' responses to changes in pressure and temperature were analysed by microscopy.

3.3 Characterisation

3.3.1 Chiral Nematic Mixtures

Whilst CB15 is a commonly used chiral dopant, the HTP is relatively low - reported to be ~8 μm^{-1}.[169] This leads to only a moderate inducement of a helical twist, therefore reasonably large concentrations are required to reduce the pitch to the extent where

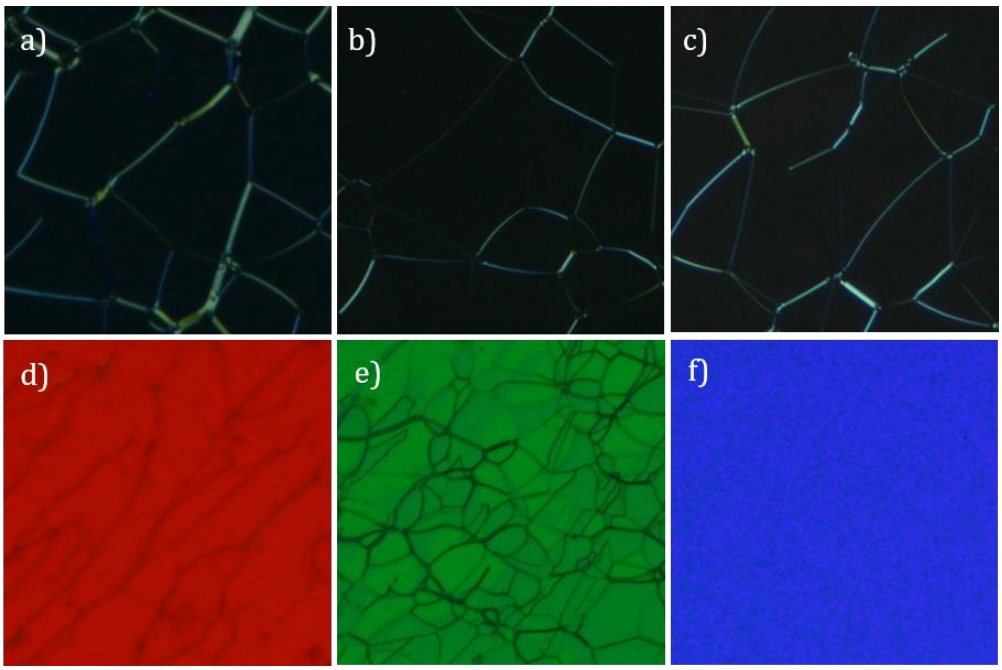

Figure 3.1. Polarised light photomicrographs of chiral nematic mixtures **M1A-F** (CB15 wt%) in reflection mode at 100x magnification: a) **M1A** (14 wt%) at 50 °C, b) **M1B** (18 wt%) at 50 °C, c) **M1C** (22 wt%) at 45 °C, d) **M1D** (29 wt%) at 40 °C, e) **M1E** (35 wt%) at 30 °C, f) **M1F** (41 wt%) at 27 °C.

Table 3.1. Optical and thermal properties of chiral nematic mixtures **M1A**-**F**, established using microscopy on heating.

Mixture	CB15 wt%	Colour	T_{NI} /°C
M1A	14	IR	58
M1B	18	IR	56
M1C	22	IR	51
M1D	29	Red	47
M1E	35	Green	42
M1F	41	Blue	28

selective reflection occurs in the visible region. The optical and thermal properties of **M1A**-**F**, observed by microscopy in reflection mode, are summarised in Table 3.1. It was found that 29 wt% of CB15 was required to produce a red selective reflection (**M1D**, Figure 3.1, d), while over 40 wt% was required to produce a blue selective reflection (**M1F**, Figure 3.1, f). Lower concentrations of CB15 produced a selective refection in the infrared (**M1A-C**, Figure 3.1, a-c). Due to the disruption to the mesophase caused by the dopant, the phase stability of the pre-elastomer mixture drops from 58 °C to 28 °C when moving from an infrared-reflecting to a blue-reflecting mixture.

The mixtures of **M2A**-**D** were also investigated by polarised light optical microscopy and their optical and thermal properties are summarised in Table 3.2. Unlike the mixtures of **M1**, no concentrations of CB15 higher than 24 wt% were investigated for **M2** as it was assumed that a similar effect to **M1** would be observed, as will be discussed later. Similar to the mixtures **M1A-C**, it was found that **M2A-D**, containing 17-24 wt% CB15, exhibited

Table 3.2. Optical and thermal properties of chiral nematic mixtures **M2A**-**C**, obtained by microscopy on heating.

Mixture	CB15 wt%	Colour	T_{NI} /°C
M2A	17	IR	53
M2B	19	IR	54
M2C	22	IR	49
M2D	24	IR	45

an infrared selective reflection. The phase stability is slightly reduced compared to the mixtures containing **M1A-C**, as the initial phase stability of pure **M2** is already considerably lower.

Mixtures containing the monomer with a long spacer (*n* = 11), **M3A** and **M4A-B**, were also studied by microscopy. The optical and thermal properties are summarised in Table 3.3. Similar to the mixtures containing the short spacer (*n* = 4) monomers, 41 wt% of CB15 produced a blue selective reflection (**M4B**, Figure 3.2, b). The phase stability is low however, due to a combination of the high percentage of CB15 required, and the lower initial phase transition temperature of the monomer - a result of the longer spacer and side chains within the monomer structure.

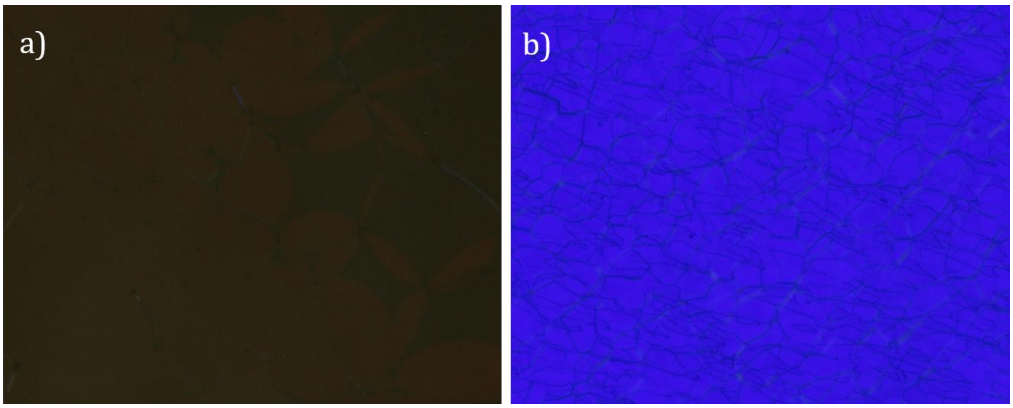

Figure 3.2 Polarised light photomicrographs of chiral nematic mixtures in reflection mode at 100x magnification: a) **M4A** (22 wt%) at 30 °C and b) **M4B** (41 wt%) at 20 °C.

Table 3.3. Optical and thermal properties of chiral nematic mixtures **M3A** and **M4A-B**, obtained by microscopy on heating.

Mixture	CB15 wt%	Colour	T_{NI} /°C
M3A	18	IR	46
M4A	22	Red/IR	39
M4B	41	Blue	25

3.3.2 Doped Chiral Nematic Elastomers

Following polymerisation, the chiral nematic elastomers **E1A-F** were initially analysed by microscopy. The thermal analysis**,** by temperature-controlled microscopy, confirmed an increase of T_{NI}, suggesting that the polymerisation was successful. As shown in Figure 3.3, it can be seen that the planar alignment is maintained, along with the reflection colours possessed by the monomers, albeit with the introduction of more defects compared to the monomer mixture. An accurate determination of T_{NI} was challenging due to the retention of the *Grandjean* texture and a slow reduction in the intensity of the colour over a broad range, rather than a sharp transition as in the mixture.

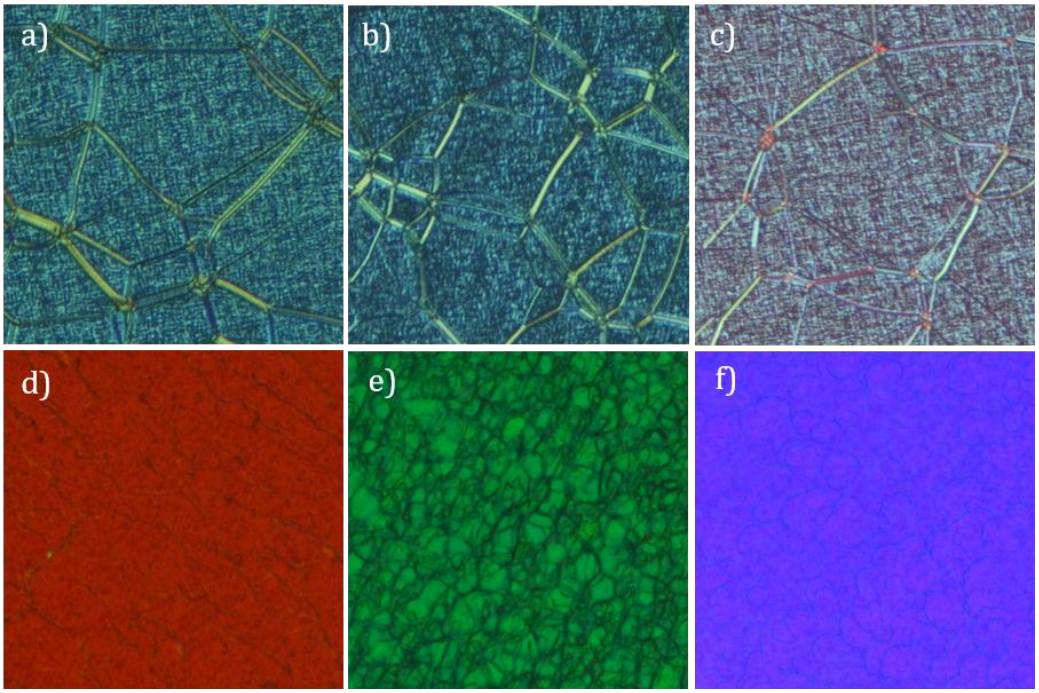

Figure 3.3. Polarised light photomicrographs of doped chiral nematic elastomers **E1A-F** (CB15 wt%) in reflection mode at 100x magnification: a) **E1A** (14 wt%) at 50 °C, b) **E1B** (18 wt%) at 31 °C, c) **E1C** (22 wt%) at 45 °C, d) **E1D** (29 wt%) at 40 °C, e) **E1E** (35 wt%) at 29 °C, f) **E1F** (41 wt%) at 27 °C.

To characterise any change in reflection properties on heating and cooling, **E1A-F** were analysed by UV-vis spectroscopy; the findings of which are summarised in Table 3.4. As a representative sample, the spectra of **E1E** is shown in Figure 3.4. Samples were positioned on the hot stage perpendicular to the fiber optic probe, and the reflection measured as a function of temperature. A measurement was taken every 5 °C, which resulted in a temperature range for T_{NI}, stated in Table 3.4, when the peak intensity dropped between these measurements. The intensity of the reflectance values obtained were arbitrary in

respect to the distance between the probe and the sample, and so were normalised to 50% to account for the theoretical maximum that can be reflected by a chiral nematic helix with a single handedness. The detected peak for **E1A** was on the limit of the detection range of the spectrometer, therefore λ_{max} for this elastomer is potentially erroneous. When heating from room temperature to the clearing point, a small red-shift of a few nm occurred. As expected for a chiral LCE, the selective reflection disappears upon isotropisation and reappears on cooling as the helical alignment is restored.

Table 3.4. Optical and thermal properties of doped chiral nematic elastomers **E1A-F**, obtained by UV-vis spectroscopy.

Elastomer	CB15 wt%	λ_{max} /nm	T_{NI} /°C
E1A	14	1040	86-93
E1B	18	954	75-80
E1C	22	781	70-80
E1D	29	633	65-69
E1E	35	526	45-50
E1F	41	470	30-36

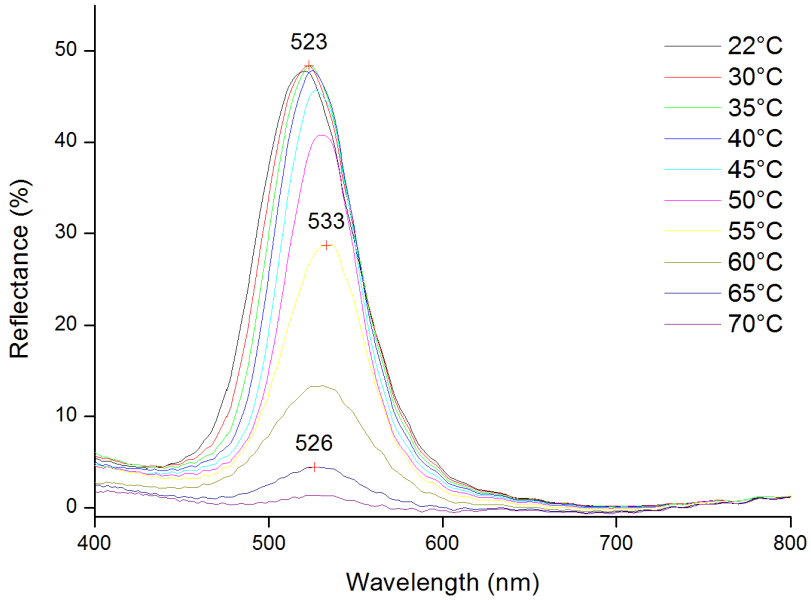

Figure 3.4. UV-vis reflection spectra of chiral elastomer **E1E.** On heating from room temperature to 70 °C, λ_{max} is red shifted and a decrease in peak intensity is observed due to the emergence of the isotropic phase.

Table 3.6. Optical and thermal properties of doped chiral nematic elastomers **E3A** and **E4A**-**B** pre-acetone wash, obtained by UV-vis and microscopy.

Elastomer	CB15 wt%	λ_{max} /nm	T_{NI} /°C
E3A	18	945	55
E4A	22	735	50
E4B	41	432	34

The doped chiral nematic elastomers **E2A**-**D** were also analysed by microscopy and UV-vis spectroscopy (Table 3.5). The low loadings of CB15 in this series mean that λ_{max} are in the near-infrared region. An increase of T_{NI} relative to the monomer mixture and the observed reversible selective reflection on heating and cooling suggests that the polymer network is sufficiently cross-linked.

The doped elastomers with a longer spacer (n = 11), **E3A** and **E4A-B**, also displayed chiral nematic phases (Figure 3.5) with increased T_{NI} compared to the monomer mixtures, indicating successful polymerisation. In comparison to the elastomers containing a short spacer, λ_{max} of the elastomers **E3A** and **E4A**-**B** is slightly shorter (Table 3.6). For example, **E2C** and **E4A** are both doped with 22 wt% CB15 yet λ_{max} of **E4A** is 55 nm shorter. This could be due to the largely decoupled mesogens having an increased ability to rotate, as the mesogen is not hindered as much by the polymer backbone, and therefore the pitch is

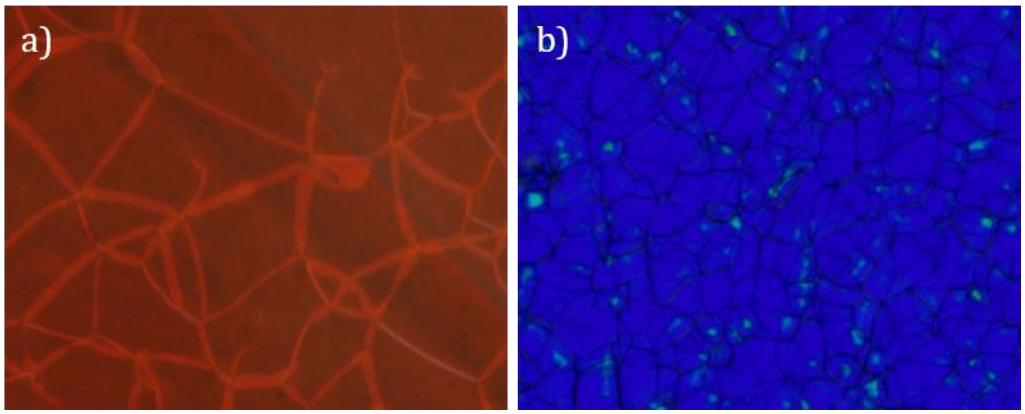

Figure 3.5. Polarised light photomicrographs of doped chiral nematic elastomers in reflection mode at 100x magnification: a) **E4A** (22 wt%) at 35 °C and b) **E4B** (41 wt%) at 23 °C.

decreased.

The phase stabilities of the doped chiral nematic elastomers **E2A-D**, **E3A** and **E4A-B** are also reduced significantly in comparison to the **E1A-F** series of doped chiral nematic elastomers. This is mirrored in the phase stabilities of the achiral nematic elastomers, where the difference between **E2**-**E4** is much smaller compared to **E1** and is due to the stability of the **M1** monomer structure with a short spacer and peripheral chains as previously discussed.

3.3.3 Chiral Imprinted Elastomers

The chiral dopant within the elastomers **E1A-F** and **E2A-D** was removed by dousing the glass-supported film with acetone onto tissue paper, thereby swelling the elastomer film and washing out the dopant, then allowing the film to dry at room temperature. This was repeated five times to ensure the dopant had been removed. Once the acetone had evaporated and the chiral nematic phase reappeared, it was immediately clear that a large contraction in the pitch had occurred (Figure 3.6) and it was not simply a kinetic memory of the N* phase because the elastomer is swollen by the acetone. The films were then analysed using polarised light microscopy (Figure 3.7) and UV-vis spectroscopy (Figures 3.8 and 3.9).

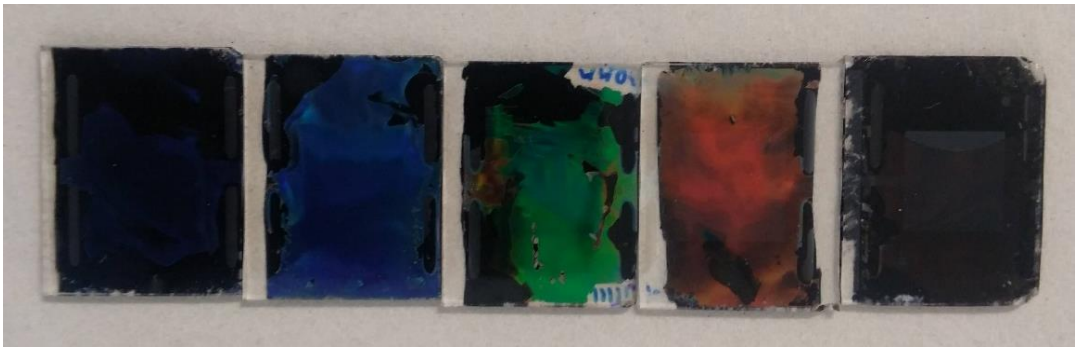

Figure 3.6. Photograph of the washed elastomer films at room temperature (Left->Right (CB15 wt%)): **WE1E** (35 wt%), **WE1D** (29 wt%), **WE1C** (22 wt%), **WE1B** (18) and **WE1A** (14 wt%).

The selective reflection wavelengths (λ_{max}) of **E1A-F** (**WE1A-F**) and **E2A-D** (**WE2A-D**), before and after the removal of the dopant, are shown in Table 3.7. The λ_{max} is red-shifted slightly as the temperature approaches T_{NI} by ~20-40 nm perhaps as a result of the helix unwinding near to the phase transition (Table 3.8). A reflection peak in the UV region for the imprinted elastomer **WE1F** could not be obtained because it was outside the detection range of the spectrometer's probe. On first inspection of $\Delta\lambda_{max}$ of **WE1A-D**, within the visible range, there appears to be a decrease in the pitch after washing of ~200 nm.

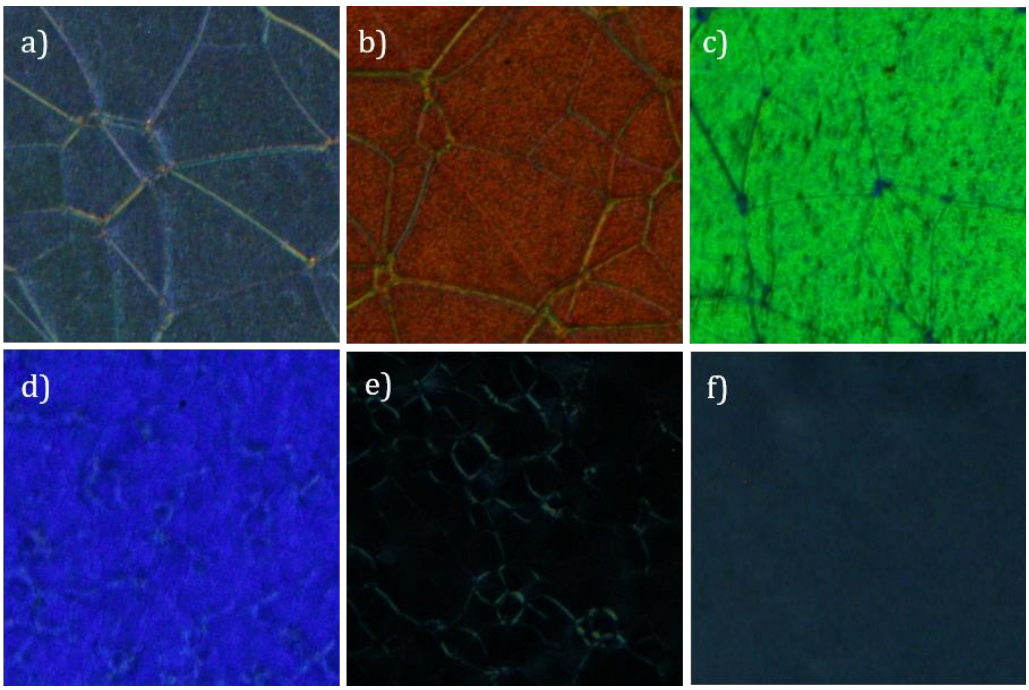

Figure 3.7. Polarised light photomicrographs of washed elastomers **WE1A-F** (CB15 wt%) in reflection mode at 100x magnification: a) **WE1A** at 30 °C (14 wt%), b) **WE1B** at 30 °C (18 wt%), c) **WE1C** at 30 °C (22 wt%), d) **WE1D** at 30 °C (29 wt%), e) **WE1E** at 32 °C (35 wt%), f) **WE1F** at 23 °C (41 wt%).

Table 3.7. Shift in the selective reflection wavelength of chiral imprinted elastomers **WE1A-E** and **WE2A-D** before and after removal of CB15, obtained by UV-vis at room temperature.

Elastomer	CB15 wt%	λ_{max} Before CB15 Removed /nm	λ_{max} After CB15 Removed /nm	$\Delta\lambda_{max}$ /nm
WE1A	14	1040	936	104
WE1B	18	954	683	271
WE1C	22	781	539	242
WE1D	29	633	429	204
WE1E	35	526	385	141
WE2A	17	1011	738	273
WE2B	19	947	667	280
WE2C	22	790	544	246
WE2D	24	725	493	232

However, when lower loadings of CB15 are used, i.e. (**W**)**E1A**, this is reduced to only a ~100 nm contraction, although this could be due to the peak wavelength of **E1A** residing in the IR region, also outside of the probe's detection range. For **WE2A-D** the selective reflection wavelength is blue-shifted to a similar degree (~250 nm). Following the extraction of the CB15 and any unreacted monomer, the volume of the polymer reduces

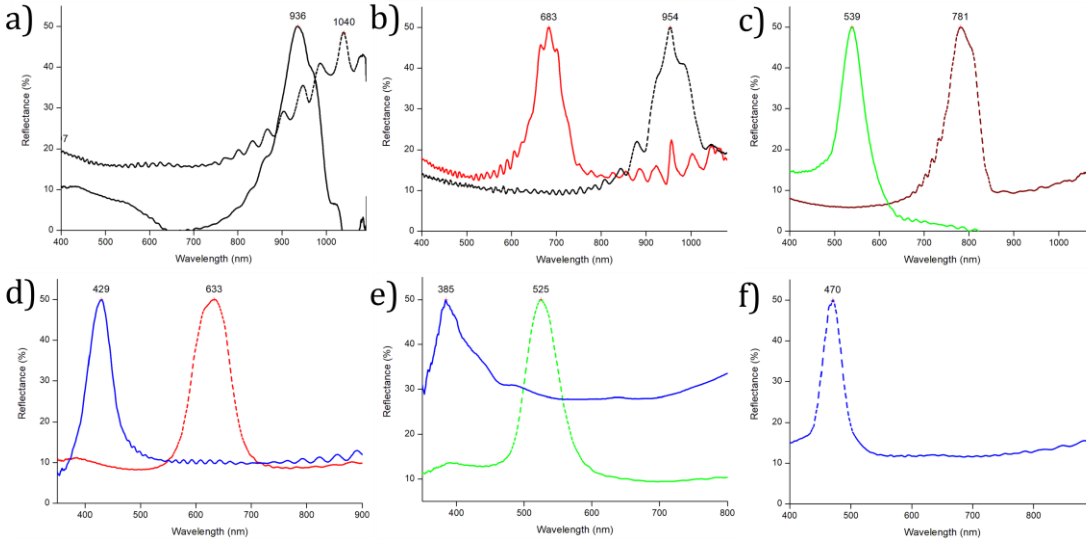

Figure 3.8. Reflection UV-vis of chiral imprinted elastomers: a) **E1A**, b) **E1B**, c) **E1C**, d) **E1D**, e) **E1E** and f) **E1F**. Pre-acetone wash (----) and post-acetone wash (—).

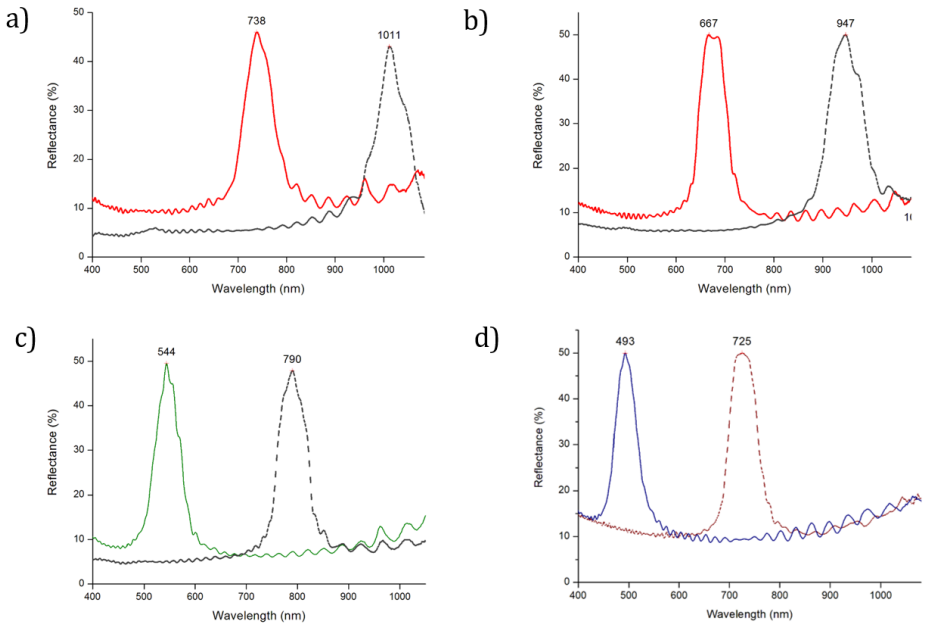

Figure 3.9. Reflection UV-vis of chiral imprinted elastomers: a) **E2A**, b) **E2B**, c) **E2C** and d) **E2D**. Pre-acetone wash (----) and post-acetone wash (—).

as the mass is removed. This causes a contraction of the pitch as the helix is bound to the polymer. This effect is similar to that found by Hasson using a terminally attached acrylate[170,171], who found a shift of ~230 nm with 30 mol% CB15, whilst Noh and Park also reported similar results (~200 nm) using the reactive mesogen mixture RMM727 and different percentages of CB15.[136] The relationship between the percentage of CB15 used to dope the elastomer and λ_{max} is summarised in Figure 3.10. Ignoring (**W**)**E1A**, plotting the wt% of CB15 against the shift in wavelength after washing reveals a negative linear relationship. However, this is counterintuitive to what may be expected when considering

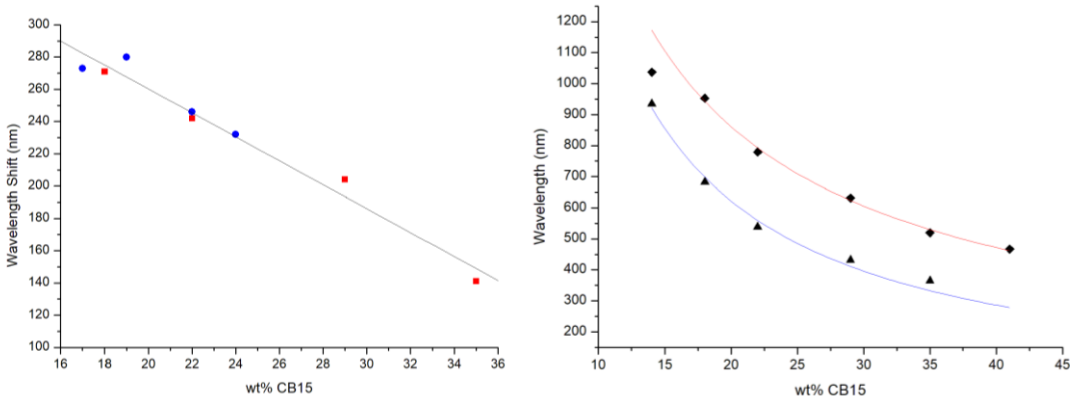

Figure 3.10. Left: Plot of $\Delta\lambda_{max}$ following dopant removal against wt% of CB15 used in the imprinted elastomers **WE1B-E** (■) and **WE2-D** (●). Right: Selective reflection wavelength (λ_{max}) as a function of CB15 wt% concentration in **E1A-F**: chiral doped elastomer (◆), chiral imprinted elastomer (▲).

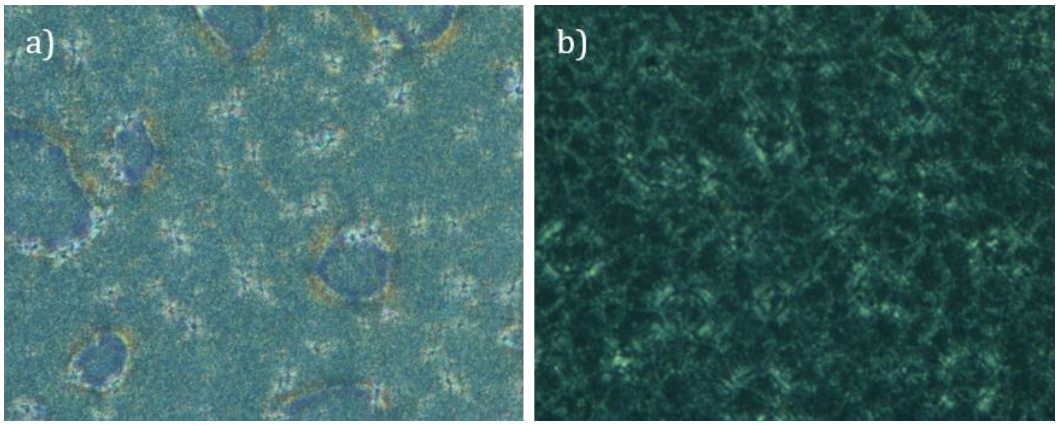

Figure 3.11. Polarised light photomicrograph of washed elastomers in reflection mode: a) **WE4A** at 23 °C and b) **WE4B** at 23 °C.

the argument that the shrinkage is due to the removal of the dopant and the reduction in volume, as one would expect that with higher dopant loadings there would be a greater contraction. Why then this is the case is unclear - one simple explanation is an inconsistent removal of the CB15 from the polymer network, although this would more than likely lead to no trend and the washing of the samples multiple times should minimise the likelihood of this.

Contrary to the elastomers with a short spacer (n = 4), the elastomers **WE3A** and **WE4A-B** with a longer spacer (n = 11) do not demonstrate the same optical behaviour on removal of the chiral dopant. It can be seen in Figure 3.11 that, following the removal of the dopant, the imprint of the chiral nematic helix is lost from within the elastomer network and no selective reflection is visible. The remaining optical texture is similar to an achiral nematic elastomer. Analysis of the films by UV-vis spectroscopy (Figure 3.12) shows no reflection peak within the detection limit of the fibre optic probe (<1100 nm), agreeing with the

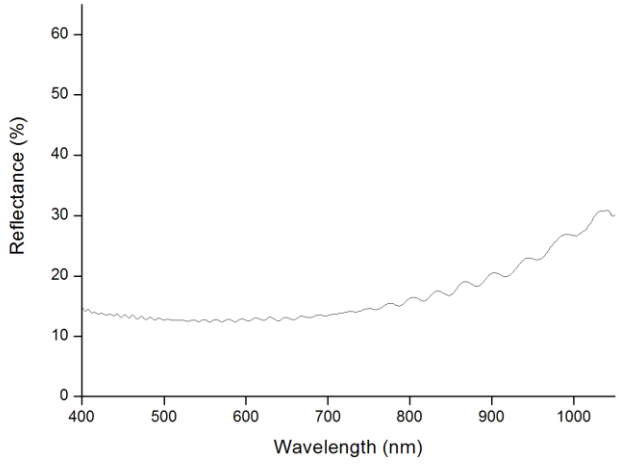

Figure 3.12. Reflection UV-vis of washed elastomer **WE4A** at 35 °C.

microscope observations. Large holes within the film are also evident but this is likely due to the rapid swelling and contraction caused by the introduction and evaporation of the acetone.[172] The lack of imprinted network suggests that the degree of coupling between the mesogenic unit and the polymer backbone is a crucial factor in the process of imparting the helical macrostructure to the polymer and only occurs if the interaction between the polymer backbone and the mesogen is strong enough. The longer spacer grants a greater degree of freedom to the mesogen, leading to the loss of the supramolecular rotation of the director. Once the chiral dopant is removed, the coupling must be strong enough or else the polymer network minimises the elastic energy and the elastomer functions as an achiral nematic elastomer.

In addition to the pitch contraction, the removal of the chiral dopant has a secondary effect. Whilst the phase stabilities of the doped chiral nematic elastomers **E1A-E1F**, **E2A-D**, **E3A**, **E4A-B**, are increased on polymerisation as expected[173] (Tables 3.4-3.6), they are still reduced compared to the achiral elastomers **E1-E4**. This is likely due to the CB15 still acting as an impurity (CB15 is not liquid crystalline itself). However, once the CB15 is

Table 3.8. Optical and thermal properties of chiral imprinted elastomers **WE1A-F** and **WE2A-D**, obtained by UV-vis and DSC. Glass transition temperatures taken from midpoint on cooling. Phase transition temperatures taken from the onset on heating.

Elastomer	CB15 wt%	Initial λ_{max} /nm (40 °C)	Final λ_{max} /nm (T_{NI})	T_g /°C	T_{NI} /°C	ΔH /J g^{-1}
WE1A	14	937	971	41.9	117.8	1.48
WE1B	18	683	704	42.3	118.7	1.53
WE1C	22	539	558	45.9	119.2	1.69
WE1D	29	429	436	45.5	116.7	1.49
WE1E	35	385	385	37.2	106.6	1.21
WE1F	41	n/a	n/a	45.0	114.6	1.73
WE2A	17	740	756	29.7	81.2	0.66
WE2B	19	667	686	24.8	79.3	1.01
WE2C	22	544	556	27.8	81.9	0.67
WE2D	24	493	504	26.6	79.8	1.06

Table 3.9. Thermal properties of elastomers **WE3A** and **WE4A-B** post-acetone wash, obtained by DSC. Glass transition temperatures taken from midpoint on cooling. Phase transition temperatures taken from the onset on heating.

Elastomer	CB15 wt%	T_g /°C	T_{NI} /°C	ΔH /J g^{-1}
WE3A	18	12.7	79.7	0.74
WE4A	22	0.2	69.8	0.75
WE4B	41	5.0	74.6	1.07

extracted, we find that the phase stabilities of the imprinted chiral elastomers, **WE1A-F** and **WE2A-D** (Table 3.8), are restored to close to that of the achiral nematic elastomers **E1** and **E2** (Table 2.3). This confirms that the alignment of the helix is imprinted into the polymer network sufficiently that the selective reflection persists after extraction, yet the mesophase is now no longer disrupted to the same extent. The phase stabilities of the washed elastomers **WE3A** and **WE4A-B** (Table 3.9) are also increased once the dopant is removed, close to the achiral **E3** and **E4** (Table 2.3). Albeit not identical, along with a slightly reduced glass transition temperature, perhaps indicating the incomplete evaporation of the acetone before measurement.

3.4 Stimuli Responsiveness

Chiral nematic elastomers have been proposed as sensors, due to their ability to change colour in response to external stimuli such as changes in pressure or temperature, or even to detect biomolecule concentrations.[174–176] In addition to this, chiral imprinted elastomers have been shown to enantioselectively take up chiral molecules.[172,177] The imprinted elastomers created here were subjected to changes in pressure and temperature and the response was recorded.

Small samples of the imprinted elastomers **WE1B-D** and **WE2B** were carefully cut and removed from their glass cells using a scalpel, immersed in PEG200, and covered with a glass coverslip. The films were heated to above the glass transition temperature of the elastomers to ensure the polymer chains were in the rubbery state and, therefore, responsive to external stimuli. The elastomers **WE3A** and **WE4A-B** were not investigated due to the lack of imprinted structure after the removal of the chiral dopant.

3.4.1 Pressure

To test the response of the chiral imprinted elastomers to applied pressure, **WE1B** and **WE1C** were selected, as the full RGB colour range is potentially accessible. Following the removal of the film from the cell, it was observed that the pitch elongated - **WE1B** appeared dark on the black background as it now reflected near-infrared light rather than red (Figure 3.13) and **WE1C** reflected red light instead of green (Figure 3.14). Therefore, it is likely the cell provides support and stabilises the helix or the action of removing the film releases strain in the elastomer, as some damage to the films is noticeable.

Pressure was applied to the coverslip (and consequently the elastomer) using a spatula. A compression of the elastomer parallel to the chiral nematic helical axis causes the pitch to shorten, as the helix and the polymer backbone are strongly coupled, and therefore a blue-shift should be observed.[178] The compression is greatest at the point of contact and a gradient emanating outwards is seen (Figures 3.13 and 3.14). The response time to the application and removal of the stimuli was on the order of seconds with the elastomers quickly returning to their original size and colour, indicating that they were sufficiently crosslinked. Pallfy-Muhoray investigated a macroscopic polymer-stabilised (50% achiral dopant) film made from a chiral end-on monomer and achiral nematic liquid crystal which responded to uniaxial compression along the helical axis with a blue shift. Their measurements were conducted at 75 °C, above the T_g of the elastomer (70 °C), to enable mechanical deformation and it took ~15 minutes to fully return to its original pitch.[179] Our

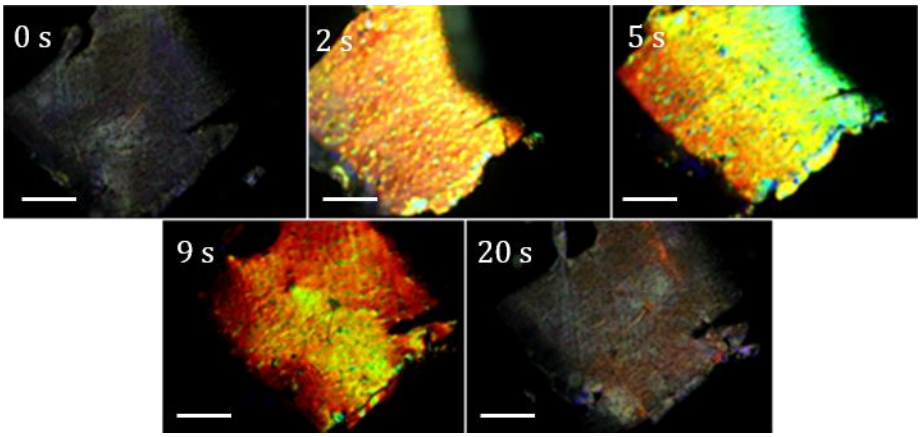

Figure 3.13. Screenshots from a video of a cut film of **WE1B** at 82 °C in PEG200, in reflection mode. Pressure is applied to the coverslip in the upper right hand corner, and then released. Scale bar = 200 μm.

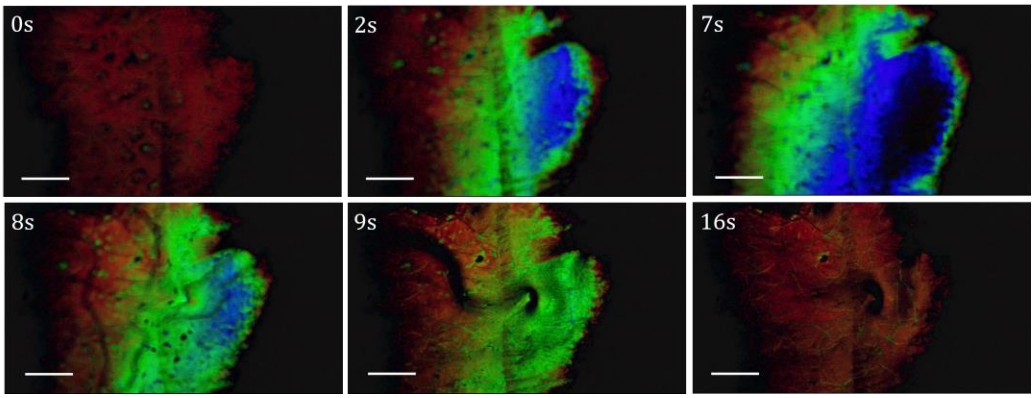

Figure 3.14. Screenshots from a video of a cut film of **WE1C** at 100 °C in PEG200, in reflection mode. Pressure is applied to the coverslip on the right hand side and then released, allowing the elastomer to relax back to its original pitch. Scale bar = 200 μm.

elastomers demonstrate a much quicker response. This could be due to the small size of the sample that we investigated compared to Pallfy-Muhoray, as they also noted a decreased time to relax back to the original shape with decreasing area.

We found that below 80 °C a much larger force was required to prompt an optical response, likely due to a reduced flexibility of the polymer chains even though this temperature is well above the glass transition temperature of the elastomer (42 °C). Therefore, the imprinted elastomer **WE1B** was heated to 82 °C, whilst **WE1C** was heated to 100 °C - far into the nematic phase and above T_g.

A sample of **WE2B** was also cut and analysed using the same method. Like the samples of **WE1B** and **WE1C**, the cut film of **WE2B** also experienced a change in pitch compared to when in the glass cell. However, instead of an elongation of the pitch, a contraction occurred, with green light reflected instead of red (Figure 3.15). Why this occurs is unclear but is perhaps due to the cutting process being done in the rubbery state as opposed to the brittle glassy state like **WE1B** and **WE1C**. Heated to 40 °C, the film was also responsive to pressure, although the response was not as fast and the relaxation back to the original state took longer to achieve. The temperature at which the imprinted elastomer became responsive was much lower compared to **WE1B**, at ~30 °C and closely agreeing with the DSC measurement of its T_g (25 °C)**.** This increased flexibility is due to the lower T_g of **E2**, caused by the longer peripheral chains of the mesogen and an associated increase in free volume of the elastomer network. This makes **WE2B** potentially more interesting from an application viewpoint due to its proximity to room temperature and therefore the reduced level of external heating required to become responsive.

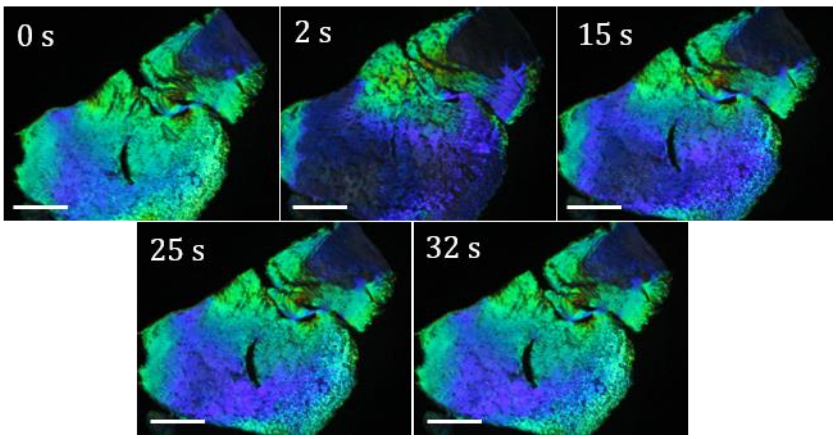

Figure 3.15. Screenshots from a video of a cut film of **WE2B** in PEG200, in reflection mode at 40 C. Pressure is applied to the coverslip in the centre of the film, and then released. Scale bar = 200 μm.

3.4.2 Temperature

The investigation of a cut film of the imprinted elastomer **WE1D** led to the observation that the colour of the unsupported film exhibits a larger temperature dependence to that seen when in the glass cell (Figure 3.16). When on the glass substrate, the λ_{max} of **WE1D** is 429 nm at 40 °C and shifts to 436 nm on heating to ~125 °C (Table 3.8), however, once cut

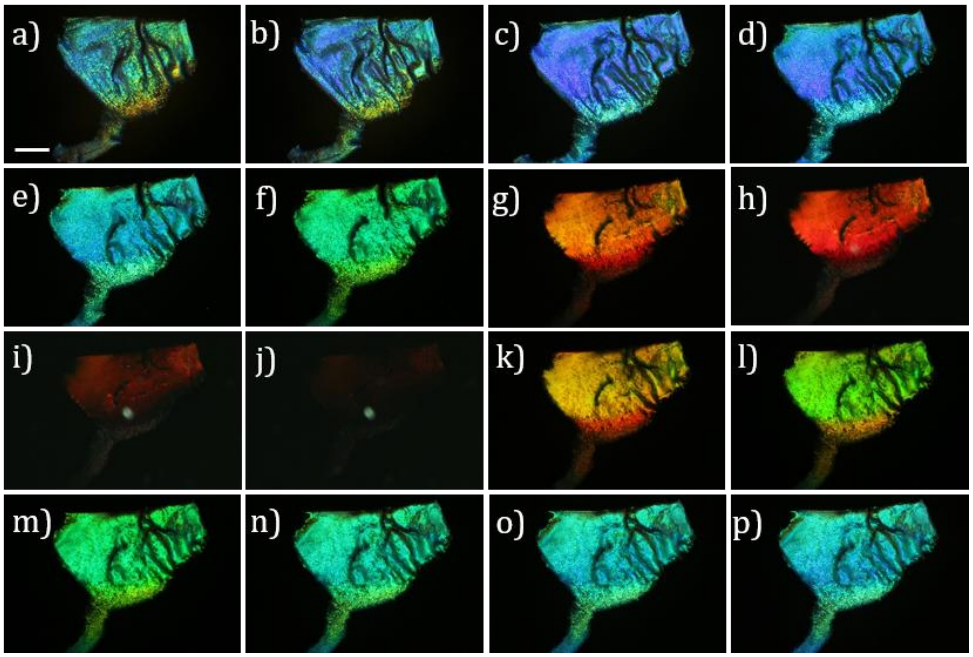

Figure 3.16. Polarised light photomicrographs of **WE1D** in PEG200 undergoing a heat/cool cycle in reflection mode: a) 65 °C, b) 70 °C, c) 80 °C, d) 90 °C, e) 100 °C, f) 115 °C, g) 125 °C, h) 128 °C, i) 131 °C, j) 135 °C, k) 120 °C, l) 118 °C, m) 110 °C, n) 90 °C, o) 70 °C, p) 50 °C. Scale bar = 200 μm.

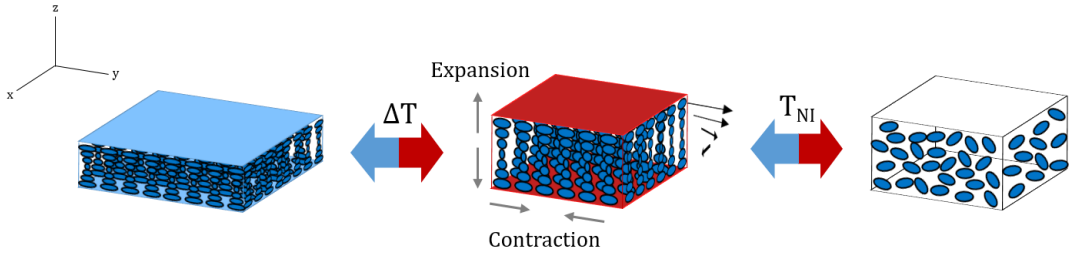

Figure 3.17. Cartoon representation of actuation on approach to T_{NI} in samples of **WE1**. The increasing pitch occurs due to the expansion of the chiral nematic elastomer perpendicular to the director(s).

it can be seen that a red-shift in colour from blue to red occurs as the phase transition is approached. This is due to the expansion of the helix as the order parameter approaches zero (Figure 3.17). As the isotropic phase is entered the colour is lost, however it is restored on the re-entrance into the liquid crystal phase. There is a slight discrepancy between the phase transition temperatures of **WE1D** found by DSC (117 °C) and by microscopy (~125 °C), although this could be due to the exposed heating element of the hot stage leading to an inaccurate temperature reading.

On closer inspection of the imprinted elastomer **WE1D,** it is apparent that with a change in temperature to the cut elastomer film that there is also a macroscopic shape change (Figure 3.18). Initially, it can be seen that the film is rippled due to the cutting process.

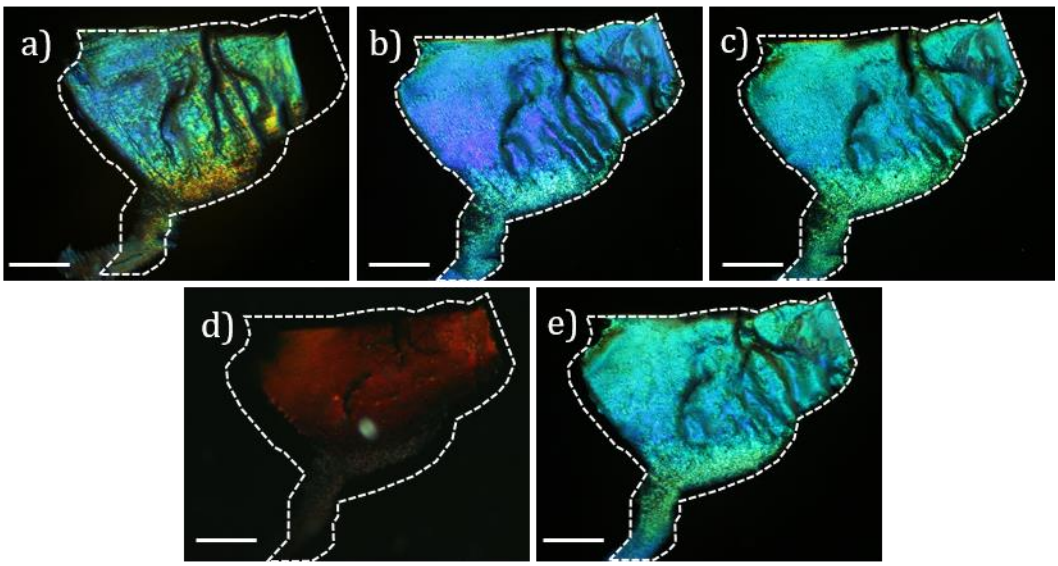

Figure 3.18. Polarised light photomicrographs of **WE1D** in PEG200 undergoing a heat/cool cycle in reflection mode: a) 65 °C, b) 90 °C, c) 100 °C, d) 131 °C, e) 50 °C. Outline corresponds to that of b) which was judged to have the largest area. Scale bar = 200 μm.

However, once the polymer chains cross a flexibility threshold the film partially smooths itself out and a slight blue-shift can be seen (Figure 3.17, a, b). This smoothing out is likely related to the glass transition (**WE1D**, T_g = 46 °C) although, as was seen with the responsiveness of **WE1B-C**, it occurs at a much higher temperature than expected.

Once the temperature approaches the isotropic phase, the dimensions of the film contract in the xy-plane. Nearing the phase transition, the sample elongates along the helix axis and results in the red-shift observed. The overall alignment of a chiral nematic with planar alignment in a thin film is anisotropic and for a known actuating system such as these LCEs based on **M1**, exactly this behaviour can be rationalised; at the phase transition expansion occurs perpendicular, and contraction parallel, to the alignment direction. Due to the strong coupling between the mesogen and backbone, this leads to an expansion in the *z*-axis and a contraction in the *xy*-plane, owing to the conservation of volume. This also explains the small blue-shift as the film unfolds itself (Figure 3.17, a, b), consequently reducing its thickness and contracting the pitch slightly. Pallfy-Muhoray found in their investigations that the helical pitch has a linear dependence on the film thickness.[179] On cooling, the film returns close to the original dimensions and pitch as the memory of the imprinted chiral nematic phase is restored.

3.5 Conclusion

A series of chiral nematic mixtures were created using the monomers **M1**-**M4** and the chiral dopant CB15, and the thermal and optical properties were characterised. Increasing concentrations of dopant led to chiral nematic phases with selective reflection ranging from the infrared to blue, whilst also reducing the phase stability. The mesogen structures of **M1-M4** were also important factors in the thermal stabilities and mixtures of **E1** (having the shortest chain lengths) possessed higher clearing points accordingly. Photopolymerisation of the doped chiral nematic monomers with a crosslinker, in planar alignment cells, produced thin films of chiral nematic elastomers that retained the reflection colour of the monomer mixtures.

Swelling of the elastomer with acetone removed the chiral dopant and subsequently caused a reduction in the volume of the network. This resulted in a large blue-shift (~200 nm) in the selective reflection wavelength of the elastomers with short spacers and strong coupling between the mesogens and backbone. This degree of coupling was found to be an important factor in the retention of the supramolecular helix. It was necessary to have

a short linking spacer for the memory to be recalled after isotropisation, as a longer spacer length lost the imprint of the helix and any selective reflection. Secondary to this optical effect, the phase stabilities of the imprinted elastomers were restored to close to that of the original achiral elastomers.

An investigation into the stimuli responsiveness of the imprinted elastomers revealed that when heated high above their glass transition temperature into the rubbery state they were sensitive to compression and exhibited reversible blue-shifts with application of strain parallel to the helical axis, which was quickly recovered on removal. Another imprinted elastomer was found to demonstrate this responsiveness near to room temperature due to its low glass transition temperature. An imprinted chiral elastomer from **M1** also showed reversible macroscopic shape changes and changes in the selective reflection wavelength on heating and cooling due to the expansion of the polymer backbone perpendicular to the coupled helix. These results can further the development of robust optical sensors made from liquid crystal elastomers as the selective reflection colour disappears and reappears when exposed to changes in temperature and pressure and in the presence of solvents that can swell the elastomer.

Chapter 4:
Actuating Nematic Elastomer Microparticles

4 Actuating Nematic Elastomer Microparticles

4.1 Introduction

This chapter discusses the creation of nematic elastomer microparticles from the monomers synthesised in this thesis, using microfluidics. The design of the microfluidic chip that was used is also detailed. The internal mesogen alignment in the droplets and particles was studied by polarised optical microscopy (POM). The particles' morphology was further studied by scanning electron microscopy (SEM). The responsiveness of the microparticles to changes in temperature was investigated by POM.

4.2 Microfluidics

In recent years, microfluidics has become a powerful tool for the creation of bespoke and highly complex emulsions.[180–184] An emulsion can easily be created by mixing two immiscible fluids, adding a surfactant and shaking, however this results in a large distribution of droplet sizes. On the other hand, microfluidics is capable of producing droplets with very low polydispersity. The formation of droplets using microfluidics can be likened to an analogy of turning on a tap to produce a droplet or a stream of water, depending on the flow rate. When the flow rate is slow enough the interfacial tension between the water and the surrounding air causes a single droplet to form at the opening of the tap. Likewise, when a fluid flows into a second fluid in which it is immiscible, a stream of droplets can be produced at the interface. These systems are referred to as oil-in-water (*o/w*) or water-in-oil (*w/o*) emulsions. Droplets of liquid crystal in an aqueous carrier are an example of an oil-in-water emulsion that can be produced *via* a number of flow regimes such as coaxial flow and hydrodynamic flow-focusing (Figure 4.1).[180,181,185,186]

The hydrodynamic flow conditions in a microfluidic device are described by the dimensionless Reynolds number (*Re*) and capillary number (*Ca*). The Reynolds number is defined as $Re = uL/\nu$, where u is the velocity of the fluid, L is the linear dimension of the flow and ν is the kinematic viscosity. The capillary number is defined as $Ca = \eta Q/\sigma$, where

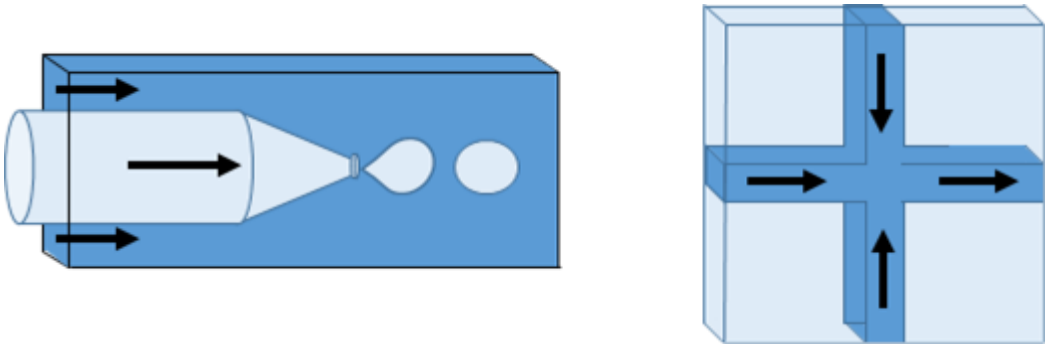

Figure 4.1. Cartoon illustration of a coaxial flow microcapillary device (left) and a hydrodynamic flow-focusing device (right) capable of making droplets[186].

η is the viscosity of the outer fluid, Q the velocity of the outer fluid and σ the interfacial tension between the two phases.[187] Reynolds numbers < 10 are associated with lamellar flow in microfluidics. An increase in *Ca* leads to a decrease in droplet size as the shearing forces on the forming droplet increase.[188] The ratio of the inner and outer phase flow rates can be varied to modify the droplet diameter. Increasing the flow rate of the outer phase or decreasing the flow rate of the inner phase leads to smaller droplets and vice versa.[188] However, there is a point where the inner flow becomes too fast relative to the outer flow and consequently the dripping mode transitions to a jetting mode; the droplets are then formed downstream at the end of the jet but the breakup is less predictable and the polydispersity is higher.[189]

The design of the inlet channel geometry can have a significant effect on the droplet size polydispersity at a certain capillary number.[187] Microfluidic devices capable of flow-focusing have traditionally been created using PDMS (poly(dimethylsiloxane)) but their construction is complicated, requiring access to a clean room and the use of special techniques such as oxygen plasma bonding and surface treatment to ensure hydrophilicity for *o/w* emulsions.[190,191] The channels are typically made using a mould and whilst the channel dimensions can be varied in size, the square geometry of the channels means that, if small enough, the walls could negatively influence the formation of the droplets.[187]

Typically, microfluidics is used with fluids at room temperature and has been successfully utilised to create droplets of room temperature liquid crystals.[95,105,107,192] However, the monomers used in this thesis are nematic at higher temperatures. This presents a technical challenge as the microfluidic chip and tubing must be heated otherwise the monomer may partially crystallise and block the tubing, thereby interfering with, or even stopping, the flow. Very large (300-500 μm) actuating microparticles and shells have

previously been synthesised by the Zentel group using monomer **M1** *via* a microfluidic technique that allowed heating, and hence the production of, droplets in the nematic phase and which were cured 'on-the-fly'.[94] However, this microfluidic method has several disadvantages: a high viscosity of the nematic phase leads to larger droplet sizes, and the heating of the system is challenging. Therefore, the use of an organic solvent to maintain the isotropic phase whilst also reducing the viscosity is an alternative solution, as first used by Fernández-Nieves to make bipolar-aligned nematic droplets.[95,113]

4.2.1 Coaxially Aligned Flow Focussing Microfluidic Device

4.2.1.1 Chip Design

When using an organic solvent, a microfluidic device that can withstand it is required. This constraint rules out the use of most readily available plastics, as they would fatigue with repeated exposure to most organic solvents under the high-pressure conditions, leading to structural failure. Wu *et al* used a polyether ether ketone (PEEK) microcross to make a

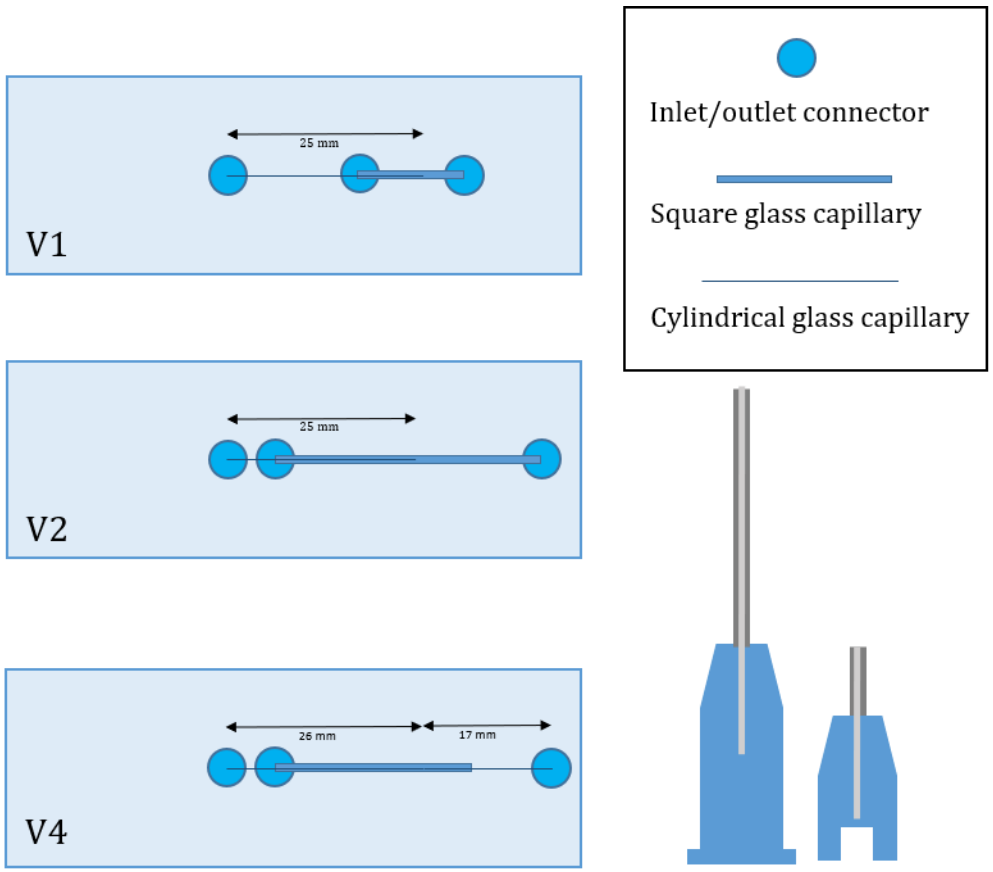

Figure 4.2. Schematic diagram of V1/2/4 of the microfluidic chip and an inlet/outlet connector made from a 25G syringe needle. Capillary lengths indicated.

hydrodynamic flow-focusing device.[193] However, the opacity of PEEK means that the junction where the droplets are created cannot be viewed, which makes troubleshooting any problems difficult, for example if the cross is blocked by debris, and the droplet size and polydispersity can only be gauged at the end of the experiment. Initially, an off-the-shelf polyetherimide (PEI) microcross which was optically transparent was trialled, however the required solvent resistance was not satisfied. Using syringe needles and a transparent plastic cross-junction, Li *et al* also fabricated a device and found the needle diameter to be a limiting factor in the droplet size, being able to make droplets down to 25 μm with a 34G needle.[194] Utada *et al* demonstrated that it is possible to construct a microfluidic device using glass capillaries, which have excellent solvent resistance and optical transparency.[186] This device utilises coaxial flow of two immiscible fluids to produce droplets at the point at which the two phases meet. Its basic construction is shown in Figure 4.1, where a round glass capillary supplying the inner droplet phase is positioned within a square glass capillary, through which the outer phase flows.

It is possible to align coaxially a cylindrical capillary in a square capillary when the outer diameter of the cylinder and inner diameter of the square match. Square capillaries with an internal diameter (I.D.) of 1.0 mm and cylindrical capillaries with an outer diameter (O.D.) of 0.87 mm were selected, as this ensured that even with any variation in the manufacturing tolerances of the components they would still fit. The ends of the cylindrical capillaries were pulled and tapered to a point using a Sutter P-30 micropipette puller, followed by sonication for a few seconds to break the tip. Using this method it was possible to control the diameter of the tip by varying the sonication time, with a longer sonication time leading to a wider tip.

The design and construction of the chip was iterated and improved over time, as issues were encountered, until the final version (V9, Figure 4.6). The fundamental design is simple, with the main channel interfaced to inlet and outlet ports to allow external tubing to be attached. The continuous phase (3 wt% PVA solution) is flowed through the square capillary, while the organic phase containing the monomer and photoinitiator flows through the inner cylindrical capillary. This coaxial flow results in the inner phase being encompassed in three dimensions as it exits the capillary orifice and therefore, compared to the PDMS chip design, the surface properties of the channel should not influence the droplet generation. The layout of the chip is somewhat constrained by its intended working location, under an upright microscope, and therefore the distance between the outer phase inlet and the outlet must be greater than the diameter of the microscope

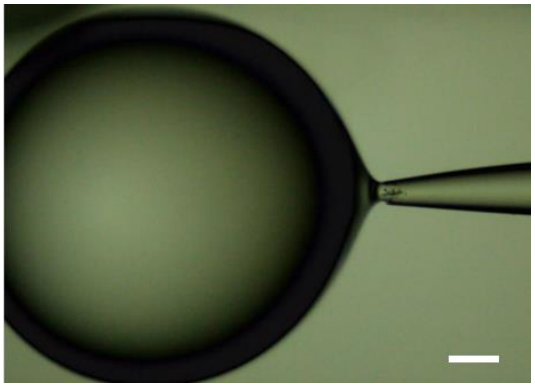

Figure 4.3. Photomicrograph of a large droplet of toluene (**P1-MF4**) at 100x magnification. Produced by a V3 chip with a 40 µm tip Scale bar = 100 µm.

objective (Figure 4.2, V1 --> V2). The dimensions and restrictions of the Mettler Toledo FP82HT hot stage were also taken into consideration to allow simultaneous heating and viewing of the chip, if desired in the future.

The inlet/outlet ports were created from 23G syringe needles (0.51 mm O.D., 0.26 mm I.D.) and were cut, blunted and crafted to allow fitment over the capillaries (Figure 4.2). The choice of a small internal diameter needle and the reduction in the size of the connector was made to reduce the swept volume - the volume of fluid that is retained in the chip before it reaches the capillary tip. By doing so, the volume of the inner phase required for an experiment is reduced and therefore the amount of material wasted at the end of an experiment is minimised. The use of small diameter polytetrafluoroethylene (PTFE) tubing (1.06 mm O.D., 0.56 mm I.D.) to connect to the chip further reduced the swept volume.

Initially, a single cylindrical capillary (Figure 4.2 V1-V3) was used in the chip but this was found to produce large droplets (Figure 4.3). This is likely due to the flow of the outer

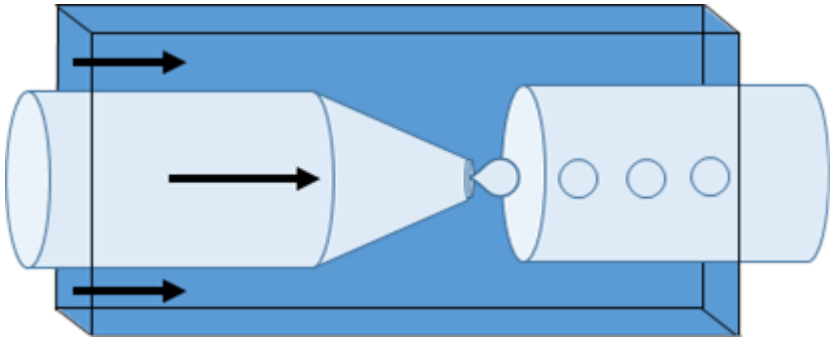

Figure 4.4. Cartoon of a coaxially aligned flow-focusing device using two glass capillaries.

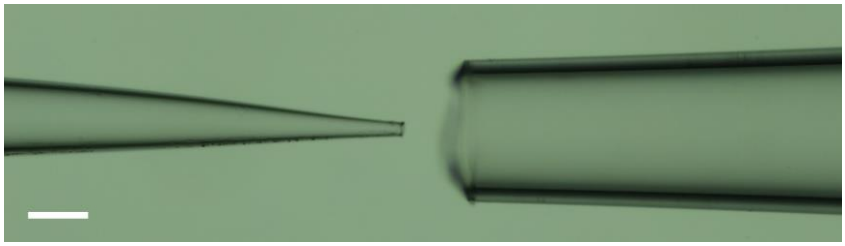

Figure 4.5. Photomicrograph of microfluidic chip V8.6 at x100 magnification. Scale bar = 100 µm.

phase not exerting enough shearing force on the droplet to pinch off until the droplet is very large, despite trialling high flow rates. However, the combination of the relatively poor early chip construction process and high flow rates (up to 10 mL/hr) resulted in leaks on the chip. To help overcome the issue, a 'collection' capillary with a larger orifice, positioned close to the inner phase capillary, was used (Figures 4.4 & 4.5), as well as improving the bonding technique to increase the pressure resistance. The presence of the collection capillary leads to smaller droplets; as the outer fluid enters the narrower collection capillary it experiences an increase in velocity, which in turn causes the droplets to pinch off earlier.[195] Using two capillaries does however increase the difficulty of the chip construction, as the two capillaries need to be aligned centrally in three dimensions.

The chip was further modified to improve the construction process and its usability (V4-V9). A fourth outlet was added to the chip, positioned over the exit of the square capillary (Figure 4.6). This facilitates cleaning and removal of larger pieces of debris that would

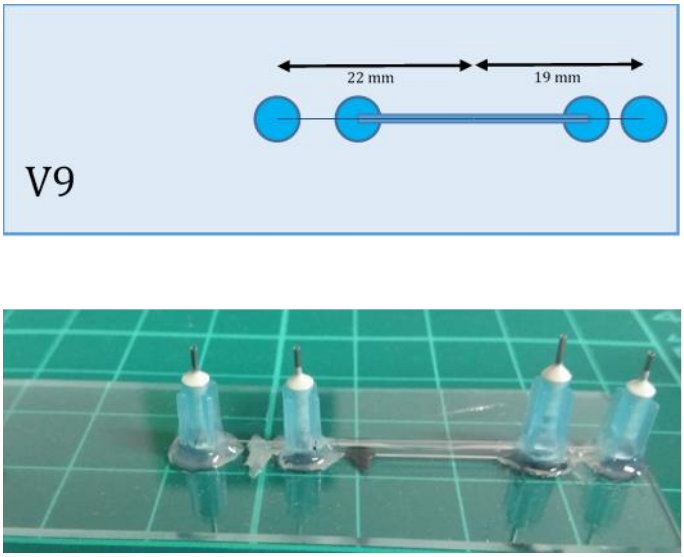

Figure 4.6. Top: Schematic diagram of the V9 microfluidic chip. Bottom: Photograph of the V9 microfluidic chip.

become trapped in the 'collection' capillary and cause a blockage. This also had the advantage of decreasing the time it takes to set up the chip for an experiment - it allows the easy removal of the air bubble that forms in the square capillary when initially filling with water, which would occasionally interfere with the droplet production during the experiment if not properly cleared.

The geometry of the flow junction has an important role in the monodispersity of a droplet population.[187] Therefore, the capillary tip should be as smooth as possible to minimise disturbance to the flow. The fragility and small size of the tips means that cutting the glass to a desired size is challenging. Ideally, the tips would be cut and polished to the desired shape and diameter with a microforge; however, access to one was not possible. Therefore, as previously mentioned, the tips of the capillaries were prepared by sonicating in a water bath for 5-20 seconds. However, early experiments used relatively poor quality tips as it was not appreciated how important the quality of the tip was to the monodispersity. Once this became clear, only tips that cleanly broke were used whilst unsuitable ones were discarded. The majority of the 'droplet' tip diameters that were used were ~20 μm. Smaller tips such as that used in **E1-MF25-27** (6 μm) produced smaller

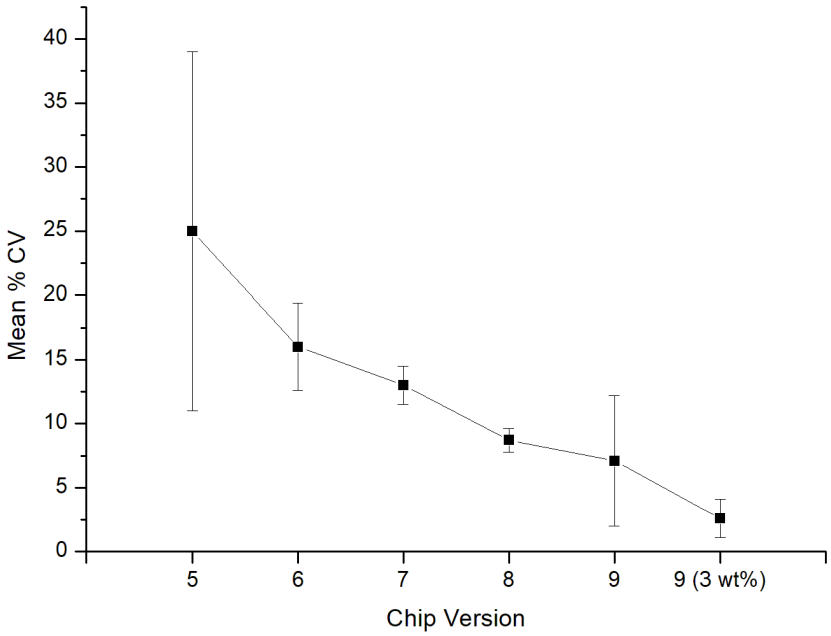

Figure 4.7. How the average droplet size distribution (calculated as %CV) of microfluidic experiments improved with successive chip iterations from V5 to V9. Error bars are calculated from the standard deviation of the %CV values of the experiments using each chip. 3wt% refers to the experiments that used 13,000-23,000 g mol^{-1} PVA and 3 wt% monomer in chloroform.

droplets but were too easily blocked by small debris, despite filtering the inner phase fluid before injection.

$$\%CV = \left(\frac{\sigma}{\mu}\right) \times 100 \qquad \text{Equation 4.1}$$

The monodispersity of a sample was calculated as the coefficient of variation (CV) given by Equation 4.1, where σ is the standard deviation and μ is the mean droplet diameter. As the chip build quality in each successive iteration improved, so too did the monodispersity of the droplets produced. Figure 4.7 illustrates how the average CV of the experiments using each version of microfluidic chip was lowered and, therefore, the monodispersity improved. Eventually it was possible to create droplets with a CV = ~2.5%. This compares well to the droplets of a similar size prepared by Weitz and Fernández-Nieves, and the much larger droplets of the Zentel group (< 3%).[107,113,121]

4.3 Method Development

Whilst the use of microfluidics has increased over the years, the methods used are still relatively new and the detail of practical techniques in the literature is sparse, for example with respect to interfacing the syringes and tubing to the chip or appropriate storage vessels. To successfully analyse the outcome of a microfluidic experiment a number of practical challenges need to be overcome, relating to the processing and handling of small volumes of droplets and microparticles.

One of the advantages of microfluidics is the control of the droplet size through the varying of the ratio of the flow rates, Q_{outer}/Q_{inner}. However, the ratio of flow rates required to form monodisperse droplets will vary depending on the exact details of the chip construction; there is a wide range used in the literature - a small search yields ratios ranging from 2.7 to 20.[125,129] The flow rates of the two fluids were controlled independently by two syringe pumps (Chemyx Fusion 400 and WPI SP100iZ). Initially, flow rates of 100 µL/hr for the inner fluid and 2000 µL/hr for the outer fluid were used as a starting point following Fan *et al*, who were able to create droplets 50 µm in diameter.[129] This was increased to 140 µL/hr for the inner and ~14-15.0 mL/hr for the outer to create small droplets; desired to improve the mesogen alignment, as discussed

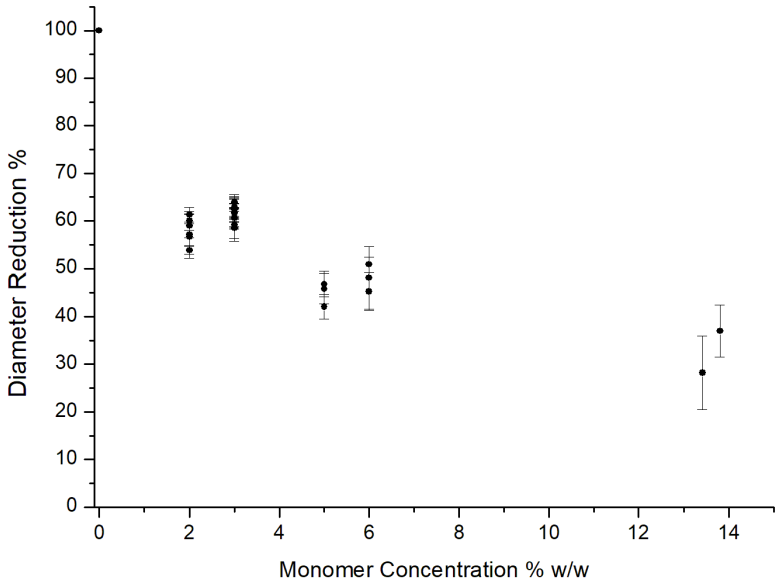

Figure 4.8. Graph demonstrating how the reduction in the diameter of nematic droplets after the evaporation of chloroform is dependent on the monomer concentration in the initial solution.

later. A higher Q_{inner} caused the transition to a jetting mode, whilst <100 µL/hr affected the monodispersity. The Q_{outer} had the larger impact on droplet size, although high flow rates >20.0 mL/hr increased the likelihood of leaks due to high pressures within the chip.

The use of a suitable organic solvent enabled further control of the final droplet size, in addition to the variation of the inner and outer flow rates. The selected solvent must meet a number of criteria: it must dissolve the monomer, have some solubility in water, and have a low boiling point. It was found that the solubility of **M1** in toluene at high concentrations was quite poor and the few literature experiments using solvent evaporation used rather high concentrations. In their experiments to produce bipolar droplets Fernández-Nieves *et al* used chloroform to reduce the viscosity[113] and it was found that **M1** had improved solubility in chloroform. A reduction in diameter occurs due to evaporation of the solvent from the droplet; due to the small but non-zero solubility of chloroform in water.[113] By varying the ratio of chloroform to monomer, the droplet diameter could be tuned. Fernández-Nieves found that the final droplet diameter could be crudely estimated by $D_{LC} = D/(1 + \chi)^{1/3}$, where D is the initial droplet diameter and χ is the volume ratio of liquid crystal to chloroform.[113] The later microfluidic experiments increased the concentration of chloroform from 94% to 97% w/w as this was found to improve the droplet monodispersity, perhaps due to a decrease in viscosity of the inner phase (Figure 4.8), and lead to smaller final droplet sizes.

The outer phase consists of a solution of PVA (3 wt%) in ultrapure Milli-Q water, chosen to act as a stabiliser to prevent droplet coalescence whilst also promoting parallel surface anchoring within the droplets once the nematic phase is formed. The solution was filtered with a 0.20 μm cellulose syringe filter to remove particulates that may block the channels or interfere with the droplet formation. PVA with a relatively high molecular weight of ~90,000-100,000 g mol^{-1} and with partial hydrolysis (~88%) of the acetate groups was found to give the longest-lived, stable droplets in suspension polymerisation[196], which forms similar droplets to those created by microfluidics. This stability may be due to better adsorption at the interface between monomer and water compared to fully hydrolysed PVA, which is more hydrophilic, leading to a thicker film of polymer surrounding the droplet. Therefore, PVA (85,000-124,000 g mol^{-1}, 87-89% hydrolysis) was used in the outer phase of the majority of the experiments. However, many examples of nematic droplets made using microfluidics in the literature instead use a lower molecular weight PVA, such as 13,000-23,000 g mol^{-1} or 31,000-50,000 g mol^{-1}.[113,125,129,134,197] Low molecular weight PVA (13,000-23,000 g mol^{-1}) was used for a number of experiments later in the project. It was observed that the droplet monodispersity improved (Figure 4.7, 3 wt%), although it is unclear if as a result of the lower molecular weight, and therefore viscosity[198], of the outer fluid or as a result of improvements in the quality of the microfluidic chips.

When creating aligned particles, Ohm *et al*[121] and Fleischmann *et al*[94] used a continuous polymerisation process to capture the flow-induced concentric alignment in these particles. As we wished to avoid this mechanism and use surface anchoring effects, the droplets were polymerised in a batch process. The droplets are initially in the isotropic phase after their production on the microfluidic chip and were collected in a glass petri dish containing the PVA outer phase. Initially, the petri dishes were heated to remove the chloroform; however, this also increased the rate of evaporation of the water from the outer phase, leading to the accidental drying of the outer phase and therefore ruining of the samples. In an optimised procedure, the samples were stored in the dark to prevent premature polymerisation, at room temperature for ~15-24 hours, allowing the chloroform to evaporate upon which the nematic phase forms. The PVA promotes good bipolar alignment within the droplet about 30 minutes after the initial formation of the nematic phase (Figure 4.9).

It has been shown by Fernández-Nieves[113] and Ohm[122] that the polymerisation temperature is an important factor to maintain alignment within the particles. Fernández-

Nieves found that hard particles of RMM14 that are polymerised at a lower temperature possess polydomain textures, likely due to partial crystallisation caused by the onset of polymerisation. Ohm found that in their large (300-500 μm) flow-aligned LCE particles of **E1** that the maximum shape change occurred when polymerisation was between 50-60 °C. At lower temperatures they argued that the decreased viscosity of the nematic phase hinders the flow-induced orientation, whilst at higher temperatures the increased thermal motion disturbs the nematic director.[122] Whilst the supercooled nematic phases of the monomers **M1-M4** are metastable at room temperature, the samples were annealed for 20 minutes at 55 °C before polymerisation to help preserve the alignment.

Following the UV-initiated radical polymerisation of the nematic droplets, the resulting particles were analysed by POM to assess their responsiveness to changes in temperature. As the phase transition temperature of the elastomer **E1** is above the boiling point of water, a sealed system or an exchange into a high boiling point solvent beforehand is necessary to prevent the eventual drying out of the outer phase following prolonged heating. A number of homemade cells to facilitate the exchange were constructed and trialled to allow various polymerisation conditions to be easily investigated. However, the transfer of sufficient particles for analysis between the petri dish containing the sample and the homemade cells was challenging. Overall, this method was found to be unsatisfactory, as the particles would become disturbed by any boiling residual water trapped in the cell, making the analysis difficult.

In an optimised method, multiple petri dishes were used in one microfluidic experiment to collect the droplets generated. Samples in each dish were polymerised with varying conditions, and then subjected to a series of washings using MilliQ ultrapure water to remove the PVA. The samples were heated to 80 °C for 45-60 minutes, to enhance the dissolution of the PVA into the water, after which the solvent was removed and replaced by clean ultrapure water. This was repeated three times before the exchange into PEG 200 (b.p >150 °C). It was found that in cases of insufficient washing and removal of the PVA, miscibility issues were observed when the PEG 200 was introduced, leading to precipitation of the PVA, which obstructed the observation of the particles by microscopy. Particles that were to be analysed by SEM were washed with this method and then dried in a vacuum oven at 35 °C.

4.4 Nematic Droplets

The first step in creating nematic elastomer microparticles was to produce droplets containing mixtures of the monomers, the crosslinker 1,6-hexanediol diacrylate and the photoinitiator diphenyl(2,4,6-trimethylbenzoyl)phosphine oxide. These droplets were prepared using the microfluidic chips developed. A selection of the experimental conditions to make droplets using **M1**-**M4** and the RS Exposure Unit LV202-E are summarised in Table 4.1. A more comprehensive list of the experiments conducted can be found in Chapter 7. Droplets/particles are named according to the convention of [**MX**/**PX**/**EX**)-**MFY**], where MX/PX/EX identifies the monomer, polymer or elastomer, MF signifies a microfluidic experiment, and Y the chronological experiment identifier. The monomer **M1** has been studied and used to make micro objects in the literature, as previously discussed in Chapter 1. The majority of the experiments in this Chapter used **M1** as it allows for direct comparisons to the literature to be made and was synthesised in the largest quantity. Monomers **M2-M4** were used to investigate the properties of particles with lower phase transition temperatures and to assess if different degrees of shape change resulted from their different chemical structures.

For example, in **E1-MF29**, using a V8 microfluidic chip, droplets containing chloroform, monomer **M1** (6% w/w), the crosslinker 1,6-hexanediol diacrylate (10 mol%) and the photoinitiator 2,4,6-trimethylbenzoyldiphenylphosphine oxide (2 mol%) were prepared, using flow rates of Q_{inner} = 140 µL/hr and Q_{outer} = 15.0 mL/hr. The droplet ($D_{droplet}$) and collection ($D_{collection}$) capillary tip diameters were 25 µm and 190 µm respectively. The chloroform was evaporated over 18 hours, reducing the droplet size from an average of 54 µm (CV = 3.3%) to 28 µm (CV = 9.6%).

A new, more powerful UV source (Omnicure LX500, Excelitas Technologies) was purchased to reduce polymerisation times. A selection of the experimental conditions to make droplets using **M1** and **M4** and, from these, particles using the Omnicure LX500, discussed later, are summarised in Table 4.2 and Table 4.3. Nematic droplets containing the pre-polymer mixtures (monomer **M1** and 2,4,6-trimethylbenzoyldiphenylphosphine oxide (2 mol%)) and pre-elastomer mixtures (monomers **M1** or **M4**, 1,6-hexanediol diacrylate (10 mol%) and 2,4,6-trimethylbenzoyldiphenylphosphine oxide (2 mol%)) were prepared using the optimised microfluidic method. The change in PVA molecular weight, from 85,000-124,000 g mol^{-1} (87-89% hydrolysis) to 13,000-23,000 g mol^{-1} (87-89% hydrolysis), was discussed in the previous section.

Table 4.1. Experimental details of microfluidic experiments to create nematic droplets of **M1-M4,** 10 mol% 1,6-hexanediol diacrylate and 2 mol% diphenyl(2,4,6-trimethylbenzoyl)phosphine oxide. PVA: 3 wt%, 85,000-124,000 g mol^{-1} (87-89% hydrolysis). UV-initiated radical polymerisation used an RS Exposure Unit LV202-E.

Experiment	Chip	Tip Sizes /μm	Monomer Conc. /% w/w	Inner Flow Rate /μL hr^{-1}	Outer Flow Rate /mL hr^{-1}	Mean Droplet Diameter	Solvent Evaporation /Hours
E1-MF18	V6.5	20/ 275	6	110	20.0	Isotropic: 60 μm (CV: 14%) Nematic: 35 μm (CV: 18%)	24
E1-MF25	V7.4	6/ 230	6	75	15.0	Isotropic: 24 μm (CV: 8%) Nematic: 16 μm (CV: 13%)	13.5
E1-MF26	V7.4	6/ 230	6	120	23.0	Isotropic: 24 μm (CV: 8%) Nematic: 17 μm (CV: 14%)	13.5
E1-MF27	V7.4	6/ 230	6	120	23.0	Isotropic: 24 μm (CV: 8%) Nematic: 16 μm (CV: 19%)	13.5
E1-MF28	V8.3	25/ 200	6	140	18.0	Isotropic: n/a Nematic: 29 μm (CV: 17%)	21
E1-MF29	V8.6	20/ 190	6	140	15.0	Isotropic: 54 μm (CV: 3.3%) Nematic: 28 μm (CV: 9.6%)	18
E2-MF4	V8.4	25/ 175	6	140	14.0	Isotropic: n/a Nematic: 29 μm (CV: 7.7%)	15
E3-MF2	V7.1	15/ 200	6	140	18.0	Isotropic: n/a Nematic: 28 μm (CV: 14%)	22
E4-MF1	V9.2	20/ 170	6	140	14.0	Isotropic: n/a Nematic: 30 μm (CV: 12%)	24
E4-MF2	V9.2	20/ 170	6	140	14.0	Isotropic: n/a Nematic: 32 μm (CV: 13%)	24
5CB-MF1	V7.1	15/ 190	100	50	5.0	Nematic: 61 μm (CV: 2%)	n/a
5CB-MF2	V7.2	15/ 265	3	20	11.0	Isotropic: n/a Nematic: 44 μm (CV: 9%)	16

Table 4.2. Experimental details of microfluidic experiments to create nematic polymer and particles using **M1**, and 2 mol% diphenyl(2,4,6-trimethylbenzoyl)phosphine oxide. PVA: A: 3 wt%, 85,000-124,000 g mol^{-1} (87-89% hydrolysis), B: 3 wt%, 13,000-23,000 g mol^{-1} (87-89% hydrolysis). UV-initiated radical polymerisation used an Omnicure LX500 with a 365 nm LED head.

Experiment	Chip	Tip Sizes /μm	PVA	Monomer Conc. /% w/w	Inner Flow Rate /μL hr^{-1}	Outer Flow Rate /mL hr^{-1}	Mean Droplet Diameter	Solvent Evaporation /Hours
P1-MF13	V9.7	12/ 170	A	5	135	15.0	Isotropic: n/a Nematic: 35 μm (CV: 12%)	20
P1-MF14	V9.7	12/ 170	A	5	135	15.0	Isotropic: n/a Nematic: 29 μm (CV: 15%)	20
P1-MF15	V9.5	12/ 170	B	6	140	15.0	Isotropic: 53 μm (CV: 4.7%) Nematic: 29 μm (CV: 7.1%)	19
P1-MF16	V9.5	12/ 170	B	6	140	15.0	Isotropic: n/a Nematic: 28 μm (CV: 8.1%)	19
P1-MF18	V9.5	12/ 170	B	6	140	15.0	Isotropic: n/a Nematic: 29 μm (CV: 5.8%)	19

Table 4.3. Experimental details of microfluidic experiments to create nematic elastomer particles using **M1** and **M4**, 10 mol% 1,6-hexanediol diacrylate and 2 mol% diphenyl(2,4,6-trimethylbenzoyl)phosphine oxide. PVA: A: 3 wt%, 85,000-124,000 g mol^{-1} (87-89% hydrolysis), B: 3 wt%, 13,000-23,000 g mol^{-1} (87-89% hydrolysis). UV-initiated radical polymerisation used an Omnicure LX500 with a 365 nm LED head.

Experiment	Chip	Tip Sizes /μm	PVA	Monomer Conc. /% w/w	Inner Flow Rate /μL hr^{-1}	Outer Flow Rate /mL hr^{-1}	Mean Droplet Diameter	Solvent Evaporation /Hours
E1-MF37	V9.1	20/ 170	A	6	140	14.0	Isotropic: n/a Nematic: 35 μm (CV: 10%)	20
E1-MF38	V9.3	20/ 170	A	6	125	15.5	Isotropic: 59 μm (CV: 2.7%) Nematic: 29 μm (CV: 1.5%)	19
E1-MF41	V9.12	25/ 240	B	3	140	20.0	Isotropic: 105 μm (CV: 1.6%) Nematic: 39 μm (CV: 2.9%)	20
E1-MF42	V9.12	25/ 240	B	3	140	20.0	Isotropic: 102 μm (CV: 2.1%) Nematic: 39 μm (CV: 2.0%)	20
E4-MF3	V9.9	15/ 165	A	6	100	9.0	Isotropic: n/a Nematic: 32 μm (CV: 20%)	24
5CB-MF3	V9.4	25/ 170	A	3	140	16.0	Isotropic: n/a Nematic: 20 μm (CV: 17%)	16

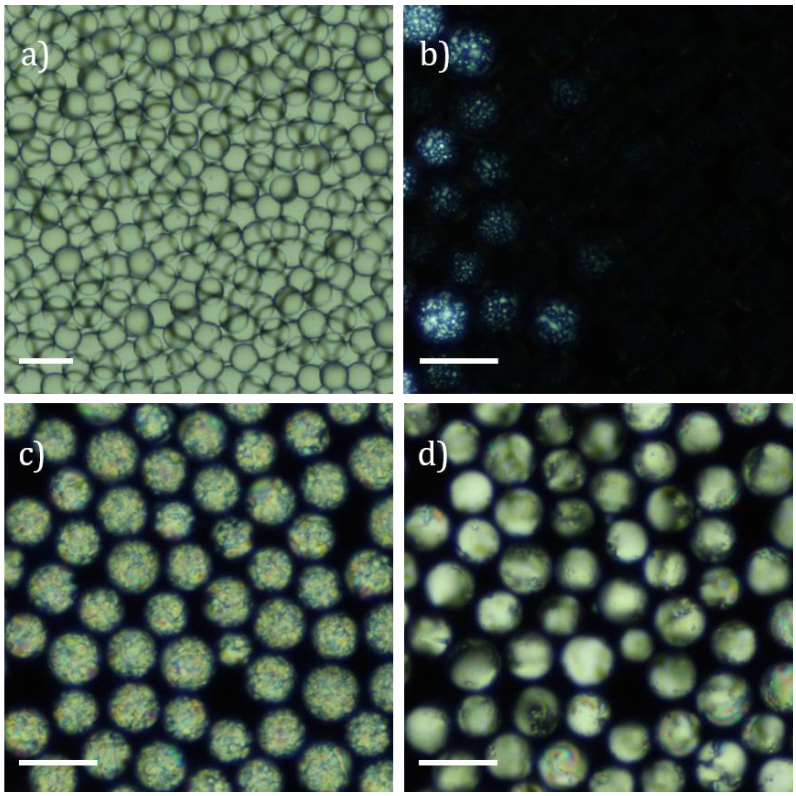

Figure 4.9. Polarised light photomicrographs of droplets from **E1-MF29**: a) the isotropic droplets reduce in size as the chloroform evaporates, b-d) the nematic phase forms and aligns over time due to the PVA outer phase stabilising the droplets and promoting parallel surface anchoring. a: 100x magnification, b-d: 200x magnification. Scale bars = 50 μm.

Typical of all the droplets containing monomers **M1-M4**, the texture development and analysis is discussed. Figure 4.9 shows a time-lapse of droplets from **E1-MF29**. When the chloroform has evaporated sufficiently, the nematic phase formed (Figure 4.9, b) and over a short time the initial polydomain texture (Figure 4.9, c) gave way to an aligned texture as the mesogens reorient within the droplet due to the PVA/water host promoting parallel surface anchoring (Figure 4.9, d). The parallel alignment within the droplets is indicated by the characteristic baseball texture of a bipolar configuration that is observed when rotating the droplets between crossed polarisers, as shown in Figure 4.10. However, in some instances the internal alignment would not appear to be perfectly bipolar, with some

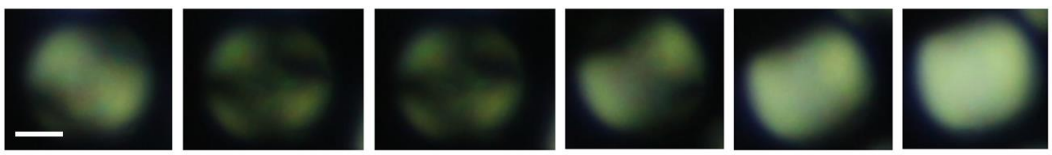

Figure 4.10. Observing the baseball texture of a bipolar droplet from **E1-MF38** though rotation under crossed polarisers at 500x magnification. Scale bar = 10 μm.

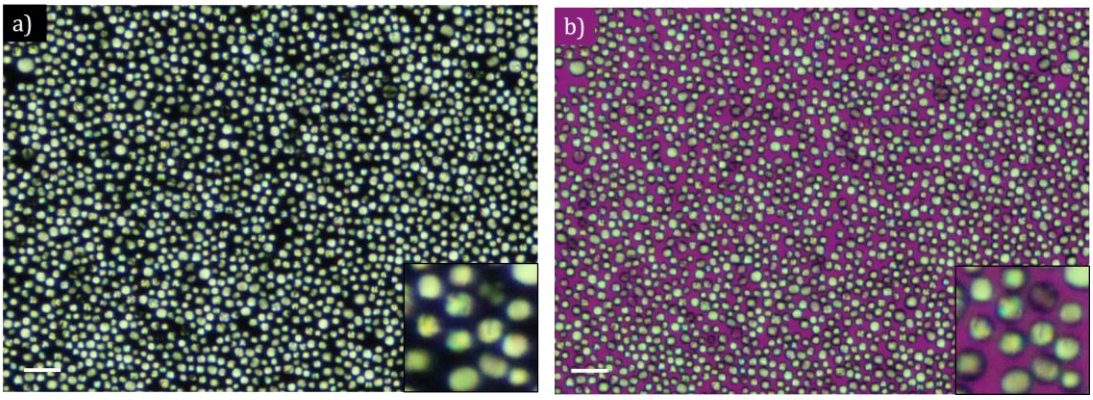

Figure 4.11. Polarised light photomicrographs of droplets from **E1-MF27** at 100x magnification. a) crossed polarisers, b) λ plate. Inset are droplets magnified for a clearer view of the textures. Scale bars = 50 μm.

apparent inhomogeneity in the alignment of the droplets. Using the same microfluidic technique, small nematic droplets were made (**E1-MF25-27**, ~16 μm). The smaller droplets as far as observable, show similar textures and birefringence between crossed polarisers and a λ plate to the larger droplets (Figure 4.11). To further verify, droplets of 5CB (**5CB-MF1-3**) were also prepared. 5CB is known to readily adopt a bipolar configuration in water and PVA/water.[105,113] The droplets of 5CB with diameters of 61 μm show similar textures to **M1-M4** (Figure 4.12, a). Both the droplets of **M1-M4** and 5CB possess a high order white birefringence colour according to the Michel-Levy chart. When viewed through a λ plate (Figure 4.12, b), this does not change; therefore, this appearance must be due to the positive birefringence and the diameter, i.e. the thickness, of the droplets. Overall, the internal alignment does not appear to be affected by the mesogen structure or the droplet size. When changing the length of the peripheral chains, as in **E2-MF4** (Figure 4.13, a) or to a long spacer, as in **E3-MF2** and **M4-MF2** (*n* = 11, Figure 4.13, b-c), the droplets exhibit similar aligned textures.

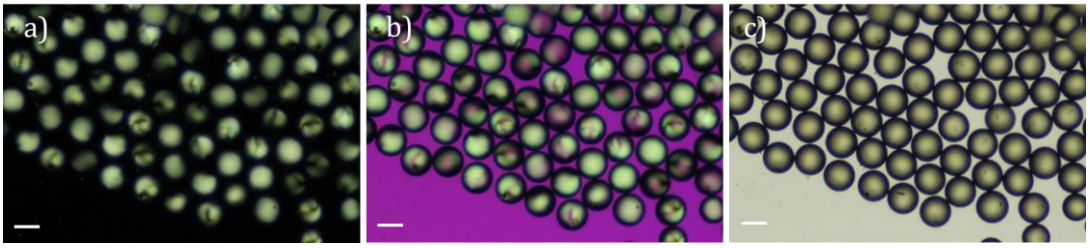

Figure 4.12. Polarised light photomicrographs of bipolar aligned droplets of 5CB from **5CB-MF1** at 200x magnification: a) crossed polarisers, b) λ plate, c) brightfield. Scale bar = 50 μm.

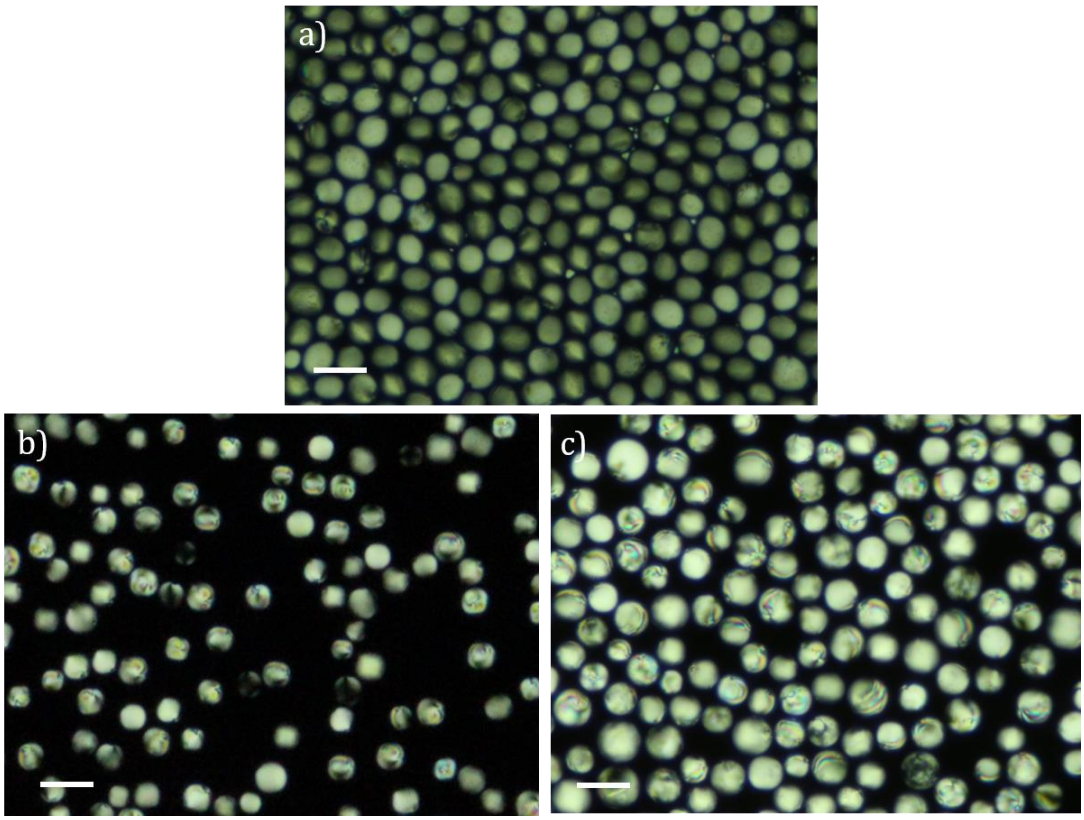

Figure 4.13. Polarised light photomicrographs of nematic droplets from a) **E2-MF4** b) **E3-MF2** and c) **E4-MF2** at 100x magnification. Scale bar = 50 μm.

The droplets were encouraged to form a monolayer (Figure 4.14, a) by gently swirling the petri dish to increase the concentration of droplets in the centre. They self-assemble into a close-packed hexagonal monolayer due to the low polydispersity. The statistical analysis of the experiments, *i.e*. the calculation of the mean droplet diameters and polydispersity

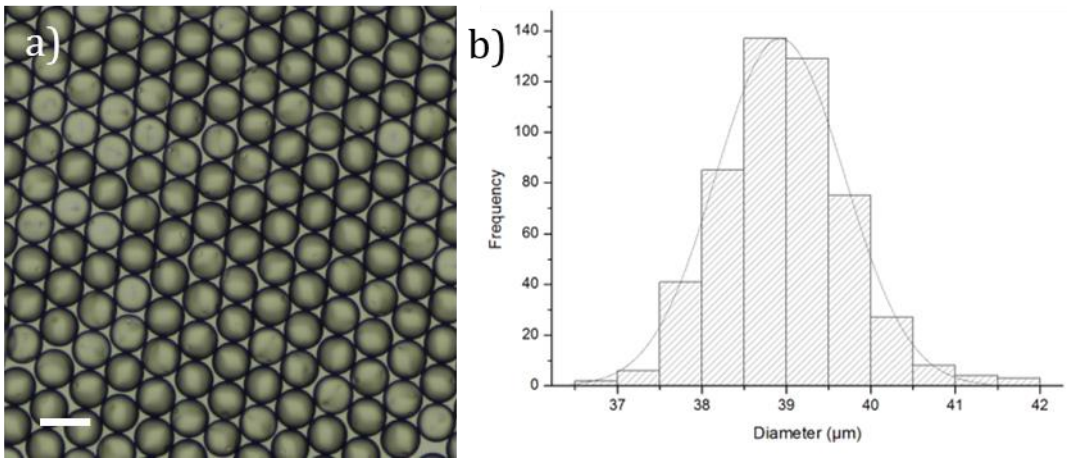

Figure 4.14. a) Brightfield photomicrograph of a monolayer of droplets from **E1-MF41** at 100x magnification. Scale bar = 50 μm. b) Particle size distribution of **E1-MF42**.

(*CV*) (Figure 4.14, b), was aided by the large population of droplets able to be viewed in a single image (usually >500) due to the high packing density of the monolayer.

4.4 Spherical Elastomer Particles

This section discusses the creation of nematic elastomer particles from droplets produced using microfluidics and a UV curing box (RS Exposure Unit LV202-E).

Following the evaporation of the chloroform from the droplets and the alignment of the nematic phase, the droplets containing **M1**-**M4**, photoinitiator and crosslinker were exposed to UV light to initiate the radical polymerisations. The RS Exposure Unit LV202-E that was used is a relatively low power UV source, capable of outputting ~140 mW cm^{-2} from 3 cm away. An account of the experimental conditions and outcomes of creating the elastomer particles **E1-MF1-31**, **E2-MF1-4**, **E3-MF1-3** and **E4-MF1-2** is given in Chapter 7, whilst the most noteworthy observations are described and discussed below.

An example of the optimised method used to create elastomer particles of **E1** is described. The droplets containing **M1**, crosslinker and photoinitiator were heated to 55 °C to

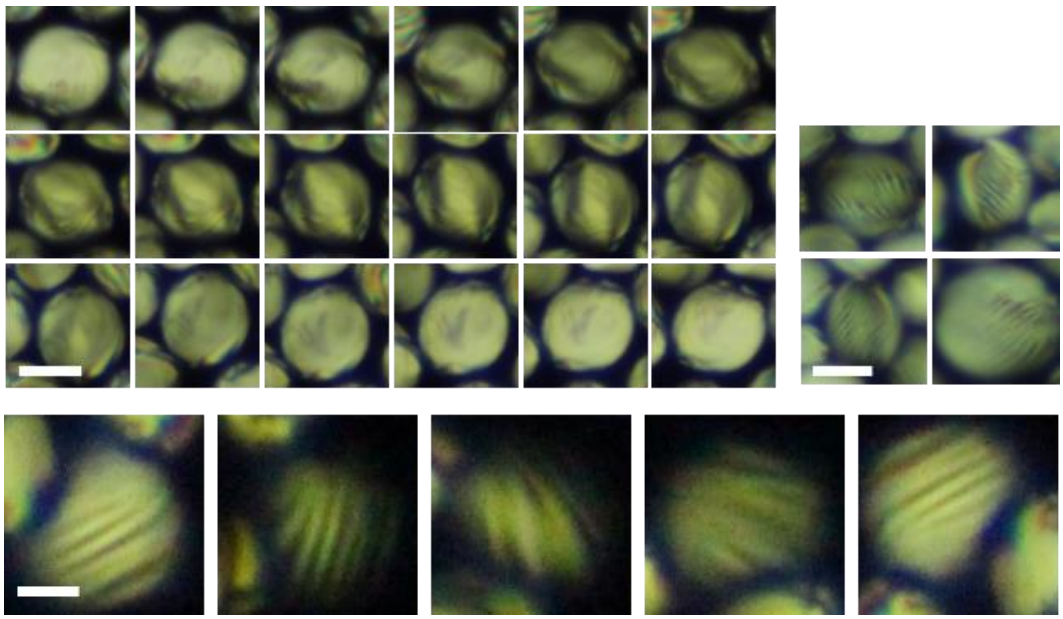

Figure 4.15. Polarised light photomicrographs of nematic elastomer particles at x200 magnification: Top Left: Nematic elastomer particle from **E1-MF23** rotated by 10° increments (scale bar = 20 μm). Top Right: Nematic elastomer particles from **E1-MF28**. Striations are visible when the focus is adjusted to the surface of the particle (scale bar = 20 μm). Bottom: Nematic elastomer particle from **E2-MF3.** Rotating through 180° reveals the striations (scale bar = 10 μm).

maintain the nematic phase during polymerisation and enhance the particle's shape change as previously discussed. The radical polymerisation was initiated at 365 nm, 3 cm from the UV source (RS Exposure Unit LV202-E) for 45 minutes. This was found to be sufficient to polymerise the thin films of **E1-E4** and is for a much longer time and at a higher intensity than Ohm[122] (~1s, 47 mW cm^{-2}) and similar to the conditions used by Marshall.[35]

Following polymerisation, particles of **E1** were studied by POM. Rotation of the particles under crossed polarisers reveals the shifting isogyres and indicates that at least some alignment is retained through the polymerisation process (Figure 4.15, top left, **E1-MF23**). Further to this, under crossed polarisers, striations on some of the particles alternate between light and dark depending on the relative orientation (Figure 4.15, bottom, **E1-MF28**). Analysis of **E1-MF29** by SEM found a winkled texture on the surface of some particles and that they are not perfectly spherical but slightly 'egg-shaped' (Figure 4.16). SEM of particles from **E1-MF18** (Figure 4.17) again shows striations or ridges on the surface of the particles and the alignment of them suggests the polymer chains follow the parallel orientation of the mesogens to the surface of the particle. It was noticed that striations were not present in all experiments however. Why the striations form is unclear but may be due to a buckling or wrinkling of the polymer, with the folds in the surface appearing as the light and dark lines in POM. Wrinkling is a low-strain buckling behaviour due to a compressive strain that exceeds a critical threshold[199] – i.e. the shrinkage of the polymer that occurs during polymerisation[200,201] – and has been observed and investigated in films of liquid crystal polymer by Kang *et al*.[202] They considered an anisotropic contraction of the LCP and speculated that heat from a plasma-induced crosslinking at 120 °C on the top layer of the polymer is the origin of the strain that causes

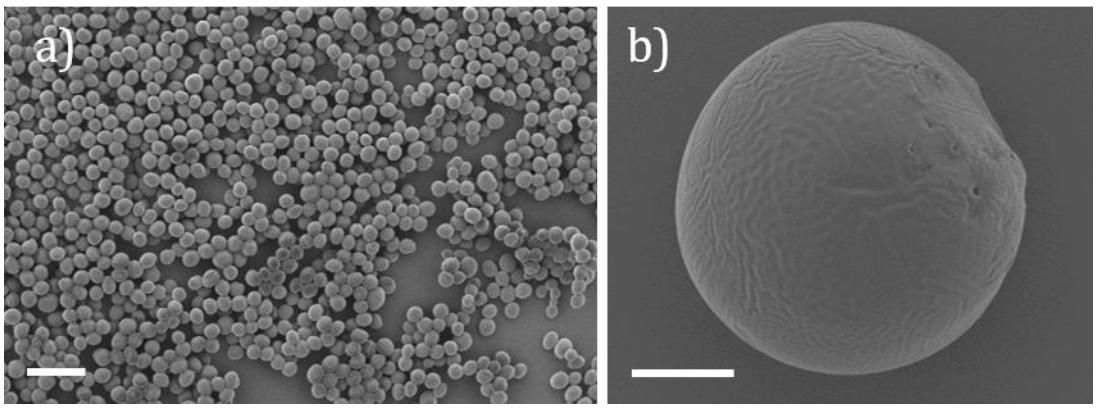

Figure 4.16. Scanning electron photomicrographs of elastomer particles from **E1-MF29**: a) at x75 magnification, scale bar = 100 μm. b) particle at x2300 magnification, scale bar = 10 μm.

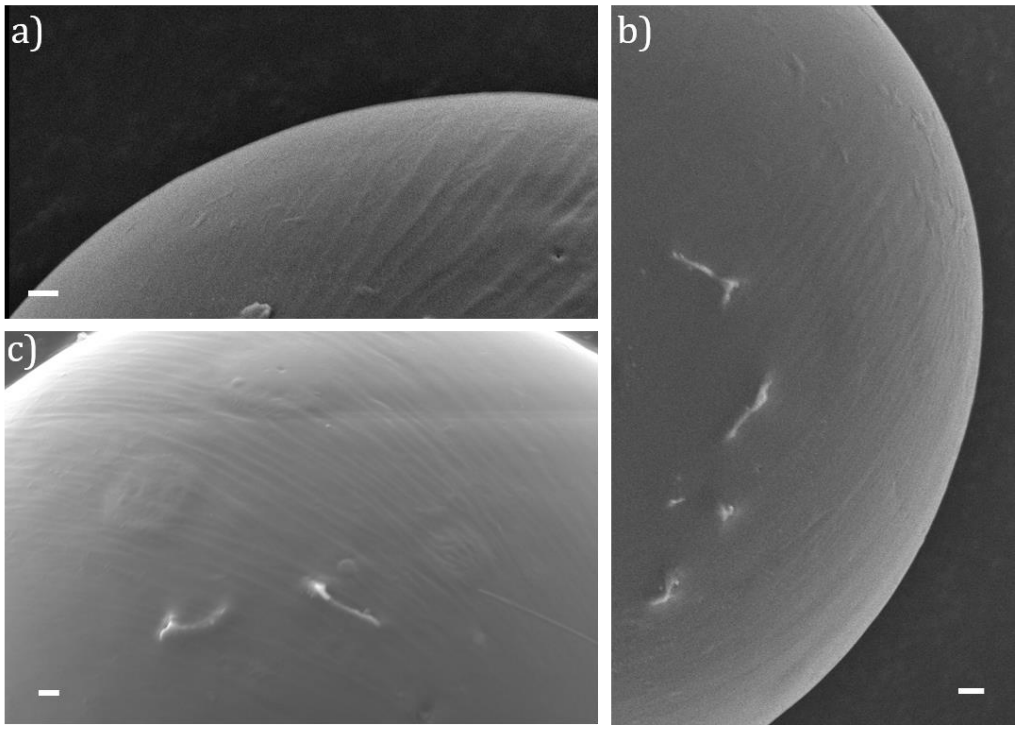

Figure 4.17. Scanning electron photomicrographs of the striations on elastomer particles from **E1-MF18**: a) x4500 magnification, b) x3700 magnification, c) x4300 magnification. Scale bars = 1 μm.

wrinkling. Photopolymerisation of an LCE may lead to the outer layer curing before the bulk of the monomer is reacted. Therefore, different thermal expansion properties of the monomer and polymer could induce the buckling. Agrawal *et al* found that a thin film of polystyrene spin-cast onto an LCE would form striations perpendicular to the nematic director at higher temperatures and parallel to the nematic alignment at lower temperatures due to the buckling response.[203]

Also observed in the SEM analysis are small holes (< ~1 μm) in a number of the particles. Im *et al* were able to create hollow particles of polystyrene by swelling the particles in toluene or styrene and quenching with liquid nitrogen, which caused a void to form as the solvent migrated from the centre to the surface as it solidified.[204] Under vacuum they found the solvent was removed, leaving holes which could be tuned by varying the solvent - faster evaporating solvents (i.e. toluene) led to larger holes. Therefore, the holes we observe could be due to a small volume of chloroform remaining in the particle which only escapes during the vacuum oven drying process - in our case as the remaining volume of chloroform is assumed to be low, this perhaps explains the size of the holes.

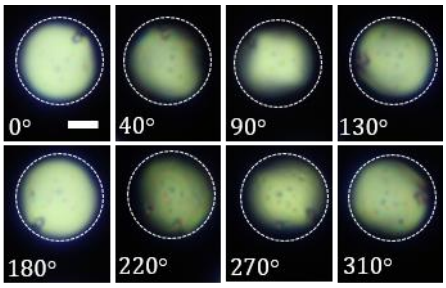

Figure 4.18. Rotation of nematic elastomer particle **E2-MF4** at 200x magnification. The dotted line denotes the outline of the particle to better observe the isogyres on the dark background. Scale bar = 10 μm.

In polymerisation experiments for **M2** (such as **E2-MF1-4**), the droplets made by microfluidics were heated to 55 °C to maintain the nematic phase and irradiated for 45 minutes at 365 nm, 3 cm from the UV source (RS Exposure Unit LV202-E). In all experiments, the particles retain the alignment of the droplets, although this is perhaps not a perfect bipolar alignment, as the characteristic baseball texture is not clearly observed on rotation (Figure 4.18). However, the isogyres do shift as the particles are rotated relative to the crossed polarisers, indicating some planar internal mesogen alignment. 'Egg shaped' particles were also occasionally produced – the likely origin of this will be discussed later.

In an optimised procedure, similar to that to obtain particles of **E1** and **E2**, the droplets of monomer **M3** and **M4** with a long spacer (n = 11) were polymerised. Heated to 55 °C and 45 °C respectively, the droplets were polymerised for 45 minutes, 3 cm from the UV source (RS Exposure Unit LV202-E). Polymerisation of **M4** was completed at a lower temperature due to the lower phase stability of the monomer. The elastomer particles (such as **E3-MF2**

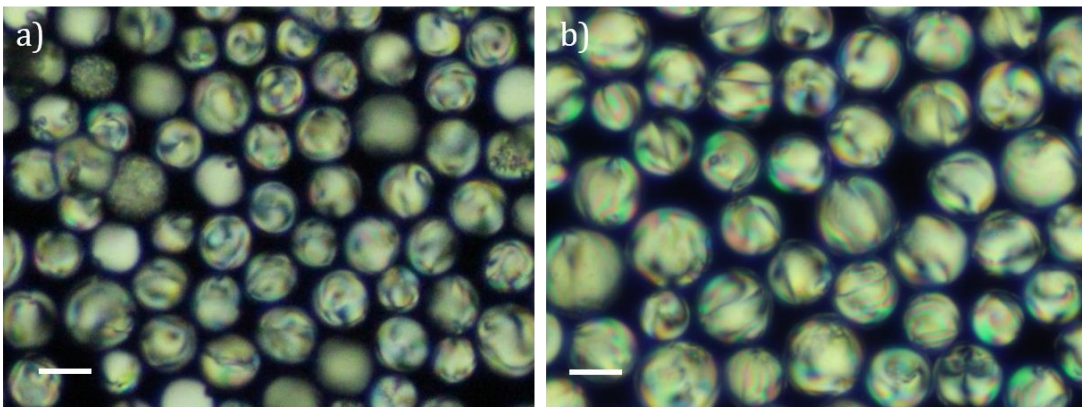

Figure 4.19. Polarised light photomicrographs of nematic elastomer particles from a) **E3-MF2** and b) **E4-MF2** at 200x magnification. Scale bar = 25 μm.

and **E4-MF2,** Figure 4.19) retain the bipolar textures of the droplets with baseball textures observed.

The analysis of particles from **E4-MF1 and E4-MF2** by SEM (Figure 4.20) did not show evidence of striations on the surface of the particles. This could be due to the low T_g of **E4** enabling the flexible polymer chains rearrange and smooth out the wrinkles or alternatively, due to the decoupled polymer backbone not aligning as well with the planar alignment of the mesogens.

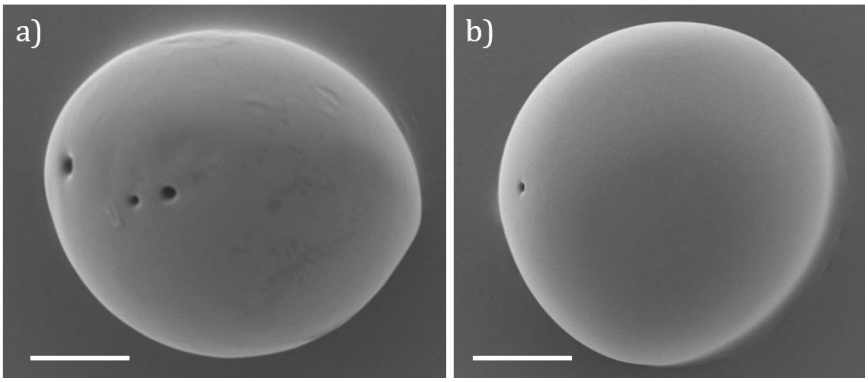

Figure 4.20. Scanning electron photomicrographs of elastomer particle from **E4-MF1**, b) particle from **E4-MF2**. x2500 magnification. Scale bar = 10 µm.

4.4.3 Temperature Response

4.4.3.1 Short Spacer

The response of the elastomer particles to being heated past the phase transition temperature was then investigated. The temperature of the phase transitions differed slightly to that found by DSC, which could be due to the open hot stage that was required to accommodate the petri dish leading to inaccurate temperature measurements. However, this was consistent across all the samples. As the phase transitions of the elastomers **E1-E4** are close to or above 100 °C, the particles required transferring to the higher boiling point solvent PEG200. As discussed earlier, the particles were transferred into PEG after a number of water replacement steps to prevent the precipitation of the PVA.

As an example of the response, and representative of the majority of the particles of **E1**, particles from **E1-MF29** are discussed. Heating the particles in the petri dish at 10 °C

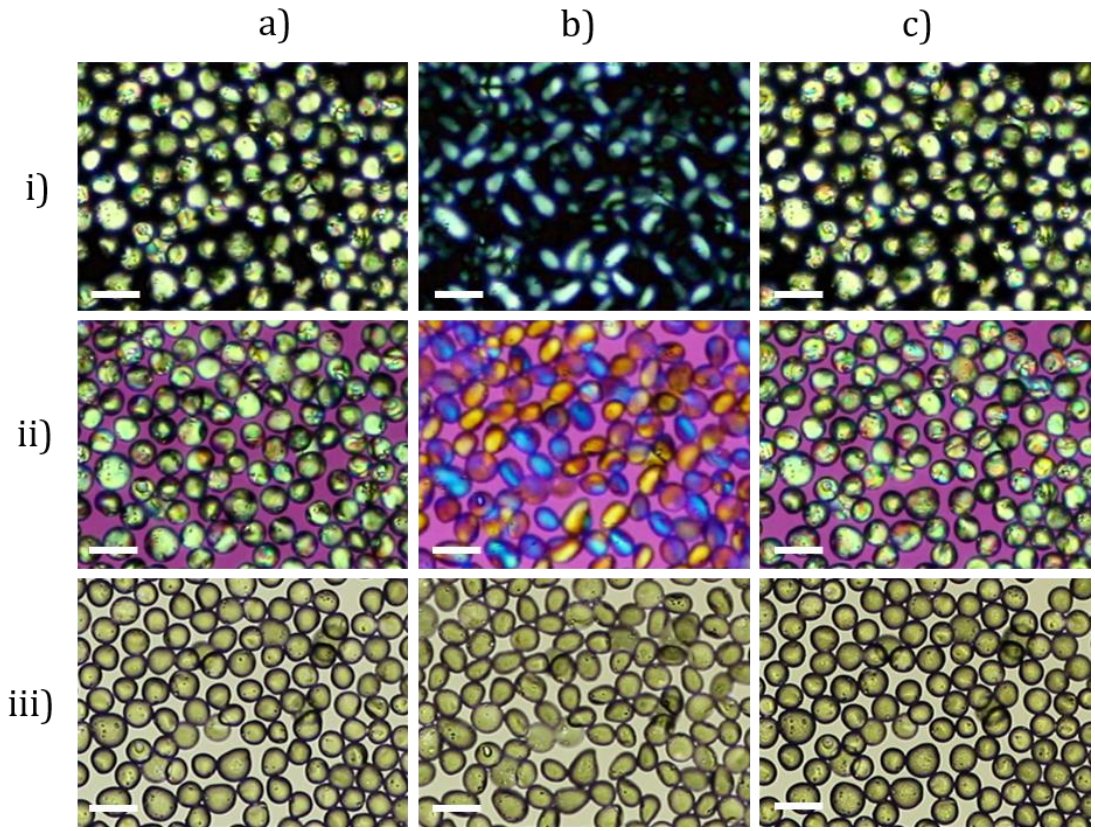

Figure 4.21. Polarised light photomicrographs of nematic elastomer particles of **E1-MF29** in PEG200 at 100x magnification: a) 100 °C, b) 130 °C, c) 100 °C. i) crossed polarisers, ii) λ plate, iii) brightfield. Scale bars = 50 μm.

minute^{-1}, it was observed that on the transition from the nematic phase into the isotropic phase a change of shape occurred (Figure 4.21). A video (Movie 1) of the heating experiment is available on the attached CD. The majority of the particles elongate in one axis and contract in a perpendicular axis, parallel to the director alignment, to form particles with aspect ratios > 1, whereas some of the particles are seen to increase in diameter. When the particles are cooled back into the nematic phase the original size and spherical shape is restored (Figure 4.21, c) which suggests that the degree of crosslinking is sufficient to recall the original polymer chain alignment. Repeated heating and cooling of the particles leads to a similar response.

The aspect ratios (AR) of a sample of 15 particles from **E1-MF29** were calculated before and after the shape change using ImageJ. The AR is defined as $l_{\text{major}}/l_{\text{minor}}$, where l_{major} and l_{minor} are the lengths of the major and minor axes of the particle. However, some error is inherent in this calculation as the measurements were done manually and one cannot be

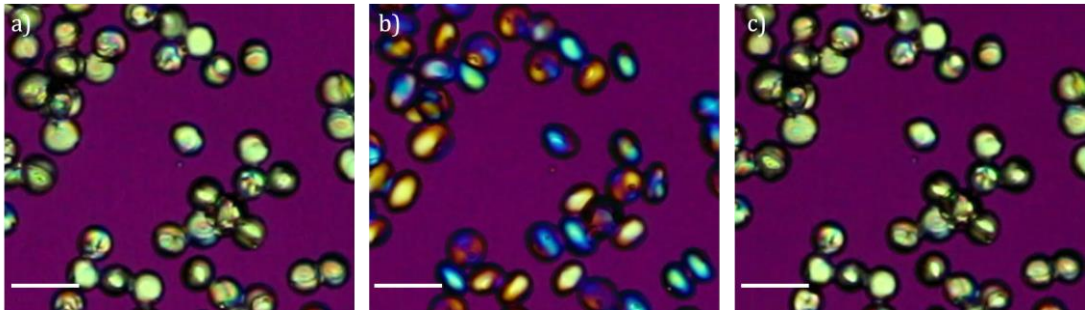

Figure 4.22. Polarised light photomicrographs of nematic elastomer particles of **E2-MF4** in PEG200 at 100x magnification using a λ plate: a) 80 °C, b) 90 °C, c) 80 °C cooled. Scale bars = 50 μm.

sure that the particle is being observed directly from the side, and therefore the width could be overestimated. The average AR in the nematic phase was found to be 1.06, whilst in the isotropic phase this increased to 1.45 - an average increase in aspect ratio of 37%. In these particles, an average contraction of 22% in the minor axis and 13% expansion in the major axis was measured on heating or, alternatively, a 28% expansion of the minor axis on cooling (the expansion was defined as $(l_{nematic}\text{-}l_{iso})/l_{nematic}$, and the contraction as $(l_{iso}\text{-}l_{nematic})/l_{iso}$). It is possible that the actuation could be improved by using smaller particles. A smaller diameter may lead to improved internal alignment from the increased penetration of the surface anchoring throughout the particle. To test this idea, 20 particles of **E1-MF26**, which possessed smaller diameters (mean: 17 μm, CV = 14%), were also analysed. It was found that the average aspect ratio increased from 1.01 to 1.37 on heating (an average increase of 36%). This suggests that the internal mesogen alignment is similar to the larger particles of **E1-MF29** (28 μm). The magnetically aligned micropillars of **E1** (30 μm in width) with the same concentration and structure of crosslinker were fabricated by Wei *et al* and were found to be capable of contracting in length by 30% on cooling, indicating that the surface anchoring imparts a similar level of alignment.[21]

Heating of the elastomer particles made from **M2**, such as **E2-MF4,** from the nematic phase into the isotropic phase at ~90 °C also triggers a change in shape similar to that of particles of **E1** (Figure 4.22). When the particles are cooled back into the nematic phase the original spherical shape is restored (Figure 4.22, c), again suggesting that the crosslinking is sufficient to remember the original alignment. The particles can be heated and cooled multiple times and still respond in a similar way. However, some particles were seen to fuse together after repeated heating and cooling, this is known to occur in acrylates above the glass transition.

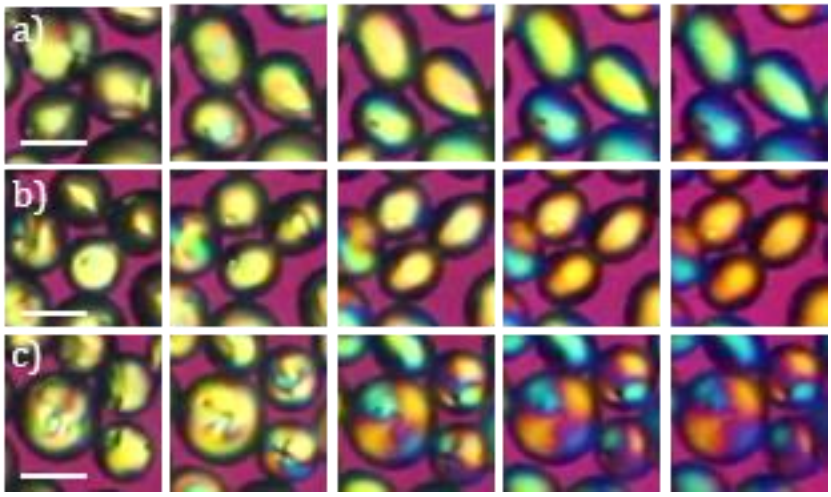

Figure 4.23. Polarised light photomicrographs of **E1-MF28** in PEG200, heated through the phase transition from 110 °C to 130 °C at 5 °C minute^{-1}, viewed between a λ plate. Scale bar = 30 μm.

Using ImageJ, the aspect ratios of a sample of 10 particles from **E2-MF4** were calculated before and after the shape change. The average aspect ratio in the nematic phase was found to be 1.10, whilst in the isotropic phase this increased to 1.52. Therefore, a 38% change in the aspect ratio was found to occur. This is similar to the change calculated for the nematic elastomer particles from **M1** (such as **E1-MF29**), which suggests that the magnitude of the actuation is unaffected by the increased peripheral chain length on the monomer structure, which only serves to decrease the nematic to isotropic transition temperature and therefore the temperature that the shape change occurs at. This is in agreement with one of the few other investigations that have sought to relate monomer structure to actuation: Wei *et al* studied the effect of modifying the peripheral tail lengths of monomer **M1** (carbon atoms = 1, 2, 4, 6, 8) and found LCE micropillars had no significant difference in contraction percentage.[36]

The use of a λ plate allows one to infer information about the relative orientation of the fast and slow axes of a birefringent material and therefore the orientation of the mesogens and polymer chains within the particles. Light interacting with mesogens with a positive birefringence orientated parallel to the optic (slow) axis of the λ plate will experience a positive shift in the birefringence (appearing blue), whilst with mesogens perpendicular, the birefringence will be negatively shifted (appearing yellow). When in the nematic phase the particles exhibit a high order white birefringence colour. When the particles are heated into the isotropic phase it was expected that the loss of nematic ordering, and therefore birefringence, would cause the particles to appear optically isotropic under

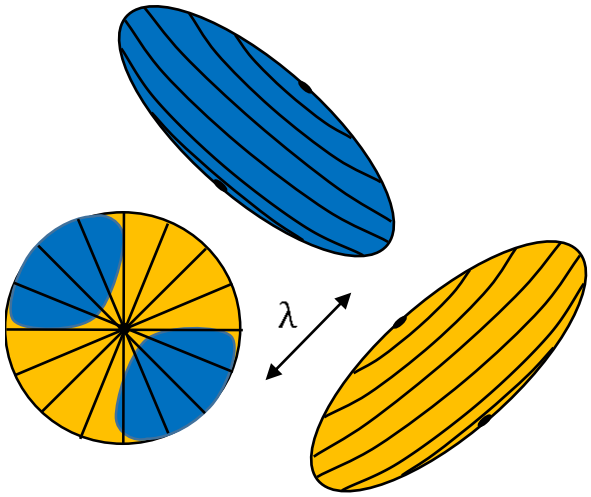

Figure 4.24. Cartoon representation of the possible alignment of the strained polymer chains within the elongated particles. The addition and subtraction birefringence colours observed when viewed using crossed polarisers and a λ plate assume a negative birefringence from the polyacrylate. The location of the boojums due to the bipolar alignment are also depicted for reference.

crossed polarisers. It was observed that the particles retain a low birefringence after the change in shape (Figure 4.21, b). The mesogens in the particles are randomly orientated in the isotropic phase; however, the polymer chains may still possess some orientational order, perhaps due to the confinement and deformation of the particle. This order is likely the manifestation of an internal stress within the polymer or due to the retention of some anisotropy at the crosslinking points.[205] Further to this, when viewed through the λ plate, blue and yellow birefringence colours are seen (Figure 4.23), however the colours are inverted compared to what is expected for a positively birefringent material. Therefore, the colour likely arises from a negative birefringence of the polymer backbone (Figure

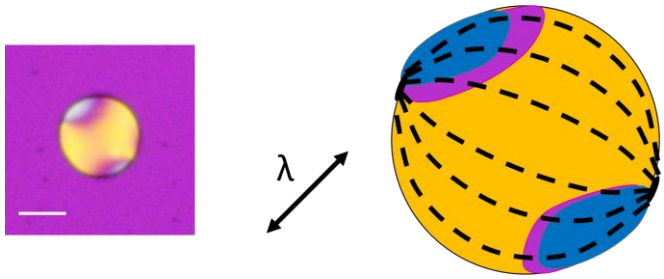

Figure 4.25. Polarised light photomicrograph of a droplet of 5CB (**5CB-MF2**) in PVA, viewed through a λ plate and compressed between a glass coverslip and slide. Confinement of 5CB with planar surface anchoring leads to the bipolar configuration. Birefringence is increased (blue) when the director is parallel and subtracted (yellow) when perpendicular to the slow axis of the λ plate (indicated by the arrow). Scale bar = 50 μm.

4.24). The small negative stress-induced birefringence of poly(methyl acrylate) was studied by Saiz *et al*.[206] The highly polarisable carbonyl group, perpendicular to the chain axis, is responsible for the negative birefringence. To ensure that the interpretation of the slow axis of the λ plate was correct, an analysis of the mesogen orientation in droplets of 5CB was conducted (**5CB-MF2**). 5CB is a positively birefringent material and is known to adopt a bipolar configuration in PVA/water. Figure 4.25 shows a droplet of 5CB viewed through a λ plate and illustrates the mesogen alignment and expected colours for the bipolar configuration. The observed colours confirm that the slow axis of the waveplate is as expected.

As previously discussed, monodomain liquid crystal elastomers contract parallel to the director and expand perpendicular due to the loss of the anisotropic radius of gyration in the isotropic phase. Therefore, if the internal alignment of a particle is in a well-aligned bipolar configuration it is predicted that the particle would flatten like a pancake.[121] A particle viewed side-on would appear to elongate, whilst if viewed down the defect axis the particle would appear to increase in diameter (Figure 4.26). This is exactly what is observed in particles of **E1** and **E2**, therefore suggesting that the bipolar alignment of the droplet is retained and transferred to the polymer network.

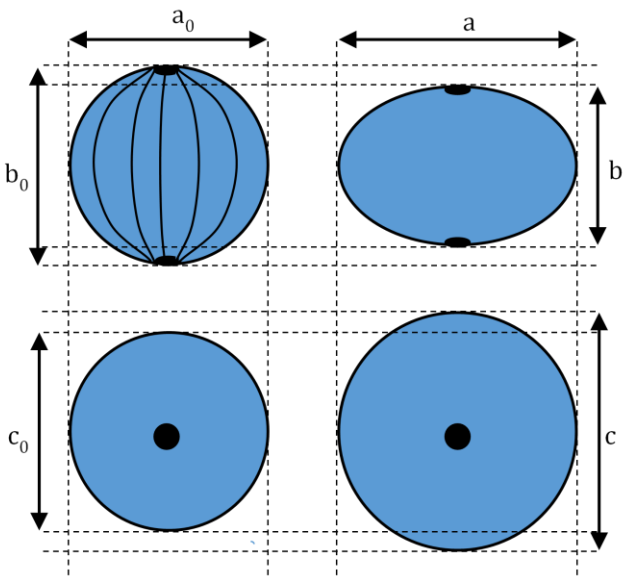

Figure 4.26. Cartoon illustrating the change in shape (the expansion perpendicular and contraction parallel to the director) of a bipolar liquid crystal elastomer particle following the phase transition. The diameter of the original spherical particle = a_0, b_0, c_0. For an elongated particle 'a' and 'c' = the new major axes and 'b' = the new minor axis.

The large (>250 um) LCE particles produced by Ohm *et al* using **E1** elongate and contract in a similar way, with an original aspect ratio of 0.93 that increased to 1.55.[121,122] They reasoned that the mesogens were flow aligned through the shearing of the viscous silicone outer phase into an (escaped) concentric alignment and confirmed this alignment through X-ray diffraction of single particles.[120] However, they observed no flattening particles that would suggest a bipolar alignment, as we do (Figure 4.23, c). In the same study Ohm also made a batch of large elastomer particles that were left to stand before polymerisation, similar to the preparation of our particles. They found that these particles displayed a "weak and undefined" shape change and suggested that this response implied a bipolar configuration, but it is perhaps more likely that the shape change was weak due to the large particles lacking the required internal mesogen alignment. Our results demonstrate that with a suitably small droplet the surface-aligning forces alone can impart the necessary alignment, as the droplets are isotropic during production and are left to develop the nematic phase for hours before polymerisation and therefore no flow-alignment can occur.

4.4.3.2 Long Spacer

Following the same procedure as the particles of **E1** and **E2**, particles of the nematic elastomers with a long spacer, **E4,** were transferred into PEG200 following the polymerisations. Even though the phase transition temperatures of the elastomers **E4** are below the boiling point of water, and so could be heated into the isotropic phase, the high evaporation rate of water at ~80 °C could cause issues with the experiments. Therefore, PEG200 was still used as the solvent for the heating experiments. After removing the PVA by exchanging into water, then PEG200, the particles' responses to temperature were investigated.

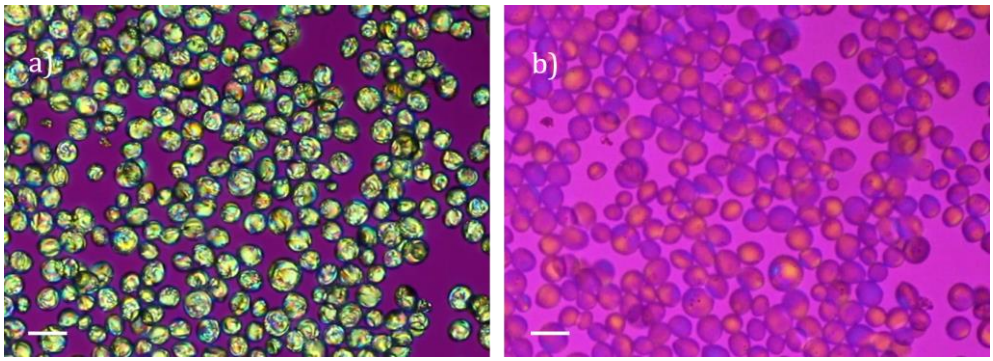

Figure 4.27. Polarised light photomicrographs of elastomer particles **E4-MF2** in PEG200 at 100x magnification using a λ plate: a) 50 °C and b) 90 °C. Scale bars = 50 μm.

For example, heating a petri dish containing the elastomer particles **E4-MF2** shows that a much smaller change in shape occurs at the phase transition (Figure 4.27). The aspect ratios of a sample of 10 particles were calculated before and after the shape change. The average AR in the nematic phase was found to be 1.12, whilst in the isotropic phase this only increased to 1.16, which corresponds to only a 3% change in the aspect ratio. This is likely due to the long undecyloxy spacer largely decoupling the mesogen from the polymer backbone and therefore the anisotropy of the mesogens is only just transferred to the polymer. The low glass transition temperature of **E4** should ensure that the backbone is in its flexible state at the much higher phase transition temperature. Therefore, any actuation (or lack of) is likely due to the spacer decoupling rather than the elastomer being trapped in the glass and resisting the shape change. Interestingly, it was observed that in the particles of the long spacer elastomers, the transitional birefringence colours (Figure 4.28, b, c, e) when viewed through a λ plate are reversed compared to the short spacer elastomers. The sign of the birefringence is unlikely to be different for the short and long spacer polymers, suggesting that the alignment of the polymer is affected by the spacer length. In contrast to the elastomer particles of **E1** and **E2**, the elastomer is not stressed,

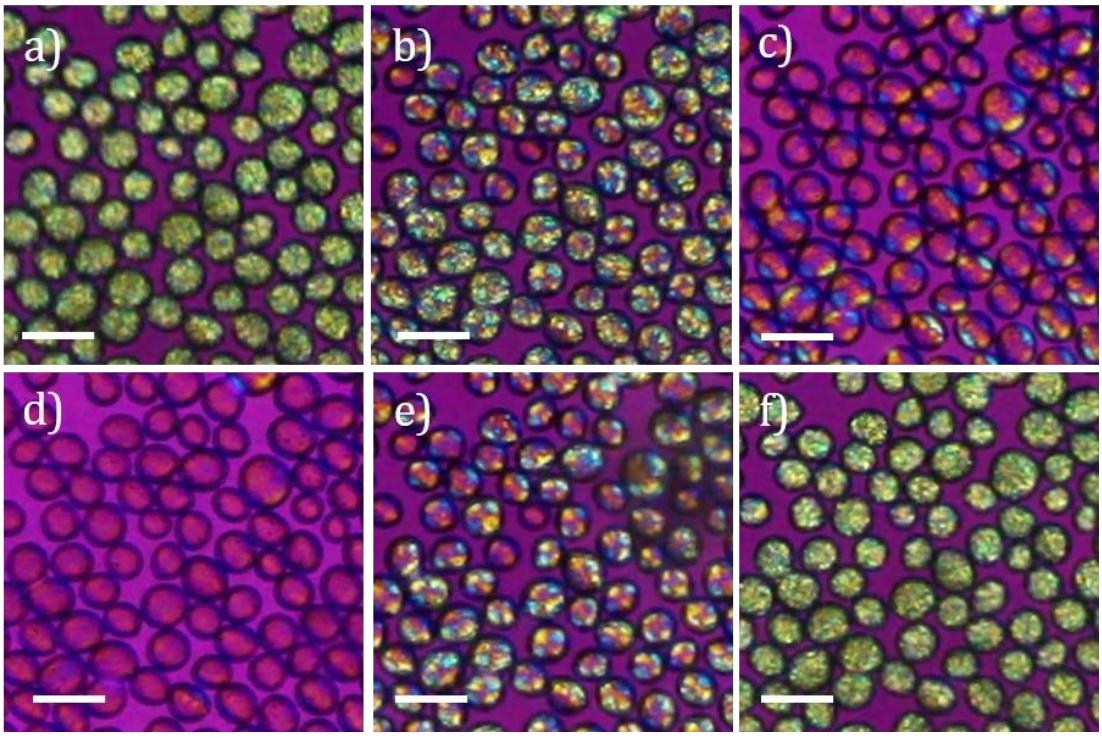

Figure 4.28. Polarised light photomicrographs of elastomer particles **E4-MF1** heated and cooled through the phase transition in PEG200 at 100x magnification using a λ plate: a) 75 °C, b) 80 °C, c) 85 °C, d) 90 °C, e) 70 °C, f) 65 °C. Scale bars = 50 μm.

and the birefringence of the polymer backbone is not observed in many of the particles when in the isotropic phase. (Figure 4.28, d).

Wei *et al* also demonstrated that the extent of the actuation in LCE micropillars could be modified by changing the length of the spacer in the **M1** monomer system.[21] A 31% contraction was reported for the elastomer with an ethyloxy spacer as the shorter spacer leads to it behaving more like a main chain elastomer, whilst a hexyloxy spacer was found to respond with an 18% contraction as a longer spacer leads to it behaving more like an end-on attached elastomer with a reduced polymer chain anisotropy.

4.4.4 Isotropic Polymerisation

To further investigate the effect of alignment on actuation, polydomain elastomer particles of **E1** were prepared (**E1-MF30**) by initiating the radical polymerisation whilst heated in the isotropic phase at 88 °C for 45 minutes, 3 cm away from the UV source.

Following polymerisation, a polydomain texture is observed upon cooling into the nematic phase (Figure 4.29), indicating a lack of alignment within the particle. Further to this, no change in shape was detected on heating or cooling into the isotropic phase and the particles show no sign of stress birefringence. This supports the idea that the observed changes in shape of the elastomer particles polymerised in the nematic phase are a result of the anisotropic alignment of the mesogens being captured during the network formation.

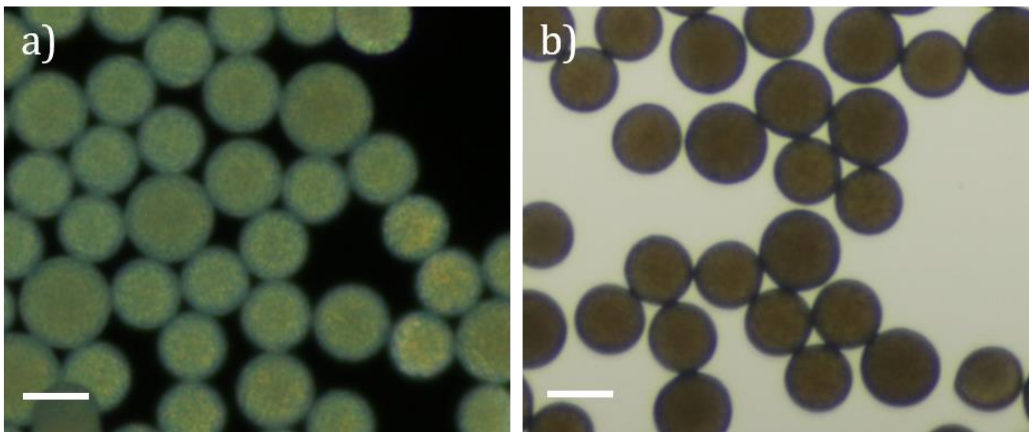

Figure 4.29. Polarised light photomicrographs of elastomer particles of **E1-MF30** at room temperature at x200 magnification: a) crossed polarisers, b) brightfield. The polydomain textures are a result of the polymerisation occurring in the isotropic phase. Scale bar = 25 μm.

4.5 Irradiation with Omnicure LX500

This section discusses the creation of anisometric nematic polymer and elastomer particles using the Omnicure LX500 LED UV spot curing system; which was purchased half-way through the project with the aim of reducing the polymerisation time. The Omnicure LX500 produces a narrow beam of UV light with a reported peak irradiance of up to 14 W cm^{-2} from a distance of 1 cm.[163] The irradiance of the beam drops off sharply as the distance from the centre of the spot increases, following the inverse square law. The energy supplied by the source could be changed by either varying the distance to the sample or by adjusting the 'intensity' – a value relating to the power output of the unit which could not be calibrated at the time (see Table 4.4). Only particles using **M1** (R = C_4H_9, n = 4, **E1-MF32-44, P1-MF13-18**) and **M4** (R = C_7H_{15}, n = 11, **E4-MF3**) were made using the Omnicure LX500.

4.5.2 Polymerisation

As discussed earlier, isotropic droplets containing **M1** were produced using microfluidics (Table 4.2). The nematic droplets that formed following the evaporation of the chloroform were heated to 55 °C and irradiated for different lengths of time and intensities, summarised in Table 4.4, and discussed below.

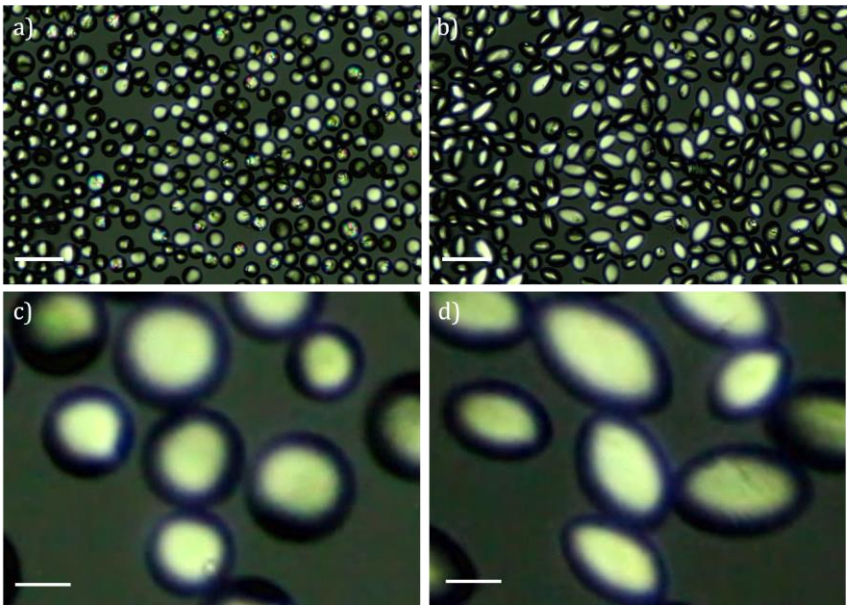

Figure 4.30. a-b) Screenshots from a video of **P1-MF13** in PVA (3 wt%) at x100 magnification: a) droplets of nematic mixture before irradiation, b) droplets of nematic polymer immediately (~1 second) after exposure. Polarisers slightly uncrossed. Scale bar = 100 μm. c-d) Enlargement of a-b to highlight the elongation. Scale bar = 20 μm.

Table 4.4. Polymerisation conditions to create anisometric nematic particles using **M1** with the Omnicure LX500. Polymerisation at 55 °C.

Experiment	UV Exposure Time /Seconds	LX500 'Intensity'	Distance /cm	Mean Aspect Ratio (CV)
P1-MF13	1800	100%	6	1.71 (11%)
P1-MF14	1800	100%	6	1.76 (12%)
P1-MF15	1200	100%	14	1.57 (9%)
P1-MF16	600	100%	6	1.68 (9%)
P1-MF17	1200	100%	3	1.74 (9%)
P1-MF18	1200	5%	6	1.16 (10%)
E1-MF32	100	100%	6	1.48 (14%)
E1-MF33	300	100%	6	1.68 (12%)
E1-MF36	720	100%	6	1.38 (22%)
E1-MF37	1200	100%	7	1.55 (10%)
E1-MF38	1200	100%	7	1.29 (10%)
E1-MF42	1800	7%	30	1.05 (2%)
E1-MF44	2	100%	14	1.24 (5%)

Surprisingly, it was observed that the droplets underwent an instantaneous shape change immediately on exposure to the UV light. A video (Movie 2) is on the attached CD. For example, droplets of **P1-MF13** elongated along one axis and contracted in a perpendicular axis, into a spindle-like shape with a mean aspect ratio of 1.71 (Figure 4.30). The angle of the LED and therefore the beam, relative to the droplets in the petri dish, was varied from ~45° in **P1-MF13** to 0° in **P1-MF14** but this was not found to affect the direction of elongation. Instead the droplets appear to elongate preferentially with respect to their orientation along their poles (Figure 4.30, c-d) and the brightness of the particles appears greatest when they are angled at ~45° to the polarisers, suggesting a planar alignment. It was observed in a tumbling particle of **P1-MF16** (Figure 4.31) that the defects were situated at the apexes of the spindle. If a planar surface anchoring within the particle is assumed then a bipolar configuration may be more energetically favourable to place the

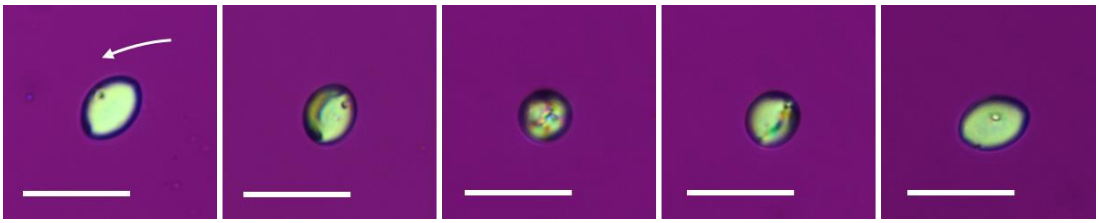

Figure 4.31. Polarised light photomicrographs of a nematic polymer particle from **P1-MF16** tumbling, revealing a defect at the apex of the spindle at x200 magnification with a λ plate. The arrow indicates the direction of the tumble. Scale bar = 50 μm.

defects at the apexes of the spindle, as the mesogens would be required to splay, as opposed to requiring a higher energy bend for a concentric alignment.

On rotation of the particles under crossed polarisers the change in birefringence observed, and therefore the director configuration within, is slightly unclear (Figure 4.32). For a bipolar alignment, a maximum birefringence should be observed when the long axis of the particle is at 45° and 135° relative to crossed polarisers. However, only at 45° is the maximum brightness seen across the entire particle (Figure 4.32, b). At 135° the increase in brightness is localised to a central band (Figure 4.32, d), indicating some alignment at

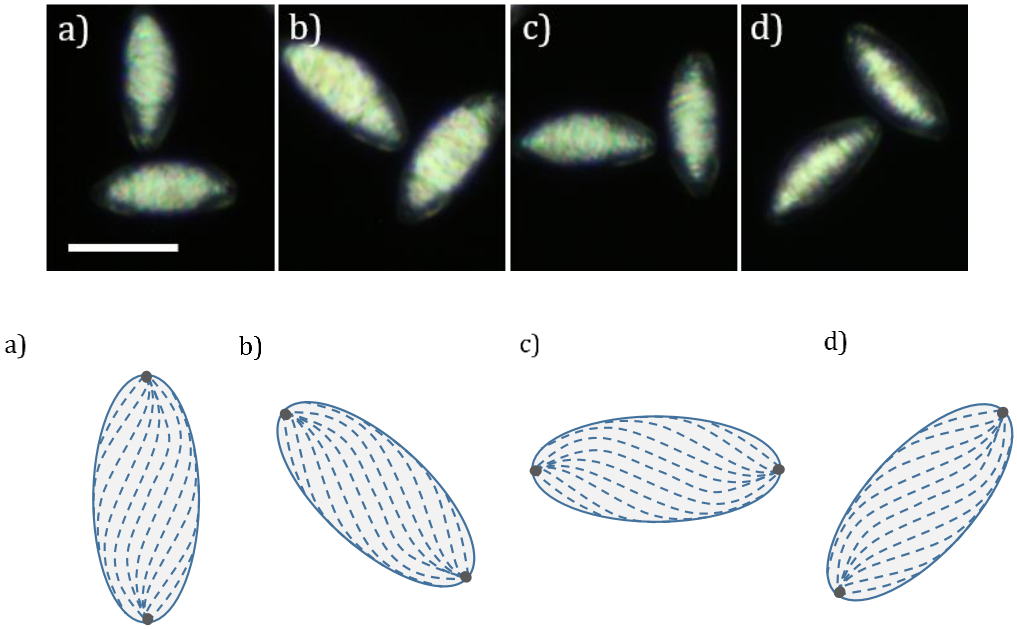

Figure 4.32. Top Row: Polarised photomicrograph of nematic polymer particles of **P1-MF16** at x500 magnification. Rotation of particles relative to crossed polarisers: a) 0°, b) 45°, c) 90°, d) 135°. Scale bar = 40 μm. Bottom Row: Cartoon of the possible director configuration of a twisted bipolar spindle particle, corresponding to each orientation.

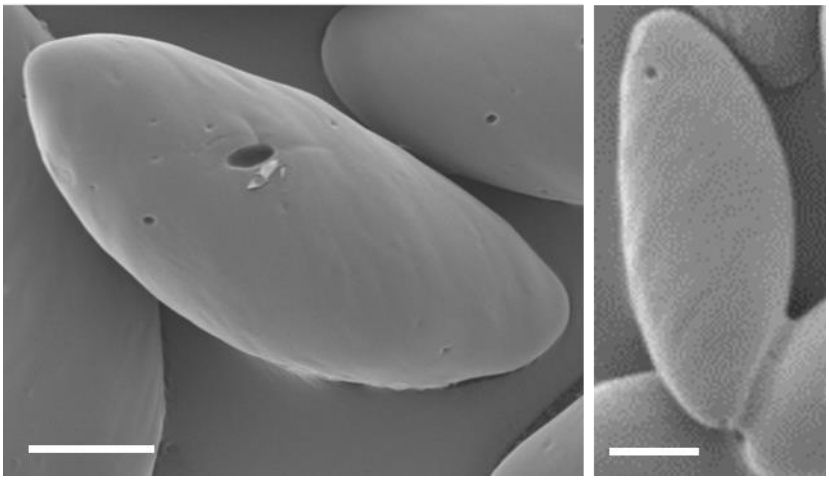

Figure 4.33. Scanning electron photomicrographs of anisometric polymer particles of **P1-MF16** at x2300 and x1630 magnifications. Twisted striations on the surface are faintly visible on both particles. Scale bars = 10 μm.

the edges of the particle in this orientation. This POM analysis suggests that the mesogen alignment is perhaps more complicated than a simple bipolar alignment. A comparison of the maximum brightness of both orientations - by converting the images into 8-bit in ImageJ - does however indicate similar values for both orientations and a reduction of ~12% when aligned parallel to the polarisers (Figure 4.32, a, c). Further to this, when the particles are aligned parallel to the polarisers the expected isogyres in the centre of the particle due to a bipolar alignment are absent. This suggests that it may possess a twisted bipolar configuration.[99] SEM of the particles of **P1-MF16** reveals faint striations on the surface that also twist around the particles (Figure 4.33). Similar to the striations found on the spherical elastomer particles discussed earlier, the wrinkles/striations are aligned parallel to the molecular alignment. Wang *et al* also observed a twist in some anisotropic polymer particles made by anisotropic de-swelling.[59] They found that a twisted configuration was present in ~75% of the particles with a large (~1.9) aspect ratio, compared to only ~6% of particles with a small (~1.2) aspect ratio, and suggest that the twist arises from a mechanical instability that occurs during shrinkage of the anisotropic polymer network. Also, like the other particles, small holes on the surface are observed and as before are likely to be caused by the evaporation of small volume of residual chloroform when vacuum drying the particles.

The origin of the ellipsoidal shape is perhaps due to a combination of the bipolar alignment and an anisotropic polymerisation of the particle. Lee *et al* reported finding similar anisometric particles made from magnetically aligned droplets of RM257/5CB

(~50 μm) when irradiated with a 2000 mW cm^{-2} UV source.[207] They found that bipolar particles with an aspect ratio of ~2 could be formed and the aspect ratio could be slightly increased or decreased by aligning the nematic director parallel or perpendicular with the UV beam using the magnetic field, whilst radial particles remained spherical. They suggested that the anisotropic polymerisation was due to a phase separation of the RM257 and the 5CB into 'polymer rich' and 'polymer poor' domains which polymerised at different rates. However, our results challenge this explanation as there is no possibility of phase separation, especially in the anisometric polymer particles. In addition to this, Fleischmann *et al* created anisotropic nematic elastomer shells and reasoned that a combination of a flow-aligned bipolar configuration and an anisotropic polymerisation were the origin of the ellipsoidal shape.[123] The top part of the shell would be polymerised preferentially to the bottom as it receives a larger dose, as the light has a reduced distance to travel. In our case the droplets are much smaller (~30 μm compared to ~500 μm), although this may still be significant. They also proposed that the polymerisation at the poles of the shell (where the defects reside) occurs at a slightly slower rate compared to the centre section of the shell, leading to an anisometric shape, as the change in the elasticity due to polymerisation occurs at different time periods.

Radicals for polymer chain propagation are generated though the absorption of energy by the photoinitiator, causing the excitation of the initiator and leading to bond homolysis.[208] Anisotropic polymerisation has been shown to occur in flat films of liquid crystal polymer by Broer.[209] The dichroic ratio (DR) is the ratio of the absorbed light parallel and perpendicular to the director and is proportional to the square of the ratio of the parallel and perpendicular polymerisation rates (Equation 4.2).[209]

$$DR = \frac{A_{\parallel}}{A_{\perp}} \propto \left(\frac{R_{\parallel}}{R_{\perp}}\right)^2 \qquad \text{Equation 4.2}$$

However, the photoinitiator used in our study is isotropic in shape and so one would assume that the dichroic ratio = 1. Nonetheless, if there is a transfer of anisotropy to the photoinitiator, perhaps through restricted movement within the nematic host, this effect could be a possible explanation.

The shape of a nematic droplet is controlled by the balance between the interfacial tension and the elasticity of the droplet. Very small nematic droplets have been found to adopt an elongated shape to reduce the elastic deformation due to the 'stiffness' of the director

dominating.[210] Calculations by Zhang *et al* revealed that vesicles in a nematic solvent were able to deform from spherical to spindle, with defects at the poles, dependent on the balance of elastic and surface forces.[211] Droplets are usually spherical because interfacial tension (γ) attempts to minimize surface energy. Caggioni *et al* produced anisotropic droplets formed from soft wax crystal scaffolds and suggest they are able to persist when the interfacial Laplace pressures (Equation 4.3) are balanced by the internal elasticity.[212–214]

$$\Delta P = \frac{2\gamma}{r} \qquad \text{Equation 4.3}$$

Therefore, it is suggested that the exposure to a large dose of UV radiation to initiate the polymerisation causes the internal elasticity to increase suddenly. Due to the strongly anisotropic coupling between the forming polymer backbone and mesogen orientation, the deformation is also anisotropic and can overcome the Laplace pressure, before the system can equilibrate. As discussed in more detail later on, indeed no shape deformation is observed upon polymerisation of droplets of **M4**, where little correlation between mesogen and backbone orientation exists.

4.5.2.1 Effect of Intensity/Irradiance

When the LX500 was positioned so that the entire monolayer was not fully covered by the beam it was noted that some particles on the edges of the monolayer did not possess the same aspect ratio as those in the centre. As the irradiance decreases further away from the centre of the beam, this variation could be due to their exposure to a lower irradiance compared to the particles in the centre of the dish. Therefore, to test this hypothesis, samples of particles were subjected to different levels of irradiance by either varying the 'intensity' or the distance of the UV source to the sample (Table 4.4). Nematic droplets of **M1** without crosslinker were prepared, in part to ascertain if the crosslinker had any role in the elongation mechanism. The particles were heated to 55 °C and irradiated, upon which they elongated. The polymerisation time was also varied to optimise the procedure.

Analysis of the anisometric particles by SEM and microscopy (Figure 4.34) reveals a correlation between the intensity of the UV light and the mean aspect ratio. The 'intensity' vs mean aspect ratio was plotted (Figure 4.35), where 'intensity' was derived as the product of the intensity setting on the Omnicure LX500 and the inverse square of the distance of the droplets from the LED head. At 100% intensity and 14 cm away from the source (**P1-MF15**), the mean aspect ratio was calculated to be 1.57. Increasing the irradiance by moving the UV source closer (6 cm (**P1-MF16**) and 3 cm (**P1-MF17**)) at 100% intensity increased the average aspect ratio of the samples to 1.68 and 1.74 respectively, suggesting a plateau of the response. However, by decreasing the intensity output to 5% from 6 cm away (**P1-MF18**), slightly misshaped particles with an aspect ratio of 1.16 were produced. Spherical elastomer particles (**E1-MF42**) with an aspect ratio of 1.06 were created using 7% intensity from 30 cm away (~140 mW cm^{-2}, matching the output of the RS Exposure Unit LV202-E). Particles subjected to a lower irradiance have more spherical aspect ratios, perhaps due to a more homogeneous rate of polymerisation throughout the particle. This can also explain the appearance of the slightly 'egg-shaped'

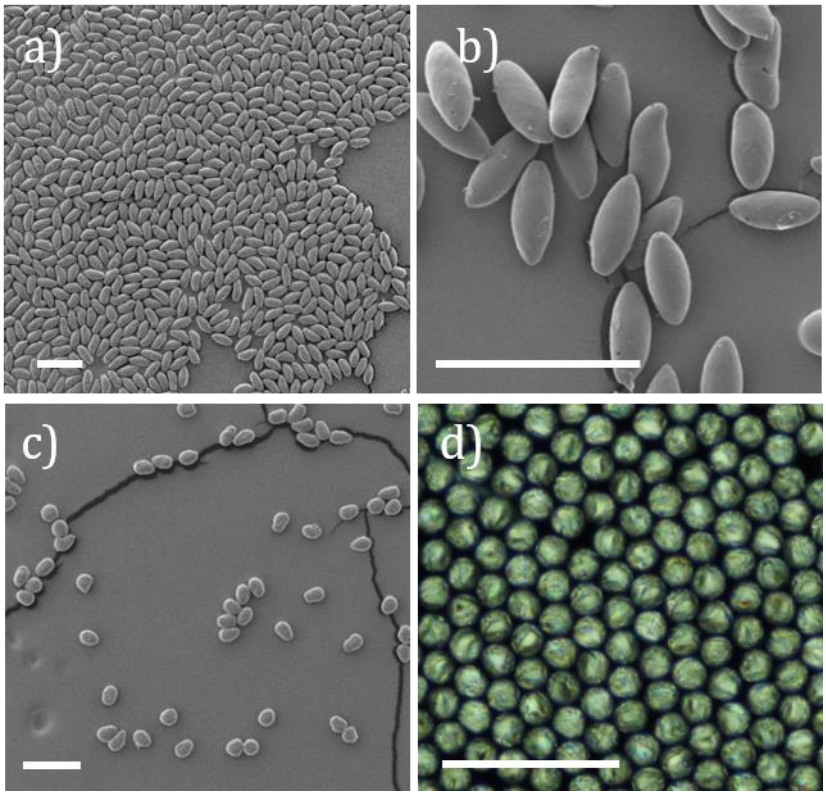

Figure 4.34. a)-c) Scanning electron photomicrographs of anisometric nematic polymer particles of **P1** polymerised at different intensity levels: a) 100%, 14 cm (**P1-MF15**), b) 100%, 6 cm (**P1-MF16**), c) 5%, 6 cm (**P1-MF18**). Magnification: a) x60, b) x270, c) x75. d) Polarised light photomicrograph of nematic elastomer particles made at 7%, 30 cm, (**E1-MF42**) at x200 magnification. Scale bars = 100 μm.

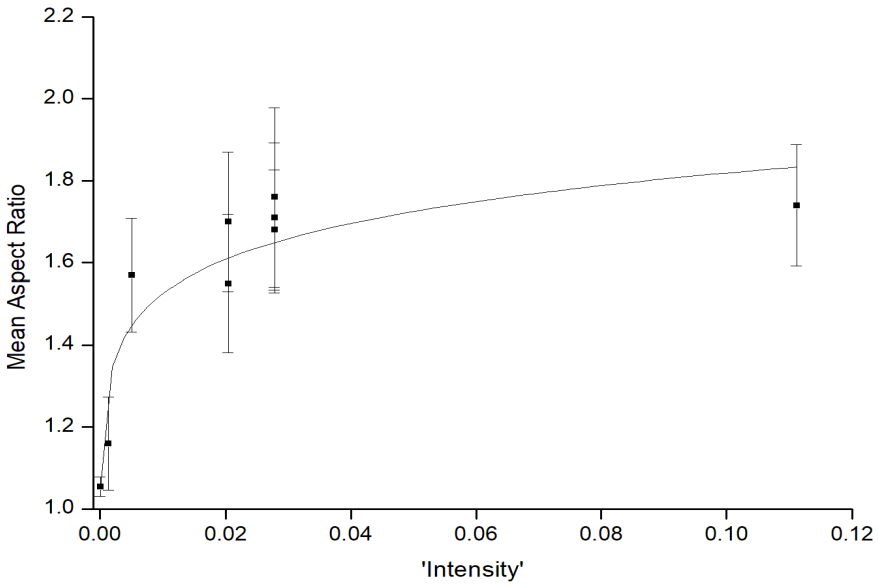

Figure 4.35. Plot of 'intensity' against mean aspect ratio of the photo-deformed particles. The 'intensity' was derived as the product of the intensity setting on the Omnicure LX500 and the inverse square of the distance of the droplets from the LED head.

elastomer particles described earlier, made using the RS Exposure Unit LV202-E. Droplets of **E1-MF44** were exposed to the UV LED for 2 seconds (100% intensity from 14 cm away).

Further to these results, following drying of the particles, analysis by SEM revealed that an additional increase in the aspect ratio occurred. In the samples measured, this increased to an average of 2.4 from 1.7 for those created at high intensity and 1.4 from an average of 1.2 for those created at low intensity. The aspect ratios were calculated from brightfield or λ plate images to clearly identify the edges of the particles, so why there is a discrepancy is unclear, unless the particles undergo a further extension on drying/residual solvent removal. The anisometric bipolar-aligned polymer particles obtained by Mondiot *et al* were found to have an aspect ratio of 1.4 with 20 mol% of reactive mesogen.[114] By lowering the percentage of monomer to 10 mol%, and therefore increasing the percentage of templating liquid crystal that is removed, the shrinkage was greater and particles with aspect ratios of 2.4 were created. Clearly then our method of subjecting bipolar aligned droplets to high intensity UV light is comparable but with the advantage of using only a single component.

4.5.1.2 Effect of Mesogen Decoupling

To further probe the conditions necessary for creating anisometric particles, droplets of monomer **M4** were prepared and irradiated at 100% intensity from 6 cm at 45 °C for 20 minutes (**E4-MF3**). In contrast to those made from **M1** (n = 4), elastomer particles with the monomer separated from the backbone by the longer (n = 11) spacer were not found to change shape on exposure to UV light (Figure 4.36). A change in aspect ratio from 1.04 to only 1.05 was measured although this is within the error of the measurement technique and therefore it is likely that no change has occurred. As there is only very weak coupling between the backbone and mesogens in this elastomer, the radius of gyration of the polymer chains is likely isotropic. This result further suggests that the deformations observed in the **P1** and **E1** particles are, in part, also linked to the strong anisotropy of the polymer network imparted by the nematic phase.

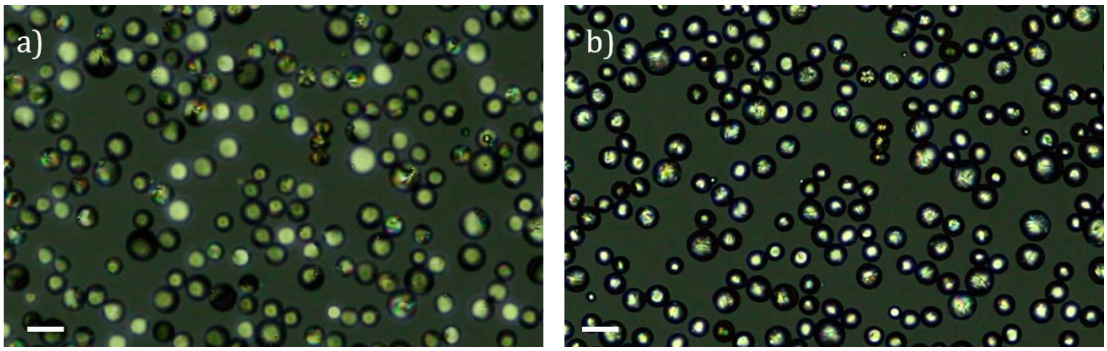

Figure 4.36. Stills from a video of elastomer microparticles of **E4-MF3** in PVA (3 wt%) at x100 magnification, with the polarisers slightly uncrossed: a) before UV irradiation b) after UV irradiation. Scale bar = 50 μm.

4.5.2 Temperature Response

The response of the anisometric nematic elastomer and polymer particles of **M1** to changes in temperature were studied.

4.5.2.1 Elastomer Particles

After polymerisation, the anisometric nematic elastomer particles **E1-MF37** in PVA were washed with water and transferred to PEG200. On heating the particles into the isotropic phase, it is observed that the particles exhibit a very large reversible shape change - an inversion of the long and short axes, passing through a spherical intermediate (Figure 4.37). This video is available as Movie 3 on the attached CD. The inversion of the axes leads

to large changes in the aspect ratio - an analysis of 20 particles found that the average aspect ratio reversibly changed from 1.7 to 0.6 on heating and cooling (a ~200% change). Assuming that the polymer chains within the particles are aligned along the long axis in a bipolar configuration, the isotropisation causes the contraction parallel and expansion perpendicular to this long axis (i.e. the director). The size of the actuation suggests that the anisotropic coupling of the backbone and the mesogen is very strong, perhaps due to the anisotropic polymerisation, and is increased significantly compared to the spherical elastomer particles that are polymerised with a low irradiance such as **E1-MF29**. In fact, the magnitude of this is more like that of a main chain liquid crystal elastomer.[215]

As previously discussed, in the nematic phase, particles of **E1** have a higher order white birefringence colour. When heated into the isotropic phase the anisometric elastomer particles of **E1-MF37** show blue and yellow birefringence colours identical in colour and orientation to the bipolar elastomer particles with short spacers and strong backbone coupling (**E1/E2**), made with the RS Exposure Unit LV202-E. This suggests some residual

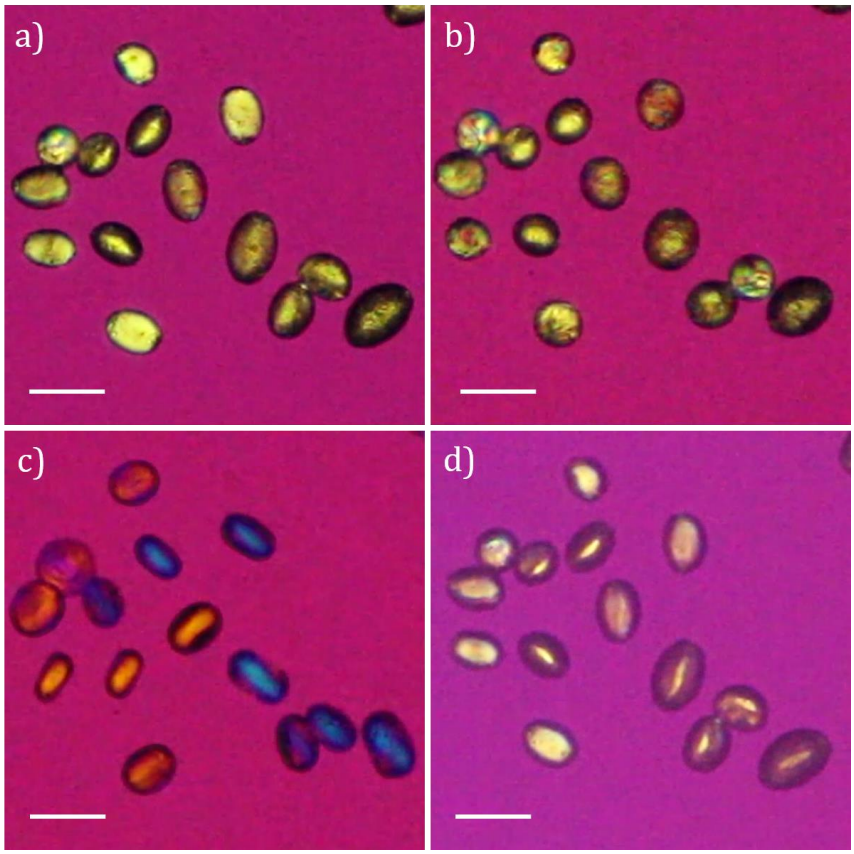

Figure 4.37. Polarised photomicrographs of the heating and cooling of anisometric elastomer microparticles of **E1-MF37** in PEG200 at x100 magnification, viewed through a λ plate: a) 100 °C, b) 118 °C, c) 125 °C, d) 100 °C. Scale bar = 50 μm.

alignment with the long axis of the particle and that the birefringence is from the stretched polyacrylate backbone.

4.5.2.2 Polymer Particles

Like the elastomer particles, after polymerisation, the anisometric nematic polymer particles **P1-MF15** in PVA were washed with water and transferred to PEG200 (Figure 4.38, a, b). Upon heating into the isotropic phase, the particles quickly shrink in aspect ratio. With no crosslinking points to anchor the polymer chains, the now isotropic radius of gyration of the polymer chains leads to the particles adopting a spherical geometry (Figure 4.38, c). Unlike the elastomer particles of **E1-MF37**, no blue or yellow birefringence colour is observed with a λ plate as the polymer chains are not strained and can freely move to new positions due to the absence of crosslink points. On cooling back into the nematic phase the shape memory of the polymer chains' original orientation is not recovered, resulting in a polydomain texture (Figure 4.38, d) which is not influenced by the surface anchoring of the solvent due to the viscosity of the polymer. Further heating and cooling of these poorly aligned particles produced no shape change response.

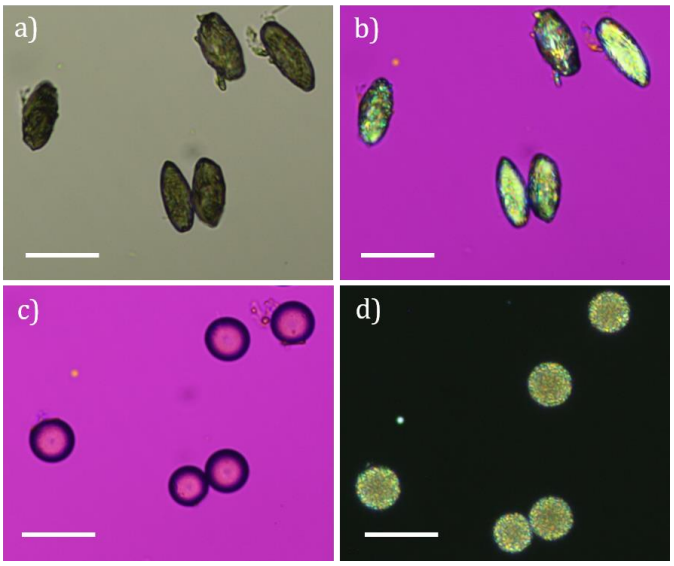

Figure 4.38. Polarised photomicrographs of the heating and cooling of anisometric polymer microparticles of **P1-MF15** in PEG200 at x200 magnification: a) 20 °C (bright field), b) 20 °C (λ plate), c) 125 °C (λ plate), and d) 100 °C (crossed polarisers). Scale bar = 50 µm.

It should be noted that the elongation on irradiation of the polymer and elastomer particles was a consistently observed effect over many experiments, however at the very end of the project a reduction in the particles' elongation upon irradiation was observed. The reason for this, at the time of writing, is unclear, and ultimately resulted in spherical particles despite changing to a new batch of photoinitiator and crosslinker. It is very likely that the intensity output of the UV source degraded over time, as other issues were observed within the group including unsuccessful polymerisations, but this was not possible to verify at the time of writing.

4.6 Conclusion

Nematic liquid crystal polymer and elastomer microparticles have been created using a microfluidic approach. A coaxially aligned flow-focusing microfluidic device was constructed, and improvements in the build quality of the device and methodology led to the production of monodisperse droplets ($CV < 3\%$). Small (~30 μm) droplets containing photo-polymerisable mixtures of laterally-attached side chain liquid crystal monomers **M1-M4** were produced with bipolar-aligned textures due to the surface anchoring of the dilute PVA host.

Polymerisation of the droplets with low irradiance UV light in the nematic phase created aligned LCE microparticles. The change in the shape of the particles on heating and cooling through the phase transition was ascribed to the internal mesogen alignment captured during polymerisation. The magnitude of the shape change was affected by varying the spacer length due to the reduction in the transfer of anisotropy from the mesogens to the polymer backbone. Stress birefringence was only observed in particles with strongly anisotropic backbones due to the deformation of the confined polymer. The lack of stimuli responsiveness in particles with isotropic chain orientations is further evidence that strong coupling between the mesogen and backbone is necessary for shape changing liquid crystal elastomers. The crosslinked nature of the elastomer was confirmed by the reversibility of the shape change. Lengthening of the peripheral chains in the monomer structure allowed for the temperature of the shape change to be reduced, without affecting the extent of the shape change. Lowering the actuation temperature is an important consideration for almost any potential application of LCE.[118]

Anisometric nematic polymer and elastomer microparticles with a spindle-like shape and large aspect ratio (~2) were fabricated using bipolar-aligned droplets and high intensity

UV. It was found that the elongation on irradiation only occurred in polymers with a short (n = 4) spacer, whilst particles with a longer (n = 11) spacer remained spherical, highlighting the importance of the coupling between the nematic phase and the forming polymer backbone. It was also found that the aspect ratio of the particles could be controlled by varying the intensity of the UV light to initiate polymerisation. At low levels of irradiance, the particles retained the spherical shape of the original droplets; however, at high irradiance the particles possess a large aspect ratio. Heating and cooling of the anisometric elastomer particles found a ~200% change in the aspect ratio indicating a good internal alignment and a strongly anisotropic backbone. Polymer particles exposed to the same conditions did not retain the anisometric shape after heating into the isotropic phase, instead returning to a spherical shape with a polydomain alignment due to the lack of crosslinking points in the network to remember the original orientation at the time of polymerisation. Xu *et al* fabricated anisometric polymer particles by using constrained droplets in a microfluidic channel, producing disks and rods of differing aspect ratios depending on the channel geometry.[93,96] Wang *et al* were also able to generate different shaped polymer particles, such as spindles, disks and tear-shaped, through the templating of a reactive mesogen with a nematic liquid crystal, followed by its removal, to de-swell the particles anisotropically.[114,216] Whilst both of these routes are certainly versatile ways of creating anisometric polymer particles there is extra complexity involved in the preparation, such as the washing step to remove the templating 5CB or the precise channel dimensions required in the microfluidic chip. Our results demonstrate the first examples of spindle-shaped anisometric LCEs with large deformations due to surface alignment. The particles could be further developed with azobenzene liquid crystal polymers potentially affording micro stirrers with large deformations through the exposure to light.

Chapter 5:

Responsive Chiral Nematic Microparticles

5 Responsive Chiral Nematic Microparticles

5.1 Introduction

This chapter discusses the creation of chiral nematic polymer and elastomer microparticles; made using the monomers synthesised in this thesis, and the microfluidic technique developed in the previous chapter. The thermal and optical properties of the particles, as well as their response to changes in pressure, were analysed by polarised light optical microscopy (POM).

One of the aims of this thesis was to develop chiral nematic elastomer microparticles, capable of selective reflection due to the alignment imparted from surface anchoring. As found and discussed in Chapter 2, the chiral monomers **CM1-8** and polymers **CP1-8** have good phase stabilities but do not possess a visible selective reflection due to the long pitch of the chiral nematic phase, instead likely reflecting in the infrared. Therefore, droplets of the chiral monomer **CM1** and **CM6** were used to investigate the response of infrared-reflecting elastomer microparticles. The chiral monomer **CM9** and polymer **CP9** contain a different chiral group with a strongly twisted chiral nematic phase, which consequently leads to a visible red selective reflection. However, the extremely low phase stability of the elastomer mixture would not be suitable for the preparation of droplets in a PVA/water host. Therefore, chiral nematic droplets of **CM9**, without a crosslinker, were chosen for further investigation into the creation of polymer microparticles capable of visible selective reflection. As discussed in Chapter 3, mixtures of the monomer **M1** and the chiral dopant CB15 were investigated; producing chiral elastomers that had a tuneable visible selective reflection. The good phase stability of the chiral doped monomers meant that these mixtures were suitable to create elastomer microparticles by the microfluidic method developed in this thesis.

5.2 Chiral Nematic Droplets

Before the investigation of the properties of responsive chiral nematic elastomers microparticles, droplets of the mixtures were first studied. Droplets were produced by using a flow-focussed microfluidic chip. For the investigation into elastomers **CE6**, the monomer **CM6**, crosslinker and photoinitiator were prepared (**CE6-MF1-3**); the experimental details are summarised in Table 5.1. The full details of the microfluidic conditions to make droplets of **CM9** (**CP9-MF1-3**) and droplets of **M1** and chiral dopant CB15 (**E1D-MF1-2**, **E1E-MF1-5** and **E1F-MF1-3**) can be found in Chapter 7 - Experimental, whilst those discussed in this chapter are summarised in Tables 5.2 and 5.3.

Table 5.1. Experimental details of microfluidic experiments to create chiral nematic droplets, using chiral monomers **CM1** and **CM6**, 10 mol% 1,6-hexanediol diacrylate and 2 mol% diphenyl(2,4,6-trimethylbenzoyl)phosphine oxide. Chip: V9 (**CE6-MF1-3)**, V5 (**CE1-MF1**). PVA: 3 wt%, 13,000-23,000 g mol^{-1} (87-89% hydrolysis) (**CE6-MF1-3**). 85,000-124,000 g mol^{-1} (87-89% hydrolysis) (**CE1-MF1**)).

Experiment	Tip Sizes /μm	Monomer Conc. /%w/w	Inner Flow Rate /μL hr^{-1}	Outer Flow Rate /mL hr^{-1}	Mean Droplet Diameter	Solvent Evaporation /Hours
CE1-MF1	30/ 200	6%	200	13.0	Isotropic: 90 μm (CV: 8.8%) Nematic: 40 μm (CV:9.2%)	19
CE6-MF1	25 /190	5%	75	20.0	Isotropic: 95 μm (CV: 3.5%) Nematic: 55 μm (CV: 5.2%)	17
CE6-MF2	25 /190	5%	75	20.0	Isotropic: 96 μm (CV: 1.6%) Nematic: 52 μm (CV: 6.6%)	17
CE6-MF3	25 /190	5%	75	20.0	Isotropic: 94 μm (CV: 1.3%) Nematic: 50 μm (CV: 5.3%)	17

Table 5.2. Experimental details of microfluidic experiments to create chiral nematic droplets, using **CM9** and 2 mol% diphenyl(2,4,6-trimethylbenzoyl)phosphine oxide. Chip: V9. PVA: 3 wt%, 13,000-23,000 g mol^{-1} (87-89% hydrolysis).

Experiment	Tip Sizes /µm	Monomer Conc. /%w/w	Inner Flow Rate /µL hr^{-1}	Outer Flow Rate /mL hr^{-1}	Mean Droplet Diameter	Solvent Evaporation/ Hours
CP9-MF1	18/ 185	2%	100	19.0	Isotropic: 67 µm (CV: 2.5%) Nematic: 29 µm (CV: 7.8%)	17
CP9-MF2	18/ 185	2%	140	17.0	Isotropic: 70 µm (CV: 4.0%) Nematic: 30 µm (CV: 0.7%)	17
CP9-MF3	18/ 185	2%	140	17.0	Isotropic: 65 µm (CV: 1.1%) Nematic: 30 um (CV: 0.9%)	17

For example, in **CE6-MF2**, droplets containing chloroform, chiral nematic monomer **CM6** (5% w/w relative to solvent), 1,6-hexanediol diacrylate (10 mol% relative to monomer) and 2,4,6-trimethylbenzoyldiphenylphosphine oxide (2 mol% relative to monomer) were produced using a V9 chip with droplet and collection capillary tip diameters of 20 µm and

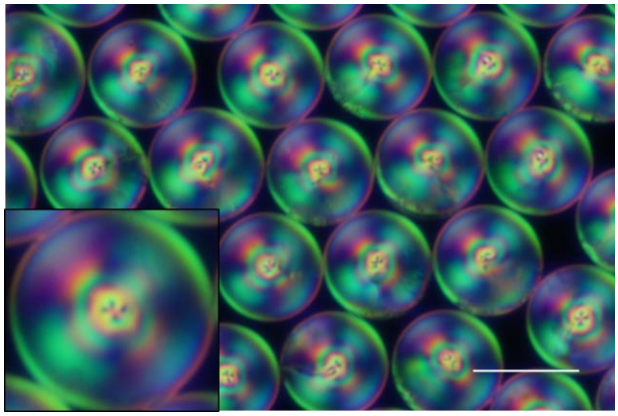

Figure 5.1. Polarised light photomicrograph of droplets of **CE6-MF2** in PVA at 21 °C in transmission mode at x500 magnification. Inset: the Maltese cross arising from the radial alignment is clearly visible. Scale bar = 50 µm.

Table 5.3. Experimental details of microfluidic experiments to create chiral nematic droplets using **M1**, CB15, 10 mol% 1,6-hexanediol diacrylate and 2 mol% diphenyl(2,4,6-trimethylbenzoyl)phosphine oxide. Chip: V9. PVA: 3 wt%, 13,000-23,000 g mol^{-1} (87-89% hydrolysis).

Experiment	CB15 (wt%)	Tip Sizes /μm	Monomer Conc. /%w/w	Inner Flow Rate /μL hr^{-1}	Outer Flow Rate /mL hr^{-1}	Mean Droplet Diameter	Solvent Evaporation /Hours
E1D-MF2	29	12/ 180	3%	140	14.0	Isotropic: 49 μm (CV: 2.8%) Nematic: 20 μm (CV: 3.8%)	20
E1E-MF1	35	25/ 200	3%	100	10.0	Isotropic: n/a Nematic: 37 μm (CV: 3.1%)	19
E1E-MF5	35	25/ 200	2%	140	17.0	Isotropic: 75 μm (CV: 2.3%) Nematic: 30 μm (CV: 2.4%)	15
E1F-MF1	41	20/ 160	3%	140	13.0	Isotropic: 72 μm (CV: 1.6%) Nematic: 26 μm (CV: 1.3%)	18

185 μm respectively, in PVA (3 wt%). Flow rates of Q_{inner} = 75 μL/hr and Q_{outer} = 20.0 mL/hr were used (these rates are different to those normally used in other microfluidics experiments using this chip due to partially blocked tubing supplying the outer phase which necessitated a higher flow rate at the syringe pump). The chloroform was evaporated over 17 hours, reducing the droplet diameter from an average of 96 μm to an average of 52 μm (CV = 6.6%). The mesogen alignment and texture was improved by annealing at 39 °C for 3 days. The droplets self-assembled into a hexagonal-packed monolayer due to the high monodispersity of the sample (Figure 5.1).

Figure 5.2. Cartoon of the radial alignment in a droplet due to planar surface anchoring of the chiral nematic helix and the resulting central defect.

Observed by POM in transmission mode, the droplets of **CM6** have Maltese cross textures due to the planar surface anchoring of the PVA/water. Within the droplet, the mesogens align parallel to the surface, with the periodic helical self-assembly resulting in a central hedgehog defect (Figure 5.2). The internal alignment was left to improve for 3 days due to the high viscosity of the chiral nematic phase. As expected, from the investigation into the chiral monomer optical properties in Chapter 2, no visible selective reflection was observed in reflection mode. The pattern of the texture is similar to other examples of chiral nematic monomers with a long pitch confined to droplets such as those made by Beltran-Gracia.[143] Droplets of **CE1-MF1**, made by microfluidics (mean diameter: 40 μm, *CV* = 9.2%), were annealed at 46 °C after the evaporation of the chloroform for 18 hours and possessed similar radial textures (Figure 5.3, a, b). However, polymerisation of these droplets in the chiral nematic phase at 40 °C using the RS Exposure Unit LV202-E for 30 minutes from 6 cm away resulted in polydomain particles, indicating that many defects were generated due to the polymerisation (Figure 5.3, c).

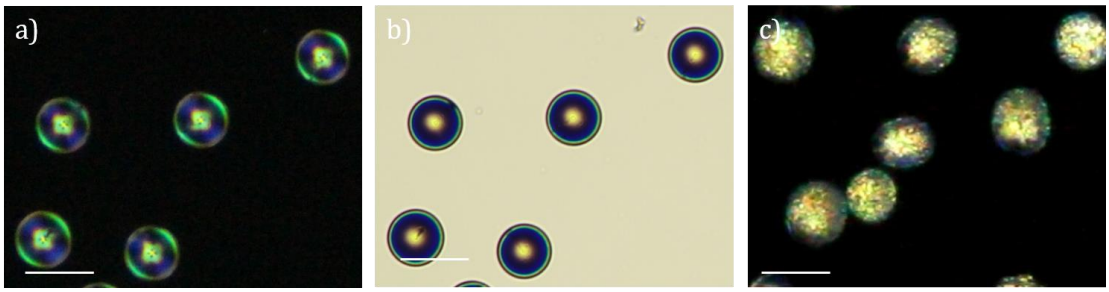

Figure 5.3. Polarised light photomicrographs of chiral nematic droplets of **CM1-MF1** at 46 °C in PVA in transmission mode at x100 magnification: a) crossed polarisers, b) brightfield, c) particles, crossed polarisers. Scale bar = 50 μm.

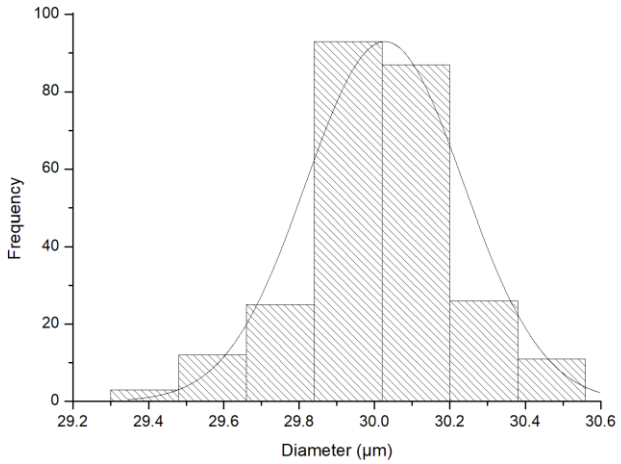

Figure 5.4. Size distribution of chiral nematic droplets of **CP9-MF2**.

Droplets of the monomer **CM9** and photoinitiator were produced using microfluidics and left to stand, allowing the chloroform to evaporate, leading to monodisperse droplets of **CM9-MF2** (mean diameter: 30 μm). The high monodispersity of the sample (*CV* = 0.7%, Figure 5.4) lead to the development of a crystal-like monolayer. The droplets were cooled to ~5 °C in the fridge, leading to the formation of the chiral nematic phase, and annealed for 24 hours to improve the alignment. The droplets were then analysed by POM in reflection and transmission modes (Figure 5.5). The internal radial alignment was indicated by the central hedgehog defect when viewed in transmission (Figure 5.5, b). In reflection mode each droplet possessed a central red spot and multiple teal coloured lines radiating from the centre to the edge of the droplet (Figure 5.5, a). The explanation for the observed patterns was proposed by Noh *et* al and Geng *et al*.[125,137] Their droplets were far

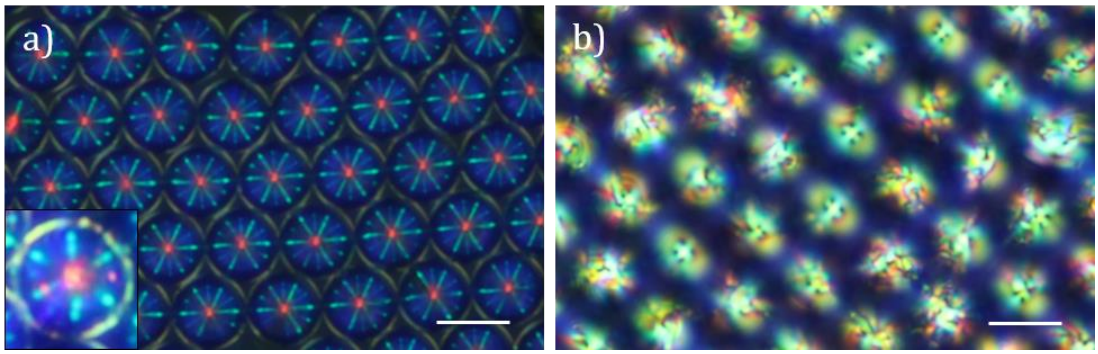

Figure 5.5. Polarised light photomicrographs of chiral nematic droplets of **CM9-MF2** at 8 °C in PVA at x200 magnification: a) reflection mode, inset: further cross-communication spots are visible when illuminated at a higher intensity, b) transmission mode. Scale bar = 30 μm.

larger (~400 μm) which allowed for an easier elucidation of the patterns but they remarked that the same mechanism applies for smaller droplets.

$$\lambda = \bar{n}\, p\, cos\theta \qquad \text{Equation 5.1}$$

The colours of the spots and lines observed in Figure 5.5 can be explained using Bragg's reflection law (Equation 5.1), where $\bar{n}$ is the average refractive index, p is the pitch and θ is the angle between the helical axis and the incoming light. Light incident to the droplet interacts with the chiral nematic helix at an angle, θ. The longest observed wavelength appears in the centre of the droplet, as light propagates down the helical axis and therefore θ = 0°. Consequently, the wavelength of light reflected is equal to $\bar{n}p$ and is therefore equal to the λ_{max} of **CM9.** However, due to the curved surface of the droplet, all other incident light will be reflected at a non-zero angle causing the blue-shift of this light to shorter wavelengths. When θ = 45°, this light is guided to a 'nearest neighbour' droplet of the same pitch and handedness, which is then reflected back to the observer as illustrated in Figure 5.6. The close hexagonal packing of the droplets means that each droplet has six 'nearest neighbours' and, due to the omnidirectional guidance of the light,

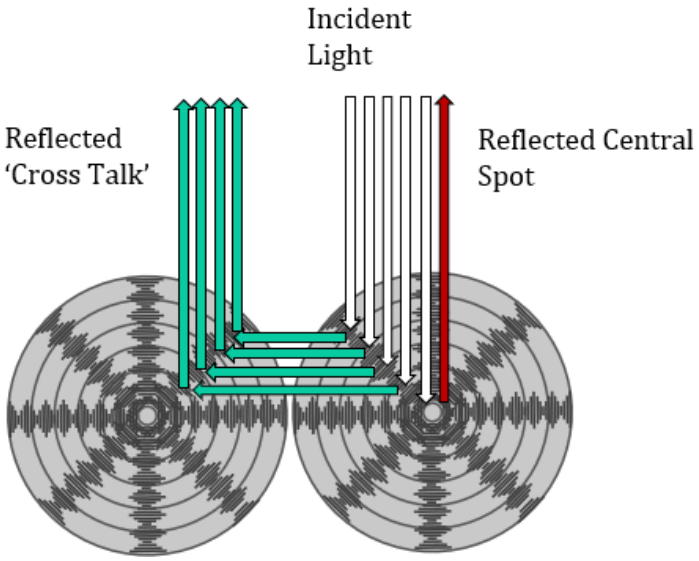

Figure 5.6. Cartoon of photonic cross-communication between adjacent droplets. Incident light at θ = 0° relative to the helix is reflected without change, whilst light at θ = 45° is reflected between droplets. The angular dependence of λ causes the shortening of the wavelength of reflected 'cross talk' spots.

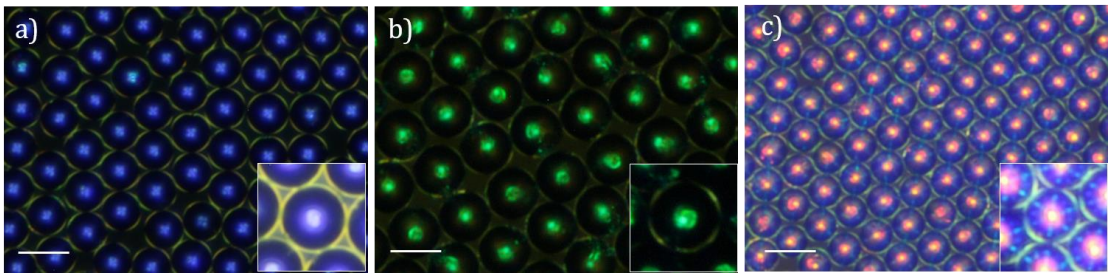

Figure 5.7. Polarised light photomicrographs of droplets of chiral nematic mixtures in PVA in reflection mode at x200 magnification: a) **E1F-MF1** (41 wt%), b) **E1E-MF5** (35 wt%) and c) **E1D-MF2** (29wt%). Insets show a droplet illuminated with higher light intensity to enhance the analysis of the cross-communication lines. Scale bar = 30 μm.

this leads to the striking patterns. If the wavelength of the red central spot is ~700 nm, the angle dependence of λ will cause the cross-talk wavelengths to be decreased to ~495 nm, matching the teal colour of the cross-communication lines in Figure 5.5. In contrast to the particles made by Noh, further cross-communication spots arising from the interactions with 'next nearest neighbour' droplets are not visible, likely due to the small size of the droplets making the detection difficult. It was not possible to analyse the droplets' reflection properties quantitively using UV-vis spectroscopy as the low intensity reflection from the droplets resulted in a noisy spectrum.

To demonstrate the control of the droplet reflection colour and investigate the properties, three colours of droplets were produced using the concentrations of CB15 in **M1** found to reflect red, green and blue light, based on the thin-film mixtures prepared in Chapter 3. When viewed in reflection mode POM, the droplets possess a coloured central reflection spot, matching that of the thin-film mixtures prepared previously (Figure 5.7), indicating good radial alignment of the mesogens. The red droplets of **E1D-MF2** (λ_{Film} = ~630 nm), containing 29 wt% CB15, do show cross-communication lines when the light intensity of the microscope is high, similar to the droplets of **CP9-MF1-3**, however no cross-communication lines are visible for the green droplets (**E1E-MF5**, λ_{Film} = ~530 nm) or blue droplets (**E1F-MF1**, λ_{Film} = ~470 nm). This is due to the cosθ dependence of λ and consequently the wavelength of the reflected cross talk is shifted outside of the visible region and into the ultraviolet. Similar to Fan *et al* and Noh *et al*, it was noticed that the crosstalk of the red droplets was directional and depended on the number of nearby neighbouring droplets and their proximity to each other. Droplets with closer neighbours possess higher intensity cross-talk lines in that direction and the steering of the light is

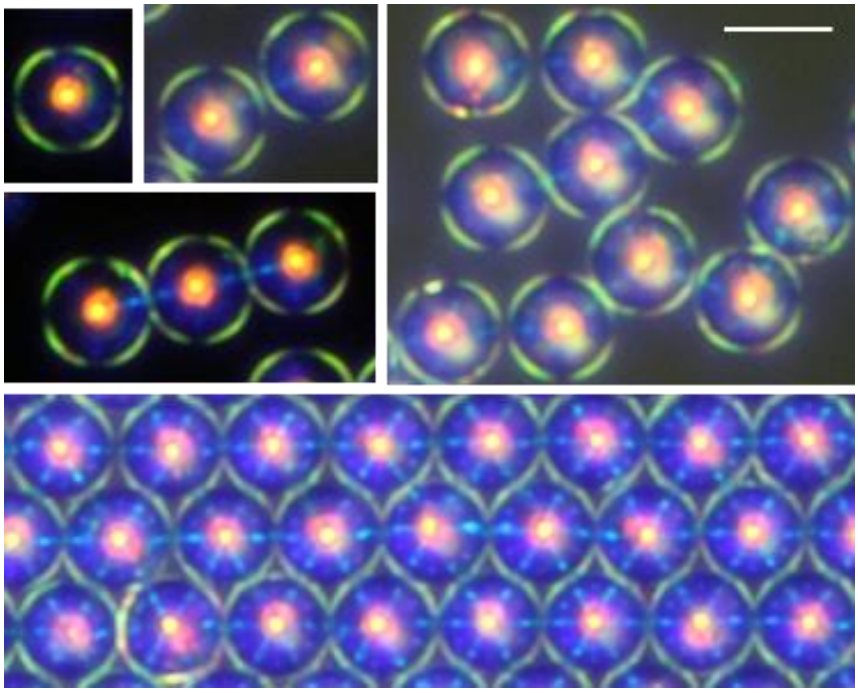

Figure 5.8. Polarised light photomicrographs of chiral nematic droplets from **E1D-MF2** in PVA in reflection mode at x200 magnification. The different cross-communication patterns between droplets depends on the number of nearby neighbouring droplets and their proximity. Scale bar = 20 μm.

dependent on the position of the droplets, demonstrating how light can be selectively routed by careful arranging of the droplets (Figure 5.8).

During the attempts at producing well-aligned droplets, larger droplets of **E1E-MF1** with average diameters of 37 μm were prepared (CV = 3.1%). However, no green central reflection spot was observed in any of the droplets (Figure 5.9). Instead, multiple smaller green specks were seen, and the texture did not improve with extended annealing time. Compared to the well-aligned droplets that contain the same mixture but are only 30 μm in diameter (**E1E-MF5**, Figure 5.7, b), it is likely that the alignment conferred by the PVA is not strong enough to extend throughout the droplets above this size, therefore, this observation is likely due to the poor alignment of the mesogens within the particle. In contrast, Seo *et al* were able to produce droplets of E7/RM257 doped with R/S-5011 with diameters between 60-180 μm and still maintained good alignment throughout, although 10 wt% PVA was used as the host, perhaps for this reason.[135] Therefore, in our system, it appears that the droplet size is crucial to the quality of the internal mesogen alignment. With a smaller diameter the quality of the selective reflection is improved.

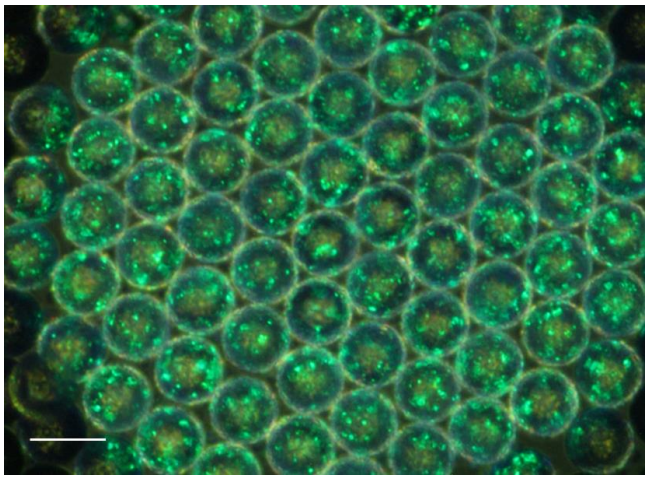

Figure 5.9. Polarised light photomicrograph of chiral nematic droplets (d = 37 μm) from **E1E-MF1** in PVA in reflection mode at x200 magnification. Multiple green reflection spots suggest a poor internal mesogen alignment. Scale bar = 40 μm.

5.3 Chiral Nematic Microparticles

The chiral nematic droplets containing **CM6** were exposed to the Omnicure LX500 to yield elastomer particles **CE6-MF1-3**, the conditions of which are summarised in Table 5.4. Analysed by POM, **CE6-MF2** (Figure 5.10, a) was the only sample regarded to have been successful - a longer polymerisation time, as in **CE6-MF3**, resulted in a degradation of the optical properties (Figure 5.10, b), whist a low irradiance exposure in **CE6-MF1** lead to no increase in the phase stability therefore it was assumed that polymerisation was not fully completed. In **CE6-MF2** the optical texture of the particles is similar to the droplets and

Table 5.4. Polymerisation conditions to create chiral nematic elastomer particles **CE6**, using **CM6**, 10 mol% 1,6-hexanediol diacrylate and 2 mol% diphenyl(2,4,6-trimethylbenzoyl)phosphine oxide. UV-initiated radical polymerisation used an Omnicure LX500 with a 365 nm LED head.

Experiment	UV Exposure Time /Seconds	Temperature /°C	UV 'Intensity'	Distance /cm
CE6-MF1	1200	39	5%	40 cm
CE6-MF2	90	39	50%	15 cm
CE6-MF3	1200	39	10%	37 cm

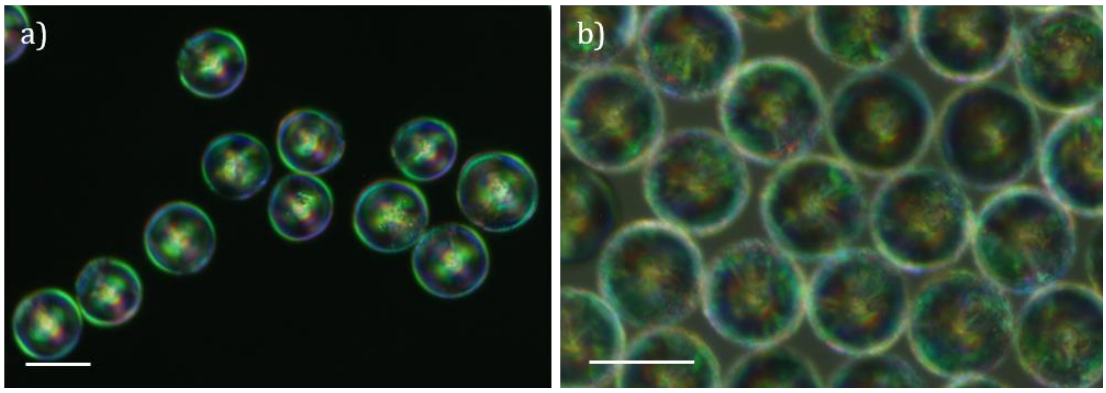

Figure 5.10. Polarised light photomicrographs of chiral nematic droplets in PVA at 21 °C: a) **CE6-MF2** in transmission at x100 magnification, b) **CE6-MF3** in reflection at x200 magnification. Scale bar = 50 μm.

no reflection spot was seen due to the long pitch. On heating above and below the phase transition the alignment is regained due to the crosslinked polymer backbone.

The chiral nematic droplets of **M1**, CB15, crosslinker and photoinitiator were polymerised using an Omnicure LX500 in the chiral nematic phase to yield elastomer particles of **E1D-F**, as summarised in Table 5.5. The irradiance of the UV that the droplets were exposed to was varied slightly: either a longer time from further away or closer but for less time, to assess which method resulted in a better alignment within the particle due to the generation of fewer defects. The particles were then studied by POM. An increase in the

Table 5.5. Polymerisation conditions to create chiral nematic elastomer particles using **M1**, CB15, 10 mol% 1,6-hexanediol diacrylate and 2 mol% diphenyl(2,4,6-trimethylbenzoyl)phosphine oxide. UV-initiated radical polymerisation used an Omnicure LX500 with a 365 nm LED head.

Experiment	CB15 (wt%)	UV Exposure Time /Seconds	Temperature /°C	UV 'Intensity'	Distance /cm
E1D-MF2	29	1800	30	50%	15
E1E-MF1	35	90	29	50%	9.5
E1E-MF5	35	1200	30	50%	9.5
E1F-MF1	41	1800	25	50%	15

phase transition temperature of **E1F-MF1** (41 wt% CB15), on heating, from ~37 °C for the droplets to ~58 °C for the particles was recorded. The nematic to isotropic transition temperature of the particles of **E1E-MF5** (35 wt% CB15) also increased from ~43 °C to ~52 °C, whilst particles of **E1D-MF2** increased to ~78 °C. Both the monomer droplet and elastomer particle phase transition temperatures found here are much higher than the same mixture in the thin films studied in Chapter 3, e.g. **M1F/E1F**, with a ~10 °C and ~20 °C increase respectively, though this is possibly due to the exposed hot stage that is required to heat the large petri dish, reducing the temperature accuracy. While it is certain that the phase stability of the particles has increased compared to the droplets the accuracy of the values is likely low. It would be preferable to record the phase transition by DSC to improve the accuracy of the measurement, like the thin-films in Chapter 3, although this was not measured due to the small quantities of particles produced being insufficient for a detectable thermal response.

The selective reflection colour of the elastomer particles in **E1D-MF2**. **E1E-MF5** and **E1D-MF1** is retained, although there is a degradation in the clarity of the texture (Figure 5.11), suggesting that the mesogen alignment has been slightly disrupted by the polymerisation process, where it is initiated preferentially in defects.[134] A small blue-shift in the selective reflection wavelength of the particles of **E1D-MF2** from red to orange was observed and the blue cross-communication lines from neighbouring particles can also still be seen. Like the droplets, the cross communication between particles of **E1E-MF5** and **E1F-MF1** were not observed due to the wavelength likely being shifted into the UV region. Due to the poor internal alignment of the droplets of **E1E-MF1** the effect of the different irradiance received on the particle texture was inconclusive, although comparing the green particles of **E1E-MF5** to the blue particles of **E1F-MF1** and the red particles of **E1D-MF2**, it could

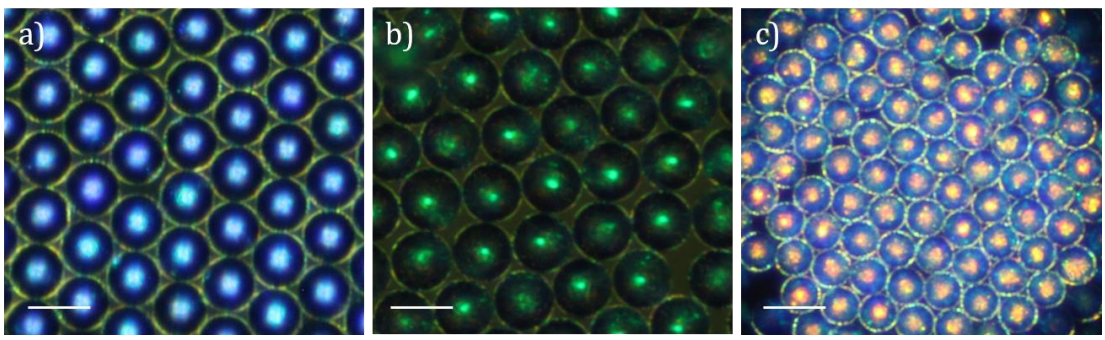

Figure 5.11. Polarised light photomicrographs of chiral nematic elastomer particles in reflection mode at x200 magnification. a) **E1F-MF1** (41 wt%), b) **E1E-MF5** (35 wt%), c) **E1D-MF2** (29 wt%). Scale bar = 30 μm.

be argued that fewer defects are observed in the particles polymerised for 20 minutes from 15 cm from the UV source.

Following the annealing of the chiral nematic droplets containing **CM9** and photoinitiator, chiral nematic polymer particles of **CP9** were produced by exposure to the Omnicure LX500 (Table 5.6). For example, chiral nematic polymer particles **CP9-MF3** were produced by exposure to the Omnicure LX500 at 50% intensity from 15 cm for 20 minutes. In only **CP9-MF3** the UV source was programmed to alternate between the on/off state every five seconds in an attempt to better preserve the internal mesogen alignment by slowing the generation of free radicals. During polymerisation the chiral nematic phase was maintained at ~10 °C using dry ice pellets placed on the hot stage.

Table 5.6. Polymerisation conditions to create chiral nematic polymer particles **CP9,** using **CM9** and 2 mol% diphenyl(2,4,6-trimethylbenzoyl)phosphine oxide. UV-initiated radical polymerisation used an Omnicure LX500 with a 365 nm LED head.

Experiment	UV Exposure Time /Seconds	Temperature /°C	UV 'Intensity'	Distance /cm
CP9-MF1	90	6	50%	9.5
CP9-MF2	180	7	50%	9.5
CP9-MF3	600	10	50%	15

Analysis by POM in reflection mode shows that the mesogen alignment within the particles is largely retained, as the central reflection spot and the cross-communication lines are still present. Like the elastomer particles however, the texture is not as defined compared to the droplet, suggesting the alignment is still slightly degraded due to the polymerisation process (Figure 5.12, a). The central reflection wavelength is blue-shifted from red to orange, likely caused by the slight shrinkage of the particle during the polymerisation. The six cross-communication lines are due to the hexagonal packing of the particles in the monolayer as discussed earlier.

The particles were heated in the petri dish to investigate their temperature response. However, these results are somewhat inconsistent. Particles of **CM9-MF1** were found to

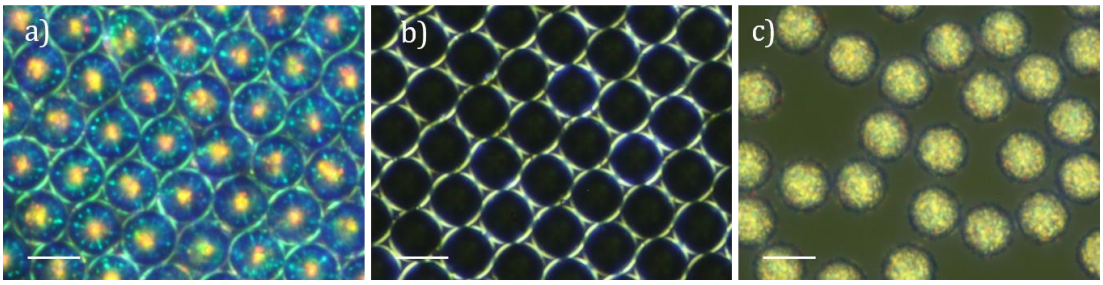

Figure 5.12. Polarised light photomicrographs of chiral nematic polymer particles of **CP9-MF3** in PVA/water in reflection mode at x200 magnification: a) 8 °C, b) 25 °C, c) 15 °C. Scale bar = 30 μm.

lose the selective reflection at ~24 °C, whilst the particles of **CP9-MF2** and **CP9-MF3** transitioned into the isotropic phase above 18 °C (Figure 5.12, b), despite a longer polymerisation time. This may suggest that the particles were not fully polymerised, but the selective reflection was not recovered on cooling (Figure 5.12, c). This is likely because of the lack of crosslinker and therefore memory of the chiral nematic phase's original director orientation. The absence of an aligned texture after isotropisation is similar to the anisometric polymer particles investigated in Chapter 4 and is likely due to the viscosity of the polymer hindering the realignment of the mesogens.

There are very few examples of chiral nematic droplets that have been successfully polymerised whilst maintaining good optical properties due to the difficulty of polymerisation without the introduction of defects. Aβhoff *et al* chose to polymerise a mixture of E7/RM257 and light responsive dopant at low intensity to minimise the defect creation to create partially polymer-stabilised particles but found that the optical texture of the particles was still degraded compared to the droplets.[134] However these droplets were large (~150 μm) and so the surface anchoring of the PVA/water may have been insufficient to maintain the alignment throughout the polymerisation. Noh and Park chose to slow the rate of radical generation in droplets of RMM727 and CB15, successfully reducing the perturbation of the mesogen alignment by programming the UV source to rapidly turn on/off.[136] In contrast, Seo *et al* were able to maintain the alignment of E7/RM257 doped with *R*/*S*-5011 by polymerising at a high intensity (~2000 mW cm^{-2}) for a short time (90s) to create chiral polymer microparticles.

It would be useful to place the elastomer particles in different solvents to enable matching of the refractive indices - leading to coloured suspensions – or to swell to different degrees and elicit an optical response. In order to use the particles in these applications, it is

necessary to first wash out the CB15 to prevent leeching when the particle is swollen. In addition, as found in Chapter 3, when the backbone is strongly coupled to the mesogen with a short spacer, the removal of the chiral dopant leads to a contraction in the pitch of the chiral nematic helix and a restoration of the imprinted achiral nematic elastomers' thermal properties. Therefore, this would lead to chiral imprinted elastomer microparticles with high phase stabilities. Noh and Park reported washing chiral particles with acetone to remove the dopant.[136] However, this proved unsuccessful as the soft particles would stick together and it was not possible in the time available to conduct a proper optimisation of this washing technique. It may be necessary to increase the percentage of crosslinker to harden the particle slightly to improve the resilience of the particles.

5.3.1 Responsive Properties

Following polymerisation, the optical properties of a chiral elastomer particle **CE6-MF2** and the chiral doped elastomer particles **E1D-MF2**, **E1E-MF5** and **E1F-MF1** and their responses to changes in pressure were investigated in a simple experiment.

A sample of chiral elastomer particles from **CE6-MF2** in PVA was transferred to a slide and covered with a glass coverslip. Pressure was exerted onto the particles using a spatula to press down on the coverslip and the response was recorded by POM in reflection mode. As the soft elastic particle is increasingly compressed, the pitch of the chiral nematic helix is also reduced and the selective reflection wavelength of the centre spot shifts from the

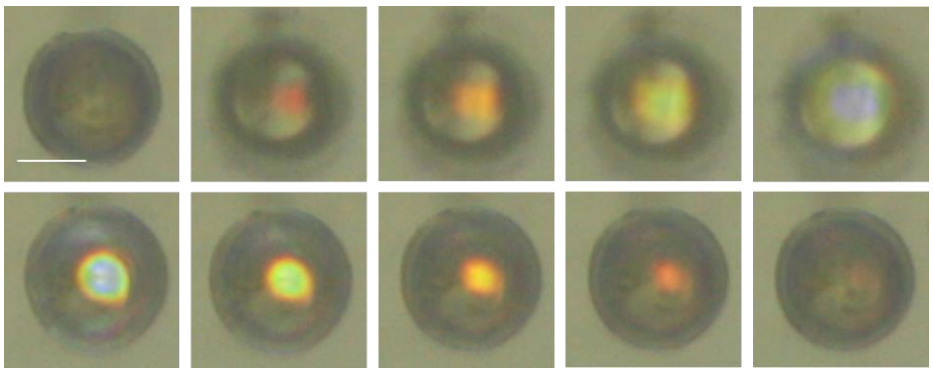

Figure 5.13. Bright field screenshots from a video of an elastomer particle of **CE6-MF2** in PVA/water at 21 °C in reflection mode at x200 magnification. In the top row, the image goes out of focus as pressure is applied to the coverslip for 2 seconds. In the bottom row, the pressure is removed, allowing the pitch to relax over 40 seconds. Scale bar = 25 μm.

infrared to blue (Figure 5.13, top row). On removal of the stress the selective reflection colour disappears out of the visible (Figure 5.13, bottom row). However, this is quite a slow process, taking ~40 seconds at room temperature. The low glass transition temperature of **CE6**, due to the long spacer in the monomer structure, leads to the particle being in its rubbery state at room temperature and as such the polymer chain orientation is deformed in response to the stress. Removal of the stress allows the polymer chains to return to their original orientation due to the memory imparted through crosslinking. Consequently, the helix also relaxes back to its original length.

Using a similar procedure, particles of the doped chiral elastomer **E1F-MF1** in PVA were transferred to a slide and covered with a glass coverslip. Pressure was exerted onto the particles using a spatula to press down on the coverslip and the response was recorded by POM in reflection mode. As the particle was compressed, the selective reflection wavelength shifted from blue to purple (Figure 5.14, a) as the pitch of the chiral nematic helix is also reduced. On removal of the stress, the selective reflection colour returned to blue as the polymer chains returned to their original orientation and the pitch of the chiral

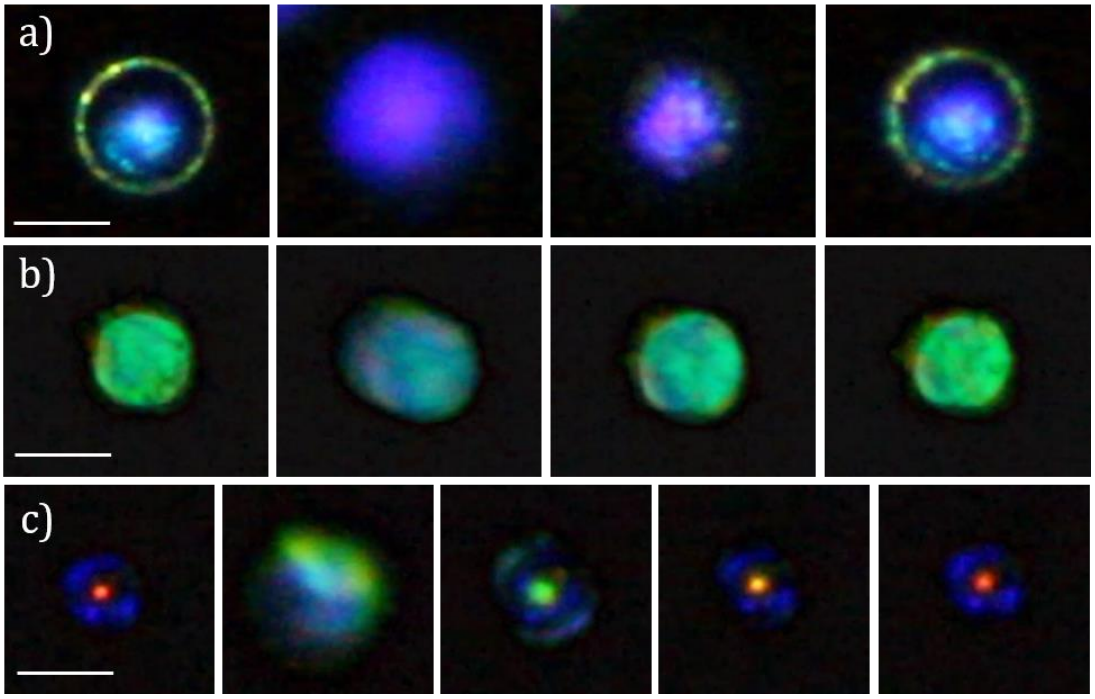

Figure 5.14. Screenshots from videos of elastomer particles in PVA at 21 °C in reflection mode at x200 magnification: a) **E1F-MF1**, b) **E1E-MF5** and c) **E1D-MF2**. Pressure is lightly applied to the coverslip with a spatula, causing the focus to change and compressing the particle which leads to a blue-shift in the selective reflection wavelength. Removal of the stress allows the quick relaxation of the helix to its original length and therefore reflection colour. Scale bar = 20 μm.

nematic helix was restored to its original length. Particles of **E1E-MF5** responded by changing from green to blue (Figure 5.14, b), whilst in particles of **E1D-MF2** (Figure 5.14, c) the central spot changed from red to green. It was found that the particles became stickier with an increasing percentage of CB15 within the elastomer. The high percentages of CB15 swell the elastomer network, lowering the glass transition temperature.

5.4 Conclusion

Using a microfluidic approach, monodisperse chiral nematic droplets with controllable sizes were produced. The droplets were made from monomers containing a chiral centre or through the chiral doping of an achiral monomer and by tuning the chiral dopant concentration these particles were capable of selective reflection of visible light over a wide temperature range. The droplets were photopolymerised to create polymer and elastomer microparticles. Due to the high monodispersity monolayers of the droplets led to the observation of the photonic cross talk between neighbouring droplets was observed and could be retained on polymerisation. In this monomer system a droplet diameter of <37 μm was found to be crucial to ensuring that the surface anchoring from the host solvent was strong enough to force a planar radial alignment within the droplet and leading to a defect-free selective reflection. Polymer particles were found to irreversibly lose the selective reflection colour on heating above the phase transition temperature; a possible application is as a non-reversible optical sensor indicating that a temperature threshold (T_{NI}) has been reached. Chiral doped elastomer particles could reversibly retain their colour on heating and cooling due to their crosslinked network.

The responsiveness of the chiral elastomer particles to pressure was then studied. The changes in colour demonstrate in principle that the particles can be used as pressure sensors, due to the coupling between the polymer backbone and chiral mesogens enabling an optical response. Furthermore, it was shown that optically-clear particles can initially selectively reflect in the infrared but respond in the visible as a function of pressure, paving the way for transparent sensors. Continued development of these particles promises new responsive coatings[217], optical micro-technologies[134], security/anti-forgery[137] and sensing applications.[135,136]

Immediate future work would look to optimise the method of washing the particles. This should lead to imprinted chiral nematic elastomer particles that require lower concentrations of chiral dopant in their production and that possess the thermal

properties of the host achiral nematic elastomer. This would enable the particles to be introduced into alternative solvents without inadvertently leeching the chiral dopant. By closely matching the refractive index of the chiral microparticles and host solvent, tuneable coloured suspensions could be created that correspond to the selective reflection characteristics of the imprinted chiral helix within the particles.

Chapter 6:

Conclusions

6 Conclusions

The overall goal of this research project was to create liquid crystal elastomer microparticles with stimuli-responsive properties, arising from a combination of confinement and surface alignment.

6.1 Material Synthesis

Firstly, to investigate the effect of the monomer structure on the thermal and responsive properties of the particles, a series of laterally attached nematic monomers were synthesised. The length of the peripheral alkyl side chains and the length of the spacer was varied and the effects of these structural changes on the nematic phase properties were studied by DSC and polarised light microscopy. Photo-induced radical polymerisation of the monomers afforded liquid crystal polymers and, with a crosslinking molecule, liquid crystal elastomers as thin films. The nematic phase stability increased on polymerisation, whilst a longer spacer decreased the glass transition temperature, widening the nematic phase range. Also prepared were a series of novel laterally attached chiral nematic acrylate monomers, bearing a chiral pendent chain derived from (*S*)-2-methylbutan-1-ol and achiral alkoxy chains of different length, forming structural isomers. A comparison of the chiral nematic-isotropic phase transition temperatures of the structural isomers suggested an influence related to the position of the chiral centre relative to the central core of the mesogen in the monomers and a larger influence in the polymers. It was found in three of the four isomer pairs studied that positioning the chiral moiety *ortho*, relative to the central core of the mesogen, and away from the spacer, increased the phase stability compared to *meta* placement in the monomers and the polymers. The monomers formed low temperature chiral nematic phases; however, the twisting effect of the chiral group was insufficient to induce a visible selective reflection. Therefore, the synthesis and characterisation of a chiral monomer and polymer with a chiral group derived from (*R*)-2-octanol was also completed; however, despite a visible selective reflection, the thermal phase properties meant that this material was only suitable for use in polymer microparticles and not elastomer microparticles.

6.2 Chiral Imprinting

To overcome the lack of visible selective reflection in the synthesised chiral monomers, a chiral dopant was used to induce a chiral nematic phase in the achiral monomers. The selective reflection wavelength was varied to cover the entire RGB spectrum by varying the concentration of the dopant. Following polymerisation, it was demonstrated that the chiral nematic helix can be imprinted into the nematic elastomer and preserved, even after the removal of the chiral dopant. Further to this, as well as the selective reflection capability of the chiral nematic being retained, the original thermal properties of the achiral elastomer are too, which leads to chiral nematic elastomers with very useful thermal properties. The degree of coupling between the mesogens and backbone was found to be an important factor in the retention of the supramolecular helix as it was necessary to have a short linking spacer for the memory to be recalled after isotropisation. A large blue shift in the selective reflection wavelength was observed on dopant extraction. It was shown that above their glass transition temperature, the elastomers exhibited fast and sensitive responsiveness to pressure. The elastomers also exhibited reversible macroscopic shape changes and related changes in reflection wavelength on heating and cooling.

6.3 Responsive Microparticles

Nematic liquid crystal polymer and elastomer microparticles were created using a microfluidic approach. A coaxially aligned flow-focusing microfluidic device was designed and constructed to produce monodisperse droplets containing a photo-polymerisable mixture. By varying the concentration of the monomer in an organic solvent, the droplet size could be tuned, in addition to that by varying the inner and outer phase flow rates. The droplets were polymerised by UV-initiated radical polymerisation to create aligned soft particles. This alignment was confirmed by the change in shape observed on heating the particles into the isotropic phase. The crosslinked nature of the elastomer was confirmed by the reversibility of the shape change. The temperature that the shape change occurred at could be controlled by minor variation of the monomer structure, whilst the extent of the shape change could be modulated through the degree of coupling between the polymer backbone and the anisotropic mesogens, agreeing with published literature.

Due to the extremely high monodispersity of the emulsions, the droplets and particles self-assembled into monolayers, which is an important pre-requisite for the formation of

tuneable photonic crystals. Using the doped chiral nematic mixtures developed, droplets capable of selective reflection of visible light over a wide temperature range were created by tuning the chiral dopant loadings. The internal alignment was considered radial, consistent with the wider literature, although the quality of the alignment was highly dependent on the droplet size. They displayed photonic cross-communication between droplets, which has been suggested for use in future optical micro-devices. The internal alignment of the droplets, as well as the selective reflection characteristics, was predominantly retained upon polymerisation of the droplets into particles. The particles were exposed to changes in external stimuli, i.e. temperature and pressure, and were found to have good sensitivity and a clear colour change response.

Anisometric nematic polymer and elastomer microparticles with large aspect ratios were also fabricated using only bipolar-aligned droplets and high intensity UV light. The origin of this deformation is unknown but possibly proceeds through a mechanism of anisotropic polymerisation. The particle aspect ratio could be controlled by varying the intensity of the UV light. At low levels of irradiance the particles retain the spherical shape of the original droplets, however at high irradiance the particles adopt a shape with a large aspect ratio. The magnitude of the shape change was found to be very large. One use of these anisotropic particles could be in the development of micro-stirrers that reversibly change shape on heating and cooling.

6.4 Future Work

Whilst the elastomer microparticles in this thesis are already smaller than most in the literature, the particle size could be further reduced and the effect of this investigated. The internal alignment may be slightly better and may lead to an increased shape change response, although the smaller size makes the resolution of the shape change by microscopy potentially harder. The UV photo-deformation of the droplets presents an interesting avenue for creating anisometric particles and further work could look to establish a more rigorous relationship between the intensity of the UV irradiance and the magnitude of the deformation, as well as using theoretical approaches to understand the underlying mechanism of why it occurs. A more thorough analysis of this particular microfluidic system, to elucidate the limits of the flow conditions to produce monodisperse droplets could also be conducted.

To further the research towards the use of the chiral particles as sensors, future work should look to optimise the method of washing the particles. This should lead to imprinted chiral nematic elastomer particles that require lower loadings of chiral dopant in their production and that possess the thermal properties of the host achiral nematic elastomer, as in the thin films. This would enable the particles to be introduced into alternative solvents without inadvertently leeching the chiral dopant. By closely matching the refractive index of the chiral microparticles and host solvent, tuneable coloured suspensions could be created that correspond to the selective reflection characteristics of the imprinted chiral helix within the particles. Alternatively, the structure of the chiral monomer could be subtly modified by removing the oxygen atom from the chiral pendent group, which should shorten the pitch length to an extent that visible or ultraviolet light selective reflection occurs. Subsequently it could be polymerised as a homo-polymer or a co-polymer, whilst retaining useful thermal and optical properties, as was originally envisioned.

Chapter 7:

Experimental

7 Experimental

7.1 - General Information

7.1.1 Chemicals

All chemicals were used as received without further purification. Accurate masses were obtained using a Mettler Toledo XPE205 DeltaRange balance.

7.1.2 Consumables

Analytical TLC was conducted on silica gel 60-F254 plates and analysed using 254 nm UV light. Purification by column chromatography used 60-μm silica gel. Glass cells with homogeneous alignment were purchased from E.H.C Co. Ltd (Japan). Borosilicate hollow round capillaries (VitroCom, I.D. 0.70 mm, 0.87 mm O.D.)) were pulled into micropipettes using a Sutter P30. Ultrapure water was obtained from a Milli-Q Direct 16 water purification system.

7.1.3 Instruments/Analysis Software

Polarised light optical microscopy (POM) was performed on a Zeiss Axio Scope.A1 polarised light microscope and used in conjunction with a Mettler Toledo FP82HT hot stage, controlled with a Mettler Toledo FP90 central processor, and a Canon 700D digital camera. Droplet/particle size and shape change analysis was completed using ImageJ analysis software. Differential scanning calorimetry (DSC) was recorded on a Mettler Toledo DSC1 with STARe acquisition and analysis software and calibrated against an indium standard. Molecular weights and molecular weight distributions were calculated by triple detection Gel permeation chromatography (GPC), using a Shimadzu RIB-20A, Wyatt Technologies miniDAWN Treos and Wyatt Technologies Viscostar II, THF as the mobile phase and calibrated against a polystyrene standard. Scanning electron microscopy (SEM) was performed on a JEOL JSM 7800F, with samples mounted on aluminium stubs and carbon wafers and sputter coated with gold using a Quorum Technologies Q150RES. Samples were vacuum dried beforehand using a Thermo Scientific Vacutherm vacuum oven. Infrared (FTIR) measurements were taken using an

Agilient Technologies Cary 630 FT-IR spectrophotometer. UV-Vis-NIR reflection spectra were obtained using an Avantes Avaspec 2048 spectrophotometer. High-resolution mass spectra (HRMS) were obtained using a Shimadzu LCMS-IT-TOF mass spectrometer in ESI mode. Elemental analysis (EA) was performed using an Elementar vario MICRO cube. Nuclear magnetic resonance (NMR) spectra were obtained using a Bruker AVANCE III (400 MHz) spectrometer and a Bruker Fourier 300 (300 MHz) spectrometer at 298K in $CDCl_3$ and analysed using Topspin analysis software.

7.2 - Monomer Synthesis

7.2.1 Synthesis of Laterally-Attached Acrylate Monomers M1-4

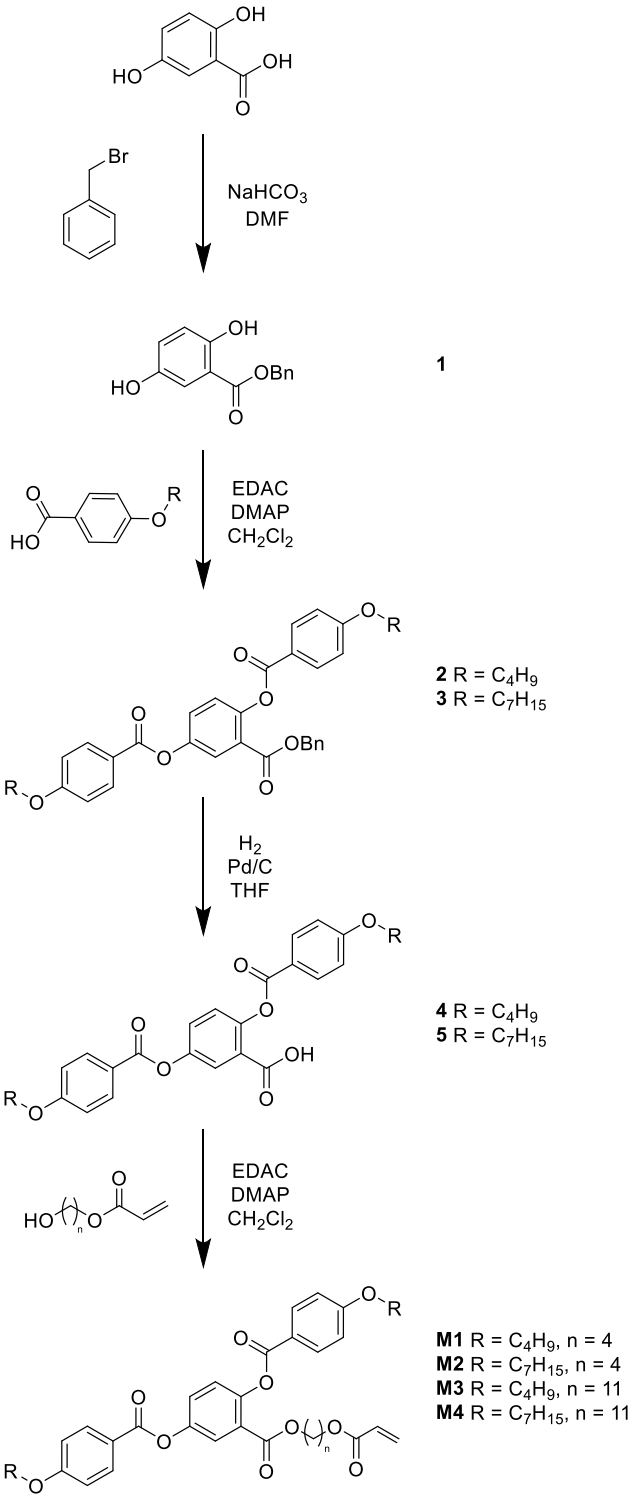

Scheme 7.1. Synthetic route to laterally-attached acrylate monomers **M1-4**.[23,38]

7.2.1.1 Benzyl 2,5-dihydroxybenzoate (1)

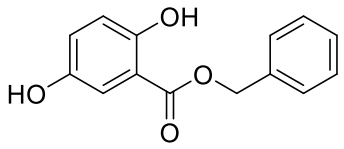

A round bottomed flask was charged with 2,5-dihydroxybenzoic acid (10.11 g, 65.6 mmol), sodium hydrogen carbonate (13.89 g, 165.4 mmol) and stirred for 1 hour at 70°C in dimethylformamide (230 cm^3). Benzyl bromide (11.25 g, 65.8 mmol) was added and stirred at 70°C overnight. The solution was allowed to cool to room temperature, diluted with distilled water (230 cm^3) and extracted 3 times with 1:1 petroleum ether: ethyl acetate (150 cm^3). The organic phase was washed twice with distilled water (450 cm^3) and dried over $MgSO_4$. The crude solid was purified *via* column chromatography on silica gel with diethyl ether as eluting solvent to yield a light orange solid.

Yield: 8.74 g, 35.8 mmol, 55%.

^{1}H NMR ($CDCl_3$) δ (ppm): 4.64 (s (br), 1H, -O**H**), 5.37 (s, 2H, -C**H$_2$**-), 6.88 (d, 1H, *J* = 8.9 Hz, Ar**H**), 7.00 (dd, 1H, *J* = 3.1, 8.9 Hz, Ar**H**), 7.32 (d, 1H, *J* = 3.1 Hz, Ar**H**), 7.34-7.45 (m, 5H, Ar**H**), 10.33 (s (br), 1H, -O**H**).

^{13}C NMR ($CDCl_3$) δ (ppm): 67.24 (**C**-O), 112.31, 114.93, 118.68, 124.33, 128.43, 128.74, 128.85, 135.29 (Ar**C**), 147.86, 156.06 (Ar**C**-O), 169.64 (**C**=O).

FTIR ν (cm^{-1}): 3394 (O-H), 3118 (C-H), 1670 (C=O), 1480 (C=C), 1301, 1208 (C-O).

HRMS (ESI): $C_{14}H_{12}O_4$ calculated $[M-H]^-$ *m/z* 243.0663, measured 243.0662.

Mp: 105-106 °C.

EA (CHNS): calculated C: 68.85%, H: 4.95%, found C: 69.01%, H: 4.98%.

7.2.1.2 Benzyl 2,5-di(4-butyloxybenzoyloxy)benzoate (2)

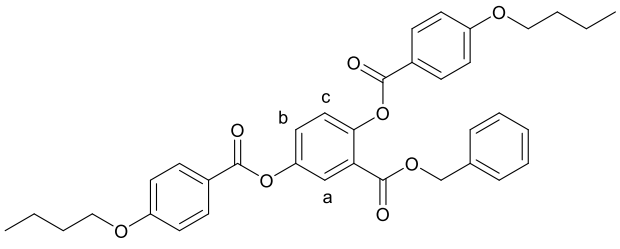

Benzyl 2,5-dihydroxybenzoate (7.00 g, 28.7 mmol), 4-butyloxybenzoic acid (11.15 g, 57.4 mmol), *N*-(3-dimethylaminopropyl)-*N*′-ethylcarbodiimide hydrochloride (11.05 g, 57.6 mmol) and 4-(dimethylamino)pyridine (1.41 g, 11.5 mmol) were added to dichloromethane (600 cm^3) and stirred for 3 days at room temperature. Purification *via* column chromatography on silica gel with dichloromethane: petroleum ether (6:4) as eluting solvent yielded a white solid.

Yield: 13.05 g, 21.9 mmol, 76%.

^{1}H NMR ($CDCl_3$) δ (ppm): 1.00 (t, 3H, *J* = 7.4 Hz, -C**H**$_3$), 1.01 (t, 3H, *J* = 7.4 Hz,-C**H**$_3$), 1.47-1.60 (m, 4H, -C**H**$_2$-), 1.77-1.87 (m, 4H, -C**H**$_2$-), 4.05 (t, 4H, *J* = 6.5 Hz, -OC**H**$_2$-), 5.19 (s, 2H, -OC**H**$_2$Bn), 6.94 (m, 4H, Ar**H**), 7.24 (s, 5H, Ar**H**), 7.26 (d, 1H, *J* = 8.8 Hz, Ar**H**$_c$), 7.46 (dd, 1H, *J* = 2.9, 8.8 Hz, Ar**H**$_b$), 7.90 (d, 1H, *J* = 2.8 Hz, Ar**H**$_a$), 8.10 (m, 4H, Ar**H**).

^{13}C NMR ($CDCl_3$) δ (ppm): 13.80 (-**C**H$_3$), 19.17, 19.19, 31.10, 31.12 (-**C**H$_2$-), 67.20, 67.95, 68.01 (**C**-O), 114.25, 114.35, 120.97, 121.28, 124.59, 125.02, 127.29, 128.16, 128.39, 128.48, 132.36, 132.39, 135.21 (Ar**C**), 148.23, 148.28, 163.48, 163.72 (Ar**C**-O), 163.82, 164.55, 164.92 (**C**=O).

FTIR ν (cm^{-1}): 2956, 2935, 2866 (C-H), 1739, 1724 (C=O), 1605 (C=C), 1245, 1163, 1060 (C-O), 854, 732, 698.

HRMS (ESI): $C_{36}H_{36}O_8$ calculated $[M+Na]^+$ *m/z* 619.2302, measured 619.2285.

Mp: Cr 112 °C N 115 °C Iso.

EA (CHNS): calculated C: 72.47%, H: 6.08%, found C: 72.76%, H: 6.25%.

7.2.1.3 Benzyl 2,5-di(4-heptyloxybenzoyloxy)benzoate (3)

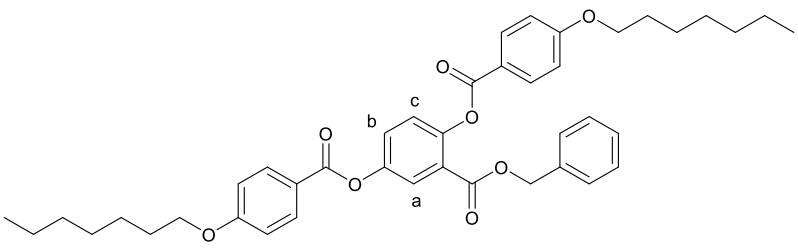

Benzyl 2,5-dihydroxybenzoate (1.86 g, 7.61 mmol), 4-heptyloxybenzoic acid (3.91 g, 16.5 mmol), *N*-(3-dimethylaminopropyl)-*N*′-ethylcarbodiimide hydrochloride (3.20 g, 16.7 mmol) and 4-(dimethylamino)pyridine (0.40 g, 3.28 mmol) were added to dichloromethane (120 cm^3) and stirred for 3 days at room temperature. Purification *via* column chromatography on silica gel with dichloromethane as eluting solvent yielded a white solid.

Yield: 4.94 g, 7.26 mmol, 95%.

^{1}H NMR ($CDCl_3$) δ (ppm): 0.89-0.93 (m, 6H, -C**H**$_3$), 1.29-1.53 (m, 16H, -C**H**$_2$-), 1.79-1.87 (m, 4H, -C**H**$_2$-), 4.05 (t, 4H, *J* = 6.5 Hz, -OC**H**$_2$-), 5.19 (s, 2H, -OC**H**$_2$Bn), 6.94 (m, 4H, Ar**H**), 7.24 (s, 5H, Ar**H**), 7.26 (d, 1H, *J* = 8.8 Hz, Ar**H**$_c$), 7.46 (dd, 1H, *J* = 2.9, 8.8 Hz, Ar**H**$_b$), 7.90 (d, 1H, *J* = 2.9 Hz, Ar**H**$_a$), 8.10 (m, 4H, Ar**H**).

^{13}C NMR ($CDCl_3$) δ (ppm): 14.09 (-**C**H$_3$), 22.61, 25.95, 25.98, 29.03, 29.11 (-**C**H$_2$-), 67.23, 68.31, 68.38 (**C**-O), 114.30, 114.39, 121.01, 121.32, 124.64, 125.04, 125.05, 127.32, 128.20, 128.42, 128.52, 132.39, 132.42, 135.25 (Ar**C**), 148.26, 148.33, 163.51, 163.76 (Ar**C**-O), 163.86, 164.58, 164.95 (**C**=O).

FTIR ν (cm^{-1}): 2926, 2855 (C-H), 1720 (C=O), 1604 (C=C), 1245, 1170, 1068 (C-O).

HRMS (ESI): $C_{42}H_{48}O_8$ calculated $[M+Na]^+$ *m/z* 703.3241, measured 703.3239.

Mp: Cr (N 95.5 °C) 105°C Iso.

EA (CHNS): calculated C: 74.09%, H: 7.11%, found C: 74.11%, H: 7.17%.

7.2.1.4 2,5-Di(4-butyloxybenzoyloxy)benzoic acid (4)

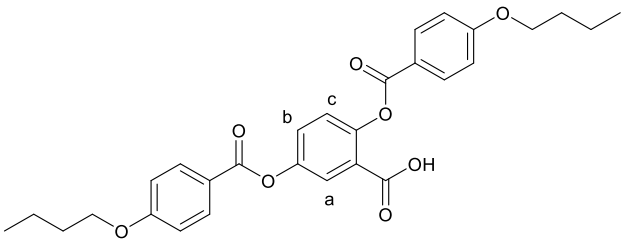

To a stirred solution of tetrahydrofuran (200 cm^3) and ethanol (30 cm^3), benzyl 2,5-di(4'-butyloxybenzoyloxy)benzoate (15.2 g, 25.5 mmol) was added. A spatula tip of palladium on carbon (10%) was added and stirred vigorously. After 3 degas cycles the reaction was left under a hydrogen atmosphere overnight. The reaction mixture was filtered over a celite pad and washed with tetrahydrofuran (150 cm^3) and the solvent removed *in vacuo*. Recrystallisation from ethanol yielded a white solid.

Yield: 10.97 g, 21.7 mmol, 85%.

^{1}H NMR ($CDCl_3$) δ (ppm): 0.99 (t, 3H, *J* = 7.4 Hz, -C**H$_3$**), 1.00 (t, 3H, *J* = 7.4 Hz, -C**H$_3$**), 1.46-1.58 (m, 4H, -C**H$_2$**-), 1.75-1.86 (m, 4H, -C**H$_2$**-), 4.05 (t, 2H, *J* = 6.5 Hz, -C**H$_2$**O-), 4.06 (t, 2H, *J* = 6.5 Hz, -C**H$_2$**O-), 6.96 (m, 4H, Ar**H**), 7.29 (d, 1H, *J* = 8.8 Hz, Ar**H$_c$**), 7.50 (dd, 1H, *J* = 2.9, 8.8 Hz, Ar**H$_b$**), 7.93 (d, 1H, *J* = 2.9 Hz, Ar**H$_a$**), 8.13 (m, 4H, Ar**H**).

^{13}C NMR ($CDCl_3$) δ (ppm): 13.80, 13.81 (-**C**H_3), 19.17, 19.18, 31.10, 31.14 (-**C**H_2-), 67.96, 68.03 (**C**-O), 114.14, 114.28, 114.37, 120.91, 121.27, 123.51, 125.16, 125.45, 128.01, 132.32, 132.38, 132.44 (Ar**C**), 148.25, 148.68, 163.55, 163.75 (Ar**C**-O), 164.51, 164.92, 168.24 (**C**=O).

FTIR ν (cm^{-1}): 2956, 2931, 2872 (C-H), 2648 (O-H), 1728, 1687 (C=O), 1605 (C=C), 1247, 1170 (C-O), 1066, 844, 759.

HRMS (ESI): $C_{29}H_{30}O_8$ calculated $[M+Na]^+$ *m/z* 529.1833, measured 529.1808.

Mp: 173-175 °C.

EA (CHNS): calculated C: 68.76%, H: 5.97%, found C: 68.71%, H: 6.10%.

7.2.1.5 2,5-Di(4-heptyloxybenzoyloxy)benzoic acid (5)

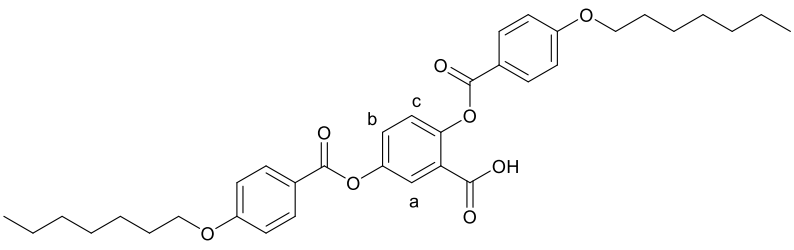

To a stirred solution of tetrahydrofuran (150 cm^3) and ethanol (23 cm^3) benzyl 2,5-di(4'-heptyloxybenzoyloxy)benzoate (5.03 g, 7.39 mmol) was added. A spatula tip of palladium on carbon (10%) was added and stirred vigorously. After 3 degas cycles the reaction was left under a hydrogen atmosphere overnight. The reaction mixture was filtered over a celite pad and washed with tetrahydrofuran (150 cm^3) and the solvent removed *in vacuo*. Recrystallisation from ethanol yielded a white solid.

Yield: 3.99 g, 6.75 mmol, 91%.

^{1}H NMR ($CDCl_3$) δ (ppm): 0.90 (t, 3H, *J* = 6.9 Hz, -C**H$_3$**), 0.91 (t, 3H, *J* = 6.9 Hz, -C**H$_3$**), 1.30-1.53 (m, 16H, -C**H$_2$**-), 1.79-1.86 (m, 4H, -C**H$_2$**-), 4.04 (t, 2H, *J* =6.5 Hz, -C**H$_2$**O-), 4.05 (t, 2H, *J* = 6.5 Hz, -C**H$_2$**O-), 6.97 (m, 4H, Ar**H**), 7.29 (d, 1H, *J* = 8.8 Hz, Ar**H$_c$**), 7.50 (dd, 1H, *J* = 2.9, 8.8 Hz, Ar**H$_b$**), 7.93 (d, 1H, *J* = 2.9 Hz, Ar**H$_a$**), 8.13 (m, 4H, Ar**H**).

^{13}C NMR ($CDCl_3$) δ (ppm): 14.07 (-**C**H_3), 22.59, 25.93, 25.94, 29.03, 29.08, 29.12, 31.74 (-**C**H_2-), 68.29, 68.36 (**C**-O), 114.30, 114.38, 120.90, 121.25, 123.41, 125.17, 125.46, 128.03, 132.38, 132.44, (Ar**C**), 148.27, 148.67, 163.57, 163.76 (Ar**C**-O), 164.51, 164.90, 167.71 (**C**=O).

FTIR ν (cm^{-1}): 2924, 2857 (C-H), 2650 (O-H), 1728, 1687 (C=O), 1605 (C=C), 1247 (C-O).

HRMS (ESI): $C_{35}H_{42}O_8$ calculated $[M+Na]^+$ *m/z* 613.2772, measured 613.2746.

Mp: 164-165 °C.

EA (CHNS): calculated C: 71.17%, H: 7.17%, found C: 71.47%, H: 7.30%.

7.2.1.6 11-Acryloyloxyundecan-1-ol (6)

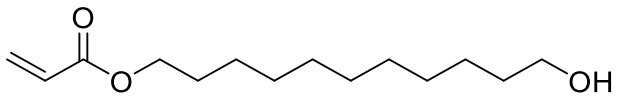

Following a literature procedure[38], to a stirred solution of chloroform/water (20 cm^3/40 cm^3) 11-bromoundecan-1-ol (10.01 g, 40.14 mmol), tetrabutylammonium bromide (3.44 g, 10.66 mmol), sodium acrylate (15.10 g, 160.54 mmol) and a catalytic quantity of butylated hydroxytoluene (acting as a radical scavenger) were added. After refluxing at 110°C for 5 days the solution was allowed to cool before being washed with 2% w/v NaOH (4 x 75 cm^3), distilled water (3 x 75 cm^3) and brine (75 cm^3). The organic layer was dried over $MgSO_4$ and the solvent removed *in vacuo* to yield a clear oil.

Yield: 8.23 g, 33.96 mmol, 85%,

^{1}H NMR ($CDCl_3$) δ (ppm): 1.23-1.42 (m, 16H,-C**H$_2$**-), 1.50-1.72(m, 5H,-C**H$_2$**-), 3.64 (t, 2H, -O**CH$_2$**-), 4.15 (t, 2H, -OC**H$_2$**-), 5.81 (dd, 1H, *J* = 1.6, 10.3 Hz, C**H$_{cis}$**), 6.12 (dd, 1H, *J* = 10.3, 17.4 Hz, C**H=**), 6.40 (dd, 1H, *J* = 1.6, 17.4 Hz, C**H$_{trans}$**)

^{13}C NMR ($CDCl_3$) δ (ppm): 25.75, 25.92, 28.62, 29.23, 29.41, 29.48, 29.56, 32.82 (-**C**H$_2$-), 63.07, 64.74 (**C**-O), 128.67, 130.44 (**C**=**C**), 166.39 (**C**=O).

7.2.1.7 4''-(Acryloyloxybutyl) 2,5-di(4'-butyloxybenzoyloxy)benzoate (M1)

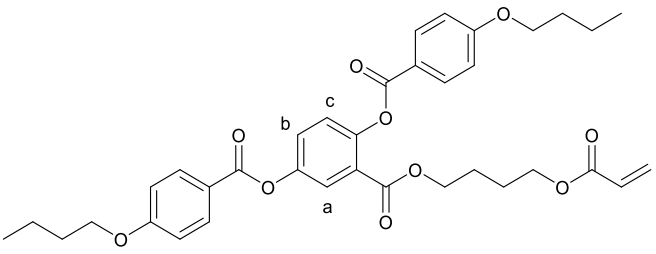

2,5-Di(4'-butyloxybenzoyloxy)benzoic acid (5.34 g, 10.5 mmol), 4-hydroxybutyl acrylate (1.7 cm^3, 12.3 mmol), *N*-(3-dimethylaminopropyl)-*N*′-ethylcarbodiimide hydrochloride (2.22 g, 11.6 mmol) and 4-(dimethylamino)pyridine (0.29 g, 2.37 mmol) were added to dichloromethane (200 cm^3) and stirred for 3 days at room temperature. Purification *via* column chromatography on silica gel with petroleum ether: ethyl acetate (9:1) as eluting solvent yielded a white solid.

Yield: 3.79 g, 6.00 mmol, 57%.

^{1}H NMR ($CDCl_3$) δ (ppm): 1.00 (t, 6H, *J* = 7.4 Hz, -C**H**$_3$), 1.46-1.56 (m, 4H, -C**H**$_2$-), 1.57-1.68 (m, 4H, -C**H**$_2$-), 1.76-1.86 (m, 4H, -C**H**$_2$-), 4.00-4.08 (m, 6H, -C**H**$_2$O-), 4.21 (t, 2H, *J* = 6.4 Hz, -C**H**$_2$O-), 5.80 (dd, 1H, *J* = 1.5, 10.4 Hz, CH**H**$_{cis}$), 6.08 (dd, 1H, *J* = 10.4, 17.4 Hz, C**H**=), 6.37 (dd, 1H, *J* = 1.5, 17.4 Hz, CH**H**$_{trans}$), 6.98 (m, 4H, Ar**H**), 7.26 (d, 1H, *J* = 8.8 Hz, Ar**H**$_c$), 7.46 (dd, 1H, *J* = 2.9, 8.8 Hz, Ar**H**$_b$), 7.89 (d, 1H, *J* = 2.8 Hz, Ar**H**$_a$), 8.15 (m, 4H, Ar**H**).

^{13}C NMR ($CDCl_3$) δ (ppm): 13.80 (-**C**H$_3$), 19.17, 25.11, 31.11 (-**C**H$_2$-), 63.88, 64.87, 68.01, 68.03 (**C**-O), 114.35, 114.37, 120.98, 121.31, 124.76, 124.97, 125.01, 127.20 (Ar**C**), 128.39, 130.65 (**C**=**C**), 132.38, 132.41, 148.08, 148.33 (Ar**C**), 163.65, 163.75, 164.04, 164.58, 164.90, 166.10 (**C**=O).

FTIR ν (cm^{-1}): 2958, 2939, 2872 (C-H), 1720 (C=O), 1605 (C=C), 1247, 1161, 1066 (C-O), 844, 759.

HRMS (ESI): $C_{36}H_{40}O_{10}$ calculated $[M+Na]^+$ *m/z* 655.2514, measured 655.2498.

DSC: Cr 72.9 °C N 85.4 °C Iso.

EA (CHNS): calculated C: 68.34%, H: 6.37%, found C: 68.63%, H: 6.49%.

7.2.1.8 4''-(Acryloyloxybutyl 2,5-di(4'-heptyloxybenzoyloxy)benzoate (M2)

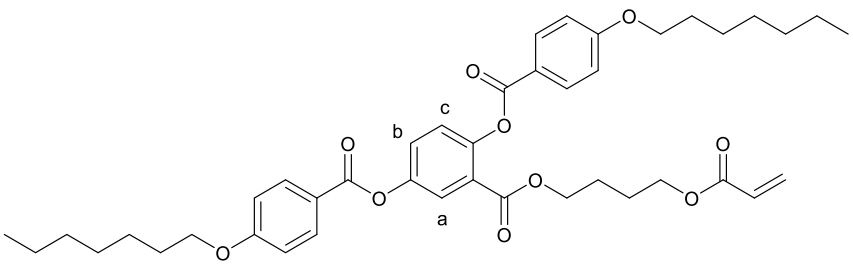

2,5-Di(4'-heptyloxybenzoyloxy)benzoic acid (2.00 g, 3.38 mmol), 4-hydroxybutyl acrylate (0.50 cm^3, 3.61 mmol), *N*-(3-dimethylaminopropyl)-*N*′-ethylcarbodiimide hydrochloride (0.70 g, 3.66 mmol) and 4-(dimethylamino)pyridine (0.089 g, 0.73 mmol) were added to dichloromethane (85 cm^3) and stirred for 3 days at room temperature. Purification *via* column chromatography on silica gel with petroleum ether: ethyl acetate (7:3) as eluting solvent yielded a white solid.

Yield: 1.80 g, 2.51 mmol, 75%.

^{1}H NMR ($CDCl_3$) δ (ppm): 0.91 (t, 6H, *J* = 7 Hz, -C**H$_3$**), 1.28-1.52 (m, 16H, -C**H$_2$**-), 1.57-1.68 (m, 4H, -C**H$_2$**-), 1.79-1.86 (m, 4H, -C**H$_2$**-), 4.01-4.07 (m, 6H, -C**H$_2$**O-), 4.21 (t, 2H, *J* = 6.3 Hz, -C**H$_2$**O-), 5.80 (dd, 1H, *J* = 1.5, 10.3 Hz, C**H**$_{cis}$), 6.08 (dd, 1H, *J* = 10.3, 17.4 Hz, **C**H=), 6.37 (dd, 1H, *J* = 1.5, 17.4 Hz, C**H**$_{trans}$), 6.98 (m, 4H, Ar**H**), 7.26 (d, 1H, *J* = 8.8 Hz, Ar**H$_c$**), 7.46 (dd, 1H, *J* = 2.9, 8.8 Hz, Ar**H$_b$**), 7.89 (d, 1H, *J* = 2.9 Hz, Ar**H$_a$**), 8.15 (m, 4H, Ar**H**).

^{13}C NMR ($CDCl_3$) δ (ppm): 14.09 (-**C**H$_3$), 22.62, 25.15, 25.96, 29.04, 29.12, 31.78 (-**C**H$_2$-), 63.92, 64.89, 68.38, 68.40 (**C**-O), 114.39, 114.42, 121.02, 121.35, 124.80, 125.00, 125.05, 127.23 (Ar**C**), 128.43, 130.65 (**C**=**C**), 132.41, 132.44, 148.12, 148.37 (Ar**C**), 163.69, 163.79, 164.07, 164.61, 164.94 (**C**=O).

FTIR ν (cm^{-1}): 2924, 2857 (C-H), 1733, 1716 (C=O), 1605 (C=C), 1243, 1169, 1064 (C-O).

HRMS (ESI): $C_{42}H_{52}O_{10}$ calculated $[M+Na]^+$ *m/z* 739.3453, measured 739.3448.

DSC: Cr 54.6 °C N 70.8 °C Iso.

EA (CHNS): calculated C: 70.37%, H: 7.31%, found C: 70.68%, H: 7.46%.

7.2.1.9 11''-(Acryloyloxyundecyl) 2,5-di(4'-butyloxybenzoyloxy)benzoate (M3)

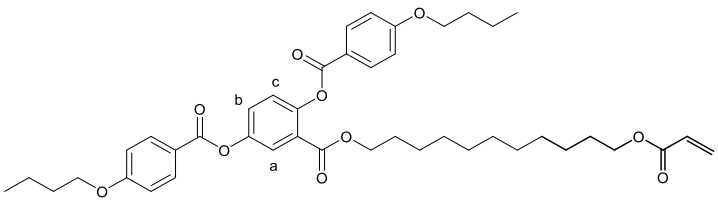

2,5-Di(4'-butyloxybenzoyloxy)benzoic acid (4.63 g, 9.1 mmol), 11-acryloyloxyundecan-1-ol (2.74 g, 11.3 mmol), *N*-(3-dimethylaminopropyl)-*N*′-ethylcarbodiimide hydrochloride (2.64 g, 13.8 mmol) and 4-(dimethylamino)pyridine (0.34 g, 2.8 mmol) were added to dichloromethane (225 cm^3) and stirred for 3 days at room temperature. Purification *via* column chromatography on silica gel with petroleum ether: ethyl acetate (9:1) as eluting solvent yielded a white solid.

Yield: 4.11 g, 5.62 mmol, 62%.

^{1}H NMR ($CDCl_3$) δ (ppm): 1.00 (t, 6H, *J* = 7.4 Hz, -C**H$_3$**), 1.12-1.40 (m, 14H, -C**H$_2$**-), 1.42-1.60 (m, 6H, -C**H$_2$**-), 1.61-1.70 (m, 2H, -C**H$_2$**-),1.76-1.86 (m, 2H, -C**H$_2$**-), 4.05 (t, 2H, *J* = 6.5 Hz, -C**H$_2$**O-), 4.06 (t, 2H, *J* = 6.5 Hz, -C**H$_2$**O-), 4.14 (t, 2H, *J* = 6.8 Hz, -C**H$_2$**O-), 4.15 (t, 2H, *J* = 6.8 Hz, -C**H$_2$**O-), 5.80 (dd, 1H, *J* = 1.4, 10.4 Hz, C**H**$_{cis}$), 6.11 (dd, 1H, *J* = 10.4, 17.3 Hz, C**H**=), 6.39 (dd, 1H, *J* = 1.4, 17.3 Hz, C**H**$_{trans}$), 6.98 (m, 4H, Ar**H**), 7.26 (d, 1H, *J* = 8.8 Hz, Ar**H$_c$**), 7.45 (dd, 1H, *J* = 2.9, 8.7 Hz, Ar**H$_b$**), 7.89 (d, 1H, *J* = 2.9 Hz, Ar**H$_a$**), 8.15 (m, 4H, Ar**H**).

^{13}C NMR ($CDCl_3$) δ (ppm): 13.80 (-**C**H_3), 19.17, 25.79, 25.90, 28.36, 28.59, 29.16, 29.22, 29.36, 29.44, 31.10, 31.11 (-**C**H_2-), 64.68, 65.63, 67.97, 68.02 (**C**-O), 114.28, 114.36, 121.01, 121.43, 124.97, 127.04, (Ar**C**), 128.63, 130.39 (**C**=**C**), 132.36, 132.43, 148.07, 148.29, 163.56, 163.73 (Ar**C**), 164.13, 164.57, 164.90, 166.31 (**C**=O).

FTIR ν (cm^{-1}): 2957, 2917, 2870, 2850 (C-H), 1722, 1703 (C=O), 1605 (C=C), 1247, 1165, 1060 (C-O), 848, 762.

HRMS (ESI): $C_{43}H_{54}O_{10}$ calculated $[M+Na]^+$ *m/z* 753.3609, measured 753.3591.

DSC: Cr 53.2 °C N 69.5 °C Iso.

EA (CHNS): calculated C: 70.66%, H: 7.45%, found C: 70.85%, H: 7.62%.

7.2.1.10 11''-(Acryloyloxyundecyl) 2,5-di(4'-heptyloxybenzoyloxy)benzoate (M4)

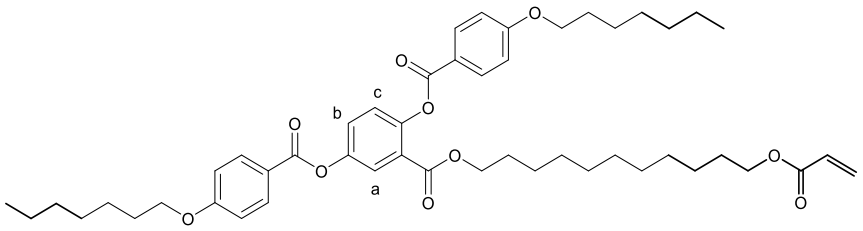

2,5-Di(4'-heptyloxybenzoyloxy)benzoic acid (1.72 g, 2.91 mmol), 11-acryloyloxyundecan-1-ol (0.79 g, 3.26 mmol), *N*-(3-dimethylaminopropyl)-*N*′-ethylcarbodiimide hydrochloride (0.62 g, 3.23 mmol) and 4-(dimethylamino)pyridine (0.079 g, 0.65 mmol) were added to dichloromethane (85 cm^3) and stirred for 3 days at room temperature. Purification *via* column chromatography on silica gel with petroleum ether: ethyl acetate (9:1) as eluting solvent yielded an off-white solid.

Yield: 1.64 g, 2.01 mmol, 69%.

^{1}H NMR ($CDCl_3$) δ (ppm): 0.91 (t, 6H, *J* = 6.8 Hz, -C**H**$_3$), 1.11-1.53 (m, 32H, -C**H**$_2$-), 1.61-1.70 (m, 2H, -C**H**$_2$-), 1.78-1.89 (m, 4H, -C**H**$_2$-), 4.01-4.08 (m, 4H, -C**H**$_2$O-), 4.10-4.18 (m, 4H, -C**H**$_2$O-), 5.80 (dd, 1H, *J* = 1.5, 10.4 Hz, C**H**$_{cis}$), 6.18 (dd, 1H, *J* = 10.4, 17.3 Hz, C**H**=), 6.39 (dd, 1H, *J* = 1.5, 17.3 Hz, C**H**$_{trans}$), 6.98 (m, 4H, Ar**H**), 7.26 (d, 1H, *J* = 8.8 Hz, Ar**H**$_c$), 7.45 (dd, 1H, *J* = 2.9, 8.8 Hz, Ar**H**$_b$), 7.89 (d, 1H, *J* = 2.9 Hz, Ar**H**$_a$), 8.15 (m, 4H, Ar**H**).

^{13}C NMR ($CDCl_3$) δ (ppm): 14.06 (-**C**H_3), 22.58, 25.78, 25.89, 25.92, 28.36, 28.58, 29.00, 29.07, 29.08, 29.15, 29.22, 29.35, 29.43, 31.73 (-**C**H_2-), 64.67, 65.62, 68.29, 68.34 (**C**-O), 114.28, 114.35, 121.00, 121.42, 124.97, 127.03 (Ar**C**), 128.62, 130.38 (**C**=**C**), 132.35, 132.43, 148.06, 148.29, 163.55, 163.72, (Ar**C**), 164.12, 164.56, 164.90, 166.30 (C=**O**).

FTIR ν (cm^{-1}): 2920, 2853 (C-H), 1728 (C=O), 1608 (C=C), 1248, 1167, 1081 (C-O), 844, 759.

HRMS (ESI): $C_{49}H_{66}O_{10}$ calculated $[M+Na]^+$ *m/z* 837.4548, measured 837.4518.

DSC: Cr 41.7 °C N 62.9 °C Iso.

EA (CHNS): calculated C: 72.21%, H: 8.16%, found C: 72.34%, H: 8.32%.

7.2.2 – Synthesis of (*S*)-4-(2-methylbutyloxy)benzoic acid and (*S*)-4-(1-methylheptyloxy)benzoic acid

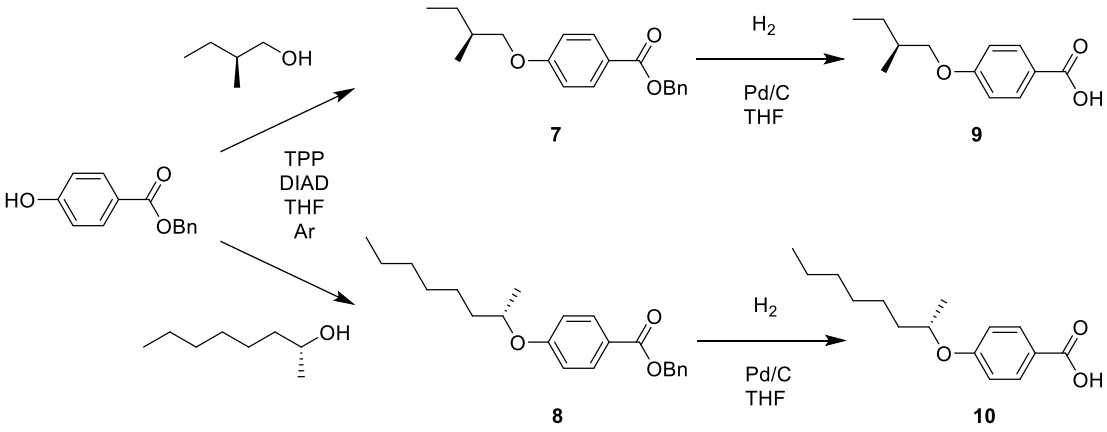

Scheme 7.2. Synthetic route to (*S*)-4-(2-methylbutyloxy)benzoic acid (**9**) and (*S*)-4-(1-methylheptyloxy)benzoic acid (**10**).

7.2.2.1 (*S*)-Benzyl-4-(2-methylbutyloxy)benzoate (7)

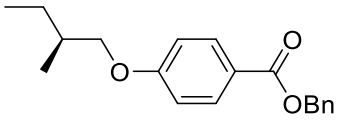

Under an argon atmosphere, triphenylphosphine (9.03 g, 34.4 mmol) was added to dry tetrahydrofuran (250 cm^3) and cooled to 0 °C. Diisopropyl azodicarboxylate (5.70 cm^3, 28.96 mmol) was added dropwise and stirred for 15 minutes during which the colour changed to a milky white. (*S*)-(-)-2-methyl-1-butanol (3.10 cm^3, 28.5 mmol) was added dropwise and stirred for 20 minutes. Benzyl 4-hydroxybenzoate (6.61 g, 28.96 mmol) was then added and the solution stirred for 21 hours at room temperature. The solvent was removed *in vacuo*, leaving a yellow oil and then re-dissolved in a minimum amount of dichloromethane. The crude mixture was filtered through a pad of silica gel, packed using dichloromethane, and washed through with dichloromethane (625 cm^3) then evaporated to ~250 cm^3. The solution was washed sequentially with 15% hydrogen peroxide (250 cm^3), saturated aqueous sodium sulfite (250 cm^3 + 125 cm^3) and brine (250 cm^3), testing for peroxides using Quantofix peroxide test strips after each wash. The final water wash was back-extracted with dichloromethane (170 cm^3) and the organic extracts combined before drying over $MgSO_4$. The dried organic layer was then subjected to a second silica pad and washed through with 250 cm^3 dichloromethane. The solvent was then removed *in vacuo* to yield a colourless oil.

Yield: 7.74g, 25.9 mmol, 91%.

^{1}H NMR ($CDCl_3$) δ (ppm): 0.96 (t, 3H, *J* = 7.4 Hz, -C**H₃**), 1.03 (d, 3H, *J* = 6.8 Hz, -C**H₃**), 1.23-1.35 (m, 1H, -C**H₂**-), 1.52-1.63 (m, 1H, -C**H₂**-), 1.83-1.95 (m, 1H, -C**H**-), 3.76-3.90 (m, 2H, -C**H₂**O-), 5.35 (s, 2H, -OC**H₂**Ar), 6.92 (m, 2H, Ar**H**), 7.32-7.47 (m, 5H, Ar**H**), 8.03 (m, 2H, Ar**H**).

^{13}C NMR ($CDCl_3$) δ (ppm): 11.42, 16.60 (-**C**H_3), 26.20 (-**C**H_2-), 34.74 (-**C**H-), 66.46 (-O**C**H_2-), 73.12 (-O**CH₂**Bn), 114.23, 122.33, 128.20, 128.23, 128.67, 131.82, 136.48 (Ar**C**), 163.36 (Ar**C**-O), 166.36 (**C**=O).

7.2.2.2 (*S*)-Benzyl-4-(1-methylheptyloxy)benzoate (8)

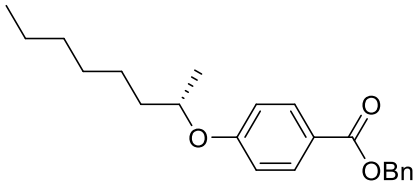

Under an argon atmosphere, triphenylphosphine (3.50 g, 13.3 mmol) was added to dry tetrahydrofuran (125 cm^3) and cooled to 0 °C. Diisopropyl azodicarboxylate (2.2 cm^3, 11.2 mmol) was added dropwise and stirred for 15 minutes during which the colour changed to a milky white. (*R*)-2-octanol (1.8 cm^3, 11.2 mmol) was added dropwise and stirred over 20 minutes. Benzyl 4-hydroxybenzoate (2.59 g, 11.2 mmol) was then added and the solution stirred for 18 hours at room temperature. The solvent was removed *in vacuo* and then re-dissolved in a minimum amount of dichloromethane. The crude mixture was filtered through a pad of silica gel, packed using dichloromethane, and washed through with dichloromethane (300 cm^3) then evaporated to ~125 cm^3. The solution was washed sequentially with 15% hydrogen peroxide (215 cm^3) followed by saturated aqueous sodium sulfite (150 cm^3 + 62 cm^3), testing for peroxides using Quantofix peroxide test strips after each wash. The final water wash was back-extracted with dichloromethane (85 cm^3) and the organic extracts combined before drying over $MgSO_4$. The dried organic layer was then subjected to a second silica pad and washed through with 250 cm^3 dichloromethane. The solvent was then removed *in vacuo* to yield a colourless oil.

Yield: 2.7 g, 7.9 mmol, 71%.

^{1}H NMR ($CDCl_3$) δ (ppm): 0.89 (t, 3H, *J* = 7.0 Hz, -C**H$_3$**), 1.32 (d, 3H, *J* = 6.0 Hz, -C**H$_3$**), 1.23-1.50 (m, 8H, -C**H$_2$**-), 1.54-1.64 (m, 1H, -C**H$_2$**-), 1.70-1.81 (m, 1H, -C**H$_2$**-), 4.40 -4.50 (m, 1H, -C**H**O-), 5.35 (s, 2H, -OC**H$_2$**Ar), 6.89 (m, 2H, Ar**H**), 7.31-7.47 (m, 5H, Ar**H**), 8.02 (m, 2H, Ar**H**).

^{13}C NMR ($CDCl_3$) δ (ppm): 14.03, 19.56 (-**C**H$_3$), 22.55, 25.39 29.18, 31.73, 36.28 (-**C**H$_2$-), 66.27 (-O**CH$_2$**Bn), 73.99 (-O**C**H-), 115.01, 121.97, 128.03, 128.06, 128.51, 131.74, 136.37 (Ar**C**), 162.26 (Ar**C**-O), 166.18 (**C**=O).

FTIR ν (cm^{-1}): 2930, 2857 (C-H), 1711 (C=O), 1605 (C=C), 1257 (C-O), 1165, 1096 (C-O), 768, 695.

HRMS (ESI): $C_{22}H_{28}O_3$ calculated $[M+H]^+$ *m/z* 341.2117, measured 355.2253.

EA (CHNS): calculated C: 77.61%, H: 8.29%, found C: 77.47%, H: 8.54%.

7.2.2.3 (*S*)-4-(2-methylbutyloxy)benzoic acid (9)

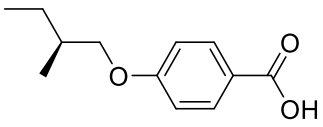

To a stirred solution of tetrahydrofuran (100 cm^3) and ethanol (15 cm^3) (*S*)-benzyl-4-(2-methylbutyloxy)benzoate (4.06 g, 13.6 mmol) was added. A spatula tip of palladium on carbon (10%) was added and stirred vigorously. After 3 degas cycles the reaction was left under a hydrogen atmosphere overnight. The reaction mixture was filtered over a celite pad and washed with tetrahydrofuran (100 cm^3) and the solvent removed *in vacuo*. Purification *via* column chromatography on silica gel with dichloromethane as eluting solvent yielded a white solid.

Yield: 2.81 g, 13.5 mmol, 99%.

^{1}H NMR ($CDCl_3$) δ (ppm): 0.96 (t, 3H, *J* = 7.5 Hz, -C**H$_3$**), 1.03 (d, 3H, *J* = 6.7 Hz, -C**H$_3$**), 1.23-1.35 (m, 1H, -C**H$_2$**-), 1.52-1.63 (m, 1H, -C**H$_2$**-), 1.83-1.95 (m, 1H, -C**H**-), 3.78-3.92 (m, 2H, -C**H$_2$**O-), 6.94 (m, 2H, Ar**H**), 8.06 (m, 2H, Ar**H**).

^{13}C NMR ($CDCl_3$) δ (ppm): 11.44, 16.62 (-**C**H_3), 26.22 (-**C**H_2-), 34.76 (-**C**H-), 73.21 (-O**C**H_2-), 114.36, 121.48, 132.47 (Ar**C**), 164.01 (Ar**C**-O), 172.10 (**C**=O).

FTIR ν (cm^{-1}): 2961 (O-H), 2920, 2865, 2658, 2540 (C-H), 1668 (C=O), 1601 (C=C), 1256 (C-O), 1169 (C-O), 1026, 956, 848, 773.

HRMS (ESI): $C_{12}H_{16}O_3$ calculated $[M-H]^-$ *m/z* 207.1027, measured 207.1027.

Mp: 105-108 °C.

EA (CHNS): calculated C: 69.21%, H: 7.74%, found C: 69.23%, H: 7.87%.

7.2.2.4 (*S*)-4-(1-methylheptyloxy)benzoic acid (10)

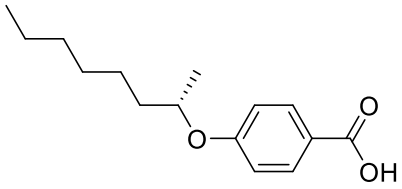

To a stirred solution of tetrahydrofuran (100 cm^3) and ethanol (15 cm^3) (*S*)-benzyl-4-(1-methylheptyloxy)benzoate (2.60 g, 7.65 mmol) was added. A spatula tip of palladium on carbon (10%) was added and stirred vigorously. After 3 degas cycles the reaction was left under a hydrogen atmosphere overnight. The reaction mixture was filtered over a celite pad, washed with tetrahydrofuran (400 cm^3) and the solvent removed *in vacuo* to yield a white solid.

Yield: 1.78 g, 7.1 mmol, 93%.

^{1}H NMR ($CDCl_3$) δ (ppm): 0.88 (t, 3H, *J* = 7.0 Hz, -C**H$_3$**), 1.33 (d, 3H, *J* = 6.1 Hz, -C**H$_3$**), 1.23-1.50 (m, 8H, -C**H$_2$**-), 1.54-1.65 (m, 1H, -C**H$_2$**-), 1.71-1.81 (m, 1H, -C**H$_2$**-), 4.42-4.51 (m, 1H, -C**H**O-), 6.91 (m, 2H, Ar**H**), 8.04 (m, 2H, Ar**H**).

^{13}C NMR ($CDCl_3$) δ (ppm): 14.05, 19.59 (-**C**H_3), 22.57, 25.42, 29.20, 30.31, 31.75, 36.31 (-**C**H_2-), 74.10 (-O**C**H-), 115.07, 121.02, 132.37 (Ar**C**), 162.91 (Ar**C**-O), 171.52 (**C**=O).

FTIR ν (cm^{-1}): 2952, 2924, 2853 (C-H), 2661, 2543 (O-H), 1670 (C=O), 1605 (C=C), 1252, 1172 (C-O), 933, 848, 777.

HRMS (ESI): $C_{15}H_{22}O_3$ calculated $[M-H]^-$ *m/z* 249.1496, measured 249.1495.

Mp: 65-67 °C.

EA (CHNS): calculated C: 71.97%, H: 8.86%, found C: 71.94%, H: 9.15%.

7.2.3 – Synthesis of Laterally-Attached Chiral Acrylate Monomer CM3

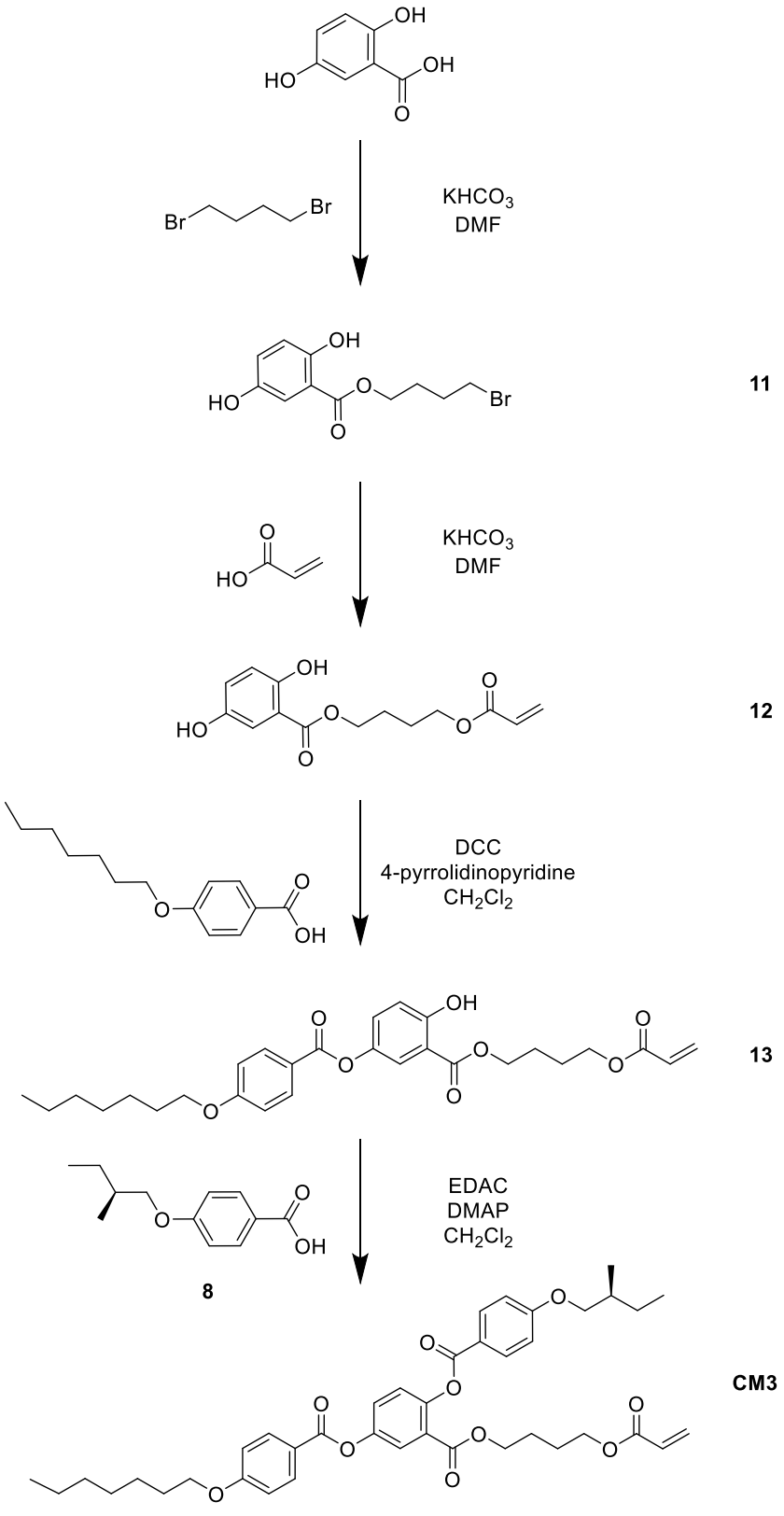

Scheme 7.3. Synthetic route to chiral acrylate monomer **CM3**.

7.2.3.1 4'-Bromobutyl 2,5-dihydroxybenzoate (11)

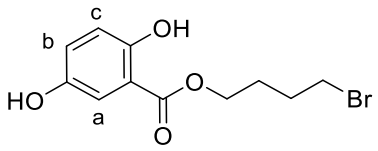

To a stirred solution of 2,5-dihydroxybenzoic acid (15.5 g, 100.6 mmol) in dimethylformamide (250 cm^3) was added 1,4-dibromobutane (49.5 cm^3, 414 mmol) and potassium hydrogen carbonate (26.8 g, 268 mmol). The reaction mixture solution was heated to 70 °C for 24 hours then left to cool to room temperature. The reaction was quenched with water (500 cm^3) and extracted twice with dichloromethane (250 cm^3). The combined organic extracts were subsequently washed ten times with distilled water (250 cm^3) to remove the residual DMF and dried over $MgSO_4$. Solvent was removed *in vacuo* to afford an orange oil that crystallised on cooling. Purification *via* column chromatography on silica gel with dichloromethane yielded a white powder.

Yield: 9.81 g, 33.9 mmol, 34%.

^{1}H NMR ($CDCl_3$) δ (ppm): 1.92-2.07 (m, 4H, -C**H$_2$**-), 3.48 (t, 2H, *J* = 6.4 Hz, -C**H$_2$**Br), 4.38 (t, 2H, *J* = 6.1 Hz, -C**H$_2$**O-), 4.63 (s (br), 1H, -OH), 6.89 (d, 1H, *J* = 9.3 Hz, Ar**H$_c$**), 7.02 (dd, 1H, *J* = 3.2, 9.3 Hz, Ar**H$_b$**), 7.28 (d, 1H, *J* = 3.2 Hz, Ar**H$_a$**), 10.33 (s, 1H, -O**H**).

^{13}C NMR ($CDCl_3$) δ (ppm): 27.21, 29.23, (-**C**H_2-) 32.95 (**C**-Br), 64.53 (**C**-O), 112.21, 114.70, 118.56, 124.19 (Ar**C**), 147.78, 155.85 (Ar**C**-O), 169.73 (**C**=O).

FTIR ν (cm^{-1}): 3355 (O-H), 2920 (C-H), 1668 (C=O), 1614, 1333, 1198 (C-O), 783 (C-Br).

HRMS (ESI): $C_{22}H_{26}Br_2O_8$ calculated $[M-H]^-$ *m/z* 574.9922, measured 574.9927.

Mp: 54-56 °C.

EA (CHNS): calculated C: 45.70%, H: 4.53%, found C: 45.94%, H: 4.69%.

7.2.3.2 4'-(Acryloyloxybutyl) 2,5-dihydroxybenzoate (12)

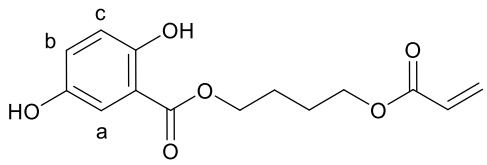

To a stirred solution of 4'-bromobutyl 2,5-dihydroxybenzoate (7.86 g, 27.2 mmol) in dimethylformamide (135 cm^3) was added acrylic acid (6.70 cm^3, 97.8 mmol) and potassium hydrogen carbonate (4.19 g, 41.9 mmol). The reaction mixture was heated to 50 °C for 24 hours, then left to cool to room temperature. The reaction was quenched with water (140 cm^3) and extracted twice with dichloromethane (70 cm^3). The combined organic extracts were subsequently washed five times with distilled water (70 cm^3) to remove the residual DMF and dried over $MgSO_4$. Solvent was removed *in vacuo* to afford an orange solid. Purification *via* column chromatography on silica gel with petroleum ether: diethyl ether (9:1 gradually increasing to 1:3) yielded a white powder.

Yield: 7.33 g, 26.2 mmol, 96%.

^{1}H NMR ($CDCl_3$) δ (ppm): 1.85-1.92 (m, 4H, -C**H$_2$**-), 3.38 (t, 2H, *J* = 6.2 Hz, -C**H$_2$**O-), 4.29 (t, 2H, *J* = 6.3 Hz, -C**H$_2$**O-), 5.09 (s (br), 1H, -O**H**), 5.85 (dd, 1H, *J* = 1.5, 10.5 Hz, C**H$_{cis}$**), 6.14 (dd, 1H, *J* = 10.5, 17.4 Hz, C**H**=), 6.43 (dd, 1H, *J* = 1.5, 17.4 Hz, C**H$_{trans}$**), 6.88 (d, 1H, *J* = 9.3 Hz, Ar**H$_c$**), 7.02 (dd, 1H, *J* = 3.2, 9.3 Hz, Ar**H$_b$**), 7.31 (d, 1H, *J* = 3.2 Hz, Ar**H$_a$**), 10.29 (s, 1H, -O**H**).

^{13}C NMR ($CDCl_3$) δ (ppm): 25.12, 25.50 (-**C**H_2-), 64.31, 65.01 (**C**-O), 112.14, 114.63, 118.53, 124.18 (Ar**C**), 128.23, 131.31 (**C**=**C**), 148.10, 155.72 (Ar**C**-O), 166.77, 169.72 (**C**=O).

FTIR ν (cm^{-1}): 3362 (O-H), 3222, 2973 (C-H), 1702, 1681 (C=O), 1616 (C=C), 1221 (C-O).

HRMS (ESI): $C_{14}H_{16}O_6$ calculated $[M+H]^+$ *m/z* 281.1020, measured 281.1002.

Mp: 72-73 °C.

EA (CHNS): calculated C: 60.00%, H: 5.75%, found C: 60.21%, H: 5.91%.

7.2.3.3 4''-(Acryloyloxybutyl) 2-hydroxy-5-(4'-heptyloxybenzoyloxy)benzoate (13)

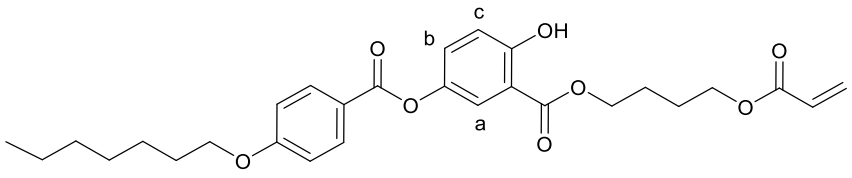

A mixture of 4'-(acryloyloxybutyl) 2,5-dihydroxybenzoate (3.17 g, 11.3 mmol), 4-heptyloxybenzoic acid (2.69 g, 11.38 mmol), N,N'-dicyclohexylcarbodiimide (7.19 g, 34.9 mmol) and 4-pyrrolidinopyridine (0.53 g, 3.58 mmol) in dichloromethane (120 cm^3) was stirred for 24 h at room temperature. The N,N'-dicyclohexylurea was filtered and the filtrate washed sequentially with water (175 cm^3), 5% acetic acid (175 cm^3) and water (175 cm^3). The organic layer was dried over $MgSO_4$ and evaporated *in vacuo*. The crude solid was subjected to column chromatography on silica gel with dichloromethane as eluting solvent to yield a viscous colourless oil.

Yield: 1.78 g, 3.57 mmol, 32%.

^{1}H NMR ($CDCl_3$) δ (ppm): 0.90 (t, 3H, *J* = 6.3 Hz, -C**H$_3$**), 1.28-1.52 (m, 8H, -C**H$_2$**-), 1.79-1.91 (m, 6H, -C**H$_2$**-), 4.05 (t, 2H, *J* = 6.6 Hz, -C**H$_2$**O-), 4.22 (t, 2H, *J* = 6.2 Hz, -C**H$_2$**O-), 4.39 (t, 2H, *J* = 6.2 Hz, -C**H$_2$**O-), 5.81 (dd, 1H, *J* = 1.5, 10.5 Hz, CH**H$_{cis}$**), 6.11 (dd, 1H, *J* = 10.5, 17.4 Hz, C**H**=), 6.39 (dd, 1H, *J* = 1.5, 17.4 Hz CH**H$_{trans}$**), 6.97 (m, AA'XX', 2H, Ar**H**), 7.03 (d, 1H, *J* = 9.0 Hz, Ar**H$_c$**), 7.31 (dd, 1H, *J* = 2.8, 9.0 Hz, Ar**H$_b$**), 7.65 (d, 1H, *J* = 2.8 Hz, Ar**H$_a$**), 8.13 (m, AA'XX', 2H, Ar**H**), 10.72 (s (br), 1H, -O**H**).

^{13}C NMR ($CDCl_3$) δ (ppm): 14.09 (-**C**H_3), 22.61, 25.28, 25.31, 25.96, 29.04, 29.11, 31.77 (-**C**H_2-), 63.85, 65.10, 68.38 (**C**-O), 112.44, 114.36, 118.53, 121.22, 122.24 (Ar**C**), 128.35 (**C**=**C**), 129.78 (Ar**C**), 130.83 (**C**=**C**), 132.31 (Ar**C**), 142.75, 159.44, 163.68 (Ar**C**-O), 165.22, 168.18, 169.58 (**C**=O).

FTIR (FTR) ν (cm^{-1}): 2928 (O-H), 2857, 1724, 1675 (C=O), 1604 (C=C), 1239, 1163 (C-O).

HRMS (ESI): $C_{28}H_{34}O_8$ calculated $[M+H]^+$ *m/z* 499.2326, measured 499.2304.

EA (CHNS): calculated C: 67.45%, H: 6.87%, found C: 67.48%, H: 7.06%.

7.2.3.4 (*S*)-4''-(Acryloyloxybutyl) 2-(4'-(2-methylbutyloxy)benzoyloxy)-5-(4'-heptyloxybenzoyloxy)benzoate (CM3)

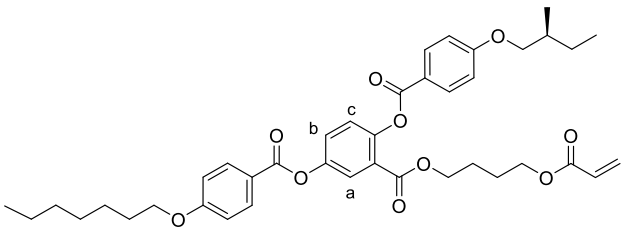

To dichloromethane (50cm^3) were added 4'-(acryloyloxybutyl)-2-hydroxy-5-(4'-heptyloxybenzoyloxy)benzoate (1.26 g, 2.53 mmol), (*S*)-4-(2-methylbutyloxy)benzoic acid (0.67 g, 3.21 mmol), N-(3-dimethylaminopropyl)-N′-ethylcarbodiimide hydrochloride (0.56 g, 2.92 mmol) and 4-(dimethylamino)pyridine (0.063 g, 0.51 mmol) and stirred for 3 days at room temperature. The organic layer was washed with water (3 x 100 cm^3) and dried over $MgSO_4$. Purification *via* column chromatography on silica gel with dichloromethane as eluting solvent afforded a white solid.

Yield: 1.59 g, 2.31 mmol, 91%.

^{1}H NMR ($CDCl_3$) δ (ppm): 0.91 (t, 3H, *J* = 6.9 Hz, -C**H$_3$**), 0.97 (t, 3H, *J* = 7.4 Hz, -C**H$_3$**), 1.05 (d, 3H, *J* = 6.8 Hz, -C**H$_3$**), 1.25-1.70 (m, 14H, -C**H$_2$**-), 1.79-1.96 (m, 3H, -C**H$_2$**-), 3.81-3.93 (m, 2H, -C**H$_2$**O-), 4.02-4.07 (m, 4H, -C**H$_2$**O-), 4.21 (t, 2H, *J* = 6.5 Hz, -C**H$_2$**O-), 5.80 (dd, 1H, *J* = 1.5, 10.4 Hz, C**H**=), 6.08 (dd, 1H, *J* = 10.4, 17.3 Hz, C**H**=), 6.36 (dd, 1H, *J* = 1.5, 17.4 Hz, C**H**=), 6.98 (m, 4H, Ar**H**), 7.27 (d, 1H, *J* = 8.7 Hz, Ar**H$_c$**), 7.46 (dd, 1H, *J* = 2.9, 8.7 Hz, Ar**H$_b$**), 7.89 (d, 1H, *J* = 2.9 Hz, Ar**H$_a$**), 8.15 (m, 4H, Ar**H**).

^{13}C NMR ($CDCl_3$) δ (ppm): 11.31, 14.09, 16.48 (-**C**H$_3$), 22.61, 22.15, 25.96, 26.10, 29.04, 29.11, 31.76, 34.65 (-**C**H$_2$-), 63.90, 64.88, 68.39, 73.14 (**C**-O), 114.41, 121.03, 121.33, 124.81, 124.99, 125.04, 127.21 (Ar**C**), 128.44, 130.64 (**C**=**C**), 132.40, 132.43 (Ar**C**), 148.12, 148.37 (Ar**C**-O), 163.79, 163.85, 164.05, 164.59, 164.93, 166.11 (**C**=O).

DSC: Cr 80.5 °C (N* 51.9 °C) Iso.

FTIR ν (cm^{-1}): 2963, 2928, 2857(C-H), 1731, 1718 (C=O), 1605 (C=C), 1243, 1165, 1066 (C-O).

HRMS (ESI): $C_{40}H_{48}O_{10}$ calculated $[M+Na]^+$ *m/z* 711.3140, measured 711.3113.

EA (CHNS): calculated C: 69.75%, H: 7.02%, found C: 69.82%, H: 7.18%.

7.2.4 – Synthesis of Laterally-Attached Chiral Acrylate Monomers CM1-2, CM4-9

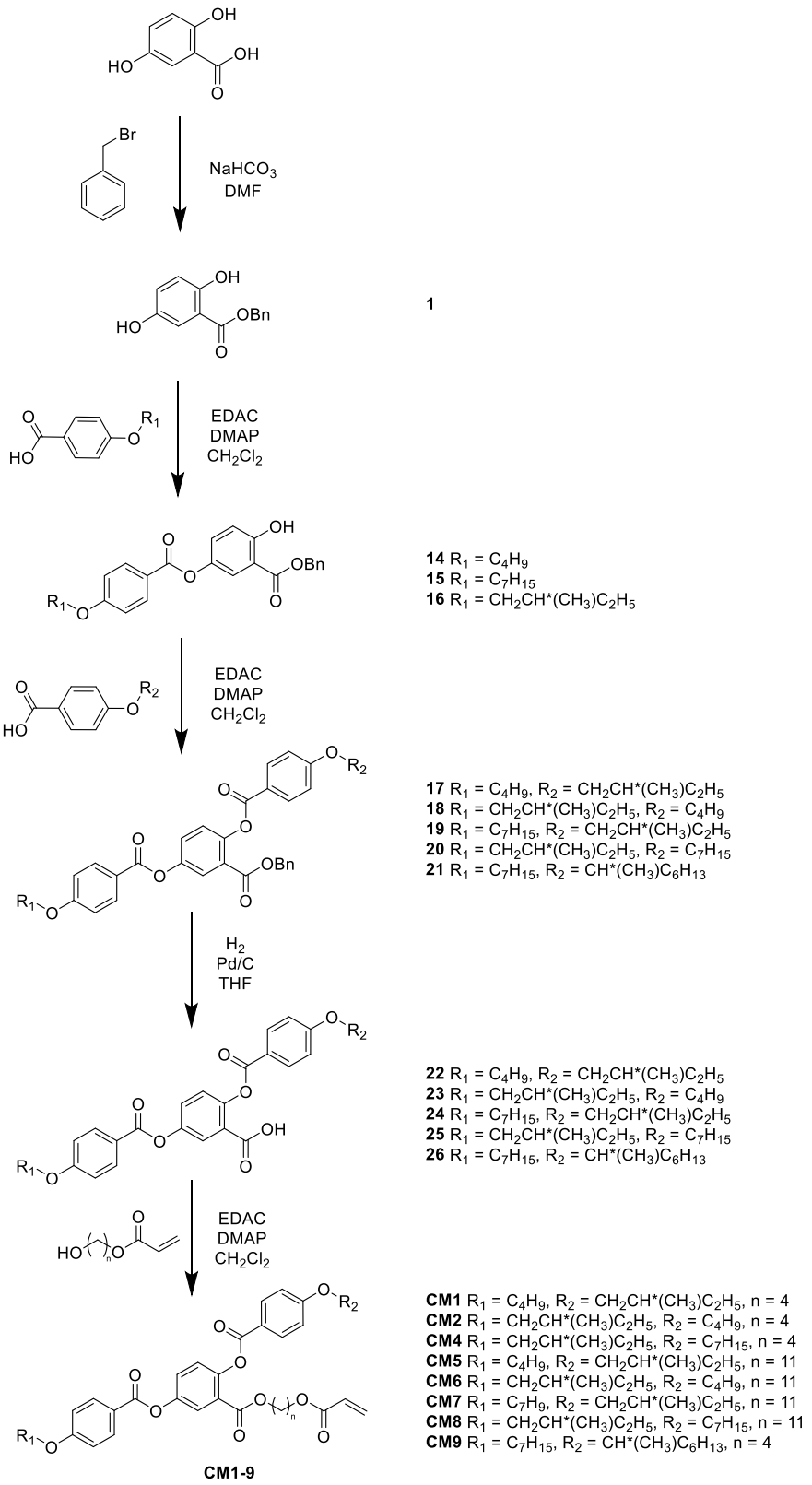

Scheme 7.4. Synthetic route to chiral acrylate monomers **CM1-2, CM4-9**.

7.2.4.1 Benzyl-2-hydroxy-5-((4'-butyloxy)benzoyloxy)benzoate (14)

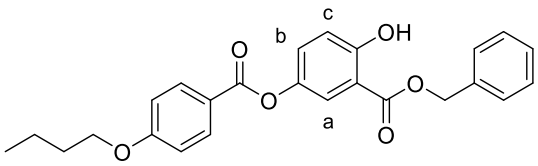

Benzyl 2,5-dihydroxybenzoate (3.25 g, 13.32 mmol), 4-butyloxybenzoic acid (2.56 g, 13.18 mmol), N-(3-dimethylaminopropyl)-N′-ethylcarbodiimide hydrochloride (3.06 g, 15.94 mmol) and 4-(dimethylamino)pyridine (0.38 g, 3.14 mmol) were added to dichloromethane (200 cm^3) and stirred for 3 days at room temperature. Purification *via* column chromatography on silica gel with dichloromethane as eluting solvent yielded a white solid.

Yield: 3.94 g, 9.38 mmol, 71%.

^{1}H NMR ($CDCl_3$) δ (ppm): 1.00 (t, 3H, *J* = 7.4 Hz, -C**H$_3$**), 1.46-1.58 (m, 2H, -C**H$_2$**-), 1.75-1.86 (m, 2H, -C**H$_2$**-), 4.05 (t, 2H, *J* = 6.5 Hz, -OC**H$_2$**-), 5.38 (s, 2H, -OC**H$_2$**Bn), 6.96 (m, 2H, Ar**H**), 7.03 (d, 1H, *J* = 9.0 Hz, Ar**H$_c$**), 7.30 (dd, 1H, *J* = 2.9, 9.0 Hz, Ar**H$_b$**), 7.33-7.46 (m, 5H, Ar**H**), 7.68 (d, 1H, *J* = 2.8 Hz, Ar**H$_a$**), 8.10 (m, 2H, Ar**H**), 10.69 (s (br), 1H, -O**H**).

^{13}C NMR ($CDCl_3$) δ (ppm): 13.79 (-**C**H_3), 19.16, 31.06 (-**C**H_2-), 67.26, 67.99 (**C**-O), 112.37, 114.28, 118.46, 121.14, 122.33, 128.34, 128.69, 129.86, 132.24, 132.41, 134.97 (Ar**C**), 142.71, 159.44, 163.61 (Ar**C**-O), 165.13, 169.36 (**C**=O).

FTIR ν (cm^{-1}): 3155 (O-H), 2965, 2939, 2873 (C-H), 1731, 1675 (C=O), 1606 (C=C), 1474, 1243, 1189, 1165, 1064, 1001 (C-O), 758, 691.

HRMS (ESI): $C_{25}H_{24}O_6$ calculated $[M+Na]^+$ *m/z* 443.1471, measured 443.1436.

Mp: 89-91 °C.

EA (CHNS): calculated C: 71.42%, H: 5.75%, found C: 71.52%, H: 5.84%.

7.2.4.2 Benzyl-2-(hydroxy)-5-(4'-heptyloxy)benzoyloxy)benzoate (15)

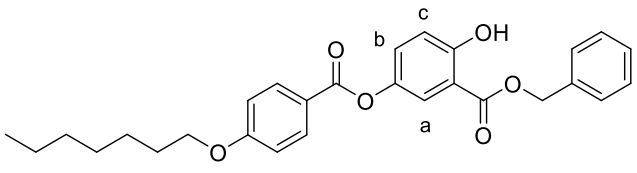

Benzyl 2,5-dihydroxybenzoate (1.44 g, 5.88 mmol), 4-heptyloxybenzoic acid (1.39 g, 5.90 mmol), N-(3-dimethylaminopropyl)-N′-ethylcarbodiimide hydrochloride (1.36 g, 7.09 mmol) and 4-(dimethylamino)pyridine (0.17 g, 1.41 mmol) were added to dichloromethane (100 cm^3) and stirred for 3 days at room temperature. Purification *via* column chromatography on silica gel with dichloromethane as eluting solvent yielded a white solid.

Yield: 2.38 g, 5.14 mmol, 87%.

^{1}H NMR ($CDCl_3$) δ (ppm): 0.91 (t, 3H, *J* = 6.8 Hz, -C**H$_3$**), 1.26-1.42 (m, 6H, -C**H$_2$**-), 1.42-1.52 (m, 2H, -C**H$_2$**-), 1.78-1.86 (m, 2H, -C**H$_2$**-), 4.04 (t, 2H, -OC**H$_2$**-), 5.38 (s, 2H, -OC**H$_2$**Bn), 6.96 (m, 2H, Ar**H**), 7.03 (d, 1H, *J* = 9.0 Hz, Ar**H$_c$**), 7.31 (dd, 1H, *J* = 2.9, 9.0 Hz, Ar**H$_b$**), 7.33-7.46 (m, 5H, Ar**H**), 7.69 (d, 1H, *J* = 2.9 Hz, Ar**H$_a$**), 8.11 (m, 2H, Ar**H**), 10.69 (s (br), 1H, -O**H**).

^{13}C NMR ($CDCl_3$) δ (ppm): 14.21 (-**C**H_3), 22.74, 26.08, 29.16, 29.23, 31.89 (-**C**H_2-), 67.43, 68.49 (**C**-O), 112.45, 114.45, 118.63, 121.30, 122.50, 128.61, 128.78, 128.86, 130.03, 132.41, 135.14 (Ar**C**), 142.88, 159.60, 163.77 (Ar**C**-O), 165.31, 169.53 (**C**=O).

FTIR ν (cm^{-1}): 3204 (O-H), 2915, 2853 (C-H), 1735, 1689 (C=O), 1605 (C=C), 1252, 1239, 1165, 1060 (C-O), 732.

HRMS (ESI): $C_{28}H_{30}O_6$ calculated $[M+Na]^+$ *m/z* 485.1935, measured 485.1923.

Mp: 75-78 °C.

EA (CHNS): calculated C: 72.71%, H: 6.54%, found C: 73.03%, H: 6.69%.

7.2.4.3 (*S*)-Benzyl-2-hydroxy-5-((4'-(2-methylbutyloxy)benzoyloxy)benzoate (16)

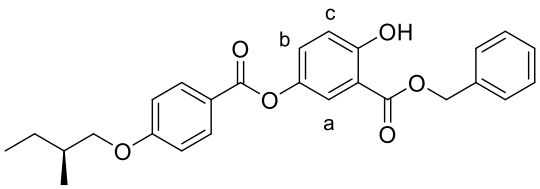

Benzyl 2,5-dihydroxybenzoate (1.75 g, 7.17 mmol), (*S*)-4-(2-methylbutyloxy)benzoic acid (1.50 g, 7.22 mmol), N-(3-dimethylaminopropyl)-N′-ethylcarbodiimide hydrochloride (1.36 g, 7.11 mmol) and 4-(dimethylamino)pyridine (0.18 g, 1.43 mmol) were added to dichloromethane (125 cm^3) and stirred for 3 days at room temperature. Purification *via* column chromatography on silica gel with dichloromethane as eluting solvent yielded a white solid.

Yield: 2.87 g, 6.60 mmol, 93%.

^{1}H NMR ($CDCl_3$) δ (ppm): 0.97 (t, 3H, *J* = 7.5 Hz, -C**H**$_3$), 1.04 (d, 3H, *J* = 6.6 Hz, -C**H**$_3$), 1.24-1.35 (m, 1H, -C**H**-), 1.54-1.64 (m, 1H, -C**H**-), 1.85-1.96 (m, 1H, -C**H**-), 3.80-3.92 (m, 2H, -OC**H**$_2$-), 5.38 (s, 2H, -OC**H**$_2$Bn), 6.96 (m, 2H, Ar**H**), 7.03 (d, 1H, *J* = 9.0 Hz, Ar**H**$_c$), 7.30 (dd, 1H, *J* = 2.9, 8.8 Hz, Ar**H**$_b$), 7.39 (m, 5H, Ar**H**), 7.69 (d, 1H, *J* = 2.8 Hz, Ar**H**$_a$), 8.10 (m, 2H, Ar**H**), 10.69 (s (br), 1H, -O**H**).

^{13}C NMR ($CDCl_3$) δ (ppm): 11.30, 16.49 (-**C**H$_3$), 26.09 (-**C**H$_2$-), 34.64 (-**C**H-), 67.30, 73.13 (**C**-O), 112.42, 114.35, 118.50, 121.15, 122.38, 128.48, 128.65, 128.73, 129.90, 132.27, 135.02 (Ar**C**), 142.76, 159.48, 163.81 (Ar**C**-O), 165.19, 169.41 (**C**=O).

FTIR ν (cm^{-1}): 3155 (O-H), 2963, 2920, 2878 (C-H), 1728, 1677 (C=O), 1605 (C=C), 1256, 1210, 1167, 1068 (C-O), 790, 731, 690.

HRMS (ESI): $C_{26}H_{26}O_6$ calculated $[M+Na]^+$ *m/z* 457.1622, measured 457.1603.

Mp: 64-66 °C.

EA (CHNS): calculated C: 71.87%, H: 6.03%, found C: 72.00%, H: 6.15%.

7.2.4.4 (*S*)-Benzyl-2-(4'-(2-methylbutyloxy)benzoyloxy)-5-(4'-(butyloxy)benzoyloxy)benzoate (17)

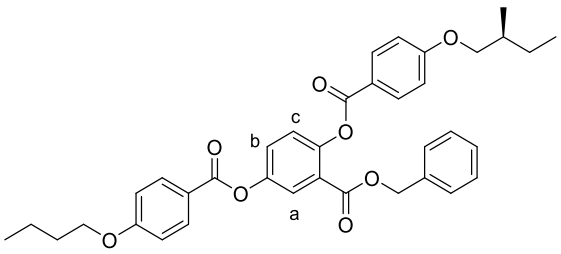

Benzyl-2-hydroxy-5-(4'-butyloxy)benzoyloxy)benzoate (3.94 g, 9.38 mmol), (*S*)-4-(2-methylbutyloxy)benzoic acid (2.35 g, 11.30 mmol), N-(3-dimethylaminopropyl)-N′-ethylcarbodiimide hydrochloride (2.74 g, 14.31 mmol) and 4-(dimethylamino)pyridine (0.35 g, 2.89 mmol) were added to dichloromethane (250 cm^3) and stirred for 3 days at room temperature. Purification *via* column chromatography on silica gel with petroleum ether: ethyl acetate (9:1) as eluting solvent yielded a white solid.

Yield: 5.36 g, 8.78 mmol, 93%.

^{1}H NMR ($CDCl_3$) δ (ppm): 0.99 (m, 6H, -C**H**$_3$), 1.06 (d, 3H, *J* = 6.7 Hz, -C**H**$_3$), 1.23-1.38 (m, 1H, -C**H**$_2$-), 1.47-1.67 (m, 3H, -C**H**$_2$-), 1.78-1.85 (m, 2H, -C**H**$_2$-), 1.88-1.96 (m, 1H, -C**H**-), 3.80-3.94 (m, 2H, -C**H**$_2$O-), 4.06 (t, 2H, *J* = 6.5 Hz, -C**H**$_2$O-), 5.19 (s, 2H, -C**H**$_2$Bn), 6.95 (m, 4H, Ar**H**), 7.24 (s, 5H, Ar**H**), 7.26 (d, 1H, *J* = 8.8 Hz, Ar**H**$_c$), 7.46 (dd, 1H, *J* = 2.9, 8.7 Hz, Ar**H**$_b$), 7.91 (d, 1H, *J* = 2.9 Hz, Ar**H**$_a$), 8.10 (m, 4H, Ar**H**).

7.2.4.5 (*S*)-Benzyl-2-(4'-(butyloxy)benzoyloxy)-5-(4'-(2-methylbutyloxy)benzoyloxy)benzoate (18)

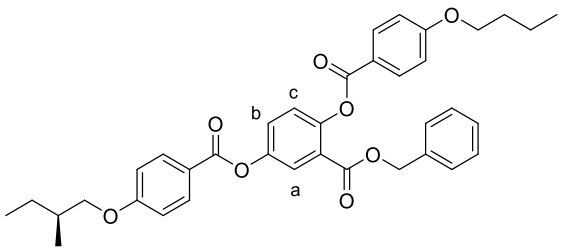

(*S*)-Benzyl-2-hydroxy-5-(4'-(2-methylbutyloxy)benzoyloxy)benzoate (2.11 g, 4.85 mmol), 4-butyloxybenzoic acid (0.94 g, 4.85 mmol), N-(3-dimethylaminopropyl)-N′-ethylcarbodiimide hydrochloride (1.12 g, 5.84 mmol) and 4-(dimethylamino)pyridine (0.14 g, 1.18 mmol) were added to dichloromethane (100 cm^3) and stirred for 3 days at room temperature. Purification *via* column chromatography on silica gel with petroleum ether: ethyl acetate (9:1) as eluting solvent yielded a white solid.

Yield: 2.75 g, 4.51 mmol, 93%.

^{1}H NMR ($CDCl_3$) δ (ppm): 0.97 (t, 3H, *J* = 7.5 Hz, -C**H**$_3$), 1.01 (t, 3H, *J* = 7.4 Hz, -C**H**$_3$), 1.05 (d, 3H, *J* = 6.8 Hz, -C**H**$_3$), 1.24-1.36 (m, 1H, -C**H**$_2$-), 1.48-1.65 (m, 3H, -C**H**$_2$-), 1.78-1.86 (m, 2H, -C**H**$_2$-), 1.86-1.96 (m, 1H, -C**H**-), 3.80-3.94 (m, 2H, -C**H**$_2$O-), 4.06 (t, 2H, *J* = 6.5 Hz, -C**H**$_2$O-), 5.19 (s, 2H, -C**H**$_2$Bn), 6.95 (m, 4H, Ar**H**), 7.24 (s, 5H, Ar**H**), 7.26 (d, 1H, *J* = 8.8 Hz, Ar**H**$_c$), 7.46 (dd, 1H, *J* = 2.9, 8.8 Hz, Ar**H**$_b$), 7.91 (d, 1H, *J* = 2.9 Hz, Ar**H**$_a$), 8.10 (m, 4H, Ar**H**).

^{13}C NMR ($CDCl_3$) δ (ppm): 11.45, 13.97, 16.63 (-**C**H$_3$), 19.36, 26.23, 31.29 (-**C**H$_2$-), 34.78 (-**C**H-), 67.38, 68.13, 73.28 (**C**-O), 114.42, 114.55, 121.09, 121.45, 124.76, 125.19, 127.47, 128.34, 128.56, 128.65, 132.52, 132.56, 135.37 (Ar**C**), 148.39, 148.46, 163.65, 164.00 (Ar**C**-O), 164.05, 164.74, 165.10 (**C**=O).

FTIR ν (cm^{-1}): 2961, 2924, 2876 (C-H), 1720 (C=O), 1604, 1510 (C=C), 1245, 1210, 1165, 1068 (C-O), 1001, 842, 759, 734, 688.

HRMS (ESI): $C_{37}H_{38}O_8$ calculated $[M+Na]^+$ *m/z* 633.2459, measured 633.2488.

Mp: 107-108 °C.

EA (CHNS): calculated C: 72.77%, H: 6.27%, found C: 72.88%, H: 6.30%.

7.2.4.6 (*S*)-Benzyl-2-(4'-(2-methylbutyloxy)benzoyloxy)-5-(4'-(heptyloxy)benzoyloxy)benzoate (19)

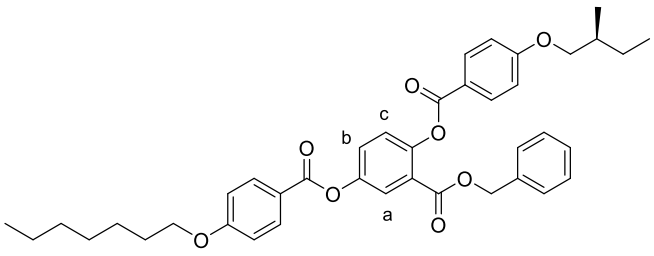

(*S*)-Benzyl-2-(hydroxy)-5-(4'-heptyloxy)benzoyloxy)benzoate (2.17 g, 4.70 mmol), (S)-4-(2-methylbutyloxy)benzoic acid (0.98 g, 4.72 mmol), N-(3-dimethylaminopropyl)-N′-ethylcarbodiimide hydrochloride (1.08 g, 5.63 mmol) and 4-(dimethylamino)pyridine (0.14 g, 1.14 mmol) were added to dichloromethane (100 cm^3) and stirred for 3 days at room temperature. Purification *via* column chromatography on silica gel with dichloromethane as eluting solvent yielded a white solid.

Yield: 2.80 g, 4.28 mmol, 91%.

^{1}H NMR ($CDCl_3$) δ (ppm): 0.91 (t, 3H, -C**H**$_3$), 0.99 (t, 3H, -C**H**$_3$) 1.06 (d, 3H, *J* = 6.8 Hz, -C**H**$_3$), 1.27-1.43 (m, 7H, -C**H**$_2$-), 1.43-1.52 (m, 2H, -C**H**$_2$-), 1.55-1.66 (m, 1H, -C**H**$_2$-), 1.79-1.87 (m, 2H, -C**H**$_2$-), 1.88-1.97 (m, 1H, -C**H**-), 3.80-3.94 (m, 2H, -C**H**$_2$O-), 4.05 (t, 2H, *J* = 6.6 Hz, -C**H**$_2$O-), 5.19 (s, 2H, -C**H**$_2$Bn), 6.95 (m, 4H, Ar**H**), 7.24 (s, 5H, Ar**H**), 7.26 (d, 1H, *J* = 8.8 Hz, Ar**H**$_c$), 7.46 (dd, 1H, *J* = 2.9, 8.8 Hz, Ar**H**$_b$), 7.91 (d, 1H, *J* = 2.9 Hz, Ar**H**$_a$), 8.10 (m, 4H, Ar**H**).

^{13}C NMR ($CDCl_3$) δ (ppm): 11.45, 14.23, 16.63 (-**C**H$_3$), 22.74, 26.09, 26.23, 29.17, 29.23, 31.90 (-**C**H$_2$-), 34.79 (-**C**H-), 68.59, 73.22 (**C**-O), 114.47, 114.53, 121.06, 121.38, 123.65, 125.33, 125.60, 128.18, 132.54, 132.58, (Ar**C**), 148.41, 148.84, 163.87, 163.91 (Ar**C**-O), 164.67, 165.08, 168.44 (**C**=O).

FTIR ν (cm^{-1}): 2961, 2926, 2857 (C-H), 1720 (C=O), 1605, 1510 (C=C), 1243, 1169, 1068 (C-O), 844, 759, 734, 690.

HRMS (ESI): $C_{40}H_{44}O_8$ calculated $[M+H]^+$ *m/z* 675.2939, measured 675.2931.

Mp: 103-105 °C.

EA (CHNS): calculated C: 73.60%, H: 6.79%, found C: 73.83%, H: 6.92%.

7.2.4.7 (*S*)-Benzyl-2-(4'-(heptyloxy)benzoyloxy)-5-(4'-(2-methylbutyloxy)benzoyloxy)benzoate (20)

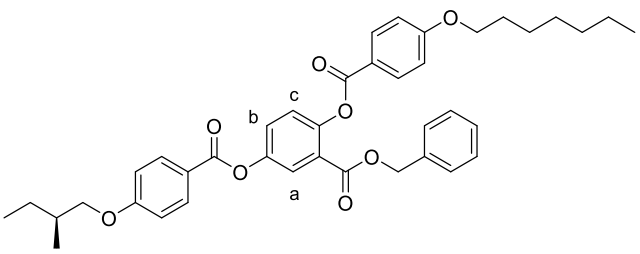

(*S*)-Benzyl-2-hydroxy-5-(4'-(2-methylbutyloxy)benzoyloxy) benzoate (2.65, 6.10 mmol), 4-heptyloxybenzoic acid (1.45 g, 6.13 mmol), N-(3-dimethylaminopropyl)-N′-ethylcarbodiimide hydrochloride (1.18 g, 6.16 mmol) and 4-(dimethylamino)pyridine (0.15 g, 1.23 mmol) were added to dichloromethane (100 cm^3) and stirred for 3 days at room temperature. Purification *via* column chromatography on silica gel with petroleum ether: ethyl acetate (19:1) as eluting solvent yielded a white solid.

Yield: 3.40 g, 5.22 mmol, 86%.

^{1}H NMR ($CDCl_3$) δ (ppm): 0.91 (t, 3H, *J* = 6.6 Hz, -C**H**$_3$), 0.97 (t, 3H, *J* = 7.4 Hz, -C**H**$_3$), 1.05 (d, 3H, *J* = 6.8 Hz, -C**H**$_3$), 1.23-1.67 (m, 10H, -C**H**$_2$-), 1.78-1.98 (m, 3H, -C**H**$_2$-), 3.81-3.94 (m, 2H, -C**H**$_2$O-), 4.05 (t, 2H, *J* = 6.5 Hz, -C**H**$_2$O-), 5.19 (s, 2H, -C**H**$_2$Bn), 6.95 (m, 4H, Ar**H**), 7.24 (s, 5H, Ar**H**), 7.26 (d, 1H, *J* = 8.8 Hz, Ar**H**$_c$), 7.46 (dd, 1H, *J* = 2.9, 8.8 Hz, Ar**H**$_b$), 7.91 (d, 1H, *J* = 2.9 Hz, Ar**H**$_a$), 8.10 (m, 4H, Ar**H**).

^{13}C NMR ($CDCl_3$) δ (ppm): 11.30, 14.09, 16.49 (-**C**H$_3$), 22.62, 25.97, 26.09, 29.04, 29.12, 31.78 (-**C**H$_2$-), 34.64 (-**C**H-), 67.23, 68.31, 73.15 (**C**-O), 114.29, 114.41, 120.97, 121.32, 124.64, 125.04, 127.32, 128.19, 128.42, 128.51, 132.38, 132.42, 135.25 (Ar**C**), 148.25, 148.32, 163.51, 163.86 (Ar**C**-O), 163.92, 164.59, 164.95 (**C**=O).

FTIR ν (cm^{-1}): 2960, 2928, 2857 (C-H), 1720 (C=O), 1605, 1510 (C=C), 1247, 1167, 1068 (C-O), 842, 759, 734, 688.

HRMS (ESI): $C_{40}H_{44}O_8$ calculated $[M+Na]^+$ *m/z* 675.2928, measured 675.2926.

Mp: 111-112 °C.

EA (CHNS): calculated C: 73.60%, H: 6.79%, found C: 73.68%, H: 7.03%.

7.2.4.8 (*S*)-Benzyl-2-(4'-(1-methylheptyloxy)benzoyloxy)-5-(4'-(heptyloxy)benzoyloxy)benzoate (21)

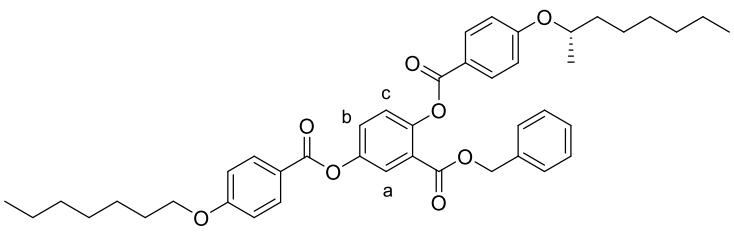

(*S*)-Benzyl-2-(hydroxy)-5-(4'-heptyloxy)benzoyloxy)benzoate (1.84 g, 3.97 mmol), (S)-4-(1-methylheptyloxy)benzoic acid (1.51 g, 6.4 mmol), N-(3-dimethylaminopropyl)-N′-ethylcarbodiimide hydrochloride (1.39 g, 6.4 mmol) and 4-(dimethylamino)pyridine (0.71 g, 6.4 mmol) were added to dichloromethane (250 cm^3) and stirred for 3 days at room temperature. Purification *via* column chromatography on silica gel with petroleum ether: ethyl acetate (9:1) as eluting solvent yielded a white solid.

Yield: 2.60 g, 3.74 mmol, 94%.

^{1}H NMR ($CDCl_3$) δ (ppm): 0.90 (t, 3H, *J* = 6.8 Hz,, -C**H**$_3$), 0.91 (t, 3H, *J* = 6.9 Hz, -C**H**$_3$) 1.06 (d, 3H, *J* = 6.1 Hz, -C**H**$_3$), 1.26-1.53 (m, 16H, -C**H**$_2$-), 1.57-1.68 (m, 1H, -C**H**$_2$-), 1.74-1.87 (m, 3H, -C**H**$_2$-), 4.05 (t, 2H, *J* = 6.6 Hz, -C**H**$_2$O-), 4.48 (m, 1H, -C**H**O-), 5.20 (s, 2H, -C**H**$_2$Bn), 6.93 (m, 4H, Ar**H**), 7.24 (s, 5H, Ar**H**), 7.26 (d, 1H, *J* = 8.8 Hz, Ar**H**$_c$), 7.46 (dd, 1H, *J* = 2.9, 8.8 Hz, Ar**H**$_b$), 7.91 (d, 1H, *J* = 2.9 Hz, Ar**H**$_a$), 8.10 (m, 4H, Ar**H**).

^{13}C NMR ($CDCl_3$) δ (ppm): 14.06, 19.63, 22.58 (-**C**H$_3$), 25.46, 25.92, 29.00, 29.01, 29.21, 31.73, 31.77 (-**C**H$_2$-), 36.33 (-**C**H-), 67.21 68.34, 74.05 (**C**-O), 114.35, 115.11, 120.97, 124.60, 125.00, 125.03, 127.29, 128.15, 128.37, 128.48, 132.36, 132.44, 135.19 (Ar**C**), 148.24, 148.27, 162.71, 163.72 (Ar**C**-O), 163.84, 164.55, 164.90 (**C**=O).

FTIR ν (cm^{-1}): 2952, 2924, 2853 (C-H), 1728 (C=O), 1605, 1508 (C=C), 1245, 1163, 1066 (C-O), 844, 759, 732, 691.

HRMS (ESI): $C_{43}H_{50}O_8$ calculated $[M+Na]^+$ *m/z* 717.3398, measured 717.3398.

Mp: (40 °C) N* 76 °C Iso.

EA (CHNS): calculated C: 74.33%, H: 7.25%, found C: 70.65%, H: 7.48%.

7.2.4.9 (*S*)-2-(4'-(2-Methylbutyloxy)benzoyloxy)-5-(4'-(butyloxy)benzoyloxy)benzoic acid (22)

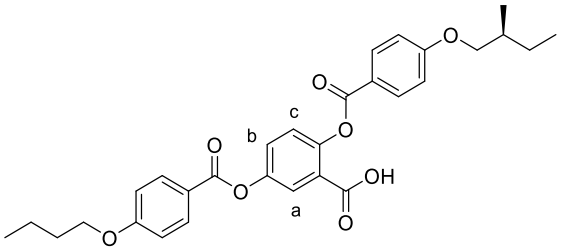

To a stirred solution of tetrahydrofuran (100 cm^3) and ethanol (15 cm^3), (*S*)-benzyl-2-(4'-(2-methylbutyloxy)benzoyloxy)-5-(4'-(butyloxy)benzoyloxy)benzoate (5.36 g, 8.78 mmol) was added. A spatula tip of palladium on carbon (10%) was added and stirred vigorously. After 3 degas cycles the reaction was left under a hydrogen atmosphere overnight. The reaction mixture was filtered over a celite pad, washed with tetrahydrofuran (150 cm^3) and the solvent removed *in vacuo* to yield a white solid.

Yield: 3.82 g, 7.34 mmol, 84%.

^{1}H NMR ($CDCl_3$) δ (ppm): 0.98 (m, 6H, -C**H**$_3$), 1.04 (d, 3H, *J* = 6.8 Hz, -C**H**$_3$), 1.23-1.36 (m, 1H, -C**H**$_2$-), 1.47-1.65 (m, 3H, -C**H**$_2$-), 1.77-1.86 (m, 2H, -C**H**$_2$-), 1.86-1.96 (m, 1H, -C**H**-), 3.80-3.94 (m, 2H, -C**H**$_2$O-), 4.06 (t, 2H, *J* = 6.5 Hz, -C**H**$_2$O-), 6.97 (m, 4H, Ar**H**), 7.24 (s, 5H, Ar**H**), 7.29 (d, 1H, *J* = 8.8 Hz, Ar**H**$_c$), 7.50 (dd, 1H, *J* = 2.9, 8.8 Hz, Ar**H**$_b$), 7.93 (d, 1H, *J* = 2.9 Hz, Ar**H**$_a$), 8.13 (m, 4H, Ar**H**).

^{13}C NMR ($CDCl_3$) δ (ppm): 11.45, 13.96, 16.63 (-**C**H$_3$), 19.33, 26.22, 31.26 (-**C**H$_2$-), 34.78 (-**C**H-), 68.19, 73.23 (**C**-O), 114.47, 114.53, 121.08, 121.41, 123.68, 125.30, 125.59, 128.10, 132.53, 132.59, (Ar**C**), 148.42, 148.80, 163.87, 163.91 (Ar**C**-O), 164.66, 165.06, 167.58 (**C**=O).

FTIR ν (cm^{-1}): 2961, 2936, 2875 (C-H), 1731, 1687 (C=O), 1605, 1510 (C=C), 1247, 1161, 1057 (C-O), 759.

HRMS (ESI): $C_{30}H_{32}O_8$ calculated $[M-H]^-$ *m/z* 519.2024, measured 519.2018.

Mp: 163-167 °C.

EA (CHNS): calculated C: 69.22%, H: 6.20%, found C: 69.49%, H: 6.32%.

7.2.4.10 (*S*)-2-(4'-(Butyloxy)benzoyloxy)-5-(4'-(2-methylbutyloxy)benzoyloxy)benzoic acid (23)

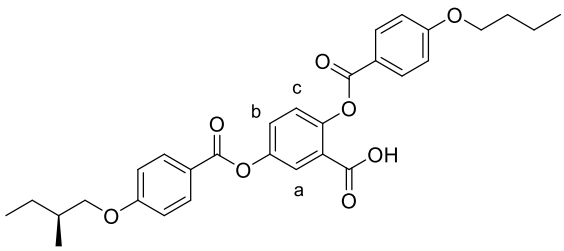

(*S*)-Benzyl-2-(4'-(butyloxy)benzoyloxy)-5-(4'-(2-methylbutyloxy)benzoyloxy)benzoate (2.73 g, 4.47 mmol) was added to dichloromethane (100 cm^3). A spatula tip of palladium on carbon (10%) was added and stirred vigorously. After 3 degas cycles the reaction was left under a hydrogen atmosphere overnight. The reaction mixture was filtered over a celite pad, washed with dichloromethane (150 cm^3) and the solvent removed *in vacuo* to yield a white solid.

Yield: 2.24 g, 4.31 mmol, 96%.

^{1}H NMR ($CDCl_3$) δ (ppm): 0.97 (t, 3H, *J* = 7.6 Hz, -C**H**$_3$), 0.99 (t, 3H, *J* = 7.4 Hz, -C**H**$_3$), 1.05 (d, 3H, *J* = 6.8 Hz, -C**H**$_3$), 1.24-1.36 (m, 1H, -C**H**$_2$-), 1.46-1.65 (m, 3H, -C**H**$_2$-), 1.76-1.85 (m, 2H, -C**H**$_2$-), 1.86-1.96 (m, 1H, -C**H**-), 3.80-3.94 (m, 2H, -C**H**$_2$O-), 4.05 (t, 2H, *J* = 6.5 Hz, -C**H**$_2$O-), 6.96 (m, 4H, Ar**H**), 7.29 (d, 1H, *J* = 8.8 Hz, Ar**H**$_c$), 7.50 (dd, 1H, *J* = 2.9, 8.8 Hz, Ar**H**$_b$), 7.93 (d, 1H, *J* = 2.9 Hz, Ar**H**$_a$), 8.13 (m, 4H, Ar**H**).

^{13}C NMR ($CDCl_3$) δ (ppm): 11.45, 13.97, 16.63 (-**C**H_3), 19.34, 26.23, 31.30 (-**C**H_2-), 34.78 (-**C**H-), 68.12, 73.28 (**C**-O), 114.45, 114.55, 121.03, 121.43, 123.66, 125.31, 125.61, 128.14, 132.53, 132.61, (Ar**C**), 148.42, 148.82, 163.72, 164.07 (Ar**C**-O), 164.69, 165.08, 167.90 (**C**=O).

FTIR ν (cm^{-1}): 2958, 2930, 2874 (C-H), 1728, 1687 (C=O), 1605, 1510 (C=C), 1247, 1165, 1070 (C-O), 842, 759.

HRMS (ESI): $C_{30}H_{32}O_8$ calculated $[M-H]^-$ *m/z* 519.2024, measured 519.2023.

Mp: 164-168 °C.

EA (CHNS): calculated C: 69.22%, H: 6.20%, found C: 68.89%, H: 6.27%.

7.2.4.11 (*S*)-2-(4'-(2-Methylbutyloxy)benzoyloxy)-5-(4'-(heptyloxy)benzoyloxy)benzoic acid (24)

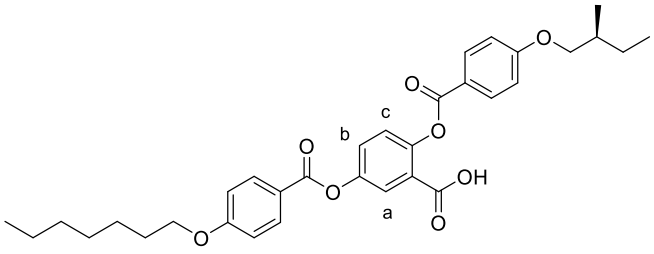

(*S*)-Benzyl-2-(4'-(2-methylbutyloxy)benzoyloxy)-5-(4'-(heptyloxy)benzoyloxy)benzoate (2.60 g, 3.98 mmol) was added to dichloromethane (100 cm^3). A spatula tip of palladium on carbon (10%) was added and stirred vigorously. After 3 degas cycles the reaction was left under a hydrogen atmosphere overnight. The reaction mixture was filtered over a celite pad, washed with dichloromethane (150 cm^3) and the solvent removed *in vacuo*. Purification *via* a short silica pad with petroleum ether: ethyl acetate (2:1) as eluting solvent yielded a white solid.

Yield: 2.00 g, 3.55 mmol, 89%.

^{1}H NMR ($CDCl_3$) δ (ppm): 0.91 (t, 3H, -C**H**$_3$), 0.97 (t, 3H, -C**H**$_3$) 1.04 (d, 3H, *J* = 6.8 Hz, -C**H**$_3$), 1.24-1.42 (m, 7H, -C**H**$_2$-), 1.43-1.52 (m, 2H, -C**H**$_2$-), 1.54-1.65 (m, 1H, -C**H**$_2$-), 1.79-1.87 (m, 2H, -C**H**$_2$-), 1.87-1.96 (m, 1H, -C**H**-), 3.80-3.94 (m, 2H, -C**H**$_2$O-), 4.05 (t, 2H, *J* = 6.6 Hz, -C**H**$_2$O-), 6.96 (m, 4H, Ar**H**), 7.29 (d, 1H, *J* = 8.8 Hz, Ar**H**$_c$), 7.50 (dd, 1H, *J* = 2.9, 8.8 Hz, Ar**H**$_b$), 7.93 (d, 1H, *J* = 2.9 Hz, Ar**H**$_a$), 8.12 (m, 4H, Ar**H**).

^{13}C NMR ($CDCl_3$) δ (ppm): 11.45, 14.23, 16.63 (-**C**H$_3$), 22.74, 26.09, 26.23, 29.17, 29.23, 31.90 (-**C**H$_2$-), 34.79 (-**C**H-), 68.59, 73.22 (**C**-O), 114.47, 114.53, 121.06, 121.38, 123.65, 125.33, 125.60, 128.18, 132.54, 132.58, (Ar**C**), 148.41, 148.84, 163.87, 163.91 (Ar**C**-O), 164.67, 165.08, 168.44 (**C**=O).

FTIR ν (cm^{-1}): 2961, 2924, 2857 (C-H), 1726, 1687 (C=O), 1605, 1510 (C=C), 1245, 1167, 1068 (C-O), 842, 757.

HRMS (ESI): $C_{33}H_{38}O_8$ calculated $[M-H]^-$ *m/z* 561.2694, measured 561.2489.

Mp: 139-142 °C.

EA (CHNS): calculated C: 70.44%, H: 6.81%, found C: 70.81%, H: 7.00%.

7.2.4.12 (*S*)-2-(4'-(Heptyloxy)benzoyloxy)-5-(4'-(2-methylbutyloxy)benzoyloxy)benzoic acid (25)

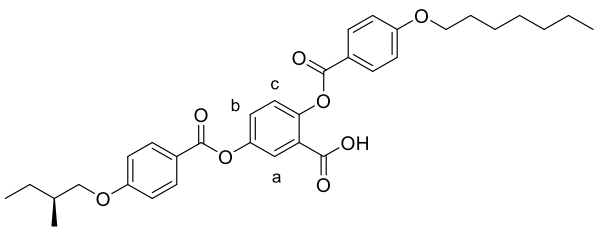

To a stirred solution of tetrahydrofuran (100 cm^3) and ethanol (15 cm^3), (S)-benzyl-2-(4'-(heptyloxy)benzoyloxy)-5-(4'-(2-methylbutyloxy)benzoyloxy) benzoate (3.04 g, 4.65 mmol) was added. A spatula tip of palladium on carbon (10%) was added and stirred vigorously. After 3 degas cycles the reaction was left under a hydrogen atmosphere overnight. The reaction mixture was filtered over a celite pad and washed with tetrahydrofuran (150 cm^3) and the solvent removed *in vacuo*. Recrystallisation from ethanol yielded a white solid.

Yield: 2.17 g, 3.86 mmol, 83%.

^{1}H NMR ($CDCl_3$) δ (ppm): 0.90 (t, 3H, *J* = 6.8 Hz, -C**H**$_3$), 0.97 (t, 3H, *J* = 7.5 Hz, -C**H**$_3$), 1.05 (d, 3H, *J* = 6.8 Hz, -C**H**$_3$), 1.25-1.66 (m, 10H, -C**H**$_2$-), 1.78-1.86 (m, 2H, -C**H**$_2$-), 1.87-1.96 (m, 1H, -C**H**-), 3.81-3.94 (m, 2H, -C**H**$_2$O-), 4.04 (t, 2H, *J* = 6.6 Hz, -C**H**$_2$O-), 6.97 (m, 4H, Ar**H**), 7.29 (d, 1H, *J* = 8.8 Hz, Ar**H**$_c$), 7.50 (dd, 1H, *J* = 2.9, 8.8 Hz, Ar**H**$_b$), 7.93 (d, 1H, *J* = 2.9 Hz, Ar**H**$_a$), 8.13 (m, 4H, Ar**H**).

^{13}C NMR ($CDCl_3$) δ (ppm): 11.45, 14.23, 16.63 (-**C**H$_3$), 22.75, 26.10, 26.23, 29.18, 29.27, 31.91(-**C**H$_2$-), 34.78 (-**C**H-), 68.45, 73.29 (**C**-O), 114.45, 114.56, 121.03, 121.41, 123.61, 125.32, 125.61, 128.17, 132.53, 132.61 (Ar**C**), 148.43, 148.82, 163.73, 164.08 (Ar**C**-O), 164.69, 165.08, 167.79 (**C**=O).

FTIR ν (cm^{-1}): 2960, 2924, 2874 (C-H), 1728, 1687 (C=O), 1605, 1510 (C=C), 1247, 1170 (C-O), 842, 759.

HRMS (ESI): $C_{33}H_{38}O_8$ calculated $[M-H]^-$ *m/z* 561.2494, measured 561.2479.

Mp: 166-168 °C.

EA (CHNS): calculated C: 70.44%, H: 6.81%, found C: 70.43%, H: 6.92%.

7.2.4.13 (*S*)-2-(4'-(1-Methylheptyloxy)benzoyloxy)-5-(4'-(heptyloxy)benzoyloxy)benzoic acid (26)

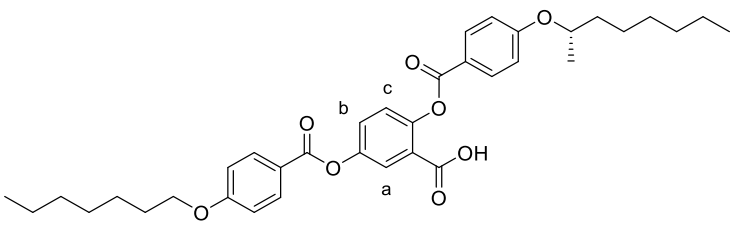

(*S*)-Benzyl-2-(4'-(1-methyheptyloxy)benzoyloxy)-5-(4'-(heptyloxy)benzoyloxy)benzoate (2.50 g, 3.6 mmol) was added to dichloromethane (100 cm^3). A spatula tip of palladium on carbon (10%) was added and stirred vigorously. After 3 degas cycles the reaction was left under a hydrogen atmosphere overnight. The reaction mixture was filtered over a celite pad, washed with dichloromethane (400 cm^3) and the solvent removed *in vacuo*. Purification *via* column chromatography with petroleum ether: ethyl acetate (2:1) as eluting solvent yielded a white solid.

Yield: 0.84 g, 1.39 mmol, 39%.

^{1}H NMR ($CDCl_3$) δ (ppm): 0.88 (t, 3H, *J* = 7.0 Hz, -C**H$_3$**), 0.91 (t, 3H, *J* = 7.0 Hz, -C**H$_3$**) 1.04 (d, 3H, *J* = 6.0 Hz, -C**H$_3$**), 1.24-1.42 (m, 14H, -C**H$_2$**-), 1.43-1.52 (m, 3H, -C**H$_2$**-), 1.55-1.66 (m, 1H, -C**H$_2$**-), 1.73-1.8 (m, 3H, -C**H$_2$**-), 4.05 (t, 2H, *J* = 6.6 Hz, -C**H$_2$**O-), 4.49 (m, 1H, -C**H$_2$**O-), 6.95 (m, 4H, Ar**H**), 7.29 (d, 1H, *J* = 8.8 Hz, Ar**H$_c$**), 7.50 (dd, 1H, *J* = 2.9, 8.8 Hz, Ar**H$_b$**), 7.93 (d, 1H, *J* = 2.9 Hz, Ar**H$_a$**), 8.13 (m, 4H, Ar**H**).

^{13}C NMR ($CDCl_3$) δ (ppm): 14.06, 14.07, 19.61 (-**C**H_3), 22.57, 22.59, 25.43, 25.93, 29.01, 29.08, 29.22, 31.75 (-**C**H_2-), 36.34 (-**C**H-), 68.35, 74.09 (**C**-O), 114.37, 115.20, 120.91, 120.95, 123.44, 125.17, 125.43, 128.02, 132.38, 132.51, (Ar**C**), 148.26, 148.67, 162.81, 163.76 (Ar**C**-O), 164.50, 164.86, 167.68 (**C**=O).

FTIR ν (cm^{-1}): 3077 (O-H), 2953, 2924, 2857 (C-H), 1727, 1687 (C=O), 1605, 1510 (C=C), 1247, 1170, 1070 (C-O), 842, 759, 691.

HRMS (ESI): $C_{36}H_{44}O_8$ calculated $[M+Na]^+$ *m/z* 627.2928, measured 627.2925.

Mp: 138-140 °C.

EA (CHNS): calculated C: 71.50%, H: 7.33%, found C: 71.70%, H: 7.51%.

7.2.4.14 (*S*)-4''-(Acryloyloxybutyl)-2-(4'-(2-methylbutyloxy)benzoyloxy)-5-(butyloxy)benzoyloxy)benzoate (CM1)

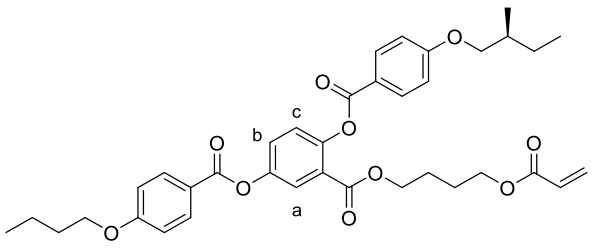

(*S*)-2-(4'-(2-Methylbutyloxy)benzoyloxy)-5-(4'-(butyloxy)benzoyloxy) benzoic acid (2.04 g, 3.92 mmol), 4-hydroxybutyl acrylate (0.65 cm^3, 4.69 mmol), N-(3-dimethylaminopropyl)-N′-ethylcarbodiimide hydrochloride (1.18 g, 6.15 mmol) and 4-(dimethylamino)pyridine (0.14 g, 1.16 mmol) were added to dichloromethane (100 cm^3) and stirred for 3 days at room temperature. Purification *via* column chromatography on silica gel with petroleum ether: ethyl acetate (9:1) as eluting solvent yielded a white solid.

Yield: 1.47 g, 2.27 mmol, 58%.

^{1}H NMR ($CDCl_3$) δ (ppm): 0.97 (t, 3H, *J* = 7.5 Hz, -C**H**$_3$), 1.00 (t, 3H, *J* = 7.4 Hz, -C**H**$_3$), 1.04 (d, 3H, J = 6.8 Hz, -C**H**$_3$), 1.12-1.38 (m, 1H, -C**H**$_2$-), 1.46-1.71 (m, 7H, -C**H**$_2$-), 1.76-1.86 (m, 2H, -C**H**$_2$-), 1.86-1.99 (m, 1H, -C**H**-), 3.78-3.95 (m, 2H, -C**H**$_2$O-), 4.03 (t, 2H, *J* = 6.2 Hz, -C**H**$_2$O-), 4.06 (t, 2H, *J* = 6.5 Hz, -C**H**$_2$O-), 4.21 (t, 2H, *J* = 6.2 Hz, -C**H**$_2$O-), 5.79 (dd, 1H, *J* = 1.5, 10.4 Hz, C**H**=), 6.08 (dd, 1H, *J* = 10.4, 17.3 Hz, C**H**=), 6.36 (dd, 1H, *J* = 1.5, 17.3 Hz, C**H**=), 6.98 (m, 4H, Ar**H**), 7.26 (d, 1H, *J* = 8.8 Hz, Ar**H**$_c$), 7.45 (dd, 1H, *J* = 2.9, 8.8 Hz, Ar**H**$_b$), 7.89 (d, 1H, *J* = 2.9 Hz, Ar**H**$_a$), 8.15 (m, 4H, Ar**H**).

^{13}C NMR ($CDCl_3$) δ (ppm): 11.42, 13.94, 16.60 (-**C**H_3), 19.32, 25.26, 26.21, 31.25 (-**C**H_2-), 34.76 (-**C**H-), 64.02, 65.00, 68.18, 73.25 (**C**-O), 114.52, 121.14, 121.43, 124.92, 125.09, 125.15, 127.33 (Ar**C**), 128.55, 130.76 (**C**=**C**), 132.51, 132.54 (Ar**C**), 148.23, 148.48 (Ar**C**-O), 163.89, 163.95, (Ar**C**-O) 164.17, 164.71, 165.05, 166.22 (**C**=O).

FTIR ν (cm^{-1}): 2963, 2935, 2874 (C-H), 1722 (C=O), 1607, 1511 (C=C), 1247, 1163, 1070 (C-O), 759.

HRMS (ESI): $C_{37}H_{42}O_{10}$ calculated $[M+Na]^+$ *m/z* 669.2670, measured 669.2653.

DSC: Cr 55.5 °C (N* 44.2 °C) Iso.

EA (CHNS): calculated C: 68.72%, H: 6.55%, found C: 68.91%, H: 6.67%.

7.2.4.15 (*S*)-4''-(Acryloyloxybutyl)-2-(4'-(butyloxy)benzoyloxy)-5-(4'-(2-methylbutyloxy)benzoyloxy)benzoate (CM2)

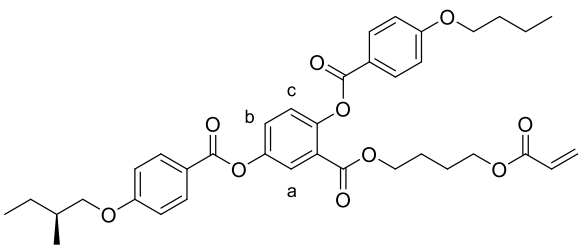

(*S*)-2-(4'-(Butyloxy)benzoyloxy)-5-(4'-(2-methylbutyloxy)benzoyloxy)benzoic acid (2.19 g, 4.21 mmol), 4-hydroxybutyl acrylate (0.60 cm^3, 4.20 mmol), N-(3-dimethylaminopropyl)-N′-ethylcarbodiimide hydrochloride (0.81 g, 4.22 mmol) and 4-(dimethylamino)pyridine (0.11 g, 0.90 mmol) were added to dichloromethane (100 cm^3) and stirred for 3 days at room temperature. Purification *via* column chromatography on silica gel with petroleum ether: ethyl acetate (9:1) as eluting solvent yielded a white solid.

Yield: 1.54 g, 2.38 mmol, 57%.

^{1}H NMR ($CDCl_3$) δ (ppm): 0.97 (t, 3H, *J* = 7.4 Hz, -C**H**$_3$), 1.00 (t, 3H, *J* = 7.4 Hz, -C**H**$_3$), 1.05 (d, 3H, *J* = 6.8 Hz, -C**H**$_3$), 1.25-1.36 (m, 1H, -C**H**$_2$-), 1.48-1.69 (m, 7H, -C**H**$_2$-), 1.77-1.86 (m, 2H, -C**H**$_2$-), 1.87-1.97 (m, 1H, -C**H**-), 3.80-3.95 (m, 2H, -C**H**$_2$O-), 4.03 (t, 2H, *J* = 6.5 Hz, -C**H**$_2$O-), 4.05 (t, 2H, *J* = 6.2 Hz, -C**H**$_2$O-), 4.20 (t, 2H, *J* = 6.3 Hz, -C**H**$_2$O-), 5.80 (dd, 1H, *J* = 1.5, 10.4 Hz, C**H**=), 6.08 (dd, 1H, *J* = 10.4, 17.3 Hz, C**H**=), 6.36 (dd, 1H, *J* = 1.5, 17.3 Hz, C**H**=), 6.98 (m, 4H, Ar**H**), 7.26 (d, 1H, *J* = 8.8 Hz, Ar**H**$_c$), 7.46 (dd, 1H, *J* = 2.9, 8.8 Hz, Ar**H**$_b$), 7.89 (d, 1H, *J* = 2.9 Hz, Ar**H**$_a$), 8.15 (m, 4H, Ar**H**).

^{13}C NMR ($CDCl_3$) δ (ppm): 11.27, 13.79, 16.45 (-**C**H$_3$), 19.16, 25.09, 26.05, 31.10 (-**C**H$_2$-), 34.60 (-**C**H-), 63.87, 64.85, 67.99, 73.11 (**C**-O), 114.33, 114.38 (Ar**C**), 120.92, 121.30 (Ar**C**-O), 124.75, 124.96, 125.00, 127.19 (Ar**C**), 128.38, 130.63 (**C**=**C**), 132.35, 132.39 (Ar**C**), 148.06, 148.32, 163.64 163.89 (Ar**C**-O), 164.02, 164.57, 164.89, 166.08 (**C**=O).

FTIR ν (cm^{-1}): 2960, 2927, 2876 (C-H), 1720 (C=O), 1605, 1511 (C=C), 1245, 1167, 1066 (C-O), 759.

HRMS (ESI): $C_{37}H_{42}O_{10}$ calculated $[M+Na]^+$ *m/z* 669.2670, measured 669.2649.

DSC: Cr 58.9 °C (N* 43.6 °C) Iso.

EA (CHNS): calculated C: 68.72%, H: 6.55%, found C: 68.95%, H: 6.66%.

7.2.4.16 (*S*)-4''-(Acryloyloxybutyl)-2-(4'-(heptyloxy)benzoyloxy)-5-(4'-(2-methylbutyloxy)benzoyloxy)benzoate (CM4)

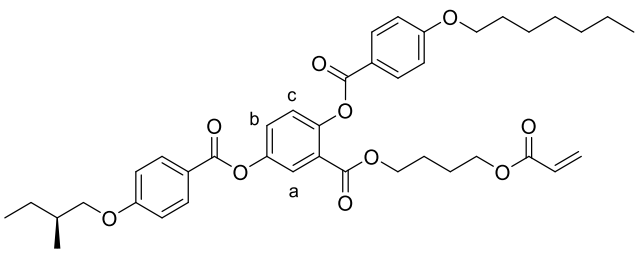

(*S*)-2-(4'-(Heptyloxy)benzoyloxy)-5-(4'-(2-methylbutyloxy)benzoyloxy)benzoic acid (1.00 g, 1.78 mmol), 4-hydroxybutyl acrylate (0.27 cm^3, 1.95 mmol), N-(3-dimethylaminopropyl)-N′-ethylcarbodiimide hydrochloride (0.37 g, 1.95 mmol) and 4-(dimethylamino)pyridine (0.049 g, 0.40 mmol) were added to dichloromethane (50 cm^3) and stirred for 3 days at room temperature. Purification *via* column chromatography on silica gel with dichloromethane as eluting solvent yielded a white solid.

Yield: 0.91 g, 1.33 mmol, 75%.

^{1}H NMR ($CDCl_3$) δ (ppm): 0.91 (t, 3H, *J* = 6.9 Hz, -C**H**$_3$), 0.97 (t, 3H, *J* = 7.4 Hz, -C**H**$_3$), 1.05 (d, 3H, *J* = 6.8 Hz, -C**H**$_3$), 1.25-1.42 (m, 7H, -C**H**$_2$-), 1.43-1.53 (m, 2H, -C**H**$_2$-), 1.54-1.69 (m, 5H, -C**H**$_2$-), 1.77-1.87 (m, 2H, -C**H**$_2$-), 1.87-1.97 (m, 1H, -C**H**-), 3.80-3.91 (m, 2H, -C**H**$_2$O-), 4.03 (t, 2H, *J* = 6.4 Hz, -C**H**$_2$O-), 4.05 (t, 2H, *J* = 6.6 Hz, -C**H**$_2$O-), 4.21 (t, 2H, *J* = 6.3 Hz, -C**H**$_2$O-), 5.80 (dd, 1H, *J* = 1.5, 10.4 Hz, C**H**=), 6.08 (dd, 1H, *J* = 10.4, 17.3 Hz, C**H**=), 6.37 (dd, 1H, *J* = 1.5, 17.3 Hz, C**H**=), 6.98 (m, 4H, Ar**H**), 7.26 (d, 1H, *J* = 8.8 Hz, Ar**H**$_c$), 7.46 (dd, 1H, *J* = 2.9, 8.8 Hz, Ar**H**$_b$), 7.89 (d, 1H, *J* = 2.9 Hz, Ar**H**$_a$), 8.15 (m, 4H, Ar**H**).

^{13}C NMR ($CDCl_3$) δ (ppm): 11.44, 14.22, 16.62 (-**C**H$_3$), 22.74, 22.27, 26.08, 26.22, 29.17, 29.24, 31.90 (-**C**H$_2$-), 34.77 (-**C**H-), 64.03, 65.01, 68.49, 73.28 (**C**-O), 114.50, 114.55 (Ar**C**), 121.10, 121.46 (Ar**C**-O), 124.91, 125.12, 125.16, 127.36 (Ar**C**), 128.55, 130.79 (**C**=**C**), 132.51, 132.56 (Ar**C**), 148.24, 148.49, 163.80, 164.06 (Ar**C**-O), 164.19, 164.73, 164.05, 166.24 (**C**=O).

FTIR ν (cm^{-1}): 2959, 2926, 2874 (C-H), 1718 (C=O), 1607, 1511 (C=C), 1245, 1165, 1066 (C-O), 759.

HRMS (ESI): $C_{40}H_{48}O_{10}$ calculated $[M+Na]^+$ *m/z* 711.3140, measured 711.3112.

DSC: Cr 72.0 °C (N* 50.5 °C) Iso.

EA (CHNS): calculated C: 69.75%, H: 7.02%, found C: 69.38%, H: 7.08%.

7.2.4.17 (*S*)-11''-(Acryloyloxyundecyl)-2-(4'-(2-methylbutyloxy)benzoyloxy)-5-(4'-(butyloxy)benzoyloxy) benzoate (CM5)

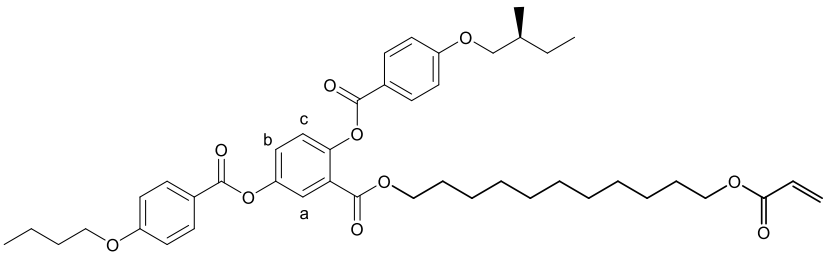

(*S*)-2-(4'-(2-Methylbutyloxy)benzoyloxy)-5-(4'-(butyloxy)benzoyloxy) benzoic acid (1.76 g, 3.38 mmol), 11-acryloyloxyundecanol (1.03 g, 4.25 mmol), N-(3-dimethylaminopropyl)-N′-ethylcarbodiimide hydrochloride (0.98 g, 5.11 mmol) and 4-(dimethylamino)pyridine (0.12 g, 1.01 mmol) were added to dichloromethane (100 cm^3) and stirred for 3 days at room temperature. Purification *via* column chromatography on silica gel with petroleum ether: ethyl acetate: dichloromethane (9:1:1) as eluting solvent yielded a white solid.

Yield: 1.64 g, 2.21 mmol, 65%.

^{1}H NMR ($CDCl_3$) δ (ppm): 0.97 (t, 3H, *J* = 7.5 Hz, -C**H**$_3$), 1.00 (t, 3H, *J* = 7.4 Hz, -C**H**$_3$), 1.04 (d, 3H, J = 6.8 Hz, -C**H**$_3$), 1.10-1.40 (m, 16H, -C**H**$_2$-), 1.42-1.60 (m, 4H, -C**H**$_2$-), 1.61-1.70 (m, 2H, -C**H**$_2$-), 1.77-1.86 (m, 2H, -C**H**$_2$-), 1.86-1.96 (m, 1H, -C**H**-), 3.80-3.94 (m, 2H, -C**H**$_2$O-), 4.06 (t, 2H, *J* = 6.5 Hz, -C**H**$_2$O-), 4.14 (t, 2H, *J* = 6.8 Hz, -C**H**$_2$O-), 4.15 (t, 2H, *J* = 6.8 Hz, -C**H**$_2$O-), 5.80 (dd, 1H, *J* = 1.5, 10.4 Hz, C**H**=), 6.11 (dd, 1H, *J* = 10.4, 17.3 Hz, C**H**=), 6.39 (dd, 1H, *J* = 1.5, 17.3 Hz, C**H**=), 6.98 (m, 4H, Ar**H**), 7.26 (d, 1H, *J* = 8.7 Hz, Ar**H**$_c$), 7.45 (dd, 1H, *J* = 2.9, 8.7 Hz, Ar**H**$_b$), 7.89 (d, 1H, *J* = 2.9 Hz, Ar**H**$_a$), 8.15 (m, 4H, Ar**H**).

^{13}C NMR ($CDCl_3$) δ (ppm): 11.44, 13.96, 16.63 (-**C**H_3), 19.34, 25.96, 26.07, 26.23, 28.53, 28.75, 29.32, 29.39, 29.53, 29.61, 31.27 (-**C**H_2-), 34.78 (-**C**H-), 64.85, 65.80, 68.19, 73.25 (**C**-O), 114.48, 114.53, 121.18, 121.56, 125.14, 127.20 (Ar**C**), 128.80, 130.56 (**C**=**C**), 132.53, 132.59 (Ar**C**), 148.24, 148.46 (Ar**C**-O), 163.89, 164.30, (Ar**C**-O), 164.75, 165.09, 166.49 (**C**=O).

FTIR ν (cm^{-1}): 2958, 2919, 2857 (C-H), 1720 (C=O), 1607 (C=C), 1247, 1161, 1072 (C-O), 844, 757.

HRMS (ESI): $C_{44}H_{56}O_{10}$ calculated $[M+Na]^+$ *m/z* 767.3766, measured 767.3733.

DSC: Cr 50.7 °C (N* 40.8 °C) Iso.

EA (CHNS): calculated C: 70.94%, H: 7.58%, found C: 71.17%, H: 7.86%.

7.2.4.18 (*S*)-11''-(Acryloyloxyundecyl)-2-(4'-(butyloxy)benzoyloxy)-5-(4'-(2-methylbutyloxy)benzoyloxy) benzoate (CM6)

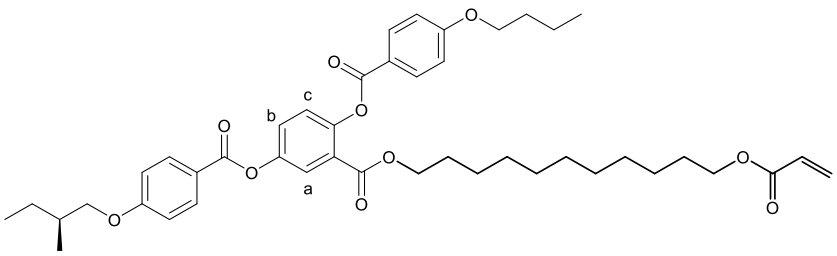

(*S*)-2-(4'-(Butyloxy)benzoyloxy)-5-(4'-(2-methylbutyloxy)benzoyloxy)benzoic acid (1.85 g, 3.55 mmol), 11-acryloyloxyundecanol (1.26 g, 5.19 mmol), N-(3-dimethylaminopropyl)-N′-ethylcarbodiimide hydrochloride (1.00 g, 5.24 mmol) and 4-(dimethylamino)pyridine (0.13 g, 1.05 mmol) were added to dichloromethane (100 cm^3) and stirred for 3 days at room temperature. Purification *via* column chromatography on silica gel with petroleum ether: acetone (19:1) as eluting solvent yielded a white solid.

Yield: 1.02 g, 1.37 mmol, 39%.

^{1}H NMR ($CDCl_3$) δ (ppm): 0.91 (t, 3H, *J* = 7.5 Hz, -C**H**$_3$), 1.00 (t, 3H, *J* = 7.4 Hz, -C**H**$_3$), 1.05 (d, 3H, *J* = 6.8 Hz, -C**H**$_3$), 1.10-1.40 (m, 16H, -C**H**$_2$-), 1.42-1.60 (m, 4H, -C**H**$_2$-), 1.61-1.70 (m, 2H, -C**H**$_2$-), 1.77-1.86 (m, 2H, -C**H**$_2$-), 1.86-1.96 (m, 1H, -C**H**-), 3.81-3.95 (m, 2H, -C**H**$_2$O-), 4.05 (t, 2H, *J* = 6.5 Hz, -C**H**$_2$O-), 4.14 (t, 2H, *J* =6.8 Hz, -C**H**$_2$O-), 4.15 (t, 2H, *J* = 6.8 Hz, -C**H**$_2$O-), 5.81 (dd, 1H, *J* = 1.5, 10.4 Hz, C**H**=), 6.11 (dd, 1H, *J* = 10.4, 17.3 Hz, C**H**=), 6.39 (dd, 1H, *J* = 1.5, 17.3 Hz, C**H**=), 6.98 (m, 4H, Ar**H**), 7.26 (d, 1H, *J* = 8.8 Hz, Ar**H**$_c$), 7.45 (dd, 1H, *J* = 2.9, 8.8 Hz, Ar**H**$_b$), 7.89 (d, 1H, *J* = 2.9 Hz, Ar**H**$_a$), 8.15 (m, 4H, Ar**H**).

^{13}C NMR ($CDCl_3$) δ (ppm): 11.45, 13.96, 16.63 (-**C**H$_3$), 19.34, 25.96, 26.07, 26.23, 28.53, 28.75, 29.32, 29.39, 29.53, 29.61, 31.28 (-**C**H$_2$-), 34.78 (-**C**H-), 64.85, 65.80, 68.14, 73.29 (**C**-O), 114.45, 114.55, 121.14, 121.60, 125.14, 127.21 (Ar**C**), 128.79, 130.56 (**C**=**C**), 132.51, 132.60 (Ar**C**), 148.23, 148.47 (Ar**C**-O), 163.73, 164.05, (Ar**C**-O) 164.30, 164.76, 165.08, 166.49 (**C**=O).

FTIR ν (cm^{-1}): 2959, 2926, 2874 (C-H), 1718 (C=O), 1607, 1511 (C=C), 1245, 1165, 1066 (C-O), 759.

HRMS (ESI): $C_{44}H_{56}O_{10}$ calculated $[M+Na]^+$ *m/z* 767.3766, measured 767.3740.

DSC: Cr 47.9 °C (N* 43.9 °C) Iso.

EA (CHNS): calculated C: 70.94%, H: 7.58%, found C: 70.96%, H: 7.77%.

7.2.4.19 (*S*)-11''-(Acryloyloxyundecyl)-2-(4'-(2-methylbutyloxy)benzoyloxy)-5-(4'-(heptyloxy)benzoyloxy) benzoate (CM7)

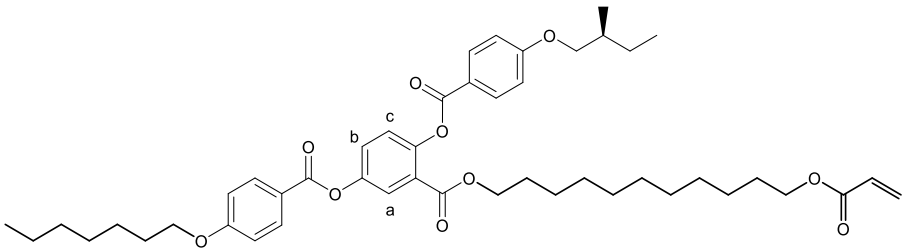

(*S*)-2-(4'-(2-methyl butyloxy)benzoyloxy)-5-(4'-(heptyloxy)benzoyloxy) benzoic acid (1.93 g, 3.44 mmol), 11-acryloyloxyundecanol (0.84 g, 3.46 mmol), N-(3-dimethylaminopropyl)-N′-ethylcarbodiimide hydrochloride (0.66 g, 3.45 mmol) and 4-(dimethylamino)pyridine (0.08 g, 0.68 mmol) were added to dichloromethane (100 cm^3) and stirred for 3 days at room temperature. Purification *via* column chromatography on silica gel with petroleum ether: ethyl acetate (9:1) as eluting solvent yielded a white solid.

Yield: 1.64 g, 2.21 mmol, 61%.

^{1}H NMR ($CDCl_3$) δ (ppm): 0.91 (t, 3H, *J* = 6.8 Hz, -C**H**$_3$), 0.97 (t, 3H, *J* = 7.4 Hz, -C**H**$_3$), 1.04 (d, 3H, *J* = 6.8 Hz, -C**H**$_3$), 1.10-1.42 (m, 22H, -C**H**$_2$-), 1.43-1.53 (m, 4H, -C**H**$_2$-), 1.61-1.70 (m, 2H, -C**H**$_2$-), 1.78-1.87 (m, 2H, -C**H**$_2$-), 1.88-1.97 (m, 1H, -C**H**-), 3.79-3.94 (m, 2H, -C**H**$_2$O-), 4.05 (t, 2H, *J* = 6.6 Hz, -C**H**$_2$O-), 4.14 (t, 2H, *J* = 6.7 Hz, -C**H**$_2$O-), 4.15 (t, 2H, *J* = 6.8 Hz, -C**H**$_2$O-), 5.80 (dd, 1H, *J* = 1.4, 10.4 Hz, C**H**=), 6.11 (dd, 1H, *J* = 10.4, 17.4 Hz, C**H**=), 6.39 (dd, 1H, *J* = 1.4, 17.3 Hz, C**H**=), 6.98 (m, 4H, Ar**H**), 7.26 (d, 1H, *J* = 8.7 Hz, Ar**H**$_c$), 7.45 (dd, 1H, *J* = 2.9, 8.7 Hz, Ar**H**$_b$), 7.89 (d, 1H, *J* = 2.8 Hz, Ar**H**$_a$), 8.15 (m, 4H, Ar**H**).

^{13}C NMR ($CDCl_3$) δ (ppm): 11.28, 14.06, 16.46 (-**C**H_3), 22.58, 25.79, 25.90, 25.92, 26.07, 28.37, 28.59, 29.01, 29.07, 29.16, 29.22, 29.36, 29.44, 31.74 (-**C**H_2-), 34.61 (-**C**H-), 64.68, 65.63, 68.35, 73.09 (**C**-O), 114.31, 114.36, 121.01, 121.40, 124.98, 127.03 (Ar**C**), 128.63, 130.38 (**C**=**C**), 132.36, 132.42 (Ar**C**), 148.07, 148.30 (Ar**C**-O), 163.73, (Ar**C**-O), 164.13, 164.57, 164.92, 166.31 (**C**=O).

FTIR ν (cm^{-1}): 2920, 2853 (C-H), 1733, 1716 (C=O), 1607 (C=C), 1245, 1165, 1068 (C-O), 759.

HRMS (ESI): $C_{47}H_{62}O_{10}$ calculated $[M+Na]^+$ *m/z* 809.4235, measured 809.4198.

DSC: Cr 33.7 °C N* 43.3 °C Iso.

EA (CHNS): calculated C: 71.73%, H: 7.94%, found C: 71.79%, H: 8.11%.

7.2.4.20 (*S*)-11''-(Acryloyloxyundecyl)-2-(4'-(heptyloxy)benzoyloxy)-5-(4'-(2-methylbutyloxy)benzoyloxy) benzoate (CM8)

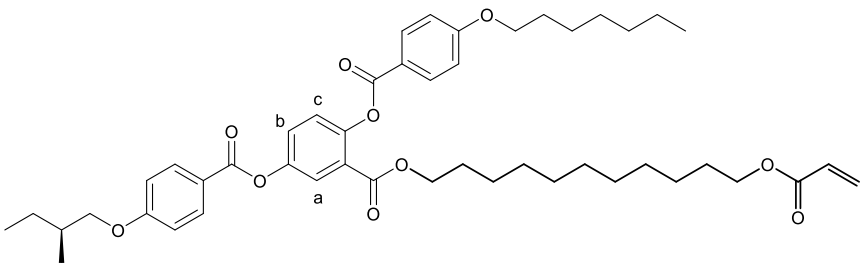

(*S*)-2-(4'-(Heptyloxy)benzoyloxy)-5-(4'-(2-methylbutyloxy)benzoyloxy)benzoic acid (1.00 g, 1.78 mmol), 11-acryloyloxyundecanol (0.48 g, 1.99 mmol), N-(3-dimethylaminopropyl)-N′-ethylcarbodiimide hydrochloride (0.38 g, 2.00 mmol) and 4-(dimethylamino)pyridine (0.049 g, 0.40 mmol) were added to dichloromethane (50 cm^3) and stirred for 3 days at room temperature. Purification *via* column chromatography on silica gel with petroleum ether: ethyl acetate (9:1) as eluting solvent yielded a white solid.

Yield: 0.87 g, 1.10 mmol, 62%.

^{1}H NMR ($CDCl_3$) δ (ppm): 0.91 (t, 3H, *J* = 6.9 Hz, -C**H**$_3$), 0.97 (t, 3H, *J* = 7.4 Hz, -C**H**$_3$), 1.05 (d, 3H, *J* = 6.8 Hz, -C**H**$_3$), 1.13-1.42 (m, 22H, -C**H**$_2$-), 1.43-1.52 (m, 4H, -C**H**$_2$-), 1.54-1.70 (m, 4H, -C**H**$_2$-), 1.77-1.87 (m, 2H, -C**H**$_2$-), 1.87-1.97 (m, 1H, -C**H**-), 3.80-3.95 (m, 2H, -C**H**$_2$O-), 4.04 (t, 2H, *J* = 6.6 Hz, -C**H**$_2$O-), 4.14 (t, 2H, *J* = 6.7 Hz, -C**H**$_2$O-), 4.15 (t, 2H, *J* = 6.8 Hz, -C**H**$_2$O-), 5.80 (dd, 1H, *J* = 1.5, 10.4 Hz, C**H**=), 6.08 (dd, 1H, *J* = 10.4, 17.4 Hz, C**H**=), 6.37 (dd, 1H, *J* = 1.5, 17.4 Hz, C**H**=), 6.98 (m, 4H, Ar**H**), 7.26 (d, 1H, *J* = 8.8 Hz, Ar**H**$_c$), 7.46 (dd, 1H, *J* = 2.9, 8.8 Hz, Ar**H**$_b$), 7.89 (d, 1H, *J* = 2.9 Hz, Ar**H**$_a$), 8.15 (m, 4H, Ar**H**).

^{13}C NMR ($CDCl_3$) δ (ppm): 11.43, 14.21, 16.61 (-**C**H_3), 22.74, 25.94, 26.05, 26.08, 26.21, 28.52, 28.73, 29.17, 29.24, 29.31, 29.37, 29.51, 29.59, 31.90 (-**C**H_2-), 34.76 (-**C**H-), 64.83, 65.78, 68.45, 73.27 (**C**-O), 114.44, 114.53 (Ar**C**), 121.12, 121.53 (Ar**C**-O), 125.12, 127.19 (Ar**C**), 128.78, 130.54 (**C**=**C**), 132.49, 132.58 (Ar**C**), 148.22, 148.45, 163.71, 164.03 (Ar**C**-O), 164.28, 164.73, 165.05, 166.46 (**C**=O).

FTIR ν (cm^{-1}): 2956, 2920, 2853 (C-H), 1724, 1703 (C=O), 1605 (C=C), 1247, 1161, 1060 (C-O), 848, 762.

HRMS (ESI): $C_{47}H_{62}O_{10}$ calculated $[M+Na]^+$ *m/z* 809.4235, measured 809.4207.

DSC: Cr 47.7 °C (N* 41.9 °C) Iso.

EA (CHNS): calculated C: 71.73%, H: 7.94%, found C: 72.07%, H: 8.17%.

7.2.4.21 (*S*)-4''-(Acryloyloxybutyl) 2-(4'-(1-methylheptyloxy)benzoyloxy)-5-(4'-heptyloxybenzoyloxy)benzoate (CM9)

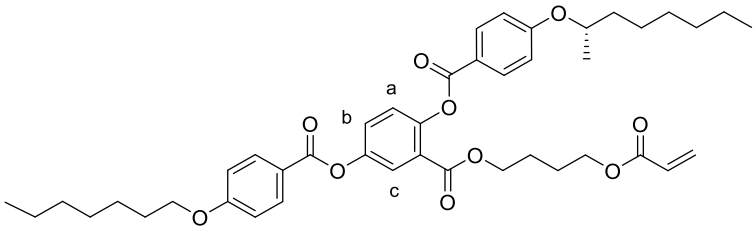

(*S*)-2-(4'-(1-Methylheptyloxy)benzoyloxy)-5-(4'-(heptyloxy)benzoyloxy) benzoic acid (0.84 g, 1.4 mmol), 4-hydroxybutyl acrylate (0.19 cm^3, 1.4 mmol), N-(3-dimethylaminopropyl)-N′-ethylcarbodiimide hydrochloride (0.26 g, 1.4 mmol) and 4-(dimethylamino)pyridine (0.17 g, 1.4 mmol) were added to dichloromethane (250 cm^3) and stirred for 64 hours at room temperature. Purification *via* column chromatography on silica gel with petroleum ether: ethyl acetate (8:2) as eluting solvent yielded a white solid.

Yield: 0.49 g, 0.67 mmol, 48%.

^{1}H NMR ($CDCl_3$) δ (ppm): 0.89 (t, 3H, *J* = 7.0 Hz, -C**H**$_3$), 0.91 (t, 3H, *J* = 6.8 Hz, -C**H**$_3$), 1.34 (d, 3H, *J* = 6.0 Hz, -C**H**$_3$), 1.25-1.42 (m, 13H, -C**H**$_2$-), 1.42-1.53 (m, 3H, -C**H**$_2$-), 1.57-1.71 (m, 5H, -C**H**$_2$-), 1.73-1.88 (m, 3H, -C**H**$_2$-), 4.04 (t, 2H, *J* = 6.1 Hz, -C**H**$_2$O-), 4.05 (t, 2H, *J* = 6.6 Hz, -C**H**$_2$O-), 4.21 (t, 2H, *J* = 6.3 Hz, -C**H**$_2$O-), 4.49 (m, 1H, -C**H**O-), 5.79 (dd, 1H, *J* = 1.5, 10.4 Hz, C**H**=), 6.08 (dd, 1H, *J* = 10.4, 17.3 Hz, C**H**=), 6.36 (dd, 1H, *J* = 1.5, 17.3 Hz, C**H**=), 6.97 (m, 4H, Ar**H**), 7.26 (d, 1H, *J* = 8.8 Hz, Ar**H**$_c$), 7.46 (dd, 1H, *J* = 2.9, 8.8 Hz, Ar**H**$_b$), 7.89 (d, 1H, *J* = 2.8 Hz, Ar**H**$_a$), 8.15 (m, 4H, Ar**H**).

^{13}C NMR ($CDCl_3$) δ (ppm): 14.06, 19.57 (-**C**H$_3$), 22.58, 25.14, 25.41, 25.93 29.01, 29.08, 29.21, 31.74, 31.76, 36.31 (-**C**H$_2$-), 63.87, 64.84, 68.36, 74.14 (**C**-O), 114.38, 115.24, 120.98, 121.02, 124.73, 124.92, 125.02, 127.20 (Ar**C**), 128.40, 130.64 (**C**=**C**), 132.38, 132.47 (Ar**C**), 148.14, 148.31 (Ar**C**-O), 162.87, 163.75, 163.99, 164.58, 164.89, 166.09 (**C**=O).

FTIR ν (cm^{-1}): 2924, 2855 (C-H), 1722 (C=O), 1605 (C=C), 1247, 1165, 1068 (C-O), 758.

HRMS (ESI): $C_{43}H_{54}O_{10}$ calculated $[M+Na]^+$ *m/z* 753.3609, measured 753.3609.

DSC: Cr 58.1 °C (N* 19.5 °C) Iso.

EA (CHNS): calculated C: 70.66%, H: 7.45%, found C: 70.79%, H: 7.60%.

7.3 Synthesis of Polymer Films

7.3.1 Nematic Polymers

The synthesis of thin films of the nematic polymers **P1**-**P4** were completed by UV-initiated radical polymerisation using the representative method below. Table 7.1 summarises the composition and polymerisation conditions.

The monomer **M1** and 2 mol% photoinitiator 2,4,6-trimethylbenzoyldiphenylphosphine oxide were dissolved in chloroform in an amber glass vial. Once mixed, the solvent was evaporated under a flow of nitrogen. The mixture was drawn into a 25-μm planar aligned glass cell in the isotropic phase by capillary action, cooled to the nematic phase and annealed for 10 minutes at 55 °C. The cell was then irradiated using an Omnicure LX500 UV spot curing system at 365 nm, for 10 minutes, at 50% intensity, from a distance of 30 cm at 55 °C. After analysis by POM, the glass cell was carefully prised open with a scalpel, following immersion in liquid nitrogen, for further analysis by DSC, NMR and GPC.

Table 7.1. Composition and polymerisation conditions of nematic polymers created by UV-initiated radical polymerisation.

Polymer	Monomer	Polymerisation Temperature/°C
P1	**M1**	55
P2	**M2**	55
P3	**M3**	55
P4	**M4**	55

Characterisation data for polymer **P1**:

^{1}H NMR ($CDCl_3$) δ (ppm): 0.90 (br m, 6H, -C**H**$_3$), 1.27-1.52 (br m, 8H, -C**H**$_2$-), 1.53-1.79 (br m, 6H, -C**H**$_2$-), 2.05 (br m, 1H, -C**H**-), 3.56-4.19 (br m, 8H, -C**H**$_2$O-), 6.81 (br m, 4H, Ar**H**), 7.09 (br m, 1H, Ar**H**), 7.29 (br m, 1H, Ar**H**), 7.74 (br m, 1H, Ar**H**), 7.97 (br m, 4H, Ar**H**).

DSC: g 41 °C N 117 °C Iso.

GPC: M_n: 1,270,000 g mol^{-1}

Polydispersity (M_w/M_n): 1.8

Characterisation data for polymer **P2**:

^{1}H NMR ($CDCl_3$) δ (ppm): 0.86 (br m, 6H, -C**H**$_3$), 1.13-1.53 (br m, 21H, -C**H**$_2$-), 1.57-1.88 (br m, 5H, -C**H**$_2$-), 2.05 (br m, 1H, -C**H**-), 3.58-4.16 (br m, 8H, -C**H**$_2$O-), 6.80 (br m, 4H, Ar**H**), 7.07 (br m, 1H, Ar**H**), 7.24 (br m, 1H, Ar**H**), 7.73 (br m, 1H, Ar**H**), 7.96 (br m, 4H, Ar**H**).
DSC: g 15 °C N 78 °C Iso.
GPC: M_n: 569,100 g mol^{-1}
Polydispersity (M_w/M_n): 1.9

Characterisation data for polymer **P3**:

^{1}H NMR ($CDCl_3$) δ (ppm): 0.94 (br m, 6H, -C**H**$_3$), 1.03-1.32 (br m, 14H, -C**H**$_2$-), 1.33-1.61 (br m, 9H, -C**H**$_2$-), 1.66-1.85 (br m, 5H, -C**H**$_2$-), 2.20 (br m, 1H, -C**H**-), 3.98 (br m, 6H, -C**H**$_2$O-), 4.06 (br m, 2H, -C**H**$_2$O-), 6.90 (br m, 4H, Ar**H**), 7.19 (br m, 1H, Ar**H**), 7.38 (br m, 1H, Ar**H**), 7.84 (br m, 1H, Ar**H**), 8.08 (br m, 4H, Ar**H**).
DSC: g 13 °C N 90 °C Iso.
GPC: M_n: 621,200 g mol^{-1}
Polydispersity (M_w/M_n): 2.3

Characterisation data for polymer **P4**:

^{1}H NMR ($CDCl_3$) δ (ppm): 0.86 (br m, 6H, -C**H**$_3$), 1.03-1.60 (br m, 34H, -C**H**$_2$-), 1.61-1.85 (br m, 6H, -C**H**$_2$-), 2.19 (br m, 1H, -C**H**-), 3.83-4.18 (br m, 8H, -C**H**$_2$O-), 6.90 (br m, 4H, Ar**H**), 7.19 (br m, 1H, Ar**H**), 7.38 (br m, 1H, Ar**H**), 7.83 (br m, 1H, Ar**H**), 8.08 (br m, 4H, Ar**H**).
DSC: g 5 °C N 75 °C Iso.
GPC: M_n: 935,800 g mol^{-1}
Polydispersity (M_w/M_n): 2.0

7.3.2 Chiral Nematic Polymers

The synthesis of thin-films of the chiral polymers **CP1**-**CP9** were completed by UV-initiated radical polymerisation using the representative method below. Table 7.2 summarises the composition and polymerisation conditions.

The monomer **CM1** and 2 mol% photoinitiator 2,4,6-trimethylbenzoyldiphenylphosphine oxide were dissolved in chloroform in an amber glass vial. Once mixed, the solvent was evaporated under a flow of nitrogen. The mixture was drawn into a 25-μm planar aligned glass cell in the isotropic phase by capillary action, cooled to the chiral nematic phase, sheared to induce a strong homogeneous alignment, and annealed for 30 minutes at 30 °C. The cell was then irradiated using an Omnicure LX500 UV spot curing system at 365 nm for 10 minutes from a distance of 30 cm at 30 °C. After microscopic analysis, the glass cell was carefully prised open with a scalpel, following immersion in liquid nitrogen, for further analysis by DSC and GPC.

Table 7.2. Composition and polymerisation conditions of chiral nematic polymers created by UV-initiated radical polymerisation.

Polymer	Monomer	Polymerisation Temperature/°C
CP1	**CM1**	30
CP2	**CM2**	30
CP3	**CM3**	30
CP4	**CM4**	30
CP5	**CM5**	30
CP6	**CM6**	30
CP7	**CM7**	30
CP8	**CM8**	30
CP9	**CM9**	10

Characterisation data for chiral polymer **CP1**:

^{1}H NMR ($CDCl_3$) δ (ppm): 0.81-0.97 (br m, 9H, -C**H$_3$**), 1.32-1.61 (br m, 10H, -C**H$_2$**-), 1.66-1.80 (br m, 3H, -C**H$_2$**-), 2.06 (br m, 1H, -C**H**-), 3.60-4.06 (br m, 8H, -C**H$_2$**O-), 6.81 (br m, 4H, Ar**H**), 7.08 (br m, 1H, Ar**H**), 7.27 (br m, 1H, Ar**H**), 7.74 (br m, 1H, Ar**H**), 7.97 (br m, 4H, Ar**H**).

DSC: g 40°C N* 75 °C Iso.

GPC: M_n: 2,456,000 g mol^{-1}

Polydispersity (M_w/M_n): 1.1

Characterisation data for chiral polymer **CP2**:

^{1}H NMR ($CDCl_3$) δ (ppm): 0.80-1.00 (br m, 9H, -C**H$_3$**), 1.16-1.70 (br m, 12H, -C**H$_2$**-), 1.81 (br m, 1H, -C**H$_2$**-), 2.06 (br m, 1H, -C**H**-), 3.58-4.10 (br m, 8H, -C**H$_2$**O-), 6.82 (br m, 4H, Ar**H**), 7.08 (br m, 1H, Ar**H**), 7.28 (br m, 1H, Ar**H**), 7.75 (br m, 1H, Ar**H**), 7.97 (br m, 4H, Ar**H**).
DSC: g 39 °C N* 60 °C Iso.
GPC: M_n: 1,319,000 g mol^{-1}
Polydispersity (M_w/M_n): 1.9

Characterisation data for chiral polymer **CP3**:

^{1}H NMR ($CDCl_3$) δ (ppm): 0.86 (br m, 9H, -C**H$_3$**), 1.07-1.54 (br m, 14H, -C**H$_2$**-), 1.55-1.86 (br m, 5H, -C**H$_2$**-), 2.06 (br m, 1H, -C**H**-), 3.57-4.13 (br m, 8H, -C**H$_2$**O-), 6.81 (br m, 4H, Ar**H**), 7.07 (br m, 1H, Ar**H**), 7.27 (br m, 1H, Ar**H**), 7.74 (br m, 1H, Ar**H**), 7.97 (br m, 4H, Ar**H**).
DSC: g 26 °C N* 65 °C Iso.
GPC: M_n: 1,670,000 g mol^{-1}
Polydispersity (M_w/M_n): 1.8

Characterisation data for chiral polymer **CP4**:

^{1}H NMR ($CDCl_3$) δ (ppm): 0.76-1.02 (br m, 9H, -C**H$_3$**), 1.13-1.54 (br m, 14H, -C**H$_2$**-), 1.57-1.88 br m, 5H, -C**H$_2$**-), 2.06 (br m, 1H, -C**H**-), 3.57-4.12 (br m, 8H, -C**H$_2$**O-), 6.81 (br m, 4H, Ar**H**), 7.07 (br m, 1H, Ar**H**), 7.27 (br m, 1H, Ar**H**), 7.73 (br m, 1H, Ar**H**), 7.96 (br m, 4H, Ar**H**).
DSC: g 31 °C N* 56 °C Iso.
GPC: M_n: 609,700 g mol^{-1}
Polydispersity (M_w/M_n): 2.5

Characterisation data for chiral polymer **CP5**:

^{1}H NMR ($CDCl_3$) δ (ppm): 0.93-1.07 (br m, 9H, -C**H$_3$**), 1.09-1.31 (br m, 23H, -C**H$_2$**-), 1.71-1.81 (br m, 4H, -C**H$_2$**-), 2.19 (br m, 1H, -C**H**-), 3.73-4.02 (br m, 8H, -C**H$_2$**O-), 6.91 (br m, 4H, Ar**H**), 7.19 (br m, 1H, Ar**H**), 7.40 (br m, 1H, Ar**H**), 7.84 (br m, 1H, Ar**H**), 8.07 (br m, 4H, Ar**H**).
DSC: g 16 °C N* 55 °C Iso.
GPC: M_n: 36,000 g mol^{-1}
Polydispersity (M_w/M_n): 2.6

Characterisation data for chiral polymer **CP6**:

^{1}H NMR ($CDCl_3$) δ (ppm): 0.93-1.07 (br m, 9H, -C**H$_3$**), 1.03-1.30 (br m, 14H, -C**H$_2$**-), 1.33-1.90 (br m, 13H, -C**H$_2$**-), 2.19 (br m, 1H, -C**H**-), 3.73-4.18 (br m, 8H, -C**H$_2$**O-), 6.91 (br m, 4H, Ar**H**), 7.18 (br m, 1H, Ar**H**), 7.38 (br m, 1H, Ar**H**), 7.84 (br m, 1H, Ar**H**), 8.08 (br m, 4H, Ar**H**).

DSC: g 17 °C N* 57 °C Iso.

GPC: M_n: 690,000 g mol^{-1}

Polydispersity (M_w/M_n): 1.5

Characterisation data for chiral polymer **CP7**:

^{1}H NMR ($CDCl_3$) δ (ppm): 0.81-1.02 (br m, 9H, -C**H$_3$**), 1.03-1.89 (br m, 33H, -C**H$_2$**-), 2.19 (br m, 1H, -C**H**-), 3.68-4.18 (br m, 8H, -C**H$_2$**O-), 6.91 (br m, 4H, Ar**H**), 7.19 (br m, 1H, Ar**H**), 7.38 (br m, 1H, Ar**H**), 7.84 (br m, 1H, Ar**H**), 8.08 (br m, 4H, Ar**H**).

DSC: g 9 °C N* 55 °C Iso.

GPC: M_n: 2,361,000 g mol^{-1}

Polydispersity (M_w/M_n): 1.7

Characterisation data for chiral polymer **CP8**:

^{1}H NMR ($CDCl_3$) δ (ppm): 0.81-1.03 (br m, 9H, -C**H$_3$**), 1.07-1.92 (br m, 33H, -C**H$_2$**-), 2.19 (br m, 1H, -C**H**-), 3.71-4.17 (br m, 8H, -C**H$_2$**O-), 6.90 (br m, 4H, Ar**H**), 7.18 (br m, 1H, Ar**H**), 7.38 (br m, 1H, Ar**H**), 7.83 (br m, 1H, Ar**H**), 8.08 (br m, 4H, Ar**H**).

DSC: g 10 °C N* 47 °C Iso.

GPC: M_n: 2,180,000 g mol^{-1}

Polydispersity (M_w/M_n): 1.6

Characterisation data for chiral polymer **CP9**:

^{1}H NMR ($CDCl_3$) δ (ppm): 0.76-0.93 (br m, 9H, -C**H$_3$**), 1.12-1.82 (br m, 25H, -C**H$_2$**-), 2.06 (br m, 1H, -C**H**-), 3.61-4.45 (br m, 8H, -C**H$_2$**O-), 6.80 (br m, 4H, Ar**H**), 7.07 (br m, 1H, Ar**H**), 7.31 (br m, 1H, Ar**H**), 7.74 (br m, 1H, Ar**H**), 7.97 (br m, 4H, Ar**H**).

DSC: g 12 °C N* 22 °C Iso.

GPC: M_n: 302,000 g mol^{-1}

Polydispersity (M_w/M_n): 2.6

7.4 Synthesis of Elastomer Films

The synthesis of thin films of the nematic elastomers **E1**-**E4** and the doped chiral nematic elastomers **E1A**-**F**, **E2A**-**D**, **E3A** and **E4A**-**B** were completed by UV-initiated radical polymerisation using the representative method below. Tables 7.3 and 7.4 summarise the polymerisation temperatures and compositions of the mixtures used.

7.4.1 Nematic Elastomers

The monomer **M1**, crosslinker 1,6-hexanediol diacrylate (10 mol%) and photoinitiator 2,4,6-trimethylbenzoyldiphenylphosphine oxide (2 mol%) were dissolved in chloroform in an amber glass vial. Once mixed, the solvent was evaporated under a flow of nitrogen. The mixture was drawn into a 10-μm planar aligned glass cell in the isotropic phase by capillary action, cooled to the nematic phase and annealed for 10 minutes at 55 °C, then irradiated using an Omnicure LX500 UV spot curing system at 365 nm, for 10 minutes, at 50% intensity, from a distance of 30 cm at 55 °C. After analysis by POM, the glass cell was carefully opened with a scalpel, following immersion in liquid nitrogen, for further analysis by DSC.

Table 7.3. Composition and polymerisation conditions of nematic elastomers created by UV-initiated radical polymerisation.

Elastomer	Monomer	Polymerisation Temperature/°C
E1	**M1**	55
E2	**M2**	55
E3	**M3**	45
E4	**M4**	55

7.4.2 Chiral-Doped Elastomers

The monomer **M1**, CB15 (22 wt%), crosslinker 1,6-hexanediol diacrylate (10 mol%) and photoinitiator 2,4,6-trimethylbenzoyldiphenylphosphine oxide (2 mol%) were dissolved in chloroform in an amber glass vial. Once mixed, the solvent was evaporated under a flow of nitrogen. The mixture was drawn into a 10-μm planar aligned glass cell in the isotropic phase by capillary action, cooled to the chiral nematic phase and annealed for 60 minutes at 45 °C then irradiated using an Omnicure LX500 UV spot curing system at 365 nm for 10 minutes from a distance of 30 cm at 45 °C. After analysis by POM and UV-Vis, the glass cell was carefully prised open with a scalpel, following immersion in liquid nitrogen. The CB15 was removed by washing the exposed film with acetone (500 μL) and allowed to air dry. The imprinted elastomer film was then re-analysed by POM, UV-Vis and DSC. The responsive properties were investigated using POM by cutting a small sample of the film, immersing in PEG200 and sandwiching between a glass slide and cover slip.

Table 7.4. Composition and polymerisation conditions of doped chiral nematic elastomer mixtures created by UV-initiated radical polymerisation.

Elastomer	Monomer	CB15 wt%	Polymerisation Temperature/°C
E1A	**M1**	14	50
E1B	**M1**	18	50
E1C	**M1**	22	45
E1D	**M1**	29	40
E1E	**M1**	35	31
E1F	**M1**	41	27
E2A	**M2**	17	35
E2B	**M2**	19	30
E2C	**M2**	22	35
E2D	**M2**	24	35
E3A	**M3**	18	40
E4A	**M4**	22	30
E4B	**M4**	41	20

7.5 Microfluidic Synthesis

The creation of nematic and chiral nematic polymer and elastomer microparticles was completed using the following developed procedures. Details of the microfluidic chip, flow rates, polymerisation conditions and experimental outcomes are summarised in Tables 7.5 – 7.17.

7.5.1 Preparation of PVA Solution

To a round bottomed flask, 3g of poly(vinyl alcohol) (M_n: 13,000-23,000 g mol^{-1}, 87-89% hydrolysis) was added. 97g of deionised water (Milli-Q) was added and then heated to reflux at 80 °C for 1 hour. The 3 wt% solution was allowed to cool to room temperature and filtered through a syringe filter (cellulose, 0.2 μm) into 15 cm^3 centrifuge tubes for storage.

7.5.2 Microfluidic Chip Construction

Borosilicate hollow round capillaries (VitroCom, I.D. 0.70 mm, 0.87 mm O.D.) were pulled using a micropipette puller (P-30, Sutter Instruments). Inner phase capillary tips were pulled to a sub-μm point (Heat: 840, micrometre: 4.5 mm) whilst collection capillaries were pulled to ~180 μm (Heat: 840, micrometre: 5.4 mm) and carefully scored with a ceramic blade to produce a clean break. Inner phase capillary tips were placed in a small PE bag, submersed in IPA, and sonicated for 5-20 seconds. The tips were inspected by microscopy, the sonication was repeated until a clean break and a tip diameter of ~ 20 μm was found.

The inlet and outlet connectors were fabricated from syringe needles (23G, I.D. 0.6 mm x 1 mm). The needle tips were cut to ~2 mm and sanded with a file to remove any metal burrs. The female luer connectors were cut and notches added to allow fitment over the square and round capillaries. The connectors were sonicated for 1 minute in isopropyl alcohol (IPA) and dried. Any remaining debris within the cut needle was removed using a small piece of PEEK tubing (O.D. 360 μm) as a pipe cleaner.

The pulled round capillaries were inserted into a square capillary (VitroCom, I.D. 1.00 mm x 1.00 mm), aligned ~80 μm apart and glued with Araldite Rapid 2-part epoxy. The tubing connectors were subsequently attached and sealed using Araldite Rapid.

7.5.3 Microfluidic Chip Set-Up

The homemade microfluidic chip was connected to the syringes, containing the inner and outer phases, and collection petri dishes (borosilicate) using thin-walled PTFE tubing (I.D. 0.5588 mm, O.D. 1.0668 mm). The chip set-up and droplet production was viewed using an upright microscope (Leica CM E). The flow of the inner and outer phases was controlled independently by two syringe pumps (Chemyx Fusion 400 and WPI SP100iZ). Deionised water (Milli-Q) was introduced into the chip to ensure any air bubbles were removed, before the attachment of the syringes containing the inner and outer phases.

The inner phase, representatively consisting of monomer **M1**, crosslinker 1,6-hexanediol diacrylate (10 mol%) and photoinitiator 2,4,6-trimethylbenzoyldiphenylphosphine oxide (2 mol%), was dissolved in chloroform and filtered using a syringe filter (PVDF, 0.2 μm) prior to use.

7.5.4 Post-Production

The glass petri dishes, containing the droplets within the PVA solution, were covered and typically stored in the dark for 15-24 hours, at room temperature, to allow the chloroform to evaporate from the droplets and the isotropic to nematic phase transition to occur. A monolayer of droplets was formed by gently swirling the dish. The petri dish containing the birefringent nematic droplets was then heated to 55 °C and exposed to UV light (365 nm) from either an RS exposure unit LV202-E or an Omnicure LX500 spot curing system.

The PVA solution was removed by washing the particles with deionised water (Milli-Q) at 80 °C for 45 minutes and replacing the water, repeated three times. Particles were either dried for analysis by SEM or exchanged into PEG200 for analysis by POM.

7.6 Synthesis of Nematic Polymer Particles

Table 7.5. Experimental details of microfluidic experiments, attempting to create nematic polymer particles using **M1** and 2 mol% diphenyl(2,4,6-trimethylbenzoyl)phosphine oxide. PVA: A: 3 wt%, 85,000-124,000 g mol^{-1} (87-89% hydrolysis), B: 3 wt%, 13,000-23,000 g mol^{-1} (87-89% hydrolysis). UV-initiated radical polymerisation used an RS exposure unit LV202-E from 6cm, unless stated.

Experiment	Chip	Tip Sizes /µm	PVA	Solvent (Monomer % w/w)	Inner Flow Rate /µL hr^{-1}	Outer Flow Rate /mL hr^{-1}	Mean Droplet Diameter	Solvent Evaporation /Hours	UV Exposure Time /Minutes (Temperature)	Observations/Notes
P1-MF1	V1	50	A	Toluene (33%)	2000	2.0	Large droplets >600 µm	-	-	-
P1-MF2	V1	50	A	Toluene (33%)	5000	2.0	-	-	-	Jetting
P1-MF3	V4	25/170	A	Toluene (50%)	1000	6.0	-	-	-	Air blockage
P1-MF4	V3	40	A	Toluene (0%)	1000	10.0	-	-	-	Outlet leak
P1-MF5	V3	40	A	Toluene (0%)	1000	4.0	Isotropic: 33 µm (CV: 60%)	-	-	-
P1-MF6	V4	25/170	A	$CHCl_3$ (18%)	1000	6.5	Isotropic: 65 µm (CV: 17%)	-	-	-
P1-MF7	V4	30/200	A	$CHCl_3$ (18%)	Unknown (by hand)	Unknown (by hand)	Isotropic: n/a Nematic: 10 µm (CV: 38%)	-	-	Heated petri dish to 60 °C – water evaporated.

Experiment	Chip	Tip Sizes /μm	PVA	Solvent (Monomer % w/w)	Inner Flow Rate /μL hr^{-1}	Outer Flow Rate /mL hr^{-1}	Mean Droplet Diameter	Solvent Evaporation /Hours	UV Exposure Time /Minutes (Temperature)	Observations/Notes
P1-MF8	V5	50/ 200	A	$CHCl_3$ (13%)	200	2.5	Isotropic: 91 μm (CV: 44%) Nematic: 37 μm (CV: 51%)	-	-	Heated petri dish at 70 °C. Burst droplets caused a film of nematic to float on PVA.
P1-MF9	V5	50/ 200	A	$CHCl_3$ (13%)	200	3.0	Isotropic: 124 μm (CV: 13%) Nematic: 89 μm (CV: 24%)	-	-	Heated petri dish at 70 °C for 40 minutes but water dried out.
P1-MF10	V5	40/ 200	A	$CHCl_3$ (14%)	200	2.5	Isotropic: 105 μm (CV: 23%) Nematic: 48 μm (CV: 46%)	2.5	6 (21 °C)	Heated droplets to 60 °C but droplets burst and formed a nematic film.
P1-MF11	V5	40/ 200	A	$CHCl_3$ (14%)	200	2.5	Isotropic: 105 μm (CV: 23%) Nematic: 48 μm (CV: 46%)	2.5	35 (76 °C)	Some particles had aligned textures and increased T_{NI} compared to monomer. Some 'egg-like' particles.
P1-MF12	V5	40/ 200	A	$CHCl_3$ (14%)	200	2.5	Isotropic: 105 μm (CV: 23%) Nematic: 48 μm (CV: 46%)	2.5	60 (76 °C)	Particles polydomain but increased T_{NI} compared to monomer.

Table 7.6. Experimental details of microfluidic experiments, attempting to create nematic polymer particles using **M1** and 2 mol% diphenyl(2,4,6-trimethylbenzoyl)phosphine oxide. PVA: A: 3 wt%, 85,000-124,000 g mol^{-1} (87-89% hydrolysis), B: 3 wt%, 13,000-23,000 g mol^{-1} (87-89% hydrolysis). UV-initiated radical polymerisation used an Omnicure LX500 with a 365 nm LED head.

Experiment	Chip	Tip Sizes /μm	PVA	Solvent (Monomer % w/w)	Inner Flow Rate /μL hr^{-1}	Outer Flow Rate /mL hr^{-1}	Mean Droplet Diameter	Solvent Evaporation /Hours	UV Exposure Time /Seconds (Temperature)	UV Intensity (Distance)	Observations/Notes
P1-MF13	V9.7	12/ 170	A	$CHCl_3$ (5%)	135	15.0	Isotropic: n/a Nematic: 35 μm (CV: 12%)	20	1800 (55 °C)	100% (6 cm)	Bipolar alignment. UV source angled 45° to dish. Elongated particle AR: 1.71.
P1-MF14	V9.7	12/ 170	A	$CHCl_3$ (5%)	135	15.0	Isotropic: n/a Nematic: 29 μm (CV: 15%)	20	1800 (55 °C)	100% (6 cm)	Bipolar alignment. UV source angled 0° to dish. Elongated particle AR: 1.76.
P1-MF15	V9.5	12/ 170	B	$CHCl_3$ (6%)	140	15.0	Isotropic: 53 μm (CV: 4.7%) Nematic: 29 μm (CV: 7.1%)	19	1200 (55 °C)	100% (14 cm)	Bipolar alignment. Elongated particle AR: 1.57. After polymerisation PVA exchanged with MilliQ water x3 for SEM Exchanged some into PEG200. Heated to 125 °C – contracted to spherical.
P1-MF16	V9.5	12/ 170	B	$CHCl_3$ (6%)	140	15.0	Isotropic: 53 μm (CV: 4.7%) Nematic: 28 μm (CV: 8.1%)	19	600 (55 °C)	100% (6 cm)	Bipolar alignment. Elongated particle AR: 1.68. After polymerisation PVA exchanged with MilliQ water for SEM.

Experiment	Chip	Tip Sizes /μm	PVA	Solvent (Monomer % w/w)	Inner Flow Rate /μL hr^{-1}	Outer Flow Rate /mL hr^{-1}	Mean Droplet Diameter	Solvent Evaporation /Hours	UV Exposure Time /Seconds (Temperature)	UV Intensity (Distance)	Observations/Notes
P1-MF17	V9.5	12/ 170	B	$CHCl_3$ (6%)	140	15.0	Isotropic: 53 μm (CV: 4.7%) Nematic: 29 μm (CV: 7.4%)	19	1200 (55 °C)	100% (3 cm)	Bipolar alignment. Elongated particle AR: 1.74. Particles on edge of dish deformed less. After polymerisation PVA exchanged with Milli-Q water x3 then exchanged into PEG200. Heated to 125 °C – contracted to spherical.
P1-MF18	V9.5	12/ 170	B	$CHCl_3$ (6%)	140	15.0	Isotropic: 53 μm (CV: 4.7%) Nematic: 29 μm (CV: 5.8%)	19	1200 (55 °C)	5% (6 cm)	Bipolar alignment. Elongated particle AR: 1.16. After polymerisation PVA exchanged with Milli-Q water for SEM.

7.7 Synthesis of Nematic Elastomer Particles

Table 7.7. Experimental details of microfluidic experiments, attempting to create nematic elastomer particles using **M1**, 10 mol% 1,6-hexanediol diacrylate and 2 mol% diphenyl(2,4,6-trimethylbenzoyl)phosphine oxide. PVA: A: 3 wt%, 85,000-124,000 g mol^{-1} (87-89% hydrolysis), B: 3 wt%, 13,000-23,000 g mol^{-1} (87-89% hydrolysis). UV-initiated radical polymerisation used an RS exposure unit LV202-E from 6 cm, unless stated.

Experiment	Chip	Tip Sizes /µm	PVA	Solvent (Monomer % w/w)	Inner Flow Rate /µL hr^{-1}	Outer Flow Rate /mL hr^{-1}	Mean Droplet Diameter	Solvent Evaporation /Hours	UV Exposure Time /Minutes (Temperature)	Observations/Notes
E1-MF1	V5	30/ 200	A	$CHCl_3$ (14%)	200	2.5	Isotropic: 73 µm (CV: 13%) Nematic: 46 µm (CV: 7.1%)	Sealed under a coverslip, annealed at 79 °C for 20 hrs.	15 (79 °C)	Bipolar alignment. Small shape change on heating at ~125 °C – reduction in size. Closed cell burst on heating. Particles stuck together.
E1-MF2	V5	30/ 200	A	$CHCl_3$ (14%)	150	4.5	Isotropic: 73 µm (CV: 13%) Nematic: 46 µm (CV: 7.1%)	Annealed at 79 °C for 19 hrs	40 (79 °C)	Bipolar alignment. 'Flat' disks created due to coverslip compressing droplets as solvent evaporated.
E1-MF3	V5	30/ 200	A	$CHCl_3$ (14%)	150	4.5	Isotropic: 73 µm (CV: 13%) Nematic: 46 µm (CV: 7.1%)	Annealed at 81 °C for 3.5 hrs in glycerol	60 (81 °C)	Bipolar alignment. T_{NI} ~125 °C, polydomain on cooling.

Experiment	Chip	Tip Sizes /μm	PVA	Solvent (Monomer % w/w)	Inner Flow Rate /μL hr^{-1}	Outer Flow Rate /mL hr^{-1}	Mean Droplet Diameter	Solvent Evaporation /Hours	UV Exposure Time /Minutes (Temperature)	Observations/Notes
E1-MF4	V5	30/ 200	A	$CHCl_3$ (14%)	200	4.5	Isotropic: n/a Nematic 73 μm (CV: 19%)	16	30 (66 °C)	Bipolar alignment. Transferred into PEG200 and sealed in homemade cell to test heating response but the water boiled and burst the cell.
E1-MF5	V5	30/ 200	A	$CHCl_3$ (14%)	200	6.0	Isotropic: n/a Nematic: 74 μm (CV: 16%)	18	30 (55 °C)	Bipolar alignment. Transferred into PEG200, heated at 110 °C for 5 minutes to boil off the water, then covered with a glass coverslip. Reversible shape change on heating/cooling to ~125 °C ~35% contraction.
E1-MF6	V4	20/ 180	A	$CHCl_3$ (13%)	200	3.0	Isotropic: n/a Nematic: 50 μm (CV: 19%)	24	30 (55 °C)	Bipolar alignment. Coalescence of droplets. Lost sample during transfer from PVA to PEG200.
E1-MF7	V5	30/ 200	A	$CHCl_3$ (14%)	200	6.0	Isotropic: 111 μm (CV: 10%) Nematic: 58 μm (CV: 11%)	20	30 (55 °C)	Bipolar alignment. Uncovered petri dish – dried out during polymerisation.
E1-MF8	V5	30/ 200	A	$CHCl_3$ (14%)	200	6.0	Isotropic: 111 μm (CV: 10%) Nematic: 58 μm (CV: 11%)	20	30 (55 °C)	Bipolar alignment. Replenished water level during polymerisation. Transferred particles in PVA to PEG200. 'Gel' formed when mixed – PVA needs washing.

Experiment	Chip	Tip Sizes /μm	PVA	Solvent (Monomer % w/w)	Inner Flow Rate /μL hr^{-1}	Outer Flow Rate /mL hr^{-1}	Mean Droplet Diameter	Solvent Evaporation /Hours	UV Exposure Time /Minutes (Temperature)	Observations/Notes
E1-MF9	V5	30/ 200	A	$CHCl_3$ (14%)	200	6.0	Isotropic: 111 μm (CV: 10%) Nematic: 58 μm (CV: 11%)	20	30 (75 °C)	Bipolar alignment. Transferred particles in PVA to PEG200 on glass slide. Shape change on heating/cooling ~125 °C AR: 0.99 to 1.50.
E1-MF10	V6.1	20/ 230	A	$CHCl_3$ (6%)	100	11.0	Isotropic: n/a Nematic: 30 μm (CV: 17%)	69	30 (75 °C)	Bipolar alignment. 'Egg-shaped'/non spherical after polymerisation.
E1-MF11	V6.1	20/ 230	A	$CHCl_3$ (6%)	100	13.0	Isotropic: n/a Nematic: 30 μm (CV: 17%)	69	-	Bipolar alignment. Sample dried out before polymerisation.
E1-MF12	V6.1	20/ 230	A	$CHCl_3$ (6%)	100	14.0	Isotropic: n/a Nematic: 30 μm (CV: 17%)	69	30 (75 °C)	Bipolar alignment. 'Egg-shaped'/non-spherical after polymerisation. Transferred to PEG200. Weak Shape change ~125 °C. Merging of particles.
E1-MF13	V6.2	20/ 250	A	$CHCl_3$ (5%)	50	15.0	Isotropic: n/a Nematic: 35 μm (CV: 20%)	42	60 (75 °C)	Bipolar alignment. Heated petri dish at 75 °C for 30 minutes before polymerisation. No shape change after polymerisation.
E1-MF14	V6.2	20/ 250	A	$CHCl_3$ (5%)	100	18.0	Isotropic: n/a Nematic: 31 μm (CV: 15%)	42	30 (75 °C)	Bipolar alignment. Heated petri dish at 75 °C for 5 minutes before polymerisation. UV at 3 cm distance. Transferred to PEG200 and heated at 110 °C for 5 minutes to remove water. On heating and cooling a shape change from spherical to flat. Air bubbles in homemade cell interfered with analysis.

Experiment	Chip	Tip Sizes /µm	PVA	Solvent (Monomer % w/w)	Inner Flow Rate /µL hr^{-1}	Outer Flow Rate /mL hr^{-1}	Mean Droplet Diameter	Solvent Evaporation /Hours	UV Exposure Time /Minutes (Temperature)	Observations/Notes
E1-MF15	V6.3	15/ 250	A	$CHCl_3$ (6%)	100	24.0	Isotropic: n/a Nematic: 23 µm (CV: 24%)	18	45 (75 °C)	Bipolar alignment. Heated to isotropic (88 °C) and cooled to nematic (75 °C) before polymerisation. Washed by centrifugation for 5 minutes x2 in MilliQ water then transferred to PEG200. Shape change ~125 °C
E1-MF16	V6.3	15/ 250	A	$CHCl_3$ (6%)	110	17.5	Isotropic: n/a Nematic: 24 µm (CV: 25%)	21	45 (75 °C)	Bipolar alignment. Heated to isotropic (90 °C) and cooled to nematic (75 °C) before polymerisation. Agitated sample before and during polymerisation. Washed particles by centrifugation (5 minutes x2) with MilliQ water then transferred to PEG200. Shape change ~125 °C.
E1-MF17	V6.5	20/ 275	A	$CHCl_3$ (6%)	110	20.0	Isotropic: n/a Nematic: 36 µm (CV: 17%)	24	45 (55 °C)	Bipolar alignment. Spherical particles washed by centrifugation (30 seconds x3) with MilliQ water.
E1-MF18	V6.5	20/ 275	A	$CHCl_3$ (6%)	110	20.0	Isotropic: 60 µm (CV: 14%) Nematic: 35 µm (CV: 18%)	24	45 (55 °C)	Bipolar alignment. Spherical particles / some 'coffee bean'-shaped particle washed by centrifugation (30 seconds x3) with MilliQ water for SEM analysis.

Experiment	Chip	Tip Sizes /µm	PVA	Solvent (Monomer % w/w)	Inner Flow Rate /µL hr^{-1}	Outer Flow Rate /mL hr^{-1}	Mean Droplet Diameter	Solvent Evaporation /Hours	UV Exposure Time /Minutes (Temperature)	Observations/Notes
E1-MF19	V6.5	20/ 275	A	$CHCl_3$ (6%)	110	20.0	Isotropic: n/a Nematic: 35 µm (CV: 18%)	24	45 (75 °C)	Bipolar alignment. 'Coffee bean'-shaped particles washed by centrifugation (30 seconds x3) with MilliQ water.
E1-MF20	V6.5	20/ 275	A	$CHCl_3$ (6%)	110	20.0	Isotropic: n/a Nematic: 34 µm (CV: 20%)	24	45 (75 °C)	'Coffee bean'-shaped particles washed by centrifugation (30 seconds x3) with MilliQ water.
E1-MF21	V6.7	15/ 200	A	$CHCl_3$ (6%)	150	18	Isotropic: n/a Nematic: 26 µm (CV: 10%)	27	45 (55 °C)	UV at 3cm distance. Agitation of sample. Sample dried out.
E1-MF22	V6.7	15/ 200	A	$CHCl_3$ (6%)	150	18	Isotropic: n/a Nematic: 26 µm (CV: 11%)	42	45 (55 °C)	UV at 5 cm distance. No agitation of sample. 'Egg-shaped' particles. Sample dried out.
E1-MF23	V7.5	10/ 150	A	$CHCl_3$ (5%)	150	19	Isotropic: n/a Nematic: 27 µm (CV: 10%)	21	45 (55 °C)	Bipolar alignment. After polymerisation PVA exchanged with MilliQ water x3 then exchanged with PEG200. Reversible shape change ~125 °C AR: 1.02 to 1.49.
E1-MF24	V7.5	10/ 150	A	$CHCl_3$ (5%)	170	17.5	Isotropic: n/a Nematic: 26 µm (CV: 14%)	21	45 (55 °C)	Bipolar alignment. Monolayer of particles. After polymerisation PVA exchanged with MilliQ water x4 then exchanged with PEG200. Reversible shape change ~125 °C AR: 1.03 to 1.44.

Experiment	Chip	Tip Sizes /μm	PVA	Solvent (Monomer % w/w)	Inner Flow Rate /μL hr^{-1}	Outer Flow Rate /mL hr^{-1}	Mean Droplet Diameter	Solvent Evaporation /Hours	UV Exposure Time /Minutes (Temperature)	Observations/Notes
E1-MF25	V7.4	6/ 230	A	$CHCl_3$ (6%)	75	15.0	Isotropic: 24 μm (CV: 8%) Nematic: 16 μm (CV: 13%)	13.5	45 (55 °C)	Monodispersity affected by debris in chip. Bipolar alignment. After polymerisation PVA exchanged with MilliQ water x6 then exchanged with PEG200.
E1-MF26	V7.4	6/ 230	A	$CHCl_3$ (6%)	120	23.0	Isotropic: 24 μm (CV: 8%) Nematic: 17 μm (CV: 14%)	13.5	45 (55 °C)	Monodispersity affected by debris in chip. Bipolar alignment. After polymerisation PVA exchanged with MilliQ water x4 then exchanged with PEG200. Reversible shape change ~125 °C AR: 1.01 to 1.37.
E1-MF27	V7.4	6/ 230	A	$CHCl_3$ (6%)	120	23.0	Isotropic: 24 μm (CV: 8%) Nematic: 16 μm (CV: 19%)	13.5	45 (55 °C)	Monodispersity affected by debris in chip. Bipolar alignment. After polymerisation PVA exchanged with MilliQ water x3 then exchanged with PEG200. Reversible shape change ~125 °C AR: 1.05 to 1.59.
E1-MF28	V8.3	25/ 200	A	$CHCl_3$ (6%)	140	18.0	Isotropic: n/a Nematic: 29 μm (CV: 17%)	21	45 (55 °C)	Monodispersity affected by debris in chip. Bipolar alignment. Monolayer of particles by tilting petri dish 0.1 gradient for 6 hours. After polymerisation PVA exchanged with MilliQ water x4 then exchanged with PEG200. Reversible shape change ~125 °C AR: 1.00 to 1.25.

Experiment	Chip	Tip Sizes /µm	PVA	Solvent (Monomer % w/w)	Inner Flow Rate /µL hr^{-1}	Outer Flow Rate /mL hr^{-1}	Mean Droplet Diameter	Solvent Evaporation /Hours	UV Exposure Time /Minutes (Temperature)	Observations/Notes
E1-MF29	V8.6	20/ 190	A	$CHCl_3$ (6%)	140	15.0	Isotropic: 54 µm (CV: 3.3%) Nematic: 28 µm (CV: 9.6%)	18	45 (55 °C)	Bipolar alignment. Monolayer of particles. After polymerisation PVA exchanged with MilliQ water x4 then exchanged with PEG200. Reversible shape change ~125 °C AR: 1.06 to 1.45.
E1-MF30	V9.3	20/ 170	A	$CHCl_3$ (6%)	140	15.0	Isotropic: 54 µm Nematic: 30 µm (CV: 9.9%)	19	45 (88 °C)	Bipolar alignment. UV from 3 cm distance in isotropic phase. Particles have a polydomain texture. No shape change on heating.
E1-MF31	V9.16	15/ 155	B	$CHCl_3$ (3%)	140	15.0	Isotropic: 66 µm (CV: 1.9%) Nematic: 26 µm (CV: 2.4%)	20	45 (55 °C)	Bipolar alignment. UV from 3 cm distance.

Table 7.8. Experimental details of microfluidic experiments, attempting to create nematic elastomer particles using **M1**, 10 mol% 1,6-hexanediol diacrylate and 2 mol% diphenyl(2,4,6-trimethylbenzoyl)phosphine oxide. PVA: A: 3 wt%, 85,000-124,000 g mol^{-1} (87-89% hydrolysis), B: 3 wt%, 13,000-23,000 g mol^{-1} (87-89% hydrolysis). UV-initiated radical polymerisation used an Omnicure LX500 with a 365 nm LED head.

Experiment	Chip	Tip Sizes /μm	PVA	Solvent (Monomer % w/w)	Inner Flow Rate /μL hr^{-1}	Outer Flow Rate /mL hr^{-1}	Mean Droplet Diameter	Solvent Evaporation /Hours	UV Exposure Time /Seconds (Temperature)	UV Intensity (Distance)	Observations/Notes
E1-MF32	V6.2	20/ 250	A	$CHCl_3$ (5%)	75	15.0	Isotropic: n/a Nematic: 44 μm (CV: 13%)	42	100 (70 °C)	100% (6 cm)	Bipolar alignment. Heated for 30 minutes at 70 °C before polymerisation. Elongation on irradiation. AR: 1.48. Some merging of particles on heating. Shape change to spherical on heating.
E1-MF33	V6.2	20/ 250	A	$CHCl_3$ (5%)	75	15.0	Isotropic: n/a Nematic: 44 μm (CV: 13%)	42	300 (70 °C)	100% (6 cm)	Extra 200 seconds irradiation of **E1-MF32**. Elongation on irradiation. AR: 1.68. Some merging of particles on heating. Shape change to spherical on heating but did not return to elongated on cooling.
E1-MF34	V6.2	20/ 250	A	$CHCl_3$ (5%)	75	15.0	Isotropic: n/a Nematic: 30 μm (CV: 15%)	42	720 (70 °C)	100% (6 cm)	Bipolar alignment. Moved dish relative to UV spot to ensure even coverage. Elongation on irradiation. AR: 1.31
E1-MF35	V6.2	20/ 250	A	$CHCl_3$ (5%)	75	15.0	Isotropic: n/a Nematic: 30 μm (CV: 21%)	42	360 (70 °C)	100% (6 cm)	Bipolar alignment. Elongation on irradiation. AR: 1.33.
E1-MF36	V6.2	20/ 250	A	$CHCl_3$ (5%)	75	15.0	Isotropic: n/a Nematic: 30 μm (CV: 20%)	42	720 (70 °C)	100% (6 cm)	Bipolar alignment. Elongation on irradiation. AR: 1.38. Merging of particles. Air bubbles in homemade cell interfere with analysis.

Experiment	Chip	Tip Sizes /μm	PVA	Solvent (Monomer % w/w)	Inner Flow Rate /μL hr^{-1}	Outer Flow Rate /mL hr^{-1}	Mean Droplet Diameter	Solvent Evaporation /Hours	UV Exposure Time /Seconds (Temperature)	UV Intensity (Distance)	Observations/Notes
E1-MF37	V9.1	20/ 170	A	$CHCl_3$ (6%)	140	14.0	Isotropic: n/a Nematic: 35 μm (CV: 10%)	15	1200 (55 °C)	100% (7 cm)	Bipolar alignment Elongation on irradiation. AR: 1.55 After polymerisation PVA exchanged with MilliQ water x3 then exchanged with PEG200. Large shape change on heating to phase transition AR: 1.7 to 0.6.
E1-MF38	V9.3	20/ 170	A	$CHCl_3$ (6%)	125	15.5	Isotropic: 59 μm (CV: 2.7%) Nematic: 29 μm (CV: 1.5%)	19	1200 (55 °C)	100% (7 cm)	Bipolar alignment. Moved dish every 5 minutes to cover entire sample. Elongation on irradiation. AR: 1.29. After polymerisation PVA exchanged with MilliQ water x3 then exchanged with PEG200. Large shape change on heating to phase transition AR: 1.30 to 0.82.
E1-MF39	V9.12	25/ 240	B	$CHCl_3$ (3%)	140	20.0	Isotropic: 99 μm (CV: 7.8%) Nematic: 39 μm (CV: 1.9%)	20	600 (55 °C)	100% (14 cm)	Bipolar alignment. Elongation on irradiation. AR: 1.25.

Experiment	Chip	Tip Sizes /μm	PVA	Solvent (Monomer % w/w)	Inner Flow Rate /μL hr^{-1}	Outer Flow Rate /mL hr^{-1}	Mean Droplet Diameter	Solvent Evaporation /Hours	UV Exposure Time /Seconds (Temperature)	UV Intensity (Distance)	Observations/ Notes
E1-MF40	V9.12	25/ 240	B	$CHCl_3$ (3%)	140	20.0	Isotropic: 102 μm (CV: 1.4%) Nematic: 38 μm (CV: 2.5%)	20	600 (55 °C)	100% (6 cm)	Bipolar alignment. Elongation on irradiation. AR: 1.27.
E1-MF41	V9.12	25/ 240	B	$CHCl_3$ (3%)	140	20.0	Isotropic: 105 μm (CV: 1.6%) Nematic: 39 μm (CV: 2.9%)	20	600 (55 °C)	100% (14 cm)	Bipolar alignment. Elongation on irradiation. AR: 1.27.
E1-MF42	V9.12	25/ 240	B	$CHCl_3$ (3%)	140	20.0	Isotropic: 102 μm (CV: 2.1%) Nematic: 39 μm (CV: 2.0%)	20	1800 (55 °C)	7% (30 cm)	Bipolar alignment. Spherical particles. AR: 1.05.
E1-MF43	V9.16	15/ 155	B	$CHCl_3$ (3%)	140	15.0	Isotropic: 65 μm (CV: 2.3%) Nematic: 27 μm (CV: 2.8%)	20	1500 (55 °C)	100% (14 cm)	Bipolar alignment. Elongation on irradiation. AR: 1.24.
E1-MF44	V9.16	15/ 155	B	$CHCl_3$ (3%)	140	15.0	Isotropic: 66 μm (CV: 3.3%) Nematic: 26 μm (CV: 1.9%)	20	2 (55 °C)	100% (14 cm)	Bipolar alignment. Elongation on irradiation. AR: 1.24.

Table 7.9. Experimental details of microfluidic experiments, attempting to create nematic elastomer particles using **M2**, 10 mol% 1,6-hexanediol diacrylate and 2 mol% diphenyl(2,4,6-trimethylbenzoyl)phosphine oxide. PVA: A: 3 wt%, 85,000-124,000 g mol^{-1} (87-89% hydrolysis), B: 3 wt%, 13,000-23,000 g mol^{-1} (87-89% hydrolysis). UV-initiated radical polymerisation used an RS exposure unit LV202-E from 6 cm, unless stated.

Experiment	Chip	Tip Sizes /μm	PVA	Solvent (Monomer % w/w)	Inner Flow Rate /μL hr^{-1}	Outer Flow Rate /mL hr^{-1}	Mean Droplet Diameter	Solvent Evaporation /Hours	UV Exposure Time /Minutes (Temperature)	Observations/Notes
E2-MF1	V5	30/ 200	A	$CHCl_3$ (5%)	200	11.0	Isotropic: n/a Nematic: 38 μm (CV: 30%)	15	30 (60 °C)	Bipolar alignment. Heated to isotropic (70 °C), cooled to nematic (60 °C) before polymerisation Reversible shape change ~90 °C, AR: 1.01 to 1.38
E2-MF2	V7.1	15/ 200	A	$CHCl_3$ (6%)	140	18.0	Isotropic: n/a Nematic: 27 μm (CV: 13%)	87	45 (55 °C)	Long evaporation time led to some coalescence of droplets. Agitated before polymerisation Bipolar alignment
E2-MF3	V7.1	15/ 200	A	$CHCl_3$ (6%)	140	18.0	Isotropic: n/a Nematic: 28 μm (CV: 15%)	87	45 (55 °C)	Long evaporation time led to some coalescence of droplets Agitated before polymerisation Bipolar alignment
E2-MF4	V8.4	25/ 175	A	$CHCl_3$ (6%)	140	14.0	Isotropic: n/a Nematic: 29 μm (CV: 7.7%)	15	45 (55 °C)	Bipolar alignment. Monolayer of particles formed. After polymerisation PVA exchanged with MilliQ water x 4 then exchanged with PEG200. Reversible shape change ~90 °C – AR: 1.1 to 1.52. Particles clumped together on prolonged heating.

Table 7.10. Experimental details of microfluidic experiments, attempting to create nematic elastomer particles using **M3**, 10 mol% 1,6-hexanediol diacrylate and 2 mol% diphenyl(2,4,6-trimethylbenzoyl)phosphine oxide. PVA: A: 3 wt%, 85,000-124,000 g mol^{-1} (87-89% hydrolysis), B: 3 wt%, 13,000-23,000 g mol^{-1} (87-89% hydrolysis). UV-initiated radical polymerisation used an RS exposure unit LV202-E from 6 cm, unless stated.

Experiment	Chip	Tip Sizes /μm	PVA	Solvent (Monomer % w/w)	Inner Flow Rate /μL hr^{-1}	Outer Flow Rate /mL hr^{-1}	Mean Droplet Diameter	Solvent Evaporation /Hours	UV Exposure Time /Minutes (Temperature)	Observations/Notes
E3-MF1	V5	30/ 200	A	$CHCl_3$ (6%)	200	13.0	Isotropic: n/a Nematic: 38 μm (CV: 50%)	16	60 (70 °C)	Bipolar alignment. Heated to isotropic (77 °C), cooled to nematic (70 °C) before polymerisation. Polymerisation unsuccessful – no change in T_{NI}.
E3-MF2	V7.1	15/ 200	A	$CHCl_3$ (6%)	140	18.0	Isotropic: n/a Nematic: 28 μm (CV: 14%)	22	45 (55 °C)	Bipolar alignment. Agitated before polymerisation UV from 3 cm distance.
E3-MF3	V7.1	15/ 200	A	$CHCl_3$ (6%)	140	18.0	Isotropic: n/a Nematic: 29 μm (CV: 11%)	42	90 (50 °C)	Bipolar alignment. Dried out but replenished water. Agitated before polymerisation UV from 3 cm distance Polymerisation unsuccessful.

Table 7.11. Experimental details of microfluidic experiments, attempting to create nematic elastomer particles using **M4**, 10 mol% 1,6-hexanediol diacrylate and 2 mol% diphenyl(2,4,6-trimethylbenzoyl)phosphine oxide. PVA: A: 3 wt%, 85,000-124,000 g mol^{-1} (87-89% hydrolysis), B: 3 wt%, 13,000-23,000 g mol^{-1} (87-89% hydrolysis). UV-initiated radical polymerisation used an RS exposure unit LV202-E from 3 cm.

Experiment	Chip	Tip Sizes /μm	PVA	Solvent (Monomer % w/w)	Inner Flow Rate /μL hr^{-1}	Outer Flow Rate /mL hr^{-1}	Mean Droplet Diameter	Solvent Evaporation /Hours	UV Exposure Time /Minutes (Temperature)	Observations/Notes
E4-MF1	V9.2	20/ 170	A	$CHCl_3$ (6%)	140	14.0	Isotropic: n/a Nematic: 30 μm (CV: 12%)	24	45 (45 °C)	Droplets: Bipolar alignment. Particles: slightly polydomain texture. Washed with MilliQ water and exchanged into PEG200. Weak shape change when heated into isotropic AR: 1.11 to 1.12.
E4-MF2	V9.2	20/ 170	A	$CHCl_3$ (6%)	140	14.0	Isotropic: n/a Nematic: 32 μm (CV: 13%)	24	45 (45 °C)	Droplets: Bipolar alignment Heated to 55 °C and cooled to 45 °C before polymerisation. Washed with MilliQ water x2 and exchanged into PEG200. Weak shape change when heated into isotropic AR: 1.12 to 1.16.

Table 7.12. Experimental details of microfluidic experiments, attempting to create nematic elastomer particles using **M4**, 10 mol% 1,6-hexanediol diacrylate and 2 mol% diphenyl(2,4,6-trimethylbenzoyl)phosphine oxide. PVA: A: 3 wt%, 85,000-124,000 g mol^{-1} (87-89% hydrolysis), B: 3 wt%, 13,000-23,000 g mol^{-1} (87-89% hydrolysis). UV-initiated radical polymerisation used an Omnicure LX500 with a 365 nm LED head.

Experiment	Chip	Tip Sizes /μm	PVA	Solvent (Monomer % w/w)	Inner Flow Rate /μL hr^{-1}	Outer Flow Rate /mL hr^{-1}	Mean Droplet Diameter	Solvent Evaporation /Hours	UV Exposure Time /Seconds (Temperature)	UV Intensity (Distance)	Observations/Notes
E4-MF3	V9.9	15/ 165	A	$CHCl_3$ (6%)	100	9.0	Isotropic: n/a Nematic: 32 μm (CV: 20%)	24	1200 (45 °C)	100% (6 cm)	Bipolar alignment. Spherical particles - no elongation on irradiation. AR: 1.05.

7.8 Synthesis of Chiral Nematic Polymer Particles

Table 7.13. Experimental details of microfluidic experiments, attempting to create chiral nematic polymer particles **CP9,** using **CM9** and 2 mol% diphenyl(2,4,6-trimethylbenzoyl)phosphine oxide. PVA: A: 3 wt%, 85,000-124,000 g mol^{-1} (87-89% hydrolysis), B: 3 wt%, 13,000-23,000 g mol^{-1} (87-89% hydrolysis). UV-initiated radical polymerisation used an Omnicure LX500 with a 365 nm LED head.

Experiment	Chip	Tip Sizes /µm	PVA	Solvent (Monomer % w/w)	Inner Flow Rate /µL hr^{-1}	Outer Flow Rate /mL hr^{-1}	Mean Droplet Diameter	Solvent Evaporation /Hours	UV Exposure Time /Seconds (Temperature)	UV Intensity (Distance)	Observations/Notes
CP9-MF1	V9.11	18/ 185	B	$CHCl_3$ (2%)	100	19.0	Isotropic: 67 µm (CV: 2.5%) Nematic: 29 µm (CV: 7.8%)	17	90 (6 °C)	50% (9.5 cm)	Annealed at ~4 °C for 48 hrs Planar alignment Droplets: red selective reflection Particles: yellow selective reflection T_{NI} ~24 °C.
CP9-MF2	V9.11	18/ 185	B	$CHCl_3$ (2%)	140	17.0	Isotropic: 70 µm (CV: 4.0%) Nematic: 30 µm (CV: 0.7%)	17	180 (7 °C)	50% (9.5 cm)	Annealed at ~4 °C for 24 hrs Planar alignment Droplets: red selective reflection Particles: yellow selective reflection, no increase in T_{NI} ~17 °C.
CP9-MF3	V9.11	18/ 185	B	$CHCl_3$ (2%)	140	17.0	Isotropic: 65 µm (CV: 1.1%) Nematic: 30 um (CV: 0.9%)	17	600 (10 °C)	50% (15 cm)	Annealed at ~4 °C for 24 hrs Planar alignment Droplets: red selective reflection UV 5s on, 5s off for 20 minutes Particles: yellow/orange selective reflection, no increase in T_{NI} ~17 °C.

7.9 Synthesis of Chiral Nematic Elastomer Particles

Table 7.14. Experimental details of microfluidic experiments, attempting to create chiral nematic elastomer particles **CE1**, using **CM1**, 10 mol% 1,6-hexanediol diacrylate and 2 mol% diphenyl(2,4,6-trimethylbenzoyl)phosphine oxide. PVA: A: 3 wt%, 85,000-124,000 g mol^{-1} (87-89% hydrolysis), B: 3 wt%, 13,000-23,000 g mol^{-1} (87-89% hydrolysis). UV-initiated radical polymerisation used an RS exposure unit LV202-E from 6 cm, unless stated.

Experiment	Chip	Tip Sizes /μm	PVA	Solvent (Monomer % w/w)	Inner Flow Rate /μL hr^{-1}	Outer Flow Rate /mL hr^{-1}	Mean Droplet Diameter	Solvent Evaporation /Hours	UV Exposure Time /Minutes (Temperature)	Observations/Notes
CE1-MF1	V5	30/ 200	A	$CHCl_3$ (6%)	200	13.0	Isotropic: 90 μm (CV: 8.8%) Nematic: 40 μm (CV: 9.2%)	19	30 (47 °C)	Heated to isotropic (54 °C), cooled to chiral nematic phase (46 °C) and annealed for 18 hrs – radial alignment. Polydomain after polymerisation. Transferred into PEG200 – no response on heating/cooling.
CE1-MF2	V5	30/ 200	A	$CHCl_3$ (6%)	200	13.0	Isotropic: 90 μm (CV: 8.8%) Nematic: 40 μm (CV: 9.2%)	19	60 (47°C)	Annealed for 18 hrs at 46 °C – radial alignment. UV at 10 cm distance. Increased T_{NI} (60 °C) but polydomain alignment on cooling.

Table 7.15. Experimental details of microfluidic experiments, attempting to create chiral nematic elastomer particles **CE6**, using **CM6**, 10 mol% 1,6-hexanediol diacrylate and 2 mol% diphenyl(2,4,6-trimethylbenzoyl)phosphine oxide. PVA: A: 3 wt%, 85,000-124,000 g mol^{-1} (87-89% hydrolysis), B: 3 wt%, 13,000-23,000 g mol^{-1} (87-89% hydrolysis). UV-initiated radical polymerisation used an Omnicure LX500 with a 365 nm LED head.

Experiment	Chip	Tip Sizes /μm	PVA	Solvent (Monomer % w/w)	Inner Flow Rate /μL hr^{-1}	Outer Flow Rate /mL hr^{-1}	Mean Droplet Diameter	Solvent Evaporation /Hours	UV Exposure Time /Seconds (Temperature)	UV Intensity (Distance)	Observations/Notes
CE6-MF1	V9.10	25 /190	B	$CHCl_3$ (5%)	75	20.0	Isotropic: 95 μm (CV: 3.5%) Nematic: 55 μm (CV: 5.2%)	17	1200 (39 °C)	5% (40 cm)	High flow rates needed due to unknown blockage on chip. Texture improved with annealing at 39 °C (3 days). No increase in T_{NI} after polymerisation.
CE6-MF2	V9.10	25 /190	B	$CHCl_3$ (5%)	75	20.0	Isotropic: 96 μm (CV: 1.6%) Nematic: 52 μm (CV: 6.6%)	17	90 (39 °C)	50% (15 cm)	High flow rates needed due to unknown blockage on chip. No loss of alignment following polymerisation. Pressure sensitive.
CE6-MF3	V9.10	25 /190	B	$CHCl_3$ (5%)	75	20.0	Isotropic: 94 μm (CV: 1.3%) Nematic: 50 μm (CV: 5.3%)	17	1200 (39 °C)	10% (37 cm)	High flow rates needed due to unknown blockage on chip. Polymerisation caused degradation of alignment.

Table 7.16. Experimental details of microfluidic experiments, attempting to create chiral nematic elastomer particles using **M1**, CB15, 10 mol% 1,6-hexanediol diacrylate and 2 mol% diphenyl(2,4,6-trimethylbenzoyl)phosphine oxide. PVA: A: 3 wt%, 85,000-124,000 g mol^{-1} (87-89% hydrolysis), B: 3 wt%, 13,000-23,000 g mol^{-1} (87-89% hydrolysis). UV-initiated radical polymerisation used an Omnicure LX500 with a 365 nm LED head.

Experiment	CB15 (wt%)	Chip	Tip Sizes /μm	PVA	Solvent (Monomer % w/w)	Inner Flow Rate /μL hr^{-1}	Outer Flow Rate /mL hr^{-1}	Mean Droplet Diameter	Solvent Evaporation /Hours	UV Exposure Time /Seconds (Temperature)	UV Intensity (Distance)	Observations/Notes
E1D-MF1	29	V9.19	12/ 180	B	$CHCl_3$ (3%)	140	15.0	Isotropic: 47 μm (CV: 2.6%) Nematic: 18 μm (CV: 1.9%)	20	600 (30 °C)	50% (15 cm)	Droplets: red selective reflection. Particles: red selective reflection.
E1D-MF2	29	V9.19	12/ 180	B	$CHCl_3$ (3%)	140	14.0	Isotropic: 49 μm (CV: 2.8%) Nematic: 20 μm (CV: 3.8%)	20	1800 (30 °C)	50% (15 cm)	Droplets: red selective reflection. Particles: red selective reflection, T_{NI} ~78 °C Pressure sensitivity tested.
E1E-MF1	35	V9.13	25/ 200	B	$CHCl_3$ (3%)	100	10.0	Isotropic: n/a Nematic: 37 μm (CV: 3.1%)	19	90 (29 °C)	50% (9.5 cm)	Annealed at 24 °C Droplets: poor alignment – multiple green reflection spots. Particles: T_{NI} 34 °C after polymerisation.

Experiment	CB15 (wt%)	Chip	Tip Sizes /μm	PVA	Solvent (Monomer % w/w)	Inner Flow Rate /μL hr^{-1}	Outer Flow Rate /mL hr^{-1}	Mean Droplet Diameter	Solvent Evaporation /Hours	UV Exposure Time /Seconds (Temperature)	UV Intensity (Distance)	Observations/Notes
E1E-MF2	35	V9.13	25/ 200	B	$CHCl_3$ (3%)	140	15.0	Isotropic: n/a Nematic: 37 μm (CV: 3.3%)	19	600 (29 °C)	50% (15 cm)	Droplets: poor alignment – multiple green reflection spots. Particles: T_{NI} 34 °C after polymerisation
E1E-MF3	35	V9.14	25/ 200	B	$CHCl_3$ (2%)	140	15.0	Isotropic: 78 μm (CV: 0.7%) Nematic: 32 μm (CV: 4.1%)	15	-	-	Water accidently evaporated overnight whilst annealing.
E1E-MF4	35	V9.14	25/ 200	B	$CHCl_3$ (2%)	140	17.0	Isotropic: 75 μm (CV: 1.9%) Nematic: 29 μm (CV: 1.5%)	15	1200 (30 °C)	50% (15 cm)	Droplets: green selective reflection. Particles: green selective reflection. T_{NI} ~44 °C Attempted washing with acetone – particles merging.
E1E-MF5	35	V9.14	25/ 200	B	$CHCl_3$ (2%)	140	17.0	Isotropic: 75 μm (CV: 2.3%) Nematic: 30 μm (CV: 2.4%)	15	1200 (30 °C)	50% (9.5 cm)	Droplets: green selective reflection. Particles: green selective reflection. T_{NI} ~44 °C Pressure sensitivity tested. Attempted washing with acetone – particles merging.

Experiment	CB15 (wt%)	Chip	Tip Sizes /μm	PVA	Solvent (Monomer % w/w)	Inner Flow Rate /μL hr^{-1}	Outer Flow Rate /mL hr^{-1}	Mean Droplet Diameter	Solvent Evaporation /Hours	UV Exposure Time /Seconds (Temperature)	UV Intensity (Distance)	Observations/Notes
E1F-MF1	41	V9.15	20/ 160	B	$CHCl_3$ (3%)	140	13.0	Isotropic: 72 μm (CV: 1.6%) Nematic: 26 μm (CV: 1.3%)	18	1800 (25 °C)	50% (15 cm)	Droplets: blue selective reflection. Particles: blue selective reflection. T_{NI} ~58 °C Pressure sensitivity tested.
E1F-MF2	41	V9.15	20/ 160	B	$CHCl_3$ (3%)	140	15.0	Isotropic: 72 μm (CV: 2.1%) Nematic: 27 μm (CV: 2.8%)	17	1800 (25 °C)	50% (15 cm)	Droplets: blue selective reflection. Particles: blue selective reflection, T_{NI} ~58 °C
E1F-MF3	41	V9.15	20/ 160	B	$CHCl_3$ (3%)	140	15.0	Isotropic: 71 μm (CV: 1.4%) Nematic: 28 μm (CV: 2.7%)	17	1800 (25 °C)	50% (15 cm)	Droplets: blue selective reflection. Particles: blue selective reflection, T_{NI} ~58 °C

7.10 Synthesis of 5CB Droplets

Table 7.17. Experimental details of microfluidic experiments, attempting to create droplets using 5CB. PVA: A: 3 wt%, 85,000-124,000 g mol^{-1} (87-89% hydrolysis), B: 3 wt%, 13,000-23,000 g mol^{-1} (87-89% hydrolysis). UV source was an Omnicure LX500 with a 365 nm LED head.

Experiment	Chip	Tip Sizes /µm	PVA	Solvent (Monomer % w/w)	Inner Flow Rate /µL hr^{-1}	Outer Flow Rate /mL hr^{-1}	Mean Droplet Diameter	Solvent Evaporation /Hours	UV Exposure Time /Seconds (Temperature)	UV Intensity (Distance)	Observations/Notes
5CB-MF1	V7.1	15/ 190	A	(100%)	50	5.0	Nematic: 61 µm (CV: 2%)	n/a	n/a	n/a	Bipolar texture.
5CB-MF2	V7.2	15/ 265	A	$CHCl_3$ (3%)	20	11.0	Isotropic: n/a Nematic: 44 µm (CV: 9%)	16	n/a	n/a	Bipolar texture.
5CB-MF3	V9.4	25/ 170	A	$CHCl_3$ (3%)	140	16.0	Isotropic: n/a Nematic: 20 µm (CV: 17%)	16	10 (20 °C)	100% (6 cm)	Bipolar texture. No elongation on irradiation.

References

1 F. Reinitzer, *Monatshefte für Chemie*, 1888, **9**, 421–441.

2 P. J. Collings and M. Hird, *Introduction to Liquid Crystals: Chemistry and Physics*, Taylor & Francis, London, 1997.

3 J. M. Geary, J. W. Goodby, A. R. Kmetz and J. S. Patel, *J. Appl. Phys.*, 1987, **62**, 4100–4108.

4 J. W. Goodby, *J. Mater. Chem.*, 1991, **1**, 307.

5 D. Demus, J. W. Goodby, G. W. Gray, H.-W. Spiess and V. Vill, Eds., *Handbook of Liquid Crystals*, Wiley-VCH Verlag GmbH & Co. KGaA, Weinheim, FRG, 1st edn., 1998.

6 I. Dierking, in *Textures of Liquid Crystals*, Wiley-VCH Verlag GmbH & Co. KGaA, Weinheim, FRG, 2003, pp. 167–212.

7 D. Broer, G. P. Crawford and S. Zumer, Eds., *Cross-Linked Liquid Crystalline Systems: From Rigid Polymer Networks to Elastomers*, CRC Press, Boca Raton, FL, 1st edn., 2011.

8 M. Warner and E. M. Terentjev, *Prog. Polym. Sci.*, 1996, **21**, 853–891.

9 V. Percec, D. Tomazos and C. Pugh, *Macromolecules*, 1989, **22**, 3259–3267.

10 R. A. Lewthwaite, J. W. Goodby and K. J. Toyne, *J. Mater. Chem.*, 1993, **3**, 241–245.

11 M. . Li, B. A, P. Davidson, P. Keller and J. . Cotton, *Phys. Rev. E*, 1993, **70**, 2297–2301.

12 F. J. Davis, *J. Mater. Chem.*, 1999, **3**, 551–562.

13 H. Jiang, C. Li and X. Huang, *Nanoscale*, 2013, **5**, 5225–5240.

14 M. H. Li and P. Keller, *Philos. Trans. R. Soc. A Math. Phys. Eng. Sci.*, 2006, **364**, 2763–2777.

15 E.-K. Fleischmann and R. Zentel, *Angew. Chemie - Int. Ed.*, 2013, **52**, 8810–8827.

16 E. M. Terentjev, *J. Phys. Condens. Matter*, 1999, **11**, R239-257.

17 S. Petsch, B. Khatri, S. Schuhladen, L. Köbele, R. Rix, R. Zentel and H. Zappe, *Smart Mater. Struct.*, 2016, **25**, 1–10.

18 P. G. De Gennes, *CR Acad. Sci. Paris, Ser. II b*, 1997, **324**, 343–348.

19 S. Mayer and R. Zentel, *Curr. Opin. Solid State Mater. Sci.*, 2002, **6**, 545–551.

20 C. M. Spillmann, J. Naciri, M. S. Chen, A. Srinivasan and B. R. Ratna, *Liq. Cryst.*, 2006, **33**, 373–380.

21 R. Wei, L. Zhou, Y. He, X. Wang and P. Keller, *Polymer (Guildf).*, 2013, **54**, 5321–5329.

22 J. Küpfer and H. Finkelmann, *Makromol. Chem., Rapid Commun.*, 1991, **12**, 717–726.

23 D. L. Thomsen III, P. Keller, J. Naciri, R. Pink, H. Jeon, D. Shenoy and B. R. Ratna, *Macromolecules*, 2001, **34**, 5868–5875.

24 A. Komp, J. Rühe and H. Finkelmann, *Macromol. Rapid Commun.*, 2005, **26**, 813–818.

25 S. Schuhladen, F. Preller, R. Rix, S. Petsch, R. Zentel and H. Zappe, *Adv. Mater.*, 2014, **26**, 7247–7251.

26 Z. Pei, Y. Yang, Q. Chen, E. M. Terentjev, Y. Wei and Y. Ji, *Nat. Mater.*, 2014, **13**, 36–41.

27 A. Rešetič, J. Milavec, B. Zupančič, V. Domenici and B. Zalar, *Nat. Commun.*, 2016, **7**, 13140.

28 H. Wermter and H. Finkelmann, *E-Polymers*, 2001, **1**, 1–13.

29 S. Krause, F. Zander, G. Bergmann, H. Brandt, H. Wertmer and H. Finkelmann, *Comptes Rendus Chim.*, 2009, **12**, 85–104.

30 D. Martella, C. Parmeggiani, D. S. Wiersma, M. Piñol and L. Oriol, *J. Mater. Chem. C*, 2015, **3**, 9003–9010.

31 M. O. Saed, A. H. Torbati, C. A. Starr, R. Visvanathan, N. A. Clark and C. M. Yakacki, *J. Polym. Sci. Part B Polym. Phys.*, 2017, **55**, 157–168.

32 H. Kim, J. M. Boothby, S. Ramachandran, C. D. Lee and T. H. Ware, *Macromolecules*, 2017, **50**, 4267–4275.

33 A. Buguin, M.-H. Li, P. Silberzan, B. Ladoux and P. Keller, *J. Am. Chem. Soc.*, 2006, **128**, 1088–1089.

34 M.-H. Li, P. Keller, B. Li, X. Wang and M. Brunet, *Adv. Mater.*, 2003, **15**, 569–572.

35 J. E. Marshall, S. Gallagher, E. M. Terentjev and S. K. Smoukov, *J. Am. Chem. Soc.*, 2014, **136**, 474–479.

36 R. Wei and X. Hua, *Mol. Cryst. Liq. Cryst.*, 2017, **643**, 83–96.

37 R. Wei, Y. He, X. Wang and P. Keller, *Macromol. Rapid Commun.*, 2014, **35**, 1571–7.

38 K. L. Davey, PhD Thesis, University of York, 2015.

39 H. Yu and T. Ikeda, *Adv. Mater.*, 2011, **23**, 2149–2180.

40 M. Yamada, M. Kondo, J. Mamiya, Y. Yu, M. Kinoshita, C. J. Barrett and T. Ikeda, *Angew. Chemie Int. Ed.*, 2008, **47**, 4986–4988.

41 Y. Ji, J. E. Marshall and E. M. Terentjev, *Polymers (Basel).*, 2012, **4**, 316–340.

42 W. Liu, L. X. Guo, B. P. Lin, X. Q. Zhang, Y. Sun and H. Yang, *Macromolecules*, 2016, **49**, 4023–4030.

43 M. Camacho-Lopez, H. Finkelmann, P. Palffy-Muhoray and M. Shelley, *Nat. Mater.*, 2004, **3**, 307–310.

44 Z. L. Wu, A. Buguin, H. Yang, J.-M. Taulemesse, N. Le Moigne, A. Bergeret, X. Wang and P. Keller, *Adv. Funct. Mater.*, 2013, **23**, 3070–3076.

45 N. Torras, K. E. Zinoviev, C. J. Camargo, E. M. Campo, H. Campanella, J. Esteve, J. E. Marshall, E. M. Terentjev, M. Omastová, I. Krupa, P. Teplický, B. Mamojka, P. Bruns, B. Roeder, M. Vallribera, R. Malet, S. Zuffanelli, V. Soler, J. Roig, N. Walker, D. Wenn, F. Vossen and F. M. H. Crompvoets, *Sensors Actuators A Phys.*, 2014, **208**, 104–112.

46 A. Sánchez-Ferrer, T. Fischl, M. Stubenrauch, A. Albrecht, H. Wurmus, M. Hoffmann and H.

Finkelmann, *Adv. Mater.*, 2011, **23**, 4526–4530.

47 A. Sánchez-Ferrer, T. Fischl, M. Stubenrauch, H. Wurmus, M. Hoffmann and H. Finkelmann, *Macromol. Chem. Phys.*, 2009, **210**, 1671–1677.

48 Y. Gao, T. Mori, S. Manning, Y. Zhao, A. D. Nielsen, A. Neshat, A. Sharma, C. J. Mahnen, H. R. Everson, S. Crotty, R. J. Clements, C. Malcuit and E. Hegmann, *ACS Macro Lett.*, 2016, **5**, 4–9.

49 Q. Mu, H. J. Qi, C. Yuan, C. M. Yakacki, X. Kuang, K. Yu, D. J. Roach, C. K. Dunn and T. J. Wang, *Soft Matter*, 2017, **13**, 5558–5568.

50 E. Chen, X. Zhang, B. Lin, M. Wang, Y. Sun, H. Yang, J. Wang and P. Keller, *Chem. Commun.*, 2016, **52**, 4313–4316.

51 X. Liu, S. K. Kim and X. Wang, *J. Mater. Chem. B*, 2016, **4**, 7293–7302.

52 J. M. Boothby, H. Kim and T. H. Ware, *Sensors Actuators, B Chem.*, 2017, **240**, 511–518.

53 J. S. Hu, B. Y. Zhang, Y. Y. Zheng and Q. Y. Li, *React. Funct. Polym.*, 2005, **64**, 1–11.

54 X. Z. He, B. Y. Zhang, J. S. Hu and M. Tian, *Liq. Cryst.*, 2005, **32**, 299–305.

55 B. Geng, L. X. Guo, B. P. Lin, P. Keller, X. Q. Zhang, Y. Sun and H. Yang, *Polym. Chem.*, 2015, **6**, 5281–5287.

56 J.-S. S. Hu, Q. Li, Y.-N. N. Liu, Y.-T. T. Song and W. Li, *Liq. Cryst.*, 2013, **40**, 1095–1104.

57 J. H. Liu, H. J. Hung, P. C. Yang and K. H. Tien, *J. Polym. Sci. Part A Polym. Chem.*, 2008, **46**, 6214–6228.

58 J. S. Hu, D. Li, Q. B. Meng and D. S. Yao, *J. Appl. Polym. Sci.*, 2012, **125**, 3849–3855.

59 J.-H. Liu, Y.-K. Wang, C.-C. Chen, P.-C. Yang, F.-M. Hsieh and Y.-H. Chiu, *Polymer (Guildf).*, 2008, **49**, 3938–3949.

60 S. Ahn, L. T. Nguyen Le and R. M. Kasi, *J. Polym. Sci. Part A Polym. Chem.*, 2009, **47**, 2690–2701.

61 W. Chiang and L.-D. Hong, *J. Polym. Sci. Part A Polym. Chem.*, 2000, **38**, 1609–1617.

62 A. Bubnov, N. Podoliak, V. Hamplová, P. Tomášková, J. Havlíček and M. Kašpar, *Ferroelectrics*, 2016, **495**, 105–115.

63 B. Y. Zhang, J. S. Hu, L. Q. Yang, X. Z. He and C. Liu, *Eur. Polym. J.*, 2007, **43**, 2017–2027.

64 N. J. Chothani, V. K. Akbari, P. S. Patel and K. C. Patel, *Liq. Cryst.*, 2016, **43**, 1636–1648.

65 C.-S. S. Hsu, P.-H. H. Chu, H.-L. L. Chang and T.-H. H. Hsieh, *J. Polym. Sci. Part A Polym. Chem.*, 1997, **35**, 2793–2800.

66 M. Yoshida, X. Fan, Y. Uemura and Y. Hatate, *J. Appl. Polym. Sci.*, 2001, **81**, 2490–2499.

67 Y. G. Jia, L. J. Han, T. Sun and X. Z. He, *Adv. Mater. Res.*, 2013, **750–752**, 863–866.

68 R. A. Lewthwaite, G. W. Gray and K. J. Toyne, *J. Mater. Chem.*, 1992, **2**, 119–124.

69 A. A. Merlo, O. M. S. Ritter, F. V Pereira, C. H. Vieira and N. P. Silveira, *J. Braz. Chem. Soc.*, 2001, **12**, 184–191.

70 P. J. Shannon, *Macromolecules*, 1984, **17**, 1873–1876.

71 A. Zhou, J. Hu, B. Du, L. Yang and B. Zhang, *J. Appl. Polym. Sci.*, 2006, **100**, 4234–4239.

72 S. Ahn, M. Gopinadhan, P. Deshmukh, R. K. Lakhman, C. O. Osuji and R. M. Kasi, *Soft Matter*, 2012, **8**, 3185–3191.

73 D. Y. Kim, S. A. Lee, M. Park, Y. J. Choi, S. W. Kang and K. U. Jeong, *Soft Matter*, 2015, **11**, 2924–2933.

74 X. Z. He, Y. F. Gao, J. J. Zheng, X. Y. Li, F. B. Meng and J. S. Hu, *Colloid Polym. Sci.*, 2016, **294**, 1823–1832.

75 T. J. White, R. L. Bricker, L. V. Natarajan, S. V. Serak, N. V. Tabiryan and T. J. Bunning, *Soft Matter*, 2009, **5**, 3623–3628.

76 S. Tokunaga, Y. Itoh, Y. Yaguchi, H. Tanaka, F. Araoka, H. Takezoe and T. Aida, *Adv. Mater.*, 2016, **28**, 4077–4083.

77 J.-H. Liu and F.-M. Hsieh, *Mater. Chem. Phys.*, 2009, **118**, 506–512.

78 H. Yang, F. Chen, J. Guo, F. Liu and J. Wei, *Liq. Cryst.*, 2010, **37**, 171–178.

79 C. Huang, C. Horng, C. Chu, S.-Y. Huang, B. You, J.-D. Lin, T. Mo, H. Lin and C. Lee, *Opt. Mater. Express*, 2015, **5**, 1419–1430.

80 C.-K. Liu, A. Y.-G. Fuh, Y.-D. Chen and K.-T. Cheng, *J. Phys. D. Appl. Phys.*, 2010, **43**, 505102.

81 C. K. Liu, K. T. Cheng and A. Y. G. Fuh, *Appl. Phys. Lett.*, 2011, **98**, 10–13.

82 F. Serra, M. A. Matranga, Y. Ji and E. M. Terentjev, *Opt. Express*, 2010, **18**, 575.

83 H. Finkelmann, S. T. Kim, A. Munoz, P. Palffy-Muhoray and B. Taheri, *Adv. Mater.*, 2001, **13**, 1069–1072.

84 J. Schmidtke, W. Stille, H. Finkelmann and S. T. Kim, *Adv. Mater.*, 2002, **14**, 746–749.

85 E. M. Terentjev, Y. Ji, F. Serra, A. R. Tajbakhsh and Y. Hirota, *Opt. Express*, 2008, **16**, 5320.

86 Y. Fuchigami, T. Takigawa and K. Urayama, *ACS Macro Lett.*, 2014, **3**, 813–818.

87 S. M. Wood, F. Castles, S. J. Elston and S. M. Morris, *RSC Adv.*, 2016, **6**, 31919–31924.

88 C. G. Schäfer, M. Gallei, J. T. Zahn, J. Engelhardt, G. P. Hellmann and M. Rehahn, *Chem. Mater.*, 2013, **25**, 2309–2318.

89 S. Całus, M. Busch, A. V Kityk, W. Piecek and P. Huber, *J. Phys. Chem. C*, 2016, **120**, 11727–11738.

90 Y. Xia, E. Lee, H. Hu, M. A. Gharbi, D. A. Beller, E. K. Fleischmann, R. D. Kamien, R. Zentel and S. Yang, *ACS Appl. Mater. Interfaces*, 2016, **8**, 12466–12472.

91 J. H. Noh, K. Reguengo De Sousa and J. P. F. Lagerwall, *Soft Matter*, 2016, **12**, 367–372.

92 J. P. F. Lagerwall and G. Scalia, *Curr. Appl. Phys.*, 2012, **12**, 1387–1412.

93 S. Xu, Z. Nie, M. Seo, P. Lewis, E. Kumacheva, H. A. Stone, P. Garstecki, D. B. Weibel, I. Gitlin and G. M. Whitesides, *Angew. Chemie Int. Ed.*, 2004, **44**, 724–728.

94 E.-K. Fleischmann, C. Ohm, C. Serra and R. Zentel, *Macromol. Chem. Phys.*, 2012, **213**, 1871–1878.

95 A. Fernández-Nieves, *Soft Matter*, 2006, **2**, 105–108.

96 M. Seo, Z. Nie, S. Xu, M. Mok, P. C. Lewis, R. Graham and E. Kumacheva, *Langmuir*, 2005, **21**, 11614–11622.

97 W. Huang and G. F. Tuthill, *Phys. Rev. E*, 1994, **49**, 570–574.

98 O. D. Lavrentovich, *Liq. Cryst.*, 1998, **24**, 117–126.

99 T. Lopez-Leon and A. Fernandez-Nieves, *Colloid Polym. Sci.*, 2011, **289**, 345–359.

100 J. Jiang and D.-K. Yang, *Liq. Cryst.*, 2018, **45**, 102–111.

101 O. O. Prishchepa, V. Y. Zyryanov, A. P. Gardymova and V. F. Shabanov, *Mol. Cryst. Liq. Cryst.*, 2008, **489**, 84–93.

102 D. S. Miller, X. Wang and N. L. Abbott, *Chem. Mater.*, 2014, **26**, 496–506.

103 S. H. Yoon, K. C. Gupta, J. S. Borah, S.-Y. Park, Y.-K. Kim, J. Lee and I. Kang, *Langmuir*, 2014, **30**, 10668–10677.

104 J. K. Gupta, J. S. Zimmerman, J. J. De Pablo, F. Caruso and N. L. Abbott, *Langmuir*, 2009, **25**, 9016–9024.

105 A. Fernández-Nieves, D. R. Link, M. Márquez and D. A. Weitz, *Phys. Rev. Lett.*, 2007, **98**, 087801.

106 P. S. Drzaic, *J. Appl. Phys.*, 1986, **60**, 2142.

107 D. Rudhardt, A. Fernández-Nieves, D. R. Link and D. A. Weitz, *Appl. Phys. Lett.*, 2003, **82**, 2610.

108 R. Arshady, *Colloid Polym. Sci.*, 1992, **270**, 717–732.

109 M. Vennes and R. Zentel, *Macromol. Chem. Phys.*, 2004, **205**, 2303–2311.

110 H. Kawaguchi, *Prog. Polym. Sci.*, 2000, **25**, 1171–1210.

111 D. R. Cairns, M. Sibulkin and G. P. Crawford, *Appl. Phys. Lett.*, 2001, **78**, 2643.

112 G. P. Crawford, R. D. Polak, A. Scharkowski, L.-C. Chien, J. W. Doane and S. Zumer, *J. Appl. Phys.*, 1994, **75**, 1968–1971.

113 A. Fernández-Nieves, G. Cristobal, V. Garcés-Chávez, G. C. Spalding, K. Dholakia and D. A. Weitz, *Adv. Mater.*, 2005, **17**, 680–684.

114 F. Mondiot, X. Wang, J. J. de Pablo and N. L. Abbott, *J. Am. Chem. Soc.*, 2013, **135**, 9972–9975.

115 X. Wang, E. Bukusoglu and N. L. Abbott, *Chem. Mater.*, 2017, **29**, 53–61.

116 X. Wang, E. Bukusoglu, D. S. Miller, M. A. Bedolla Pantoja, J. Xiang, O. D. Lavrentovich and N. L. Abbott, *Adv. Funct. Mater.*, 2016, **26**, 7343–7351.

117 H. Yang, G. Ye, X. Wang and P. Keller, *Soft Matter*, 2011, **7**, 815–823.

118 C. Ohm, M. Brehmer and R. Zentel, *Adv. Mater.*, 2010, **22**, 3366–3387.

119 L. B. Braun, T. Hessberger and R. Zentel, *J. Mater. Chem. C*, 2016, **4**, 8670–8678.

120 C. Ohm, N. Kapernaum, D. Nonnenmacher, F. Giesselmann, C. Serra and R. Zentel, *J. Am. Chem. Soc.*, 2011, **133**, 5305–5311.

121 C. Ohm, C. Serra and R. Zentel, *Adv. Mater.*, 2009, **21**, 4859–4862.

122 C. Ohm, E.-K. Fleischmann, I. Kraus, C. Serra and R. Zentel, *Adv. Funct. Mater.*, 2010, **20**, 4314–4322.

123 E.-K. Fleischmann, H.-L. Liang, N. Kapernaum, F. Giesselmann, J. Lagerwall and R. Zentel, *Nat. Commun.*, 2012, **3**, 1178.

124 G. Cipparrone, A. Mazzulla, A. Pane, R. J. Hernandez and R. Bartolino, *Adv. Mater.*, 2011, **23**, 5773–5778.

125 J. Noh, H.-L. Liang, I. Drevensek-Olenik and J. P. F. Lagerwall, *J. Mater. Chem. C*, 2014, **2**, 806–810.

126 M. Humar and I. Muševič, *Opt. Express*, 2010, **18**, 26995.

127 G. Petriashvili, M. P. De Santo, R. J. Hernandez, R. Barberi and G. Cipparrone, *Soft Matter*, 2017, **13**, 6227–6233.

128 Y. Li, D. Luo and R. Chen, *Appl. Opt.*, 2016, **55**, 8864.

129 J. Fan, Y. Li, H. K. Bisoyi, R. S. Zola, D. Yang, T. J. Bunning, D. A. Weitz and Q. Li, *Angew. Chemie*, 2015, **127**, 2188–2192.

130 L. Wang, D. Chen, K. G. Gutierrez-Cuevas, H. Krishna Bisoyi, J. Fan, R. S. Zola, G. Li, A. M. Urbas, T. J. Bunning, D. A. Weitz and Q. Li, *Mater. Horizons*, 2017, **4**, 1190–1195.

131 H. G. Lee, S. Munir and S. Y. Park, *ACS Appl. Mater. Interfaces*, 2016, **8**, 26407–26417.

132 J. H. Jang and S. Y. Park, *Sensors Actuators, B Chem.*, 2017, **241**, 636–643.

133 D. Wenzlik, C. Ohm, C. Serra and R. Zentel, *Soft Matter*, 2011, **7**, 2340–2344.

134 S. J. Aβhoff, S. Sukas, T. Yamaguchi, C. a Hommersom, S. Le Gac and N. Katsonis, *Sci. Rep.*, 2015, **5**, 14183.

135 H. J. Seo, S. S. Lee, J. Noh, J. Ka, J. C. Won, C. Park, S.-H. Kim and Y. H. Kim, *J. Mater. Chem. C*, 2017, **5**, 7567–7573.

136 K. G. Noh and S. Y. Park, *Mater. Horizons*, 2017, **4**, 633–640.

137 Y. Geng, J. Noh, I. Drevensek-Olenik, R. Rupp, G. Lenzini and J. P. F. Lagerwall, *Sci. Rep.*, 2016, **6**, 2–10.

138 S. S. Lee, S. K. Kim, J. C. Won, Y. H. Kim and S. H. Kim, *Angew. Chemie - Int. Ed.*, 2015, **54**, 15266–15270.

139 S. S. Lee, B. Kim, S. K. Kim, J. C. Won, Y. H. Kim and S. H. Kim, *Adv. Mater.*, 2015, **27**, 627–633.

140 A. Mazzulla, G. Cipparrone, R. J. Hernandez, A. Pane and R. Bartolino, *Mol. Cryst. Liq. Cryst.*, 2013, **576**, 15–22.

141 C. Provenzano, A. Mazzulla, P. Pagliusi, M. P. De Santo, G. Desiderio, I. Perrotta and G. Cipparrone, *APL Mater.*, 2014, **2**, 022103.

142 R. J. Hernández, A. Mazzulla, A. Pane, K. Volke-Sepúlveda and G. Cipparrone, *Lab Chip*, 2013, **13**, 459–467.

143 E. Beltran-Gracia and O. L. Parri, *J. Mater. Chem. C*, 2015, **3**, 11335–11340.

144 N. Leroux, P. Keller, M. F. Achard, L. Noirez and F. Hardouin, *J. Phys. II*, 2003, **3**, 1289–1296.

145 M. J. Unzue, H. A. S. Schoonbrood, J. M. Asua, A. M. Goni, D. C. Sherrington, K. Stahler, K.-H. Goebel, K. Tauer, M. Sjoberg and K. Holmberg, *J. Appl. Polym. Sci.*, 2002, **66**, 1803–1820.

146 R. Henson, MChem Dissertation, University of York, 2010.

147 S. K. Lee, M. Tokita, Y. Shimbo, K. T. Kang, H. Takezoe and J. Watanabe, *Bull. Korean Chem. Soc.*, 2007, **28**, 2241–2247.

148 A. S. Angeloni, M. Laus, D. Caretti, E. Chiellini and G. Galli, *Polym. J.*, 1988, **20**, 1157–1162.

149 E. Chiellini, G. Galli, S. Carrozzino and B. Gallot, *Macromolecules*, 1990, **23**, 2106–2112.

150 C. Pugh and R. R. Schrock, *Macromolecules*, 1992, **25**, 6593–6604.

151 A. de S. Gomes and V. Percec, *J. Polym. Sci. Part A Polym. Chem.*, 1991, **29**, 919–922.

152 V. Percec and D. Tomazos, *Polymer (Guildf).*, 1989, **30**, 2124–2129.

153 G. W. Gray and D. G. McDonnell, *Electron. Lett.*, 1975, **11**, 556–557.

154 G. W. Gray and D. G. McDonnell, *Mol. Cryst. Liq. Cryst.*, 1976, **34**, 211–217.

155 E. Bevis, Masters Thesis, University of York, 2008.

156 K. Kurp, M. Czerwiński and M. Tykarska, *Liq. Cryst.*, 2015, **42**, 248–254.

157 M. Tykarska, R. Dąbrowski, J. Przedmojski, W. Piecek, K. Skrzypek, B. Donnio and D. Guillon, *Liq. Cryst.*, 2008, **35**, 1053–1059.

158 M. Tsukamoto, T. Ohtsuka, K. Morimoto and Y. Murakami, *Jpn. J. Appl. Phys.*, 1975, **14**, 1307–1312.

159 K. C. K. Swamy, N. N. B. Kumar, E. Balaraman and K. V. P. P. Kumar, *Chem. Rev.*, 2009, **109**, 2551–2651.

160 UV Tubes Product Sheet Vilber Lourmat, 2019.

161 M. Muller, R. Zentel and H. Keller, *Adv. Mater.*, 1997, **9**, 159–162.

162 Photoinitiators for UV Curing Key Products Selection Guide 2003 Ciba Specialty Chemicals Incorportated, 2003.

163 Omnicure LX500 Brochure, *Excel. Technol.*

164 H. Leube and H. Finkelmann, *Polym. Bull.*, 1988, **20**, 53–57.

165 H. de Vries, *Acta Crystallogr.*, 1951, **4**, 219–226.

166 V. Percec and D. Tomazos, *Macromolecules*, 1989, **22**, 1512–1514.

167 H. Stevens, G. Rehage and H. Finkelmann, *Macromolecules*, 1984, **17**, 851–856.

168 H. Finkelmann and G. Rehage, *Macromol. Rapid Commun.*, 1982, **3**, 859–864.

169 E. P. Raynes and X. Jia, *Liq. Cryst.*, 2017, **44**, 1960–1967.

170 C. D. Hasson, F. J. Davis and G. R. Mitchell, *Chem. Commun.*, 1998, 2515–2516.

171 C. D. Hasson, F. J. Davis and G. R. Mitchell, *Mol. Cryst. Liq. Cryst.*, 1999, **332**, 155–162.

172 G. Palaprat, J. D. Marty, D. Langevin, H. Finkelmann and M. Mauzac, *J. Phys. Chem. B*, 2007, **111**, 9239–9243.

173 J. C. Dubois, P. Le Barny, M. Mauzac and C. Noer, *Acta Polym.*, 1997, **48**, 47–87.

174 Y. Hsiao, Y. Sung, M.-J. Lee and W. Lee, *Biomed. Opt. Express*, 2015, **6**, 5033–5038.

175 T. Benelli, L. Mazzocchetti, G. Mazzotti, F. Paris, E. Salatelli and L. Giorgini, *Dye. Pigment.*, 2016, **126**, 8–19.

176 D. J. Mulder, A. P. H. J. Schenning and C. W. M. Bastiaansen, *J. Mater. Chem. C*, 2014, **2**, 6695–6705.

177 J. D. Marty, H. Gornitzka and M. Mauzac, *Eur. Phys. J. E*, 2005, **17**, 515–520.

178 Y. Mao, E. M. Terentjev and M. Warner, *Phys. Rev. E*, 2001, **64**, 041803.

179 A. Varanytsia, H. Nagai, K. Urayama and P. Palffy-Muhoray, *Sci. Rep.*, 2015, **5**, 1–9.

180 A. S. Utada, L.-Y. Chu, D. R. Fernandez-Nieves, A.Link, C. Holtze and D. A. Weitz, *MRS Bull.*, 2011, **32**, 702–708.

181 R. K. Shah, H. C. Shum, A. C. Rowat, D. Lee, J. J. Agresti, A. S. Utada, L. Y. Chu, J. W. Kim, A. Fernandez-Nieves, C. J. Martinez and D. A. Weitz, *Mater. Today*, 2008, **11**, 18–27.

182 S.-Y. Teh, R. Lin, L.-H. Hung and A. P. Lee, *Lab Chip*, 2008, **8**, 198.

183 N. Bremond and J. Bibette, *Soft Matter*, 2012, **8**, 10549.

184 L. Shang, Y. Cheng and Y. Zhao, *Chem. Rev.*, 2017, **117**, 7964–8040.

185 P. B. Umbanhowar, V. Prasad and D. A. Weitz, *Langmuir*, 2000, **16**, 347–351.

186 A. S. Utada, E. Lorenceau, D. R. Link, P. D. Kaplan, H. A. Stone and D. A. Weitz, *Science (80-.).*, 2005, **308**, 537–541.

187 A. R. Abate, A. Poitzsch, Y. Hwang, J. Lee, J. Czerwinska and D. A. Weitz, *Phys. Rev. E*, 2009, **80**, 026310.

188 C. Serra, N. Berton, M. Bouquey, L. Prat and G. Hadziioannou, *Langmuir*, 2007, **23**, 7745–7750.

189 A. S. Utada, A. Fernandez-Nieves, H. A. Stone and D. A. Weitz, *Phys. Rev. Lett.*, 2007, **99**, 1–4.

190 S. L. Anna, N. Bontoux and H. A. Stone, *Appl. Phys. Lett.*, 2003, **82**, 364–366.

191 C.-H. Yeh and Y.-C. Lin, *Microfluid. Nanofluidics*, 2008, **6**, 277–283.

192 B. D. Hamlington, B. Steinhaus, J. J. Feng, D. Link, M. J. Shelley and A. Q. Shen, *Liq. Cryst.*,

2007, **34**, 861–870.

193 P. Wu, Y. Wang, Z. Luo, Y. Li, M. Li and L. He, *Lab Chip*, 2014, **14**, 795–798.

194 T. Li, L. Zhao, W. Liu, J. Xu and J. Wang, *Lab Chip*, 2016, **16**, 4718–4724.

195 R. M. Erb, D. Obrist, P. W. Chen, J. Studer and A. R. Studart, *Soft Matter*, 2011, **7**, 8757–8761.

196 E. Mendizabal, J. R. Castellanos-Ortega and J. E. Puig, *Colloids and Surfaces*, 1992, **63**, 209–217.

197 Y. Iwai, H. Kaji, Y. Uchida and N. Nishiyama, *Mol. Cryst. Liq. Cryst.*, 2015, **615**, 9–13.

198 M. Mohsen-Nia and H. Modarress, *J. Adhes. Sci. Technol.*, 2006, **20**, 1273–1280.

199 Y. Ebata, A. B. Croll and A. J. Crosby, *Soft Matter*, 2012, **8**, 9086–9091.

200 O. K. C. Tsui and T. P. Russell, Eds., *Polymer Thin Films*, World Scientific Publishing Co, Singapore, 2008.

201 H. Lei, L. F. Francis, W. W. Gerberich and L. E. Scriven, *AIChE J.*, 2002, **48**, 437–451.

202 S. H. Kang, J. H. Na, S. N. Moon, W. Il Lee, P. J. Yoo and S. D. Lee, *Langmuir*, 2012, **28**, 3576–3582.

203 A. Agrawal, P. Luchette, P. Palffy-Muhoray, S. L. Biswal, W. G. Chapman and R. Verduzco, *Soft Matter*, 2012, **8**, 7138–7142.

204 S. H. Im, U. Jeong and Y. Xia, *Nat. Mater.*, 2005, **4**, 671–675.

205 H. Hirschmann, P. M. S. Roberts, F. J. Davis, W. Guo, C. D. Hasson and G. R. Mitchell, *Polymer (Guildf).*, 2001, **42**, 7063–7071.

206 E. Saiz, E. Riande and J. E. Mark, *Macromolecules*, 1984, **17**, 899–902.

207 J.-H. Lee, T. Kamal, S. V. Roth, P. Zhang and S.-Y. Park, *RSC Adv.*, 2014, **4**, 40617–40625.

208 L. R. Gatechair and D. Wostratzky, in *Adhesive Chemistry*, Springer US, Boston, MA, 1984, pp. 409–438.

209 D. J. Broer, *Curr. Opin. Solid State Mater. Sci.*, 2002, **6**, 553–561.

210 P. Prinsen and P. van der Schoot, *Phys. Rev. E*, 2003, **68**, 11.

211 R. Zhang, Y. Zhou, J. A. Martínez-González, J. P. Hernández-Ortiz, N. L. Abbott and J. J. De Pablo, *Sci. Adv.*, 2016, **2**, 1–7.

212 A. B. Pawar, M. Caggioni, R. W. Hartel and P. T. Spicer, *Faraday Discuss.*, 2012, **158**, 341–350.

213 M. Caggioni, J. Lenis, A. V. Bayles, E. M. Furst and P. T. Spicer, *Langmuir*, 2015, **31**, 8558–8565.

214 M. Caggioni, A. V. Bayles, J. Lenis, E. M. Furst and P. T. Spicer, *Soft Matter*, 2014, **10**, 7647–7652.

215 Y. Hong, A. Buguin, J. M. Taulemesse, K. Kaneko, S. Méry, A. Bergeret and P. Keller, *J. Am. Chem. Soc.*, 2009, **131**, 15000–15004.

216 X. Wang, E. Bukusoglu, D. S. Miller, M. A. Bedolla Pantoja, J. Xiang, O. D. Lavrentovich and N. L. Abbott, *Adv. Funct. Mater.*, 2016, **26**, 7343–7351.

217 A. Belmonte, T. Bus, D. J. Broer and A. P. H. J. Schenning, *ACS Appl. Mater. Interfaces*, 2019, **11**, 14376–14382.